Using Sea-Level Data to Constrain the Contribution of the Greenland Ice Sheet to Contemporary and Recent Sea-Level Change

LEANNE MARY WAKE

Using Sea-Level Data to Constrain the Contribution of the Greenland Ice Sheet to Contemporary and Recent Sea-Level Change

Leanne Mary Wake

This thesis is submitted for the degree of Doctor of Philosophy at Durham University

Department of Earth Sciences

2010

Abstract

Due to the potentially wide-reaching impacts on climate and sea-level change of a declining Greenland Ice Sheet (GrIS), the mass balance of the past decade has caused concern that the ice sheet is reacting to increased temperatures of the industrial era and that the ice sheet is in the initial stages of deglaciation. Global mean sea-level has been rising at a rate of 1.8 +/- 0.5 mm/yr over the past 50 years (Bindoff et al. 2007), and this has accelerated to 3.1 +/- 0.1mm/yr (Cazenave et al., 2008) over the past decade. This study shows that although the surface mass balance of the GrIS can react quickly to changes in temperature, overall the ice sheet is in near balance over the period 1866-2005. During 1866-2005, the contribution from the GrIS to eustatic sea-level change is not larger than the error attached to current estimates of global mean sea-level rise.

A novel type of relative sea-level data gathered from salt marshes in the south west of Greenland cover the period from ~1200 to 1800AD and show that a major slowdown in local sea-level rise from ~3mm/yr to ~0mm/yr occurred around 1500-1600 AD, with no significant departure from a 0mm/yr trend thereafter. Large contributions to sea-level change from steric changes and cryospheric sources outside of Greenland are ruled out as major drivers of this deceleration in sea-level fall. Modelling results indicate that the slowdown in relative sea-level is most likely due to the combined contribution of dynamic-related ice loss from Jakobshavn Isbrae and a delayed earth response to mass loss during a period of elevated temperatures from ~1000-1500AD. When considering the saltmarsh sea-level data for the 20th century within the context of the complete time series, the magnitude of ice loss in west Greenland for the past decade does not appear to be anomalous. This analysis suggests that similar mass loss has been sustained for several centuries prior to 1500AD.

Declaration

Sections of this thesis have been approved for publication. The final published articles are supplied with this thesis:

From Chapter 3:
Wake, L. M., Milne, G. A. and Leuliette, E. *20th Century sea-level change along the eastern US: Unravelling contributions from steric changes, Greenland ice sheet balance and Late Pleistocene glacial loading*. Earth and Planetary Science Letters, 2006. **250**: p570-580.

From Chapter 5:
Wake, L. M., Huybrechts, P., Box, J. E., Hanna, E., Janssens, I. and Milne, G. A. *Surface mass-balance changes of the Greenland ice sheet since 1866*. Annals of Glaciology, 2009. **50**: p178-184.

All work presented in this thesis is the author's original contribution. Exceptions are declared and contributors duly acknowledged in the following statements:

Chapter 3:
The analysis in Section 3.4 and presented in Fig. 3.2c was performed by E. Leuliette, co-author on the publication derived from Chapter 3.

Chapter 5:
The data described in Section 5.2 and illustrated in Fig. 5.1 were provided by J. E. Box and E. Hanna, co-authors on the publication derived from Chapter 5.

Acknowledgements

I would like to thank the following people, for the following reasons:

Glenn Milne (University of Ottawa), who has contributed in all aspects of my university life since 2003. I am grateful for his advice on academic matters during both my undergraduate and postgraduate years at Durham and the inspiration to continue research into the causes of sea-level change. Also, thanks to Glenn's family; Sylvie, Benoit and Beatrice, for hospitality and for showing me all that is great about Ottawa and Ontario.

Antony Long and Sarah Woodroffe (Durham University), for allowing me on data collection field trips in Greenland. Apart from invaluable background knowledge, the field trips made an incredible difference to this thesis by making me appreciate the beauty and importance of Arctic landscapes. I am also now painfully aware of the amount of back-breaking graft needed to produce a single relative sea-level record.

Philippe Huybrechts (Vrije Universiteit Brussel) for advice on the ice modelling performed in this study, central to achieving the main project aims.

My Parents, Helen and Norman. I thank them for unwavering support and understanding throughout, but especially for a roof over my head during the breadline months of the PhD continuation year.

Liam Shaw, Mike Mawby, Matt Simpson, Jim White, Dean Wilson, Sarah Bradley, Chris Mallows, Rich Walker, Alan Rooney, Jen Waters, Dougal Jerram, Dave Selby, Alex Finlay, Gary Wilkinson, for friendship, field trips, football, large dry white wines and general hilarity during work and pub hours.

Thanks to Dave Stevenson, Gary Wilkinson (again) and the Admin staff at Durham University Earth Sciences Department for their quick responses to frivolous and sometimes laughable IT and Admin problems.

This research was funded by the Durham University Doctoral Fellowship Scheme

Contents

List of Figures

List of Tables

Page

Chapter 1: Project Background

1.1 Overview

In the last decade, much attention has been focussed on the changing environment of the Arctic due to the increase in global temperatures as demonstrated in the publication of the 'hockey-stick' curve. (Mann et al., 1998). The dataset places the temperatures of the past decade within the context of the last millennium, and appears to show that during the last ten years global temperatures have been anonymously high. Concern in the media has centred upon anthropogenic-related global warming being the primary cause of the intensification of extreme weather (e.g. tropical storms, drought), accelerated sea-level change and retreat and increased discharge of outlet glaciers in Greenland, specifically over the period from 1986-2000 (Joughin et al., 2004).

The position of Greenland renders the ice sheet more vulnerable to global warming compared to the Antarctic ice sheets. This is due to its proximity to other ice-free landmasses and the effect these exert on regional heat convection, and by extension, regional Greenlandic temperatures. Although complete melting of Antarctic ice would result in a global mean sea-level rise almost ten times that of Greenland ice (~55 m compared to ~7 m), the future of Greenland retains media interest because of its high vulnerability to warming and the impact its shrinkage would have on a number of factors, including, for example, ocean circulation, global weather patterns and the future of some of the worlds most endangered animal species (e.g. polar bears). Ice sheets play an integral part in modulating the temperature of the entire planet by regulating the net planetary albedo. This makes it vital to quantify the behaviour of the Greenland ice sheet (GrIS) during earlier periods of climatic extremes in order to better predict its future response to projected warming.

The main motivation behind this study is to improve the estimates of GrIS mass balance over the past few centuries. Global sea-level rise over the latter half of the 20th century is estimated at 1.8 +/-0.5 mm/yr (Bindoff et al. 2007), of which Greenland ice is estimated to contribute between 0 and 0.6mm/yr. Direct monitoring of mass changes of the GrIS using satellites indicates that the contribution since 2002 has moved towards 0.6mm/yr. However, just as in global sea-level change estimates, it is unclear whether this is the result of decadal variations, or the beginning of a long-term trend.

This study aims to reduce the uncertainty on Greenland's contribution to sea-level change during the past few centuries by using proxy sea-level data obtained on the west coast of Greenland, as well as tide gauges along the US east coast, to isolate the sea-level signal associated with mass changes of the GrIS. Sea-level data obtained from salt marshes are able to track sea level over century to decadal timescales, but, as yet, no such records have been collected and analysed from Greenland. This study will also bring to light any inadequacies in ice sheet and sea-level modelling (and field techniques) that need to be addressed to in order to improve estimates of recent GrIS mass changes using sea-level observations.

In this chapter, I provide background on the present-day extent of the ice sheet and its regional setting in terms of geology, oceanography and climate. These settings are used to define the boundary conditions for the models used in this thesis. Observational and modelling constraints on past changes of the ice sheet (up to the last glacial maximum) are also reviewed, given that the key aim of this thesis is to add to these constraints for the past few centuries. The chapter is concluded by defining the aims and importance of this thesis in greater detail

1.2 Present Day Extent and Regional Setting

Greenland is the biggest island on Earth, with a surface area of ~2,166,000 km^2 of which 1,756,000 km^2 are ice-covered (Henriksen et al. 2000). The largest areas of exposed land lie in the extreme north and south west. The volume of the GrIS is estimated at 2.9 x 10^6 km^3 i.e. (ice equivalent) which accounts for ~ 10% of the worlds ice (Lemke et al. 2007). As well as the ice sheet itself, some of the world's most active outlet glaciers are located in Greenland (see Fig. 1.1). The largest and most extensively studied outlet glacier in the world is Jakobshavn Isbrae. This drains ~ 7% of the ice sheet and is currently discharging ~ 50km^3 of ice per year (Rignot and Kanagaratnam, 2006). Due to the steep topography on the east coast, many outlet glaciers are able to form through the steep sided fjords. Kangerdlugssuaq and Helheim are the largest in the east, discharging 27.8 and 26.3 km^3 per year respectively in the period 1996-2000. Recent measurements (Rignot and Kanagaratnam, 2006) show that glaciers contained in the boxed area in Fig. 1.1 are discharging ~ 67km^3 of ice per year. Ice divides are created by the flow regime of the ice, which is mainly determined by bedrock topography. In general, ice flows from the centre of the ice sheet to the

margins. This creates the noticeable north-south ice divide on Fig. 1.1. Ice divides that strike approximately east-west delineate regimes with slightly different flow vectors. The largest flow regimes by area are located in the western segment of the ice sheet, where ice flow is uninterrupted due to the relatively shallow bedrock gradient compared to the east.

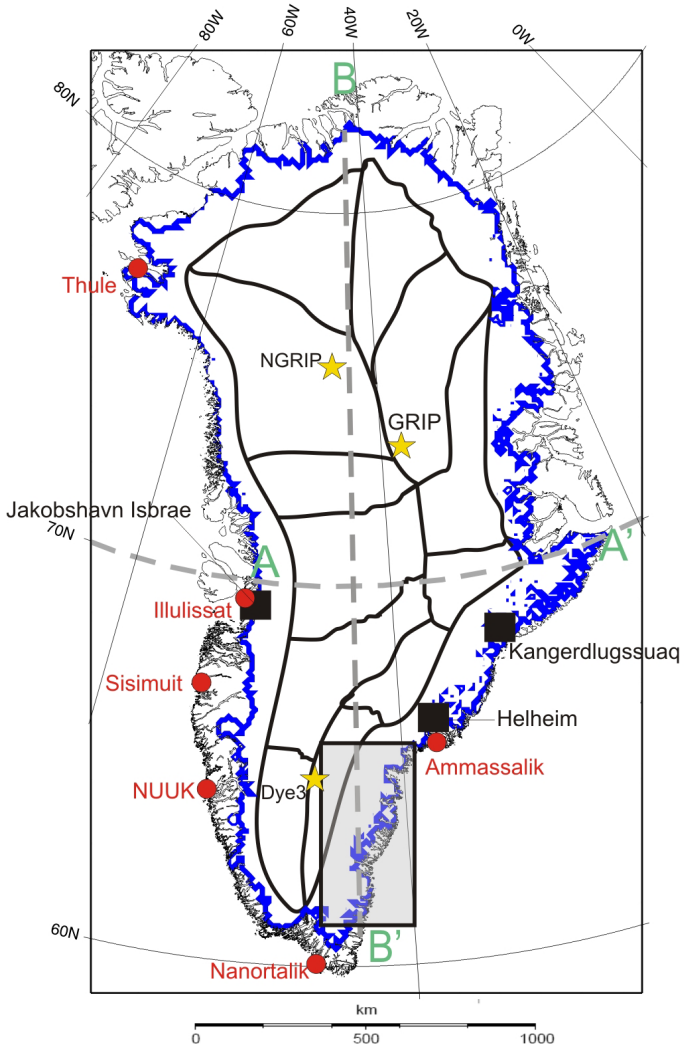

Fig. 1.1: Map of Greenland showing present day ice margin extent (blue). Major towns are shown in red (capital city: Nuuk), and the largest outlet glaciers are marked with black squares. Rectangular box shows approximate area occupied by outlet glaciers in the south. Locations of selected ice cores mentioned in the text are denoted by yellow stars. Black lines delineates approximate position of ice divides in Greenland (adapted from Thomas, 2001). Dashed grey lines show position of cross-sections A/A' and B/B' in Fig. 1.2, and scale shows 1000km distance at a constant latitude of 70°N.

The geology of the bedrock under the ice sheet is largely unknown but the inland and offshore bedrock topography is shown in Fig. 1.3. Two notable features are the linear topographic lows offshore in south-east Greenland at 66°N, 31°W and 65°N, 34°W. A third significant low striking south-west is located at 69°N, 62°W. These features are located on the ocean floor at the outlet of three major

calving glaciers: Kangerdlussuaq, Helheim and Jakobshavn Isbrae, respectively. The lineations on the ocean floor are located at 200m to 300m below sea level and offshore Jakobshavn Isbrae, iceberg plough marks have been found at depths of ~1km (Kuijpers et al. 2007) indicating that these troughs may have been shaped by icebergs and ice sheet advance/retreat across the continental shelf. The continental shelf edge is clearly delineated at the -1000m contour. This extends into the centre of Baffin Bay in the west. The continental shelf is up to 250km in width offshore south-east Greenland and 300km in the north east. The relatively shallow shelf areas enabled extension of the GrIS onto the shelf and up to the shelf edge in some areas when sea levels were low at the Last Glacial Maximum. Onshore bedrock elevation reaches a minimum of -300m in the centre of Greenland. Bedrock highs of > 2000m are found in the southern and eastern coastal margins of Greenland. On the west, above latitude 67^{o}N, the bedrock generally remains below 1000m.

There are two distinct topographic highs in Greenland (Fig. 1.3, bottom). The summit of Greenland reaches >3200m in height and lies in the central part of the ice sheet at latitude 73^{o}N with a smaller topographic high located at the southern part of the ice sheet, at 2500m in elevation. The area in between these two domes is known as the 'Saddle' area. The topography of the western section of Greenland between 65^{o}N and 70^{o}N is less steep compared to the south and east, as reflected in the bedrock topography. The GrIS follows the typical lenticular shape, with the thickest ice (3000m) located in the central area of the ice sheet (Fig. 1.3, centre). The ice sheet feeds into the ocean in south-east Greenland, via the numerous ice streams in the steep fjords. Unlike Antarctica, there are no major floating ice shelves, but the ice sheet margin almost reaches sea level in the north-west at Thule. In order to visualise the relationship between bedrock elevation, ice thickness and surface elevation, two cross-sections are shown in Fig. 1.2. The profile located at latitude 70^{o}N (Fig. 1.2, A-A') highlights how the steep topography dominates the south east coast of Greenland. At 800km, once the ice sheet reaches the steep topography of the east, it is broken up into a series of ice caps, less that 0.5km thick.

The ice sheet thins in areas where the bedrock topography is steep, due to enhanced flow on the slope. This effect is apparent at 1600km along the profile in Fig. 1.2 (B-B'). Maxima in ice thickness correspond to minima in bedrock gradient (e.g. between 400km and 1600km in Fig. 1.2 B-B'). The north-south profile (B,B') captures the two peaks in surface elevation on the ice sheet. At 1000km, the

heightened elevation is the result of maximum ice thickness. In the south (1900km), the topographic high of 2700m is mainly due to elevated bedrock.

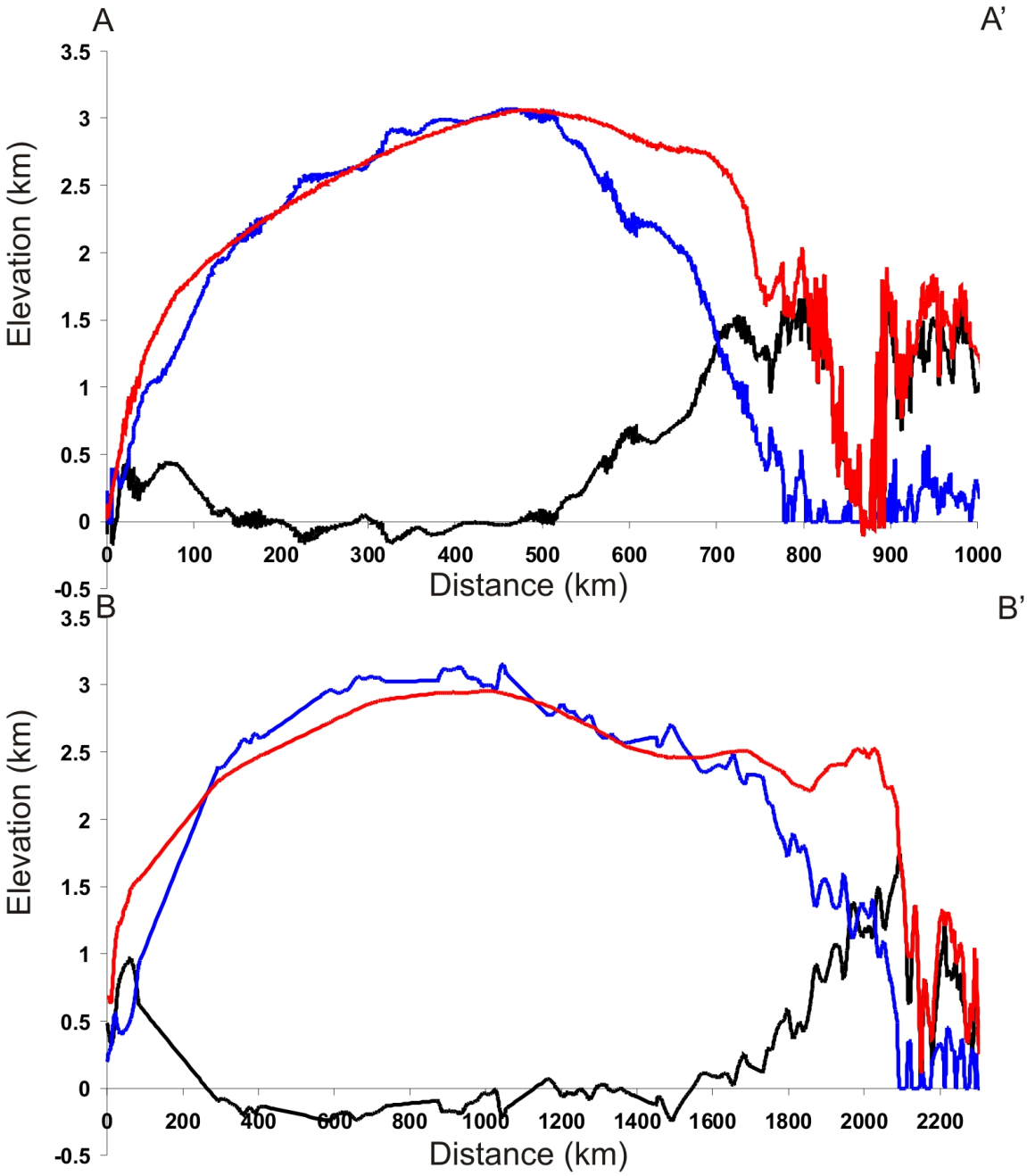

Fig. 1.2: Cross sections across Greenland at 70°N (A, A') and 43°W (B, B') generated from a 5 x 5km digital elevation model (Bamber 2001a) and bedrock and ice thickness grids (Bamber et al. 2001b), available at www.noaa.nodc.gov. Lines correspond to bedrock elevation (black), ice thickness (blue) and total surface elevation (red) above mean sea level. Distance is corrected for variation with latitude. See map in Fig. 1.1 for location of cross sections

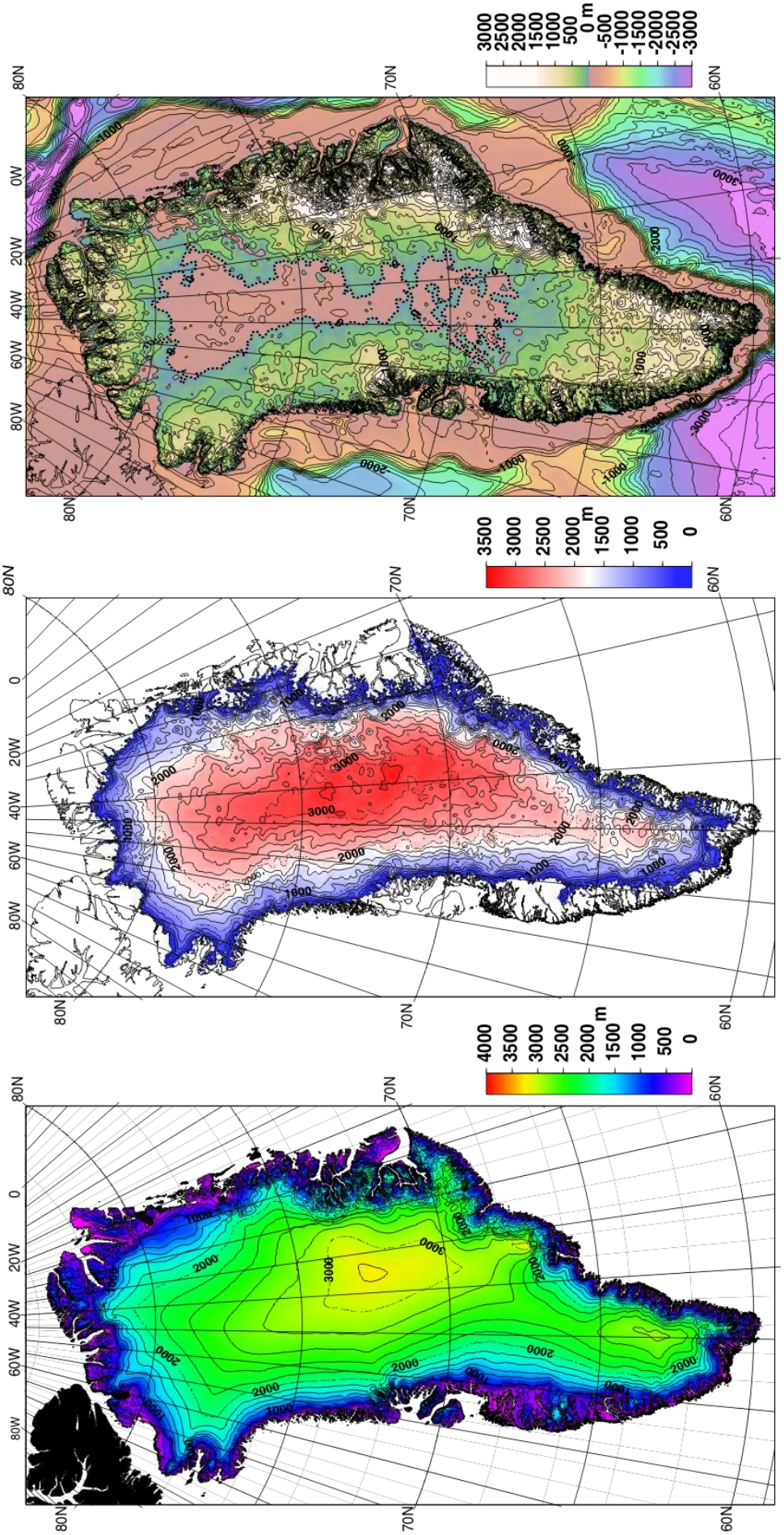

Fig. 1.3: Maps of Greenland surface elevation (bottom), ice thickness (centre) and bedrock elevation (top) determined from Digital Elevation Models (Bamber et al., 2001a and 2001b).

1.3 Regional Earth Structure and Geology

The geology of Greenland spans the last 4 billion years of Earth history. The oldest rocks in Greenland have three distinct ages and make up ~50% of the exposure (Fig. 1.4, left). The geology of Greenland is not of major significance to the aims or methodology of this study and so descriptions of rock facies are generalised. The rock type and crustal thickness distribution does, however, influence the local glaciology. Also, the crust is part of the lithosphere and so the thickness and distribution of rocks in this layer will influence the isostatic deformation (and therefore sea-level change) induced by mass changes of the GrIS. The lithosphere is the outermost section of the solid Earth and consists of the crust and uppermost mantle. The lithosphere-asthenosphere boundary is defined on the basis of the deformational behaviour of mantle rocks. The lithosphere is colder than the underlying asthenosphere and so is mechanically stronger (with some parts acting elastically over long timescales). Seismic inferences of the lithospheric thickness below Greenland give values that range from 100 – 180km (Darbyshire et al. 2004), with the thinnest (<100km) areas being in the south-east of Greenland near Kangerdlugssuaq, and the thickest lithosphere underlying central-southern Greenland. This is echoed to a degree in a study by Kumar et al. (2005), although this later study disagrees with Darbyshire et al. (2004) on the absolute values of lithospheric thickness in south-east Greenland (70km). In general, the lithosphere thickens from east to west (Kumar et al. 2005), which is not reflected in the plot of crustal thickness in Fig. 1.4 (right). Minima in crustal thickness of 33-35km act as conduits to known major ice streams feeding outlet glaciers, indicating that the ice streams may be partially driven by warm basal conditions.

The oldest rocks are located either side of the Ketildean mobile belt in south Greenland. In the western section of the Archaen craton, the formation is made up of highly metamorphosed sequences so the high rates of deformation and inconsistent ages of the rocks make determination of their sources difficult. The earliest Protorezoic rocks are located in the north-east of Greenland in the Caldeonian fold belt region (Fig. 1.4, left). Sandstones interbedded with siltstones indicate that the area was generally subsiding and changing to a lacustrine environment (Henriksen et al. 2000). These are overlain by flood basalts grading from pillow basalts to sub-aerial lavas. In the extreme east of Greenland between 70^{o}N and 76^{o}N, the succession of Protorezoic rocks covers the age range of 2000Myr ago to the start of the Palaeozoic and is up to 8km thick (Henriksen et al. 2000).

Protorezoic rocks found in the south of Greenland cover the mid-Protorezoic era (~1200 Myr ago), and are comprised of sediments: fluvial and desert quartzitic sandstones grading into conglomerates which are indicative of movement towards a dry continental setting. These are overlain by a volcanic sequence of basaltic lavas (Henriksen et al. 2000).

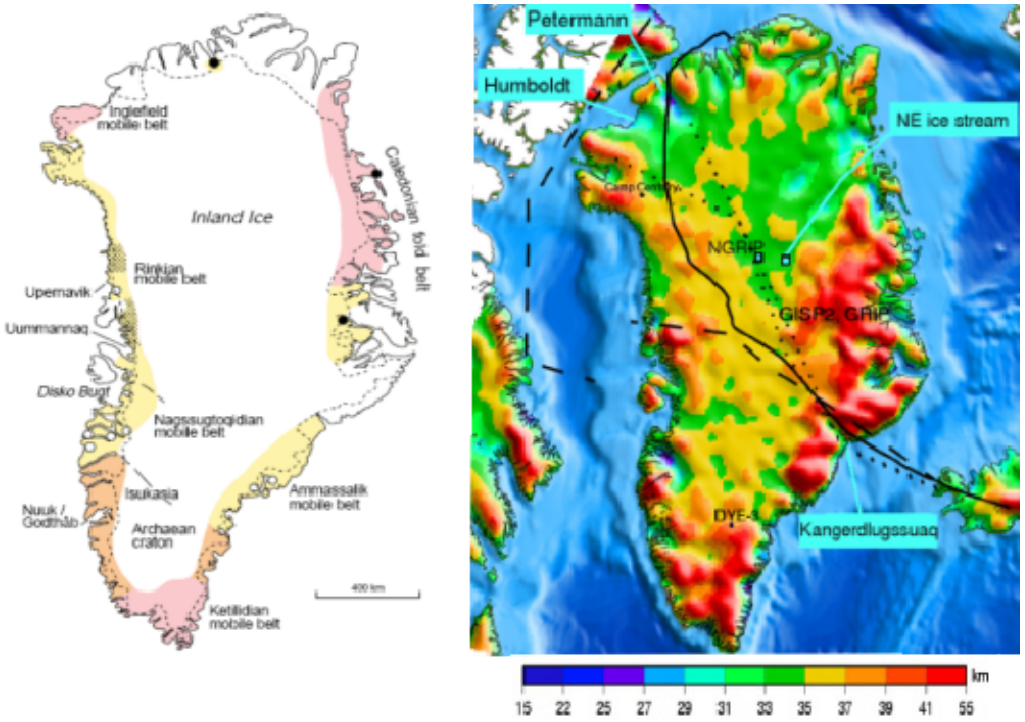

Fig. 1.4: Left image shows simplified geological map showing the oldest units exposed in Greenland: Archaen craton, 2600–3100 million years old (orange); Reworked Archaen-sourced metasediments, 1850 million years old (yellow); Early Protorezoic terrain, 1750-2000 million years old (pink). White areas: units younger than 1750 million years and inland ice. From Henriksen et al. (2000). Right image shows crustal thicknesses obtained from an isostatic analysis by Braun et al. (2007).

The relatively young sequences in Greenland are found in the extreme north of Greenland and between the Caledonian and Ammassalik mobile belts in the east (Fig. 1.4, left). In east Greenland, the Cambro-Ordovician (550-440 Myr ago) period is dominated by a ~4km thick succession of limestone-dolomite sequences. Rocks of Silurian age are not identified in eastern Greenland, and Devonian rocks lying unconformably on Silurian age sediments show a shift from a shallow marine to a continental setting. Conglomeritic and fluvial sandstones interbedded with volcaniclastic sediments are deposited due to renewed E-W extensional faulting related to the opening of the North Atlantic Ocean. Rifting episodes in the east of Greenland occurred throughout the mid Phanerozoic, turning the east of Greenland into a major depositional centre. At 250 Myr ago, continental / shallow marine conditions dominated with deposition of alluvial fan sediments, evaporites and

carbonates. These grade into deep marine shales, indicating marine incursion at this time.

In north Greenland, the early Phanerozoic (560-410 Myr ago) is represented by a succession of folded deep basin sediments. The Lower Carboniferous (370 – 350Myr ago) in north Greenland is characterised by interbedded sandstones and siltstones deposited on a folded Caledonian basement. From the mid Carboniferous until the late Permian (~350-250 Myr ago) the sequence is made up of shelf carbonates. As in east Greenland, marine transgression occurred in the Triassic and carried on until ~ 140Myr ago until the depositional setting transformed from marine-deltaic to fully marine recognised by extensive deposition (0.5-1km thickness) of mudstones.

Until 90Myr ago, Greenland was connected to Baffin Island and Eurasia. The advent of sea-floor spreading in the North Atlantic and the Labrador Sea region between 50 and 70 Myr ago caused Greenland to separate and become an island by ~ 30Myr ago (Braun et al., 2007). In the west of Greenland, 4-10km of iron-rich basaltic lavas, picrites and intermittent hyaloclastic lavas indicative of subaqueous eruption overlie the marine mudstones of the late Phanerozoic. The entire eruption episode is thought to have taken place over 2 million years. The east of Greenland contains both intrusive and extrusive Tertiary igneous sequences. During the Eocene period, the beginnings of an ice cap began to form in Greenland as evidenced by glacial deposits discovered in waters off the coast of east Greenland dated to 30-44 Myr ago (Eldrett et al. 2007, Tripati et al. 2008).

1.4 Oceanographic and Atmospheric Setting

Greenland is located in a important oceanographic setting (Fig 1.5). The Gulf Stream transports warm water to northern latitudes and so has a large effect on climate in the North Atlantic. In fact, this mechanism is thought to have played a role in the build-up of ice sheets at 2.7Myr ago when the Isthmus of Panama closed, diverting the Gulf Stream into the North Atlantic (Driscoll and Haug, 2008). The recycling of water from the Gulf Stream to form North Atlantic Deep Water is known as themohaline circulation, or Meridonal Overturning Circulation. The formation of North Atlantic Deep Water occurs on the east coast of Greenland, and to a lesser extent in Baffin Bay area. Salt water cools and sinks due to the increased density and is transported southwards at depths of 2-4km. Excessive freshwater input from the Arctic and North Atlantic is predicted to cause slow-down and eventual cessation of

thermohaline circulation by reducing the salinity of waters sinking offshore of Greenland.

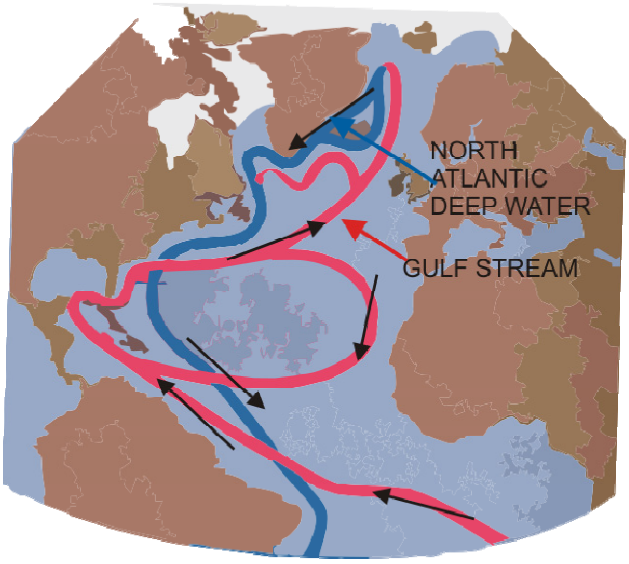

Fig. 1.5: The location of Greenland with respect to the important global ocean current systems, illustrating the Meridonal Overturning Circulation. Adapted from Ruddiman (2001).

One of the dominant weather patterns in the North Atlantic Ocean is the persistent low pressure that resides over Iceland and south-east Greenland. Coupled with the permanent high pressure that exists over the Azores, the relative strengths and position of the two systems dictate weather patterns over Europe. This is known as the North Atlantic Oscillation (NAO). A 'positive' NAO phase occurs when the pressure difference between the two systems is large, causing cool and wet conditions over the North Atlantic and Europe. In a negative phase, both pressure systems are relatively weak, so the pressure difference is small, resulting in deflection of warmer air towards Greenland.

1.5 Constraints on the Past behaviour of the GrIS

1.5.1: Methodology

Recent changes in the GrIS can be inferred directly from satellite observations of changes in spatial extent and thickness (altimetry), ice velocity (interferometry) and mass distribution (gravity). Direct constraints on ice extent prior to the satellite era are available for some areas from photographs or repeat surveys going back several decades; for earlier times, going back centuries to millennia, ice extent can be inferred from geological landforms (e.g. terminal and lateral moraines and glacial trimlines) associated with glacial erosion and deposition. Note, however, that prior to the satellite era, the spatial resolution of the data is low and so estimating

mass changes over large scales is difficult. For this reason, measurements of observables affected by changes in the ice sheet (i.e. relative sea level in the near or far-field and present-day land motion in Greenland) have been used as an additional, indirect constraint, to determine changes over multi-decadal to millennial scales. A brief summary of the main observational techniques is given below. Fig. 1.6 illustrates the temporal resolution and coverage of the methods discussed.

In contrast to sea-level data, large scale geodetic monitoring of the ice sheets is less than 20 years old, and so does not provide the long term picture needed for comparison to the sea-level datasets. To date, the most sophisticated method of measuring redistribution of mass within the cryosphere has been applied via the GRACE (Gravity Recovery and Climate Experiment) mission. The GRACE satellites are designed to track changes in the Earth's gravity field and have been in orbit at 500km above the Earth's surface since 2002. GRACE is made up of two satellites 220 km apart and linked by a microwave ranging system. Changes in the distance between the satellites are activated by the passage of the satellite over areas of strongly contrasting gravity. These changes are used to determine maps of the gravity field every month. These monthly maps can then be compared to determine where gravity is declining (e.g. in a region where ice is being lost) or strengthening.

Airborne laser altimetry measures the elevation of ice sheets. Typically, a scanning laser is mounted in a aircraft that flies ~ 500m above the ice surface (Krabill et al. 2002), and repeat surveys are flown along identical tracks several years later to determine overall elevation change. To provide an ice sheet-wide picture of elevation changes, the data are interpolated between flight lines. The accuracy of this method for measuring elevation change is in the range of 7.1-8.5 cm (Krabill et al. 2002).

The ERS Satellite (data mentioned in Table 1.1) is comprised of a radar altimeter and an imaging Synthetic Aperture Radar (SAR). Satellite radar altimetry is similar to laser altimetry, except that radar pulses are sent and received by sensors on the satellite. Differences in the round-trip time of a radar pulse are measured and translated into change in surface elevation on an ice sheet. Imagery of large scale features of an ice sheet, such as crevasses, may be generated from comparing the amplitude and form of the return wave. InSAR data involves combining images from the SAR at different points in time to create an 'Interferogram', describing changes in the ice surface in three dimensions, as a function of time. This data type is most commonly employed to measure velocity of the ice sheet surface and thus calculate estimates of ice flux and discharge (e.g. Rignot et al., 2008).

Tide gauges provide sub-annual resolution of local relative sea-level changes. However, the signal is dominated by oceanographic processes on sub-annual to decadal time scales. To isolate a potential signal associated with contemporary GrIS mass changes, time series of several decades are required to filter out the shorter-term oceanographic signals. The resulting secular trend can originate from a variety of processes - e.g. tectonic movement, on-going isostatic land motion in response to past ice mass changes, steric changes - making the interpretation in terms of contemporary ice mass changes difficult (see Chapter 3).

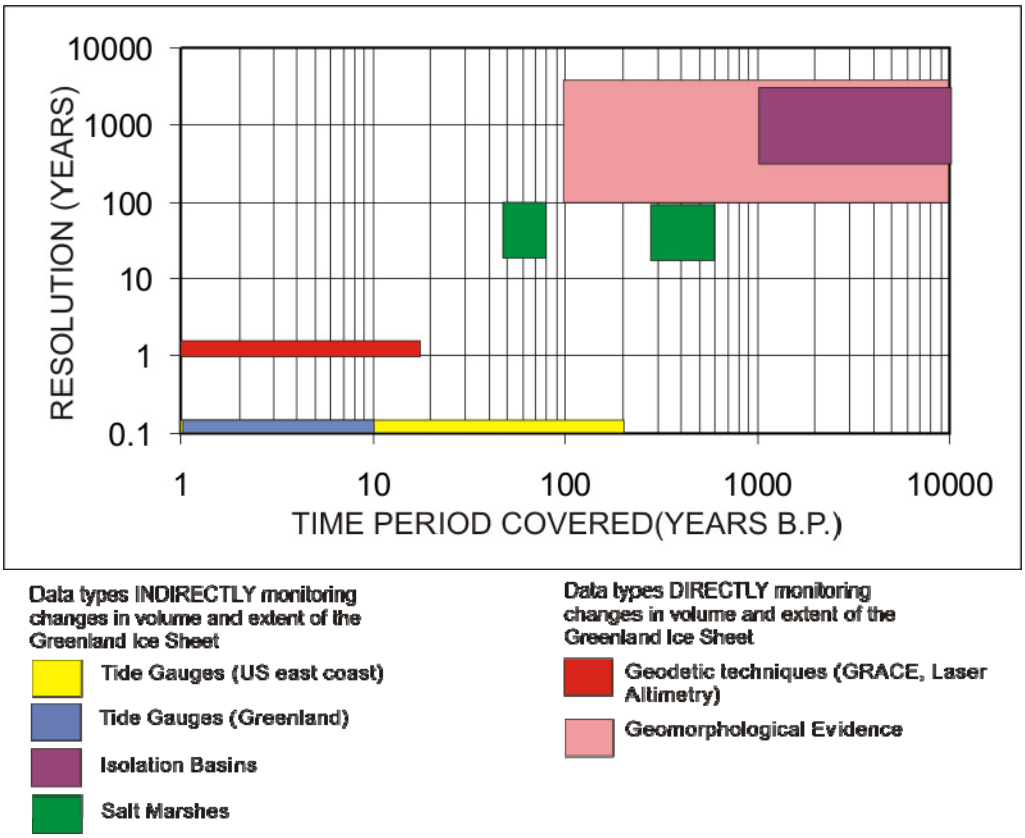

Fig. 1.6: Diagram highlighting data types employed and reviewed in this study, their time span and temporal resolution

Salt marsh sediments which reflect changing sea level will show basal freshwater peats grading into mid-high marsh sediment. The temporal resolution of the salt-marsh data is dependent on the local sedimentation rate and the dating technique applied to the samples collected but is usually decadal to multi-decadal. The time period covered depends on the sedimentation rate and the thickness of preserved sediment; typical values range from several decades to several centuries. Historic relative sea-level heights are obtained by comparing the distribution of foraminifera (calcium-based organism) and diatom (silica-based organism) assemblages in contemporary salt marshes to historical assemblages obtained in

samples from salt marsh sediment. ^{14}C dating of plant macrofossils contained in the sediment and geochemical analysis of ^{210}Pb content enables temporal constraints to be placed on the inferred relative sea-level changes. This procedure is described in more detail in Chapter 4.

Isolation basins are analysed in a similar way to salt marsh sediments. In the case of a local relative sea-level fall, a lake once connected to the ocean via a sill will become 'isolated' and the sediment accreting in the basin will be more indicative of a freshwater environment and will have no marine influence. The timing of transition from marine to freshwater sediment may be dated using any plant remains that occur near the sediment facies change. The vertical resolution of index points provided by isolation basins is mostly dependent on the accurate measurement and location of the maximum sill depth which varies from study to study. The data used in this study have a typical vertical accuracy of +/-0.55m, and temporal accuracy of +/- 300 years.

Geomorphological data such as moraine systems (Ingolfsson et al., 1990; Long and Roberts, 2002) and bedrock surface exposure ages (e.g. Roberts et al., 2008) are the only data types covering the millennial time period that can provide direct measures of ice extent to complement constraints from isolation basins and other markers of millennial-scale sea-level change (e.g. shells; Rasch and Jensen, 1997).

1.5.2 Present Day Changes

The GRACE data presented in Table 1.1 span the entire mission so far (2002-2009) and show that the mass loss has steadily been increasing from 2002-2008, contributing a maximum of 0.74mm/yr to present-day sea-level change. In contrast to the GRACE technique, laser altimetry measurements do not provide complete cover of the ice sheet. GRACE data also have limitations, however; for example, spatial resolution is such that gravity changes measured in coastal areas of Greenland may be significantly affected by mass changes in the nearby ocean since the monthly geopotential fields are provided at a spatial resolution of harmonic degree 100.

Mass loss measured in laser altimetry surveys (e.g. Thomas et al. 2006) does not account for discharge from outlet glaciers, and is more likely to represent the mass changes associated from surface mass balance only. Comparing Laser Altimetry studies with those capturing a more complete picture of ice sheet mass balance (GRACE data) where there is overlapping data shows that SMB-related

changes are likely to account for ~ 60% of mass loss (e.g. Ramillien et al. 2006 and Krabill et al. 2004).

Units:				km^3/yr i.e.	km^3/yr i.e.	mm/yr
Author(s)	**Publication Year**	**Method**	**Period**	**Volume Change**	**Error**	**Eustatic Equivalent**
Wouters et al.	2008	GRACE	2003-2008	-196	+/-27	0.5
Velicogna and Wahr	2006	GRACE	2002-2006	-248	+/-36	0.63
Luthcke et al.	2006	GRACE	2003-2005	-111	+/-17	0.28
Ramillien et al.	2006	GRACE	2002-2005	-130	+/-10	0.33
Thomas et al.	2006	ERS/Laser Altimetry	1999-2004	-115		0.29
Zwally et al.	2005	Laser Altimetry	1992-2002	13	+/-3.6	-0.03
Krabill et al.	2004	Laser Altimetry	1997-2003	-80	+/-12	0.2
"	"	"	1993-1998	-60	+/- 12	0.15
Krabill et al.	2000	Laser Altimetry	1994-1999	-51		0.13
Rignot and Kanagaratnam	2006	InSAR	1996 2005	-91 -224	+/- 31 +/- 41	0.23 0.57
Rignot et al.	2008	SMB Modelling, InSAR	2000 2004 2005 2006 2007	-156 -231 -293 -265 -267	+/-44 +/-40 +/-39 +/-39 +/-38	0.39 0.58 0.74 0.67 0.67

Table 1.1: Table showing volume changes and eustatic sea-level change associated with the GrIS over the past sixteen years.

There is broad agreement with GRACE data and the study by Rignot et al. (2008) on the amount the GrIS has contributed to RSL change over the past six years or so. Combining these estimates shows that this contribution is +0.65mm/yr over 2004-2007. Although there are no significant disagreements between the estimates, interannual variation exists in the data and this is highlighted when the contributions are averaged over slightly different time periods (e.g. compare Wouters et al. 2008 and Velicogna and Wahr 2006). The studies that provide a more complete picture of mass balance show that the GrIS appears to be making a significant, increasing contribution (0.6mm/yr) to global sea-level rise. Over the period 1993-2003, global sea-level rise was recorded at +2.5mm/yr, increasing to +3.1mm/yr by 2008 (Cazenave et al. 2008), with the above estimates indicating a significant GrIS contribution of approximately 20%.

1.5.3 Millennial and Century Scale Changes

Direct measurements of mass loss over this period are sparse and not able to give a complete picture of GrIS mass balance. One of the most extensively photographed areas is Jakobshavn Isbrae; the photographs have been used to deduce that the calving front has retreated overall since the mid 1800s (Csatho et al. 2008). While this is an important result, it is not an accurate indicator of the overall behaviour of the ice sheet.

The rate of sea-level change for the 20th century is measured to be +1.5+/-0.5mm/yr (Munk, 2002; Cazenave and Nerem, 2004), with a figure of +1.8mm/yr quoted in the recent 2007 IPCC summary for the latter half of the 20th century. Geodetic surveying of the ice sheet is limited to the last decade only, so in order to infer changes in mass balance from the GrIS over the last few decades, tide gauge data and the technique of sea-level fingerprinting have been employed. Plag and Juttner (2001) concluded that tide gauges in the intermediate field of an ice sheet (e.g. the US east coast tide gauges) are particularly useful for constraining GrIS mass balance. Their assessment indicated that RSL rates from tide gauge data are consistent with an ice sheet averaged ice thickness loss of 50 to 100mm/yr, translating to a contribution of 0.24 to 0.48mm/yr to eustatic sea-level rise over the past 50 years or so. Mitrovica et al. (2001) carefully selected a sub-set of tide gauges and found that a best fit was obtained using a eustatic contribution of +0.6 +/-0.15mm/yr to sea-level rise from the GrIS over the past century. A similar result was obtained in a later study which considered a larger number of tide gauge records (Tamisiea et al. 2003). In a later analysis, using a more realistic treatment of the thermosteric contribution, Plag (2006) concluded on a GrIS melt contribution in the range of +0.05 to +0.1mm/yr for the past 50 years. Although there is disagreement in the values obtained in these analyses – reflecting the different data sets and methods used – both studies indicate that Greenland is contributing positively to sea-level change in the 20th century. A problem inherent to the fingerprinting method is the small magnitude of the signal in comparison to other secular signals in the tide gauge data (e.g. steric changes, glacial isostatic adjustment). A primary aim of this thesis is to tackle this problem by considering data from the near-field of the GrIS (see Section 1.6).

There are a limited amount of datasets and modelling studies which can describe either directly or indirectly ice sheet deglacial chronology on century-scale timescales leading up to the 20th century. Archaeological remains of sea-side Viking

huts can help constrain relative sea-level change by providing indirect measurements of RSL assuming that the habitations remained close to sea level, but their accuracy is generally poor and is qualitative only.

During the last 1000 years, two main periods of differing climatic conditions are recognised in Greenland (Fig. 1.7). The 'Medieval Climatic Optimum' (MCO) refers to an interval (~900AD to ~1400AD, depending on location) when some areas in the northern hemisphere were relatively warmer than today. During the MCO, conditions were favourable on the coast of south-west Greenland to sustain communities of Norse immigrants. The GRIP and DYE-3 proxy temperature records show that temperature rose by +0.8°C at DYE-3 and +1.4°C at GRIP from 0AD to 900AD. After this, temperatures steadily fell but remained warmer than present at these locations until ~ 1400 (Dahl-Jensen et al. 1998).

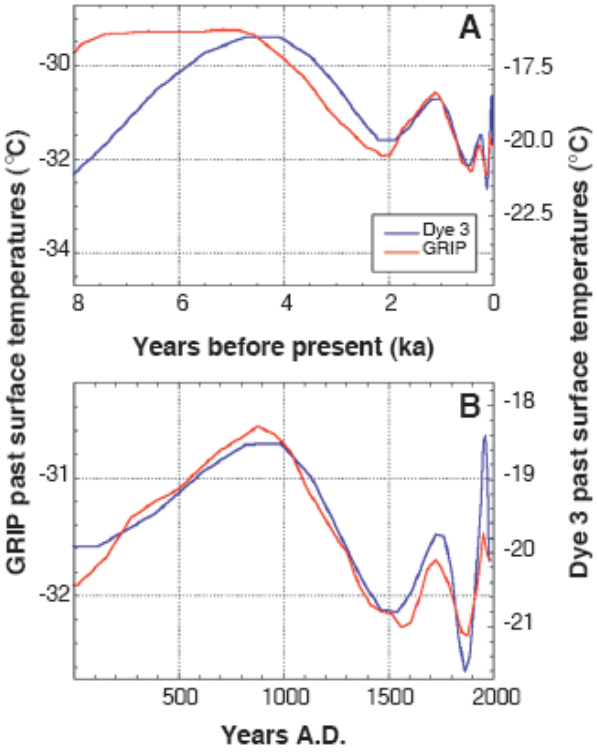

Fig. 1.7: Surface temperature record gained from the ice cores collected at GRIP and Dye-3 (see Fig. 1.1 for locations). From Dahl-Jensen et al. (1998). The Dye-3 record terminates at 7000 years before present.

Beginning at around 1300-1600 AD, temperatures dropped to values less than those a present. This relatively cold period is known as the 'Little Ice Age' (LIA), which is characterised by two distinct minima at around 1550AD and 1850AD (Fig. 1.7) at the GRIP and DYE-3 ice core locations. Ice core records show a decreasing trend in accumulation beginning at around 1400 AD and persisting until around 1800 AD (Anderson et al. 2006). Significant advance of the ice margin during the LIA (mid

19th century) is recognised in the Disko Bugt area (Weidick and Bennike, 2007). Approximately 150km east of Sisimuit, the ice margin is thought to have retreated 1-2km since the LIA maximum near the end of the 19th century (Forman et al., 2007).

The RSL response to these climatic changes is not known and is the core subject of this thesis. By employing proxy RSL data from Greenland salt marshes to bridge the data gap between 20th century and millennial scale observations, I aim to improve the constraints on GrIS mass balance from the time period of ~1500AD until the beginning of the 20th century.

1.5.4 Changes since the Last Glacial Maximum (LGM)

The global LGM is defined to occur between 21-16kyr BP, at a time of extensive global ice cover and a high in the marine $\delta^{18}O$ isotope record. From the LGM through to the late-Holocene, changes in extent of the GrIS are constrained via RSL and geomorphological observations. The output of modelling studies has been compared to a number of datasets that constrain, directly or indirectly the past areal extent of the ice (e.g. geomorphological features, RSL data).

During the LGM, the ice sheet extended offshore in a number of places around Greenland, reaching maximum size at around 16kyr BP. Modelling studies carried out by Huybrechts (2002), Fleming and Lambeck (2004) and Simpson et al. (2009) indicate that at LGM the ice margin extended offshore in west Greenland, Disko Bugt and in north-east Greenland. Predicted values of absolute ice thickness in these areas differ between studies, but 200-1000m thick ice was thought to occupy the continental shelf located offshore north-east Greenland (79-83°N,3-20°W), with the ice sheet extending into the present day ocean by 300km. In the west of Greenland, the ice extended to the present day coast and in limited places, onto the continental shelf (Fleming and Lambeck, 2004). Overall, the ice sheet is predicted to be 200-500m thinner at LGM in the centre of the ice sheet and 1000-1500m thicker around the periphery (Huybrechts, 2002).

Bennike and Bjorcke (2002) published a study that compiled all available geochemical data concerned with constraining the deglaciation history of Greenland. The bulk of the data are radiocarbon (^{14}C) dates obtained from offshore and terrestrial sediments, plant and shell material which reveal when areas became ice free. In south Greenland, around the Nanortalik region (Fig. 1.8), there is evidence for early deglaciation (12.8-14.1 kyr BP) of this sector of the ice sheet. The earliest

deglaciation timing (16.0 kyr BP) presented is found offshore of the Kangerdlugssuaq glacier and represents when this part of the continental shelf became ice free.

Fig. 1.8: Radiocarbon dates showing time (calibrated kyr) before present when areas in Greenland became ice-free. From Bennike and Bjorck (2002).

The cosmogenic exposure dating technique as used in Roberts et al. (2008) reveals the age at which the land was last covered by ice. As shown by Fig. 1.8, there is a scarcity of deglacial chronological data from south-east Greenland. Roberts et al. (2008) calculated exposure ages of between 12.8 and 9.7kyr in the area 30km west of Ammassalik. Coastal sections between Sisimuit and Nanortalik show deglaciation ages of 11.2 – 10.2 kyr. The data in Fig. 1.8 suggest that the ice sheet has retreated at an average rate of ~ 15kmkyr^{-1} from the coast at 10kyr BP to its present day position around the Sisimuit area, in response to the Holocene Thermal Maximum (HTM) between 10kyr and 5kyr before present. The HTM is a period during the Holocene when temperatures recorded at the GRIP site were at their highest in the last 100,000 years (see Fig 1.7). The difference between the temperatures at GRIP and Dye-3 is a result of elevation differences and the location with respect to different atmospheric conditions. During the HTM, the ice sheet is thought to have shrunk to ~70 % of its LGM extent in the space of approximately 4000 years (Simpson et al. 2009).

Periods of regrowth and readvance are likely to have occurred in areas when the overall mass of the GrIS was declining. In the west of Greenland, where the focus

of this study lies, Rinterknecht (2009) presented exposure ages from a 140km-long east-west transect from the ice margin to Sisimuit. This area is now ice free, but at LGM the ice sheet reached 385-730m in height 30km north west of Sisimuit, and thinned at a rate of 40-80mm/yr over a period of ~4000 years since 12.3kyr ago. Retreat of the ice sheet margin was not steady and temporarily ceased around 8.2kyr.

Unfortunately, the exposure dates contained in Fig. 1.8 are not able to reveal if there were any intermittent readvances during the general decline of the ice sheet as readvance destroys evidence of older ice limits. Such constraints may be obtained by relative sea-level studies (Long et al., 2009) and geomorphological evidence from moraines (van Tatenhove, 1996).

Relative sea-level studies from the west of Greenland near Sisimuit show that sea-level was falling rapidly in the early Holocene and reached a lowstand of ~ 4m below present sea level at around 1800 yrs ago and continued to rise until present. This sea-level rise is thought to be due to land motion associated with non-Greenland ice and a neoglacial readvance of the western portion of the ice sheet to its present day position. The magnitude and timing of deglaciation around the GrIS is illustrated to some extent by the shape of RSL curves from around the island (Fig. 1.9). Although the RSL curves will also be affected by non-Greenland processes, the curves in the north indicate that steady unloading of ice from Greenland occurred from the early-to-mid Holocene (8kyr BP) to present. In the west and south of Greenland, sea level reaches a minimum at 3kyr and 7kyr, respectively, and rises towards present (partly) as a result of neoglacial ice loading.

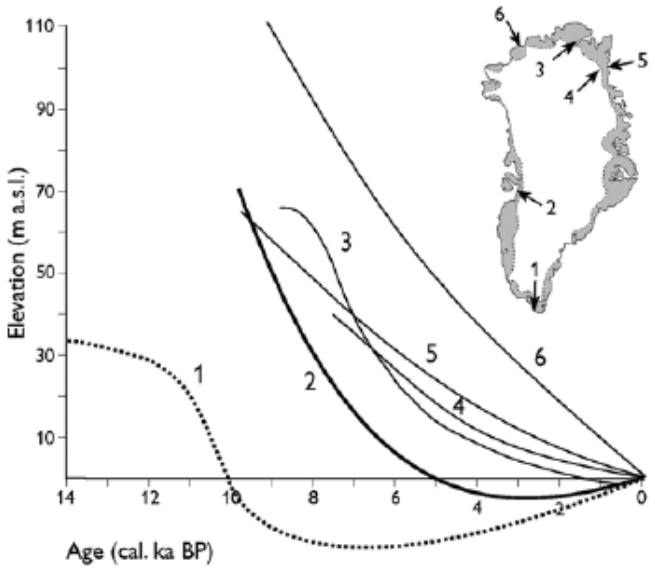

Fig. 1.9: Selection of relative sea-level curves from around Greenland. From Mikkelson et al. (2008).

In the south and west of Greenland, glacial unloading was interrupted by a period of regrowth between 6 and 3kyr BP. This is shown as a transition between RSL fall and rise. Modelling suggests the ice sheet is thought to have readvanced ~40km over the last few thousand years (Fleming and Lambeck, 2004). More recent studies, using an improved ice model (Simpson et al., 2009) suggest that this retreat-readvance could have been as much as 80km. Sea level in west Greenland is also influenced by the deglaciation of the Laurentide Ice Sheet, which was completed by ~7kyr BP. Since Greenland lies in the peripheral bulge region of this ice sheet, there is a constant contribution of sea-level rise originating from subsidence of the peripheral bulge from late glacial times and through the Holocene, particularly for the west of Greenland.

1.6 Thesis Aims and Structure

As stated in Section 1.1 and reiterated here, the overriding aim of this study is to improve estimates of GrIS mass changes during the past few hundred years. This period is particularly relevant given the transition into a warmer climate during the latter part of the 20th century and lack of direct constraints on ice sheet wide mass changes leading up to this period to use as a baseline for interpreting the recent, rapid changes (see Section 1.5.2). To achieve this aim, RSL data (instrumental and proxy) covering the period 1500 AD to 2005 are used – thus bridging the data gap shown in Fig. 1.6. The work in this thesis extends previous analyses of this type (e.g. Mitrovica et al. 2001, Plag and Juttner 2001, Tamiseia et al. 2003) by explicitly considering the steric component of sea-level change in both the near- and intermediate- field and applying the sea-level fingerprinting technique in the near-field of the GrIS to maximise the amplitude of the signal (see Section 1.5.3 and Section 2.3). The following paragraphs describe how the layout of this thesis reflects the general aims defined above.

Chapter 3 focuses on the analysis of tide gauge data located on the east coast of the US (intermediate-field sea-level analysis). While this data set was indentified as being well located to pick up a fingerprint of the GrIS (Plag and Juttner, 2001), other studies avoided data from this coast due to the relatively large glacial isostatic adjustment signal (e.g. Davis and Mitrovica, 1996). In Chapter 3, I explore in some detail both the contaminating effect associated with isostasy and that due to ocean temperature and salinity changes (steric signal). The relative contribution of GrIS mass changes is weighed against these effects (and their uncertainties) in order

to ascertain if the fingerprinting technique is a viable method to arrive at a useful estimate of GrIS mass balance, in line with the main aim of this study.

In Chapter 4, I describe the collection and analysis of salt marsh data from the near field of the GrIS. Results from existing isolation basin data which are required to constrain the millennial-scale deglaciation history of the ice sheet are also presented. Although the millennial-scale data are not analysed directly in this project, they are required to correct the century-scale RSL data for the baseline trend at each locality associated with the viscous response of the Earth to past loading changes. For this particular study, this is classed as a contaminating effect and must be accurately calculated to reveal the contemporary (climatological) contributions to the sea-level signal embedded in the salt marsh data. The relatively new method of using biostratigraphy from salt marshes as decadal to centurial proxy sea-level indicators is also described. For both data types, I will review the geochemical techniques used to determine the chronology of the near-field sea-level changes, their accuracy and limitations.

The key objective is to analyse state-of-the-art near-field proxy sea-level data in terms of the contribution arising from mass balance of GrIS over century and decadal timescales. To achieve this, a central sub-aim is the development of glaciologically realistic mass balance models of the GrIS to produce high resolution near-field sea-level fingerprint maps (see Chapter 2). Ice loading scenarios used in previous near- and intermediate- fingerprinting studies are not of high enough resolution to be used in a near-field study. To this meet this requirement, a new surface GrIS mass balance model for 1866-2005 is presented in Chapter 5. The sensitivity of the model (and RSL) history to key input model parameters and boundary conditions is also assessed.

Another aim is to determine to what extent and on what timescales the GrIS reacts to annual temperature and accumulation fluctuations by investigating periods in recent history when the GrIS faced similar climatic extremes, and how the historical mass balance changes compare to those at present. RSL trends from the new proxy sea-level data from salt marshes will shed light on mass balance changes when large-scale climatic changes were endured by the GrIS. In Chapter 6, the main focus will be on the generation of a century-scale mass balance history to try and explain century-scale trends in RSL in west Greenland. Two sets of climatological proxies are used to generate a climate forcing for the ice model.

This thesis represents the first application of sea-level fingerprinting in the near field of an ice sheet. One important aim of this study is therefore to test the

potential of this technique. Realising the potential of the technique depends upon identifying and constraining the processes that are the main regulators of near-field sea-level over century time scales. The contributing effects may not necessarily be glaciological in origin, nor result from loading changes from the GrIS. The steric component of sea-level change is likely to be significant and be highly variable at high latitudes, especially at locations proximal to ice sheets. Discharge of freshwater from outlet glaciers and annual formation of sea-ice will have a considerable effect on the properties of ocean water. In Chapter 7, density-related changes in RSL will be modelled using observations of temperature and salinity collected during the 20th century. The salt marsh data sites are located in the west of Greenland and are close to a major centre of ice discharge. Ice loss related to discharge from Jakobshavn Isbrae has the potential to affect sea-level across a wide area in west Greenland, and so this process is also assessed in Chapter 7 as a potential major contributor to the observed RSL change.

Chapter 8 will draw on all the observations and modelling presented in Chapters 3-7 to conclude on how well the two main objectives of the research have been achieved. In particular: (i) how the near-field salt marsh data have contributed to better constraining Greenland's contribution to global sea-level change over the industrial era; and (ii) whether or not changes of the GrIS in the past decade are anomalous within the period covered by the proxy sea-level data. In Chapter 8, I will also comment on the success of using of high-resolution, near-field proxy sea-level data to infer contemporary changes in the GrIS and conclude upon what additional work needs to be carried out, from the perspectives of both modelling and fieldwork, to maximise the potential of this technique. Finally, based on the results in this thesis, locations will be identified that would be well suited as future field sites to apply the method of near-field sea-level fingerprinting.

Chapter 2: Modelling Ice Sheet and Relative Sea-Level Evolution

2.1 Introduction

Central to this project is the use of a model that relates changes in land ice to changes in sea-level. This code must be applicable in both near- and far-field sea-level studies. The main focus of this chapter is to introduce the physical processes that influence sea-level change and ice sheet evolution. A summary of which processes are accounted for in this study is given to ensure the reader an indication of model accuracy. In Section 2.2, the causes of sea-level change due to redistribution of ice in the ocean-cryosphere system are described in detail, and the procedure for quantification of these changes is covered in Section 2.3. Accurate modelling spatial and temporal variations in ice mass (Section 2.4) is required to act as input to the sea-level. From this, a time dependent sea-level history can be generated and compared to trends from tide gauges in the far-field (Chapter 3) and proxy salt marsh data, collected in the near field (see Chapter 4). The process of modelling sea-level changes in the near- and intermediate-field of the ice sheet are compared in Section 2.5

2.2 Causes of Sea-level Change

Sea-level change is not globally uniform for a number of reasons, three of which are important in Greenland: (1) Ongoing mass variations of the GrIS, (2) Rebound and subsidence of the crust due to unloading of the Pleistocene ice sheets and (3) Ocean height changes forced by sea water density variations and sea water stratification. Groundwater transfer and sediment loading can affect both global and local sea-level but these effects are not important in Greenland and are not accounted for in this study.

Sea-level is defined as the height of the sea surface above the sea floor. Relative sea level (RSL) at a particular location is defined as ocean height above the sea floor, relative to the present day value at a particular datum. A complex interplay between earth deformation, changes in ice-ocean configuration, ocean currents and the rotation of the Earth causes time- and spatially dependent sea-level, and this is summarised in Fig. 2.1

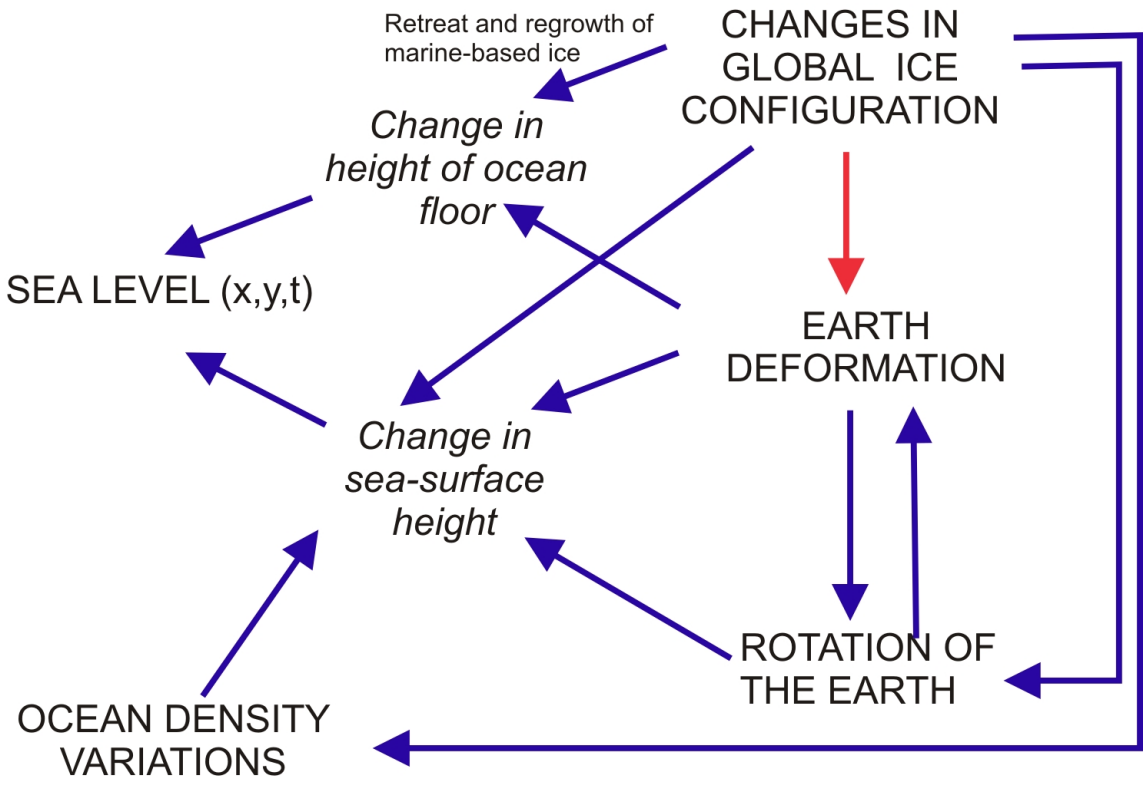

Fig. 2.1: Flow diagram summarising how a change in global ice configuration leads to sea-level change at any given point (x,y) and time (t).

Changes in the cryosphere can cause changes in sea-level through a variety of different processes. Topography of the ocean floor is directly affected by loading of the ocean basins and immediate (elastic) crustal deformation following a melting event. Sea-surface height in the immediate vicinity of the ice sheet falls as a result of reduced gravitational attraction of the ice sheet and mass redistribution. Retreat of marine-based ice sheets allows for influx of melt water into areas previously occupied by ice, varying the ocean load in this area and reconfiguring the ocean basin. Addition of glacial melt forces density changes and re-stratification of the ocean by regulating the temperature and salinity. In light of this, it is reasonable to assume that densification of the ocean would cause a secondary gravitational effect in the oceans. In a recent study (Roedelsperger et al. 2008), it was shown that this effect is negligible over timescales of 2000 years, even when considering a worst-case steric-related sea-level rise scenario (+2.3mm/yr)

The Earth is a rotating system and so any large-scale (degree 2) changes in mass re-distribution (e.g. within the cryosphere/hydrosphere) perturb the rotation vector and therefore the rotational potential. This perturbation also causes a height shift of the ocean floor and sea surface.

2.3 Modelling Changes in Sea Level due to Changes in the Cryosphere

Farrell and Clark (1976) were the first to present a formal theory for calculating sea-level changes due to changes in global ice coverage. This theory is summarised in the form of an equation – known as the 'sea-level equation – and is discussed below. In the following I introduce the sea-level equation following the discussion in Farrell and Clark (1976) by considering the contributions of changes in the gravitational potential (E2.2) and the deflection of the solid Earth. (E2.3)

The incremental change in sea level (*S*) at a location θ,λ (latitude, longitude) is a result of the change in gravitational potential of the Earth (S_ϕ) and deflection of the solid Earth (U) due to a perturbation in global ice extent, and is given by:

$$S(\theta,\lambda,t) = S_\phi(\theta,\lambda,t) - U(\theta,\lambda,t) \qquad \text{E2.1}$$

Where;

$$S_\phi(\theta,\lambda,t) = \frac{\phi^E}{g} * (\rho_I I + \rho_W S) + \sum_i \frac{\phi^V}{g} * (\rho_I I_i + \rho_W S_i) - \frac{M_I}{A_O \rho_W} - \left\langle \frac{\phi^E}{g} * (\rho_I I + \rho_W S) + \sum_i \frac{\phi_V}{g} * (\rho_I I_i + \rho_W S_i) \right\rangle_O \qquad \text{E2.2}$$

$$U(\theta,\lambda,t) = U^E(\theta,\lambda,t) + U^V(\theta,\lambda,t) \qquad \text{E2.3}$$

The first term in E2.2 describes the instantaneous change in the gravitational potential experienced at a point (θ,λ) due to the direct influence of the ice-ocean mass redistribution and resulting elastic deformation on the gravity field (ϕ^E). Changes in ice thickness ($I(\theta,\lambda)$) generated using ice sheet models such as those described in section 2.4.2.2 and resulting ocean height changes are scaled by their respective densities (ρ_I, ρ_W) to convert to loading changes. The ice and ocean loads have explicit time dependence, but the elastic response of the Earth and resulting change of potential due to this mass redistribution are assumed to be instantaneous. The time dependence of the earth response is accounted for in the second term. At time, *t*, the potential perturbation due to viscous adjustment (ϕ^V) is affected by the response of the Earth to all loading steps, *i*, from the model initiation (e.g. *t*=0). The symbol ' * ' denotes that the function that calculates the change in potential ($\phi^{E,V}$) is convolved with the ice and ocean load at each point (θ,λ) on the Earth to produce a change in potential at a specific location that is the result of all changes in ice and ocean load. The changes in

the ice and ocean loads are commonly described using a Heaviside loading history, with time steps sufficiently short to ensure a faithful replication of the 'smooth' loading history, yet large enough to result in reasonable computation times. Isostatic equilibrium is assumed at the start of the ice loading history.

The third term is the eustatic change in sea level, defined as the average change in sea-level in the ocean basin on a non-gravitating Earth due to the mass loss or gain on an ice sheet, M_I, and is uniform over the ocean area A_0. Summation of the last three terms produces a globally uniform shift in sea level that ensures conservation of mass within the system. Terms 4 and 5 are equivalent to terms 4 and 5, except that they represent the average values of Terms 1 and 2 over the ocean area, denoted by the brackets and subscript 'o'. Terms 1, 2 and 4, 5 are normalised by the gravitational acceleration (g) to convert the gravitational potential energy into a change of height in the geoid. Note that E2.2 does not account for the actual radial displacement of the Earth, only the change in potential brought about by this displacement.

Because of the gravitating effect of the sea, the term $S(\theta,\lambda)$ appears in both sides of the equation and therefore the target quantity - sea-level change - must be calculated iteratively. The distribution of ice thickness changes are assumed to be known and are specified via an input ice model. The first guess to the change in sea level (or zeroeth iterate) is the eustatic value. This yields a first solution to the equation which serves as input to determine the second iterate. This process is repeated until convergence is obtained to within a specified tolerance level. It was shown in Farrell and Clark (1976) that assumption of uniform sea level fall over the ocean basin following a glaciation event can incorrectly predict near field sea-level (within 1^o of distance from the point mass change) by up to 30 times the eustatic value when using a non-rotating rigid Earth and a non-gravitating ocean.

The response of the solid Earth to changes in ice load (E2.3) is dependent upon the rheological properties of the subsurface. In this study the Earth structure is taken from the Preliminary Reference Earth Model (PREM; Dziewonski and Anderson, 1981), which used seismic data to constrain the viscoelastic properties of the subsurface. In this study, the viscosity structure is parameterised into three layers: an upper layer with very high viscosity to simulate the lithosphere, an upper mantle region that extends from the base of the lithosphere to the 670 km seismic discontinuity and a lower mantle region that extends from this depth to the core–mantle boundary. Specific viscous parameters used are specified when necessary in each chapter. To calculate the time-dependent deformation of the Earth as a result of loading changes, an equation describing the impulse response of a Maxwell Earth is employed (Peltier,

1974). The radial displacement U, as a result of changes in ice and ocean load at any time, t , may be described as the sum of the displacement due to instantaneous elastic changes (U^E) and a later viscous response (U^V) to all loading changes (E2.3)

The sea-level equation in E2.2 has been extended to quantify the changes in sea-level brought about changes in Earth rotation (Milne and Mitrovica, 1998). Although the present day rates of sea-level change arising from changes in the rotation vector are an order of magnitude smaller than the global eustatic rate of sea-level change, exclusion of a rotational component in calculations of sea level at the LGM causes the sea-level to be over- or underestimated by several metres.

So far, changes in ice load have been assumed to be the result of mass changes from land-based ice sheets. Marine-based ice sheets have ice grounded on the sea-bed. In these areas, local sea-level is predicted to fall due to the combined effect of reduced gravitational attraction and crustal rebound. However, the influx of water into the previously glaciated area is unaccounted for in previous analyses. A revised formalism of the sea level code which includes the effect of retreat of marine-based ice sheets is presented in Milne et al. (1999). The application of a time-varying ocean geometry resulting from retreat of marine-based ice sheets causes the overall eustatic change in RSL from 18kyr to 6kyr BP to be reduced by ~ 10m. However, this process is not of any importance when modelling RSL change over decadal timescales. The version of the sea-level equation presented in Mitrovica and Milne (2003), and solved by Kendall et al. (2005) is used henceforth throughout this study to calculate changes in sea-level associated with contemporary ice mass variations from the GrIS.

2.4 Mass Changes on an Ice Sheet

2.4.1 Introduction

In this section, the main contributors to mass changes on an ice sheet are described, along with the modelling methodology applied to quantify these changes in order to generate a realistic ice load history to act as input to the sea-level code described in Section 2.3.

Fig. 2.2 shows the typical features at the margin of an ice sheet. The margin of an ice sheet is where the mass loss is at a maximum. The primary mechanisms of mass loss at the margin are the discharge of ice into the ocean via outlet glaciers and runoff of surface melt. Typically, an ice sheet gains mass in the centre by accumulation, and loses mass at the margins of the ice sheet due to ablation domination over accumulation. However, snow accumulated in the centre of an ice sheet recrystallizes

to ice and this flows to the margins, replacing some of the mass lost through ablation. If the surface mass balance and ice flow are in balance, the ice sheet is in equilibrium. These processes result in the ice sheet assuming a lenticular profile with the ice at it's thickest in the centre, causing depression of the crust.

Smaller scale dynamic processes such as calving, ice shelf break-up and fast flowing outlet glaciers enhance the mass loss at the margins. The flow of inland ice is assisted by the development of meltwater crevasses supplying the base of the ice sheet with water and thus lubricating the base. These crevasses are fed by supraglacial lakes formed by meltwater. These lakes also enhance the surface melting of the ice sheet by absorbing heat that would otherwise have been reflected.

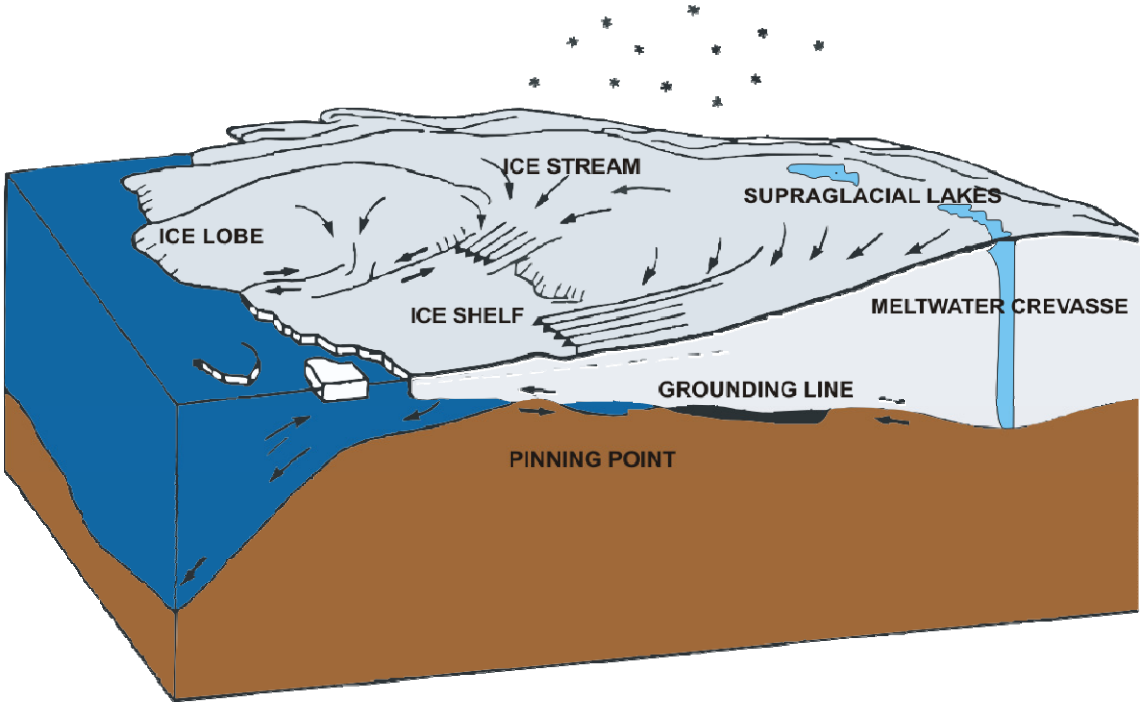

Fig. 2.2: Major features near the margin of an ice sheet.

The change of ice thickness distribution (ΔI), the input to the sea-level code, is due to a number of processes acting over differing timescales and with differing magnitudes. These are summarised in the equation (E2.4):

$$\Delta I = SMB + dI_{dynamics} + \dot{b} + R \qquad \text{E2.4}$$

Where *SMB* is surface mass balance, $dI_{dynamics}$ are the changes in ice thickness arising from ice dynamics (Section 2.4.3), $\dot{b}$ is the melt rate at the base of the ice sheet, and R encompasses ice thickness changes occurring due to random processes that cannot be modelled accurately, such as catastrophic glacier surges. The main processes

contributing to ice thickness change over an ice sheet are surface mass balance and horizontal flux divergence resulting in the outlet glacier discharge. Each of these processes will be discussed in more detail in the following sub-sections. Strictly speaking, the overall mass balance is the sum of *all* processes contributing to changes in mass (and therefore ice thickness) at any given point. In this thesis, the use of the term 'mass balance' encompasses the changes in mass brought about by SMB and dynamic compensation (flux divergence), since b and R are not considered.

2.4.2 Modelling Surface Mass Balance

Surface Mass Balance (SMB) is defined as the net mass gained or lost at the ice sheet surface over one year and is the difference between incoming precipitation and ablation. Mass is gained through a combination of snow accumulation, refreezing of any water gained from precipitation or advective movement of snow. Condensation immediately above the glacier surface adds mass to the system, if the water freezes in the snowpack. Mass gained from these processes is commonly termed 'accumulation'. Loss of mass occurs through melting, sublimation of snow into water vapour and evaporation of melt water from the ice surface. The term ablation covers all the processes of surface mass loss mentioned above.

There are two main approaches to modelling mass balance of glaciers and ice sheets: energy-balance modelling and positive degree-day (PDD) modelling. They lie at opposite ends of the modelling spectrum in terms of complexity, parameterisation and input data required. Energy balance modelling involves calculating the balance of radiative forces on an ice mass. The calculations take into account a variety of parameters involved in melting and are therefore deemed to produce a more realistic estimate of surface mass balance (assuming key parameters are well known). The method is computationally intensive and is more suited to calculating mass balance for small ice caps and mountain glaciers, as opposed to ice sheets. Application of a PDD model involves fewer input parameters and so may be applied to ice sheets. The positive degree-day method (Janssens and Huybrechts, 2000) requires only two input parameters (temperature and precipitation) and is therefore able to be used over large areas and time periods. The model algorithm and theory are explained in Section 2.4.2.2 but a brief overview of the energy-balance method is provided first (Section 2.4.2.1) to introduce some useful concepts.

2.4.2.1 Energy Balance Modelling

Mass balance estimates obtained using surface energy balance analysis takes into account surface mass gain from precipitation and condensation, and loss from evaporation and runoff. Precipitation is the total mass input to the system. Precipitation does not necessarily run off immediately, and may be incorporated into the snow pack resulting in a positive contribution to the mass balance. Similarly condensation may either runoff, or refreeze. The process of sublimation causes mass loss or gain depending on the direction of the phase change from solid to vapour. The importance of sublimation on the GrIS is highlighted in a study by Box and Steffen (2001) in which data from 50 weather stations were analysed. Sublimation follows a daily, as well as annual cycle, and spatial patterns mirror surface elevation trends. Sublimation rates of -50mm/yr (solid to vapour) are predicted in the 0-1500m elevation band over the period 1995-2000. At higher elevations (> 2000m), rates of sublimation lie in the range 0-25mm/yr.

The amount of melt (runoff) generated from the snow and ice pack is dependent on the energy flux across the ice-atmosphere interface. Energy Balance Models (EBMs) rely on accurate calculation of on the energy flux across the glacier / atmosphere interface. A number of parameters are required to calculate the flux, with most being directly available from Automatic Weather Stations (AWS). The total energy flux (Q, Wm^{-2}) at the surface is defined as (from Bougamont et al, 2005):

$$Q = (LW_I - LW_O) + (SW_I - SW_O) + LHF + SHF + F + Q_M \qquad \text{E2.5}$$

Input shortwave (SW_I)and longwave LW_I radiation can be directly measured at the surface from automatic weather stations, while reflected radiation is dependant on the absorptive properties of the snow and ice. Incoming longwave radiation is proportional to the fourth power of the surface and air temperature. LHF is the Latent Heat Flux associated with the phase changes of water. During condensation and freezing, heat energy is released. Evaporation and melting absorbs available heat energy. Sensible Heat Flux (SHF) is the transfer of heat energy occurring when there is a temperature gradient between two surfaces. This occurs by conduction and convection. For example, a negative SHF balance arises when the surface is cooler than the surrounding air on a glacier. The term, F, is the energy flux arising from the advection of heat from falling rain directly to the surface. The last term ,Q_M , is the energy used for melting which is estimated once all other terms have been accounted

for. This can be estimated directly from ablation measurements, or the melt rate may be calculated by closing the energy balance once all terms have been accounted for.

The most important terms in the energy exchange are long and shortwave radiation. The amount of longwave radiation emitting from the surface (LW_O) may be estimated from the surface temperature (T_S) using this relation (Stefan-Boltzmann relation, E2.6):

$$LW_O = \sigma T_S^{\,4} \qquad \text{E2.6}$$

Where σ is the Stefan-Boltzmann constant. A small change in temperature results in a substantial release of longwave radiation from the surface. Short-wave radiation is the incoming radiation in the visible, infra-red and ultraviolet parts of the electromagnetic spectrum. The outgoing shortwave radiation is directly proportional to the albedo (α) of the surface (E2.7):

$$SW_O = \alpha SW_I \qquad \text{E2.7}$$

Albedo is a measure of the ability of a surface to reflect shortwave radiation and ranges from 0 to 1. The albedos of snow, ice and water are the only relevant albedo parameters to the energy balance model. Dry snow that is free of impurities typically has an albedo of 0.85 (Paterson, 1994), whereas inclusion of impurities such as atmospheric dust can lower the albedo to ~ 0.4. Albedo plays an important role in ice sheet melting. Once snow has been melted, supraglacial water and exposed old snow and glacial ice lower the surface albedo to 0.1 – 0.4. This means that only 10%-40% of the incoming short wave radiation is reflected back into the atmosphere. The energy balance model of Bougamont et al (2005) applies a sophisticated technique to re-estimate surface albedo as an exponential function of the new snow layer / surficial water thickness. Clean ice typically has an albedo of 0.4. Dust layers within the ice reduce albedo to 0.21-0.29 (Paterson, 1994). This presents a challenge in both decadal and millennial scale models where the stratigraphy of ice and snow regulates the amount of melt water generated.

Calculation of net shortwave radiation (SW_I-SW_o) at the ice sheet surface is critical for the melting of snow and ice as the fraction reflected depends on the albedo as mentioned above. Before reaching the surface, incoming solar radiation may be absorbed by various gases (e.g. water vapour), aerosols (e.g. O_3) and clouds or

reflected and backscattered in the upper atmosphere. Therefore ice sheet wide energy-balance modelling in the absence of data from weather stations requires detailed knowledge of cloud cover and atmospheric composition. Calculations spanning many decades into the past are not possible using this technique.

Sensible heat flux (*SHF*) and latent heat flux (*LHF*) have more complex relationships with their surroundings, but can be described with similar equations. They depend on the following parameters: wind velocity in the immediate 10m above the surface, surface 'roughness' , temperature gradient and humidity. Sensible and latent heat flux are described by the following relations (E2.8 and E2.9 respectively)

$$SHF = \rho_a c_p C_H \bar{u}(\bar{\theta}_z - \bar{\theta}_s) \quad \text{E2.8}$$

$$LHF = \rho_a L C_E \bar{u}(\bar{q}_z - \bar{q}_s) \quad \text{E2.9}$$

Where ρ_a and c_p are the density and specific heat capacity of air. The terms C_H and C_E are the exchange coefficients for heat and vapour pressure respectively, and are to some extent, tuning parameters. Large sensible heat fluxes are driven by high wind speeds ($\bar{u}$) and significant differences in potential temperature ($\bar{\theta}$) between the surface (*s*), and some distance (*z*) above the surface. Surface roughness parameters for wind (z_w) and temperature (z_t) need to be defined to calculate turbulent heat fluxes across the surface of a glacier. Calculations of z_w show that in the ablation zone in a study area of West Greenland the roughness parameter can vary spatially by a factor of 1000 (Smeets and van den Broeke 2008). The ice surface is relatively smooth in the ablation zone characterised by small roughness lengths of the order of a few millimetres or less (10^{-5} m, Smeets and van den Broeke 2008) to 10^{-2} m near the ice margin where the surface is characterised by rumpling. The roughness lengths for snow and ice may vary from 4 x 10^{-6}m to 0.07m and 5 x 10^{-6} m to 0.12m respectively (Hock, 2005). Increasing z_w by a factor of 1000, such is the variation specified, causes the SHF measured at z=2m to be roughly doubled promoting turbulent heat flow.

However, z_t is dependant upon the surface roughness length for wind and is frequently used as a scaling parameter (Hock, 2005) when modelling incoming SW radiation. The term, L, is the latent heat of evaporation of water. The latent heat flux is dependant on the mean specific humidity at the surface of the glacier ($\bar{q}_s$) and at some

level, z, above it ($\bar{q}_z$). Positive latent heat fluxes are encouraged by large humidity gradients above a glacier. This is a measure of the amount of evaporation and sublimation occurring at the glacier surface.

In this thesis, one of the main objectives is to produce detailed (km-scale) grids of mass balance change spanning century timescales. Detailed modelling by the energy-balance method is not possible due to computational intensity and uncertainty in the parameters, so the technique adopted (PDD modelling) only focuses on the main contributor to energy balance at the glacier surface – temperature. Based on data collected from a collection of glaciers worldwide, it was found that a minimum of 70% of energy supplied to the ice surface is the result of incoming longwave radiation (Ohmura, 2001), with the emitted longwave radiation highly dependent on surface temperature (E2.6). Therefore the PDD approach makes sense for work presented here as it accounts for the influence of temperature changes and is more straightforward to apply that the energy-balance method.

2.4.2.2 Positive Degree-Day Modelling

PDD modelling requires input precipitation and temperature fields in order to simulate the processes at the surface of an ice mass. In order to simulate the amount of melt generated, monthly temperatures are calculated using a parameterisation method that generates a latitude- and elevation- dependent temperature distribution. The long-term climatic variations that impact temperature are not taken into account at this stage, but are later added to this spatial parameterisation (see Chapter 5). Location-specific temperature on an ice sheet is not stable throughout the day, so random fluctuations in temperature must be accounted for. If the average daily temperature is a few degrees below zero, occasionally the temperature exceeds zero and melt occurs because of stochastic variations.

The mean annual (E2.10), July (E2.11) and monthly, (E2.12) temperatures are defined as:

$$TMA(\theta, z) = 49.19 - [0.00792 \times z] - [0.7576 \times \theta] \quad \text{E2.10}$$

$$T(\theta, z, 7) = 30.78 - [0.006227 \times z] - [0.3262 \times \theta] \quad \text{E2.11}$$

$$T(\theta, z, k) = TMA(\theta, z) - [|\, TMA(\theta, z) - T(\theta, z, 7)\,|] \times [\cos(\frac{\pi}{6}(k-1))] \quad \text{E2.12}$$

Where *k* represents the month number and lies between 1 and 12, *z* is the surface elevation in metres and θ is latitude. The dependence of temperature on latitude was derived by applying a linear regression to temperature data obtained from stations on the ice sheet surface (Ohmura, 1987; Reeh, 1991). Over the year, the temperature cycle follows a cosine curve, with the maximum temperatures occurring in July. The annual cycle of temperature was derived from a set of observations from 5 stations on the Greenland Ice Sheet which track the complete annual temperature cycle. The use of stations based at the coast which contain more complete records is not recommended due to the 'inland effect' on temperatures as described in Ohmura, (1987).

July temperatures (when k=7) require a slightly different parameterisation, with a smaller orography-based lapse rate compared to that used for mean annual temperature. Also, low-elevation temperature 'inversions' in Greenland are frequently observed at high latitude and must be accounted for. Instead of temperature decreasing with altitude, the opposite trend occurs due to low-elevation warm pockets of air, or there is no elevation-temperature gradient at all. (e.g. see Fig. 7 in Reeh, 1991). In order to account for this, the quantity *z* in E2.10 may be substituted if E2.13 is satisfied:

If $z \le z_{INV}$ *, then* $z = z_{INV} = 20 \times (\theta - 65)$ E2.13

Where z_{INV} is the height at which the temperature inversion is predicted to occur given at a specific latitude. For example, at θ=80°N a temperature inversion is predicted at elevations below 400m.

The phase of water reaching the glacier surface is parameterised by temperature only, and the distribution is described by an error function (erf). In order to calculate the fraction of incoming precipitation that is rain, an error function is used to assess the likelihood of the monthly temperature remaining above a predefined rain limit temperature. This lies in the range of 0-2°C, with the corresponding rain fraction calculated as:

$$rfr = 0.5erf(j) + 0.5 \quad \text{E2.14}$$

Where *j* is the difference between the monthly temperature and rainlimit, expressed as a fraction of the predefined daily stochastic temperature variation. Once the solid and liquid precipitation fractions have been calculated, along with the annual temperature

distribution, the model can then initiate the melt-retention-refreezing process. This process is summarised in Fig. 2.3

Once the surface temperature has been parameterised from elevation and latitude, the number of Positive Degree-Days (PDDs) are calculated (Fig 2.3, step 1). The amount of PDDs are calculated on a monthly basis, with the average monthly temperature allowed to fluctuate by 4.2^{o}C to simulate random temperature variations at the ice sheet surface. The expected PDDs are calculated by predicting the mean monthly temperatures, and assessing the probability of fluctuation of these temperatures within the interval governed by +/- 4.2^{o}C. This number is used mainly as a tuning parameter to achieve sufficient model-observation fits on melt rates, and is similar to that used in the study by Reeh (1991). Even if the mean summer temperature is less than zero, it is unlikely to remain so over the course of a month and during the day. Studies show that melting occurs when average daily temperatures are at -5^{o}C (Reeh, 1991), so the value set for the temperature variation must reflect this over the period of a month. As well as calculating the contribution to the annual PDD sum from the average temperature, the contribution from expected daily temperature fluctuation is estimated by assuming that this variation follows a normal probability function, centred on the mean monthly temperature.

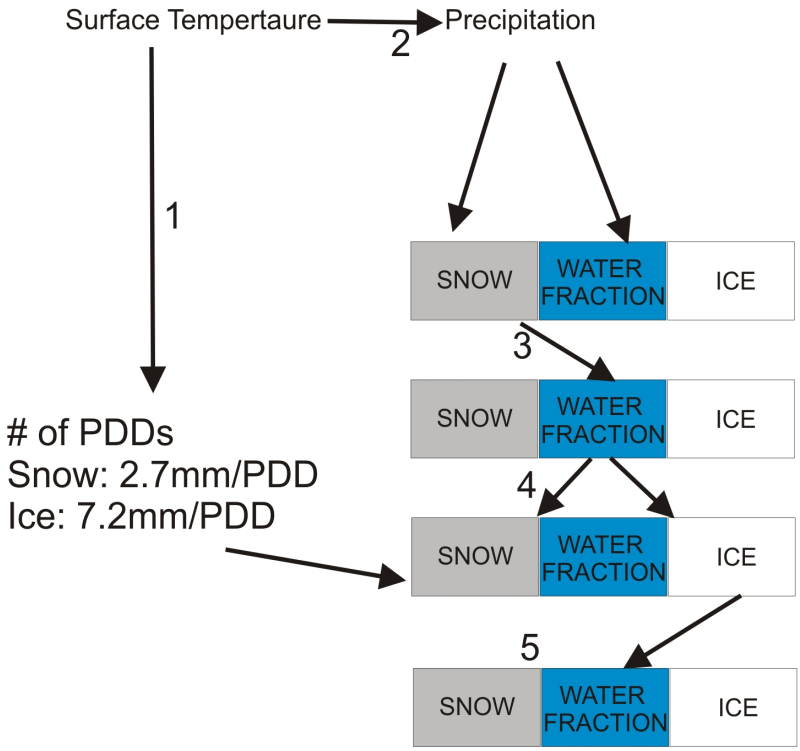

Fig. 2.3: Flow chart summarising the PDD model algorithm (Janssens and Huybrechts, 2000)

Whether the precipitation falls as rain or snow depends on the amount of time the surface temperature remains above or below a predefined temperature threshold of

1°C (although this may vary between 0 and 2°C). Rain is immediately added to the liquid-water (melt) term for later runoff, storage or refreezing (Fig. 2.3, step 2). The melting stage is now initiated, if there are any PDDs predicted by the model (Fig. 2.3, step 3). Snow is melted first at a rate of 2.7mm w.e°C^{-1} day^{-1}(where w.e. stands for 'water equivalent') also liberating any capillary water that may be trapped from earlier storage. This melt then has the possibility to be retained and the possibility of retention is proportional to the original snow cover and surface temperature. The potential of water to refreeze is calculated by assessing the temperature of the snow layer based on a simple parameterisation of thermodynamic processes at the surface of the ice (Huybrechts and de Wolde, 1999) (Fig. 2.3, step 4). If it is retained, it will form superimposed ice. Any remaining unfrozen water is added to capillary water until complete saturation of the snow cover occurs.

Once all snow has disappeared, along with capillary water, any remaining PDDs are used to melt superimposed ice formed in the previous step (Fig. 2.3, step 5), if any, and then glacier ice. This occurs at a higher rate (compared to snow) of 7.2mm w.e. °C^{-1} day^{-1}. The melting of superimposed ice and release of capillary water from previous stages does not add any additional water to ablation, as these retained and refrozen portions come from the melted fraction of the input snow cover. Degree-day factors are highly variable around Greenland, and the calculated runoff is highly sensitive to these values. The values quoted here (2.7 mm w.e. °C^{-1} day^{-1} for snow and 7.2mmw.e. °C^{-1} day^{-1} for ice) are fixed spatially and temporally and are similar to those used in Braithwaite and Olesen (1989), and are within the range of values reported by Braithwaite (1995).

The PDD model may be forced with monthly or annual precipitation values. The annual precipitation model assumes that all of the snow and precipitation is available at the start of the model run. The monthly model varies the precipitation over the year and sums positive degree days on a monthly basis, so the final annual mass balance figure is the sum of the monthly SMB values. In the SMB modelling performed for this thesis, the annual precipitation is divided evenly between each month of the year, so that the same input precipitation is available at the start of each month. This will then be converted into monthly rain and snow fractions by means of E2.14. This is the best approximation that can be applied to the monthly mass balance model in the absence of ice sheet-wide monthly precipitation values.

2.4.3 Dynamic Compensation

A significant portion of ice thickness changes are attributed to dynamic thinning and thickening due to flow of ice from the centre to the margins. This directly affects calving rate of outlet glaciers since calving rate is a balance between surging velocity and grounding line migration. For two-dimensional flow, the flux divergence $\frac{dq}{dx}$ along a flow line extending into the x dimension is described in E2.15 (Paterson, 1994) and illustrated in Fig. 2.4.

$$\frac{dq}{dx} = u_{z_2}\frac{\partial z_2}{\partial x} - u_{z_1}\frac{\partial z_1}{\partial x} + \int_{z_1}^{z_2}\frac{\partial u}{\partial x}dz \qquad \text{E2.15}$$

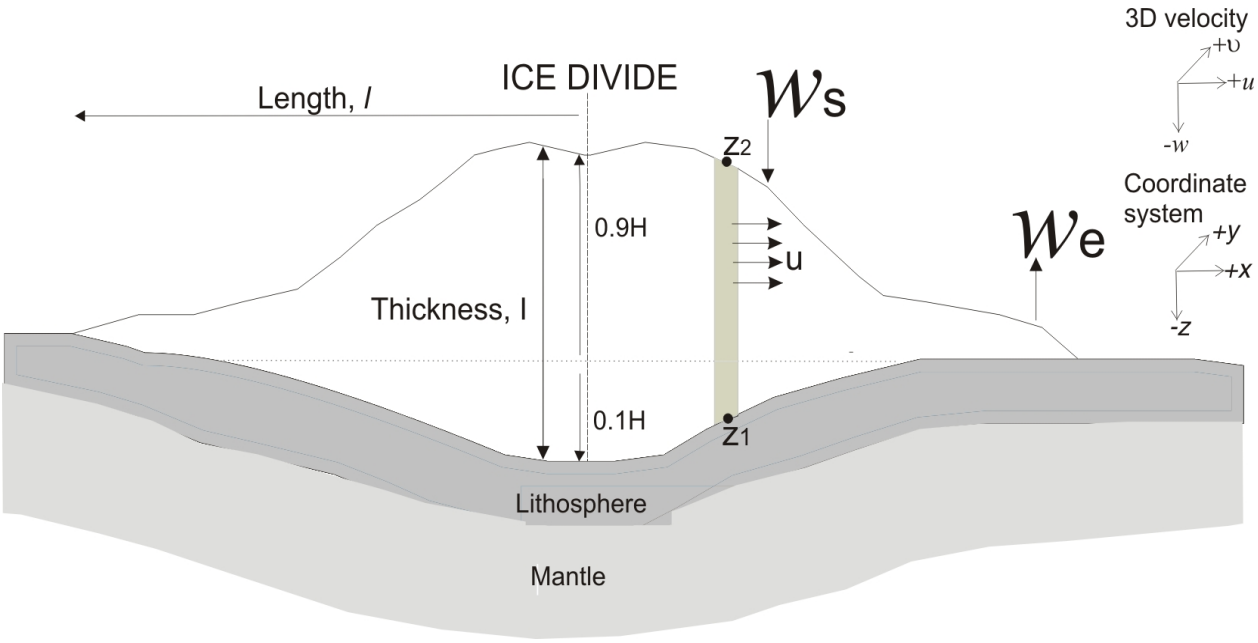

Fig. 2.4: Schematic cross section of an ice sheet showing characteristic bedrock and upper mantle deflection. Labels in the diagram are defined in the text.

Where u_{z_2} and u_{z_1} are the horizontal velocities (u) at the surface (Z_2) and basal (Z_1) coordinate positions. In this modelling experiment, the ice is assumed to be frozen to the bed (i.e. u_{z_1} =0), with no strain in the y direction (i.e. $\frac{\partial u}{\partial y} = 0$). Elevation change due to ice dynamics is the result of two types of flow. The first term in E2.15 describes the vertical displacement arising from ice sliding downslope. The integral describes the average horizontal velocity in a column if ice, between z_1 and z_2. But, assuming ice is frozen to the bed (i.e. term 2 in E2.15 is zero) and that ice is incompressible, any ice flowing downwards with velocity $-w$, will be balanced by ice flowing horizontally away

along the flow line, so $\frac{\partial u}{\partial x} = -\frac{\partial w}{\partial z}$. This equivalence means that dynamic-related changes in ice thickness, $dI_{dynamics}$, may be simply described by the sum of the vertically averaged downward flow and the contribution to vertical displacement due to flow down the surface slope:

$$dI_{dynamics} = w_{s,e} + u_{z_2} \frac{\partial z_2}{\partial x} \quad \text{E2.16}$$

The first quantity on the right hand side of E2.16 is known as the 'submergence' (subscript, 's', negative in sign due to downward movement) or 'emergence' (subscript 'e', positive in sign) velocity (Paterson, 1994). In the accumulation zone, loading of snow on the surface will enhance downward flow, therefore increasing w_s, the submergence velocity (Fig 2.4). The second term in E2.16 is dependent on the gradient of the ice sheet surface, and the surface velocity only. The surface gradient is at a maximum close to the margin, due to the lenticular surface profile of an ice sheet, so the second term in E2.16 dominates in most instances.

Generally, in the accumulation zone $dI_{dynamics}$ is negative and is positive in the ablation zone due to flow of ice reaching the margin. For a balanced ice sheet, $dI_{dynamics} = SMB$ .The boundary conditions of dynamic-related ice thickness changes is treated differently throughout the thesis, and so is explained in specific chapters.

2.4.4 Other Processes

Basal melt ($\dot{b}$; E2.4) occurs in areas where the pressure of overlying ice reduces the melting point of ice and/or there is a higher than average geothermal heat flux. The basal melt in north-central Greenland is measured to be up to 0.15m/yr at around 71°N (Fahnestock et al. 2001) and coincides with areas of fast horizontal ice flow (due to the meltwater decreasing basal friction). In this thesis, the mass balance model is not coupled to evolving basal conditions.

Transmission of surface melt to the base of an ice sheet (or increased basal met rates) enhances ice acceleration. Acceleration of ice has been shown to coincide with enhanced melting over the summer periods (Zwally et al. 2002). The degree of correlation with summer melt shows that this is not entirely a random process. The effect of this mechanism is not accounted for in this modelling study due to the high complexity the coupling mechanism between surface melt, melt water transmission to

base and resulting glacier speed-up. Although peaks in horizontal velocity coincide with peaks in positive degree-day sum, no significant overall trend in horizontal velocity is measured over the period 1996-1999 in west central Greenland (Zwally et al. 2002). Recent work by Joughin et al. (2008) supports the work by Zwally et al. (2002) that speed up of ice occurs during the summer months (i.e. periods of high meltwater production). However, the study shows that Jakobshavn Isbrae is more responsive to changes in ice front position, rather than periods of peak melt production, indicating that the process of basal lubrication is not likely to lead to substantial mass loss though outlet glaciers. A second study (Van der Wal et al., 2008) supports the observation in Zwally et al. (2002) that speed up of ice is mainly a seasonal occurrence in response to increased melt. All studies (Zwally et al., 2002, Van der Wal et al., 2008, Joughin et al., 2008) suggest that basal lubrication is not predicted to play a major part in amplifying the response of the ice sheet to the expected future warming.

2.5 Modelling Layout

In this section I will describe how the methodologies of modelling sea-level change (Section 2.3) and ice sheet evolution (Section 2.4) are applied in the near and far-field of an ice sheet.

The rate of change of sea-level ($\frac{\partial S}{\partial t}$) in both the intermediate and near-field of the GrIS may be described as the total of four quantifiable components (E2.17):

$$\frac{\partial S}{\partial t}(\theta,\lambda) = \frac{\partial S_{GrIS}}{\partial t}(\theta,\lambda) + \frac{\partial S_{V}}{\partial t}(\theta,\lambda) + \frac{\partial S_{St}}{\partial t}(\theta,\lambda) + \frac{\partial S_{Non-GrIS}}{dt}(\theta,\lambda) \qquad \text{E2.17}$$

Where $\frac{\partial S_{GrIS}}{\partial t}$ is the contribution to sea-level change due to ongoing mass changes of the GrIS. The term $\frac{\partial S_{V}}{\partial t}$ is the change in sea-level arising from the ongoing viscous response to millennial scale changes in ice sheets. Sea-level changes due to steric variations in ocean height are accounted for in the term $\frac{\partial S_{St}}{\partial t}$. Changes in global ice cover unrelated to are not the focus of this thesis, but estimates of their contribution to observed sea-level change unrelated to Greenland ($\frac{\partial S_{Non-GrIS}}{\partial t}$) is acknowledged and quantified where possible using available studies.

For the analysis of tide gauges in the intermediate field of the GrIS, GrIS melt scenarios are prescribed on the basis of studies monitoring the changes in surface

elevation and ice thickness over Greenland. These geometries of ice thickness change are assumed to be valid for the last 50 years. The sea-level response at each tide gauge on the US east coast due to these changes is calculated using the formalism described in Section 2.3. The deglaciation histories of Tushingham and Peltier (1991) and Peltier
(2004) are used in conjunction with a specified earth model and the sea-level code (Section 2.3) to compute the present-day sea-level response ($\frac{\partial S_V}{\partial t}$)to the deglaciation of the North American Ice Sheets.

For the near-field ,$\frac{\partial S_V}{\partial t}$, refers mainly to the millennial-scale sea-level change brought about by ice loading changes of the GrIS, but sea-level in Greenland is also influenced by the deglaciation of the North American Ice Sheets. The sea-level change in west Greenland due to the combined contributions of the GrIS and deglaciation of the North American Ice Sheets is not computed directly in this study. The synthesis and validation of the millennial-scale deglaciation history of the GrIS is included in a separate project and described in (Simpson et al. 2009). Instead, $\frac{\partial S_V}{\partial t}$ is estimated directly from sea-level proxies recording millennial-scale changes in west Greenland (see Chapter 4). To estimate $\frac{\partial S_{GrIS}}{\partial t}$, a detailed ice loading history is generated using the PDD model described in Section 2.4.2.2. The specific methodology is described in more detail in Chapters 5 and 6.

In both the near- and intermediate field, the main aim is to isolate the sea-level change associated with mass balance changes in the Greenland Ice Sheet by accounting for the temporal evolution of the contaminating signals ($\partial S_V, \partial S_{St}, \partial S_{Non-GrIS}$). Steric-related changes ($\frac{\partial S_{St}}{\partial t}$) are calculated in the same way in the near- (Chapter 7) and intermediate- (Chapter 3) field using temperature and salinity profiles specific to the area. The term on the left-hand side of E2.17 now acts as a direct constraint on the contribution to sea-level change from Greenland Ice Sheet mass balance changes once these contaminants have been removed. In the intermediate field, sea-level changes ($\frac{\partial S}{\partial t}$) are observed at tide gauges. Analysis of tide gauge data in terms of the four contributions in E2.17 is described in Chapter 3. In the near-field, $\frac{\partial S}{\partial t}$ is observable in isolation basins and proxy salt-marsh data. The process of extracting trends in sea-level from isolation basins and salt marsh sediments is described in more detail in Chapter 4.

Chapter 3: Using the US East Coast Tide Gauges to search for a Sea-level Fingerprint from the Greenland Ice Sheet

3.1 Introduction

The tide gauge record from the eastern seaboard of the US displays a distinct spatial variation in sea-level change. This variation has been attributed to a number of different processes, including oceanographic effects (Gornitz et al. 1982) neotectonic motions (Douglas, 1991) and the ongoing isostatic deformation of this region in response to the most recent glacial cycle of the current ice age (Davis and Mitrovica, 1996 and Di Donato et al, 2000).

A recent study (Davis and Mitrovica, 1996) applied a model of glacial isostatic adjustment to show that the isostatic component of the signal can fit the majority of the observed variation and so concluded that this process is potentially the primary contributor to the signal. If this is the case, the tide gauge observations represent a useful data set with which to constrain parameters in models of glacial isostatic adjustment (such as mantle viscosity structure and models of North American ice history).

A number of recent studies have shown that the sea-level rise associated with global warming is characterised by large spatial variations. This climate signal has two primary components: that associated with the melting of grounded ice (mass contribution component) and that associated with the density changes of ocean water through changes in temperature (thermosteric effect) and salinity (halosteric effect). The sea-level change associated with the negative mass balance of a given continental ice reservoir is predicted to be significantly less than the eustatic value in a broad region centred on the ice reservoir but greater than this value in the far-field of the melt source (Mitrovica et al. 2001). For example, a net melt of the Greenland Ice Sheet (GrIS) would result in falling sea levels throughout much of the Arctic and North Atlantic oceans and produce an increase in sea-level rise moving southwards along the US east coast.

Estimates of the halo- and thermosteric effect on a global scale from observations of ocean temperature changes show variations of up to a few mm/yr over relatively short distances (hundreds of km) (Cazenave and Nerem, 2004). Furthermore, estimates derived from different data sets produce results that display similar large-scale patterns but can differ significantly in specific regions, such as the US east coast (see, for example, Fig. 3 in Lombard et al., 2005). The current globally averaged rate of steric sea-level change lies in the range of -0.5 to

+0.8mm/yr for the twentieth century (Leuliette and Miller 2009, Cazenave et al. 2009, Antonov et al. 2002) of which the halosteric component is thought to contribute less than 10% (Antonov et al. 2002).

In this chapter, tide gauge data from the US east coast are revisited with the aim of investigating the contribution of the 20th century climate-related signals to the observed spatial trend. The work presented in this chapter extends the work of Davis and Mitrovica (1996), as in situ oceanographic data are utilised to further correct the data for changes in steric height, rather than assuming a constant rate for dynamic height variation at each site. The residual trends are then interpreted in terms of GIA and a fingerprint arising from the GrIS.

The application of tide gauge data to constrain recent ice sheet stability is particularly relevant given the relatively poor understanding of processes that have contributed to the observed mean global sea-level rise of 1.5 +/- 0.5 mm/yr during the 20th century (e.g. Cazenave and Nerem, 2004 and Munk 2002.). The recent (2007) report published by IPCC quotes the 20th century rate of sea-level change as 1.8 +/- 0.5 mm/yr, with the rate over 1993-2003 measured at 3.1 +/-0.7mm/yr. The sea-level budget and magnitude of the climate-controlled component of sea-level change was, up until fairy recently, uncertain and was termed 'The Sea-level Enigma' (Munk, 2002). Recent work by Domingues et al. (2008) has closed the sea-level budget over the period 1961-2003 with the combined contribution from the ice caps estimated at +0.5mm/yr.The contribution from Greenland alone (+0.21 +/- 0.07 mm/yr) is better quantified over the 'satellite-era (1993-2003) but obtaining a better constraint on the long-term (50–100 yr) stability of the GrIS is an important step towards resolving the current debate of whether the GrIS is at present losing mass anomalously.

The primary goal of this chapter is to determine if the tide gauge data from the US east coast can provide useful constraints on GrIS mass balance over the past 50 years. This differs slightly from the work carried out by Mitrovica et al. (2001) and Tamisiea et al. (2001), since only a subset of US tide gauges were employed in their studies. Although long tide gauge records (> 50 years in length) are preferable, the study is limited by the temporal coverage of the oceanographic data (1955-2005). In summary, I aim to utilise tide gauge data available from the US east coast to isolate the sea-level fingerprint associated with melting of the GrIS over the past 50 years, and assessing whether previous inferences of earth structure gained from tide gauge analyses (Davis and Mitrovica, 1996) are significantly different when the data have been corrected for the climatic

components and an updated version of the deglacial history of the Laurentide Ice Sheet

In Section 3.2 I describe the tide gauge selection criteria used to best achieve the above stated aims. Then, using data from 27 tide gauges, I investigate the contribution to sea-level change on the US east coast as a result of (1) mass loss from the GrIS (Section 3.3, 3.6) (2) deglaciation of the NAIS (or GIA; Section 3.5, 3.6,) (3) ocean density variations (Section 3.4). For the first and second of these processes the sensitivity of the signal to key model parameters is explored in order to better understand the signal and gauge the potential of the data for constraining specific parameters. The results of the sensitivity analysis are employed to infer a unique combination of a GrIS melt signal and specific viscosity model. I will also comment on the success of the method for constraining the contribution of the Greenland to 20th century sea-level change and proposals to improve the method to further constrain Greenland's contribution to global sea-level change.

3.2 Criteria for Selection of Tide Gauges

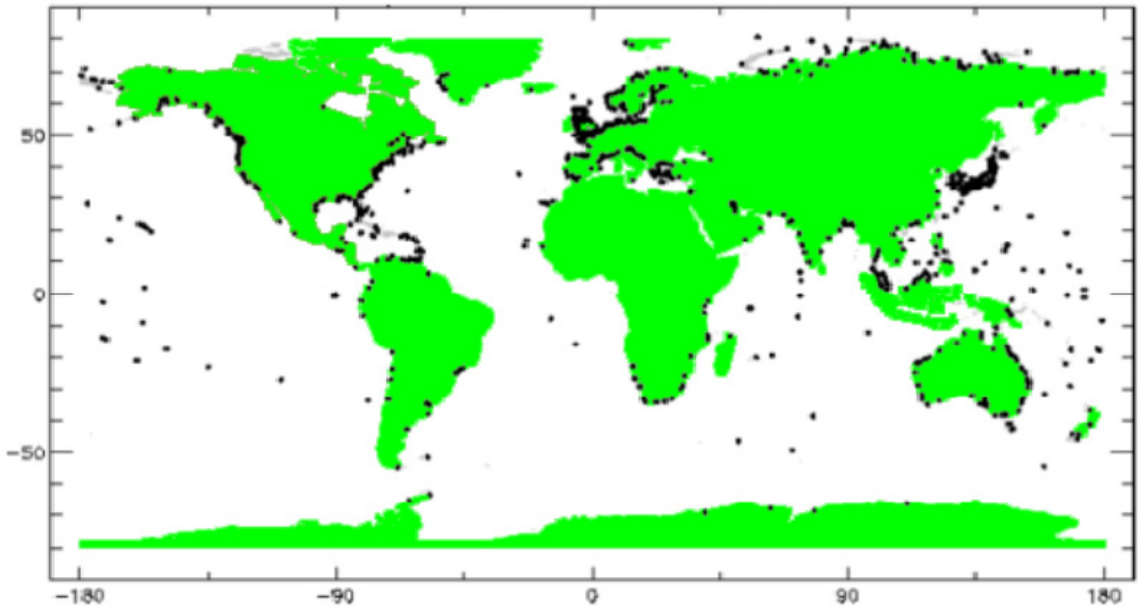

Fig. 3.1: Geographical distribution of tide gauges datasets held by PSMSL. Image obtained from www.pol.ac.uk/psmsl.

This first step in the analysis is to select tide gauge data that are suitably placed to monitor input to the ocean from the GrIS. The PSMSL (Permanent Service for Mean Sea Level) is an online archive of global sea-level data gained

from tide gauges around the world. Fig. 3.1 shows the geographical distribution of tide gauge records held by the PSMSL (Woodworth and Player, 2003).

The distribution of tide gauges is significantly biased towards the northern hemisphere, with many of the longer-term data series (> 100 years in length) also mainly available at northern hemisphere sites. Data are available in two formats, 'Metric' and 'RLR' (Revised Local Reference). For meaningful reconstruction of secular trends, the sea-level heights provided by the local authority operating the tide gauges must be reduced to a local datum (a 'revised local reference'). This ensures continuity between measurements, especially if a local datum needs to be relocated for any reason.

Tide gauges in eastern USA between latitudes 25^{o}N and 50^{o}N are ideally positioned to capture a sea-level trend associated with mass changes from the GrIS. For example, a 1mm/yr eustatic melt rate from Greenland results in a sea-level change that increases from + 0.1mm/yr in north-east USA to + 0.8mm/yr in Florida as these values scale linearly with eustatic melt rate (Mitrovica et al. 2001). Assuming that steric and GIA signals can be removed with sufficient accuracy it should be possible to pick out a GrIS melt signal in the data if the ice sheet has experienced considerable mass loss (~0.5 mm/yr eustatic) during the 20th century.

Tide gauges used in this analysis were selected on the basis of the following constraints:

1. Record length must be longer than 40 years. This will reduce the possibility that rates of sea-level change are biased as a result of decadal and annual fluctuations.

2. They are distal to known sites of sediment loading and are tectonically quiescent. Sediment loading and non-GIA deformation processes are not considered in this study and so sites near to river deltas and active margins are omitted.

3. Data files contain RLR values.

Rates of sea-level change were calculated using linear regression for the period 1950 or earlier to 2005 where possible. The primary aim is to identify a spatial trend in the data associated with GrIS mass changes and so sea-level rates were calculated relative to a reference site (Baltimore) to remove any spatially uniform trends within the signal. The data, shown in Fig. 3.2a, exhibit a long-wavelength pattern that is characterised by an increase of +2 mm/yr between

latitudes 25°N and 37°N, followed by a decrease of similar magnitude between 37°N and 43°N.

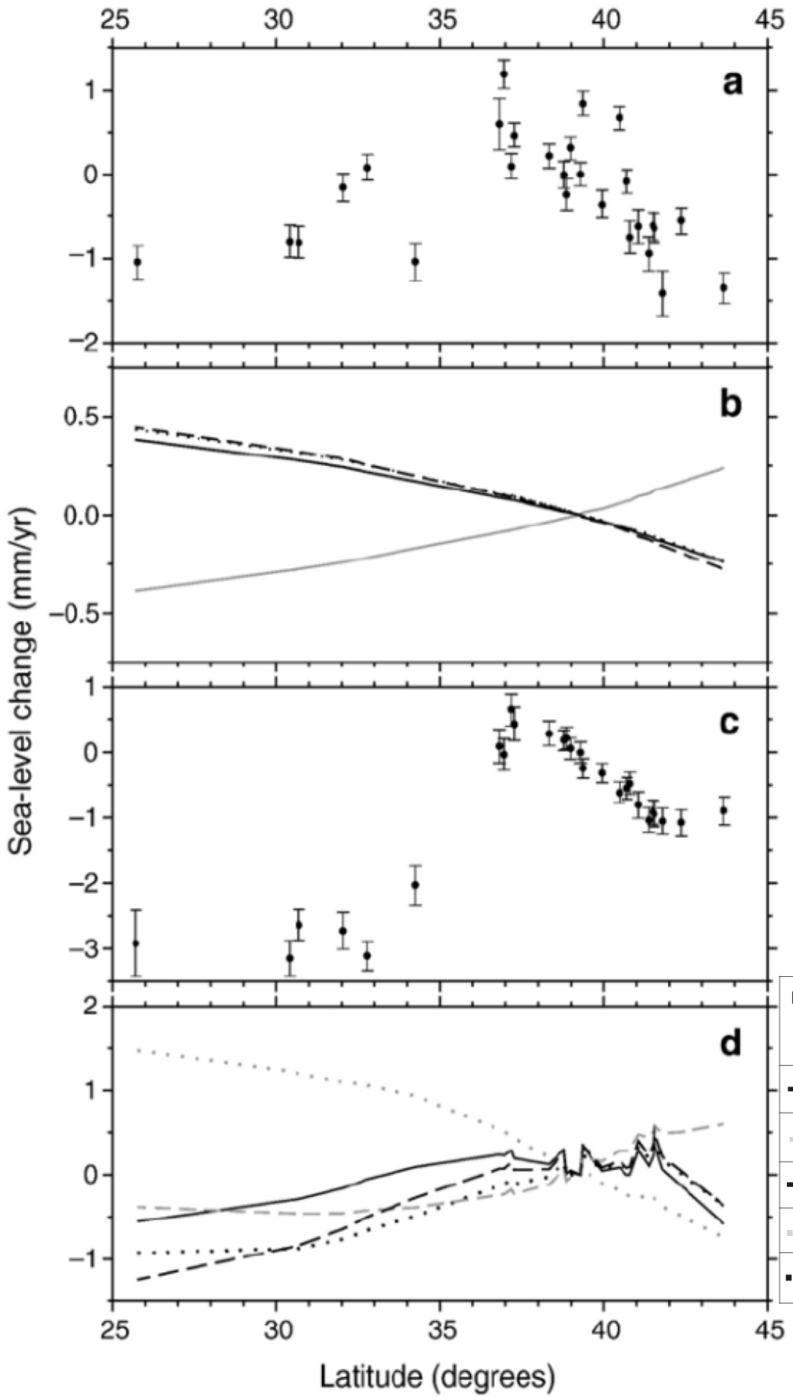

Line	Lithospheric thickness, L (km)	Lower Mantle Viscosity, υ_{LM} (Pa s)	Upper Mantle Viscosity, υ_{UM} (Pa s)
———	96	1×10^{22}	5×10^{20}
— — —	96	1×10^{21}	5×10^{20}
— — —	96	5×10^{22}	5×10^{20}
■ ■ ■	96	1×10^{22}	1×10^{20}
■ ■ ■	96	1×10^{22}	1×10^{21}

Fig. 3.2: (a) Rates of sea-level change estimated from tide gauge time series of length 40–95 years. Note that all rates shown are relative to the site Baltimore (39.3°N) to remove any spatially uniform component of the signal. A standard error of 1−σ is indicated. (b). Predicted sea-level changes at the tide gauge sites (relative to Baltimore) for four different GrIS mass balance scenarios; a negative mass balance equivalent to 1 mm/yr of eustatic sea-level rise (black lines; see Section 3.3 for details of models) and a positive mass balance of the same magnitude based on a uniform scaling of ice thickness (gray line). (c) Estimated sea-level changes at the tide gauge sites (relative to Baltimore) due to the steric effect (see Section 3.4 for details). A standard error of 1−σ is indicated. (d) Predicted sea-level changes at the tide gauge sites (relative to Baltimore) due to the ongoing solid earth deformation associated with the most recent glacial cycle. Predictions are shown for five different earth viscosity models (see accompanying table).

Some of the primary features of the sea-level trend evident in Fig. 3.2(a) have been explained in terms of GIA (e.g. Davis and Mitrovica 1996). For example, the maximum in sea-level rise at 37°N is believed to be due to the collapse of the forebulge associated with the NAIS. Also, reduced rates of sea-level rise north of 37°N are though to be a result of the increasing proximity to the uplift centre in the Hudson Bay region. In the next sections, the contributing signals (Fig. 3.2 b, c and d) are explored.

3.3 The Sea-level Signal due to Mass Changes of the GrIS

To compute the sea-level signal associated with changes in the GrIS during the past 50yrs three different mass balance scenarios are developed using the 5 km by 5 km digital elevation model of the GrIS available from the National Snow and Ice Data Centre (Bamber et al. 2001a, 2001b). Construction of the mass balance models and their resulting sea-level signal are described in this section.

A number of studies have provided estimates of GrIS thickness variations based on direct observations of the ice sheet over the past 10–20 yr (e.g. Rignot and Thomas, 2002)). These studies indicate that the pattern of ice thickness changes shows considerable spatial variation, with some areas exhibiting growth while others show a net melt. In order to consider the sensitivity of the data to details of the recent GrIS history, three models with different levels of complexity were constructed**.** Model 1 was constructed by simply scaling the present-day digital elevation model (Bamber et al. 2001a, 2001b) to produce a uniform melt rate. Model 2 was engineered to produce a uniform melt rate due to low altitude, peripheral thinning of the ice sheet (e.g. Krabill et al. 2000). Model 3 is based loosely on the result of Thomas et al. (2000) and comprises four regions separated by the line of latitude 69°N and the line of longitude 40°W. The northwest and southeast quadrants experience a net mass loss with the northeast and southwest components experiencing a net growth. The total mass loss still equates to +1mm/yr eustatic sea-level rise, but the inclusion of areas of growth on the GrIS served to test whether the fingerprint on the US east coast would be influenced by the different geometries of ice loss in Models 1-3.

For each model, the magnitude of melt is defined to be constant at +1 mm/yr of eustatic equivalent sea-level rise, and is assumed to last for a period of 50 years. For completeness, Model 1 was also scaled to contribute negatively to eustatic sea-level change (i.e. -1mm/yr). The value of +/- 1mm/yr was chosen since

the predicted sea-level signal is directly proportional to net mass balance of the ice sheet for a given melt scenario and so choosing a value of 1 mm/yr is convenient for scaling purposes. Mitrovica et al. (2001) estimated a contribution from Greenland of +0.6mm/yr to 20th century eustatic sea-level change, therefore, the value of +1mm/yr may be considered as a relatively "safe" upper bound on this parameter.

The sea-level signals, computed using the sea-level code described in Chapter 2, associated with the 4 mass balance scenarios are shown in Fig. 3.2b. It is evident that the rate of sea-level change at each site is insensitive to melt geometry, so the use of US tide gauges is limited to determining the net mass balance of the GrIS and not the pattern of mass loss over the ice sheet.

3.4 The Sea-level Signal due to Changes in Ocean Density

Recent studies have shown that estimates of steric sea level in a particular region can differ significantly depending on the data used (e.g. Lombard et al. 2005, Miller and Douglas, 2004). The datasets available from NODC (National Oceanographic Data Centre) include gridded 0.5 x 0.5 degree temperature and salinity fields for all 33 standard depth levels (ranging from 0-3000m) as defined by NODC. These are compiled using raw temperature and salinity profiles collected from various sources. When calculating the steric signal for the US east coast, the procedure followed is similar to that described in (Miller and Douglas. 2004) so as to minimise any bias associated with the interpolation of hydrographic data available from the World Oceanographic Atlas (WOA)

Specifically, raw hydrographic profile data obtained from the World Ocean Database 2001 (WOD01) were used to compute density (steric) changes associated with both temperature and salinity variability. Only traditional bottle, salinity–temperature–depth (STD), and conductivity–temperature–depth (CTD) measurements to 500 m were used. Dynamic heights (0–500 m) were calculated for each profile by computing specific volume anomalies at observed levels and then integrating in the vertical. In order to correctly average over regions with significant variation of mean dynamic topography, dynamic height deviations were computed relative to a 1°×1° mean dynamic topography interpolated to the actual location of each observation. These deviations were subsequently converted into dynamic height anomalies by subtracting mean annual and semi-annual cycles based on a least-squares fit to all measurements within a given region. For each tide gauge station, the dynamic height anomalies from the closest 1000 profiles were converted

to steric height, and a trend was computed from a least-squares fit after outliers were removed. At each site, the steric trend was computed over a time period that is consistent with the tide gauge time series to ensure that the steric and tide gauge rates could be compared directly.

The estimate of the steric contribution to the sea-level trend at the tide gauge locations is shown in Fig. 3.2c. The most striking feature of the steric signal is that the overall pattern is qualitatively similar to that shown in the tide gauge data (Fig. 3.2a), with a sea-level maximum between 37^{o}N and 38^{o}N, and a fall at lower latitudes. The main difference is that the increase in the rate of sea-level rise between 34°N and 37°N is more pronounced and of larger magnitude in the steric signal. The large gradient at this location is likely associated with movement of the Gulf Stream during the monitoring period (Levitus et al., 2005). The Gulf Stream is an extremely dynamic atmosphere-ocean physical system. For example, using observations of sea-surface height change, Frankignoul et al. (2001) demonstrated that the position of the axis of the Gulf Stream deviated by +/- 2^{o} over the period 1993-1998. Tide gauge series at latitudes greater than 45^{o}N show no anomalous variation around 1993-1998 indicating that this particular signal is likely to be smaller than the noise in the tide gauge records. A recent study by Bingham and Hughes (2009) demonstrated that patterns in sea-level height modelled off the east coast of the USA may be reflecting changes in Meridonal Overturning Circulation (MOC). Comparison of sea-surface altimetry with modelled ocean height anomalies arising from changes in MOC transport in the 100-1300m depth range indicated that both processes are highly correlated. Although changes in the MOC were only modelled from 1986-2000, the interannual variability and correlation with tide gauges at latitudes > 45^{o}N emphasises the importance in using tide gauge records of length > 40 year to suppress the influence of these dynamic ocean-atmosphere processes on the estimated sea-level trends.

3.5 The Sea-level Signal due to Deglaciation of the Laurentide Ice Sheet

The North American Ice Sheets (NAIS) reached their maximum extent between 27,000 ^{14}C and 24,000 ^{14}C years before present (Dyke et al. 2002), several thousand years before the Last Glacial Maximum. During this time, the ice sheet covered much of Canada, extending past the Great Lakes and linking to Greenland via the Innuitian Ice Sheet. The major outflow centre of the NAIS was situated in the Hudson Bay region and was fed mainly by the Innuitian Ice Sheet (Northern

Canada), and the main Laurentide Ice Sheet (central Canada). The Cordilleran Ice Sheet was located in the Rocky Mountains; with the main ice flow directed towards the east to the ice divide (Fig. 3.3) although there were smaller localised flow towards the west via valley glaciers (Clague and James, 2002)

The NAIS had completely disappeared by 7,000 ^{14}C years before present (Tushingham and Peltier, 1991), with only small ice caps remaining from this time to present in the Innuitian Ice Sheet area. The total eustatic contribution of the NAIS is estimated to be in the range 64.3m to 92m (Clark and Mix, 2002), of which the Laurentide component is estimated to be 76 – 85m (Clark and Mix, 2002). In comparison, complete deglaciation of the present-day GrIS is estimated to contribute less than 7m to global mean sea level.

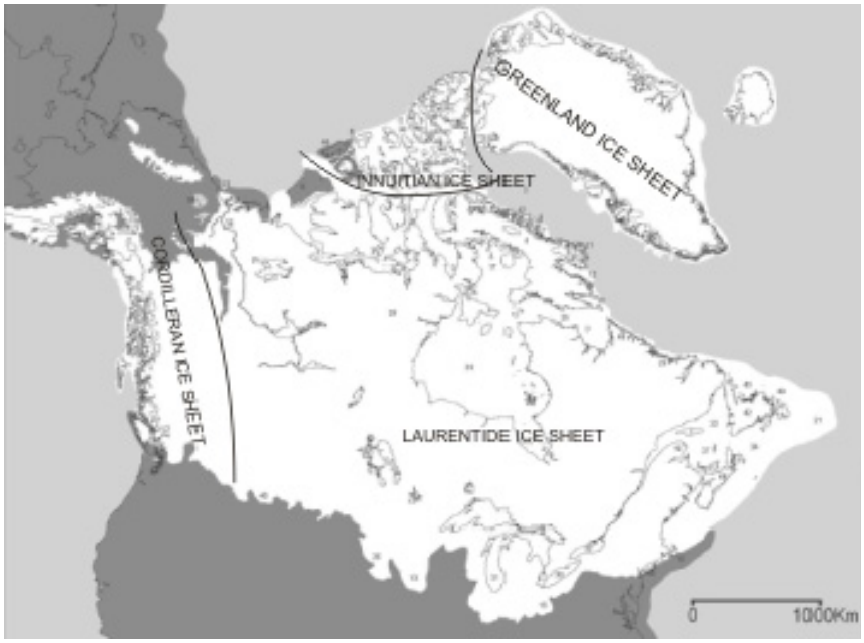

Fig. 3.3: Figure adapted from Dyke et al. 2002. showing the approximate locations and extents of the NAIS at the LGM.

To predict the present-day sea-level change at the tide gauge sites associated with ongoing isostatic deformation in response to the most recent glacial cycle, the ICE-3G deglaciation history (Tushingham and Peltier, 1991) was adopted. This model was modified to include a glaciation phase by assuming that the ice build-up follows the time reversed pattern of ice retreat except that the time increment between each loading episode is 7 kyr (compared to 1 kyr for the deglaciation period). In the ICE-3G model, global ice extent reached the present-day distribution by 5 kyr BP. The present-day uplift rate calculated using the modified ICE-3G model and a reference Earth model is presented in Fig. 3.4.

The maximum uplift rate is predicted in the Hudson Bay area, where the centre of the Laurentide Ice Sheet was located. The greatest rates of land subsidence (sea- level rise) are observed offshore north-east America. At latitudes 30°N-40°N, variation in uplift rates is small, with rates varying within +/-0.5mm/yr. The profile line of the tide gauge sites lies oblique to the maximum gradient of GIA-related sea-level change, so peripheral bulge subsidence is not captured clearly in the data shown in Fig. 3.2a

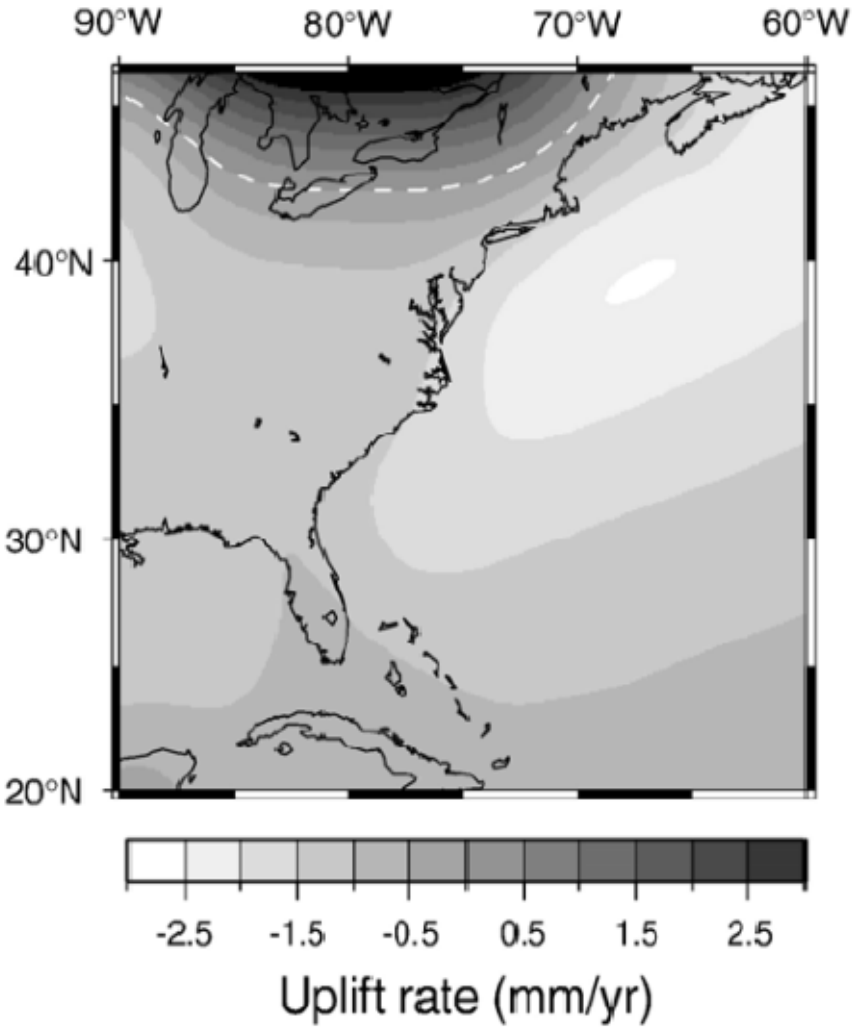

Fig. 3.4 Crustal uplift pattern associated with deglaciation of the NAIS for a reference earth model: L=96km, υ_{UM} = 5 x 10^{20} Pa s, υ_{LM} = 1 x 10^{22} Pa s. Dashed white line signifies zero mm/yr contour.

The sea-level responses predicted using the modified ICE-3G load history and a suite of different Earth models are presented in Fig. 3.2d. The response using the reference earth model shows the characteristic sea-level fall at latitudes north of 40N, with maximum values of several millimetres per year recorded in the Hudson Bay area (not shown on Fig. 3.4), where maximum uplift rates are predicted. The

response to deglaciation between the latitudes of ~32°N and 40°N produces a sea-level rise. Although this area was not ice covered, loading of the crust over Canada caused crustal flexure and up-warping at lower latitudes. The sea-level rise modelled in these regions is due to submergence of the peripheral bulge region associated with the Laurentide Ice Sheet. Increasing lower mantle viscosity (υ_{LM}) to 5 x 10^{22} Pa s translates to a stiffening of the lower mantle. This forces the mantle to become increasingly resistant to flow (causing longer response times to loading), and the wavelength of crustal flexure becomes larger effectively forcing the peripheral bulge region south (Fig. 3.2d, black dashed line). Small values of υ_{LM} force the GIA related sea-level change to assume a smooth profile, with a gentle decrease in rate of 1mm/yr from 44°N to 26°N (Fig. 3.2d, grey dashed line).

Changes in υ_{UM} have the largest effect at sites between 26°N and 38°N, because the main influence of this parameter is to modulate the magnitude of the peripheral bulge. Large values for upper mantle viscosity (υ_{UM}) result in a narrowing of the peripheral bulge region. In Fig. 3.2d, the black dotted line displays the characteristic geometry of RSL change associated with a deglaciated continent: Lower rates of sea-level rise at sites located > 42°N near the uplift centre, slight increase in sea-level rise at mid-latitudes (39°N- 42°N) due to peripheral bulge subsidence, with sea-level fall beyond (latitude < 39°N). However, decreasing the upper mantle viscosity produces a broader region of uplift, which is reflected at latitudes > 39°N. A smooth transition from sea-level fall to rise (+ 1mm/yr North-South differential) is modelled for υ_{UM} = 1 x 10^{20} Pa s (grey dotted line). The loss of the 'peripheral bulge region' in the low υ_{UM} case is related to the "channel-like" flow geometry exhibited by earth models with a relatively weak upper mantle viscosity and a large upper-to-lower mantle viscosity increase (Officer et al. 1988). This geometry of flow produces a pattern of vertical deformation (and sea-level change) that is distinctly different to that predicted using the other viscosity models considered, due to the majority of the upper mantle flow being horizontal, rather than vertical. Also, using a model with low υ_{UM} allows most of the adjustment of the Earth to be completed more quickly than compared to models with higher υ_{UM} .

3.6 Determining the preferred Earth Model using US East Coast Tide Gauge Data: The Influence of Climate Signals

Because the US east coast tide gauges have been used to determine earth viscosity structure, it is important to investigate the bias incurred due to neglecting the signals associated with GrIS mass balance and regional ocean temperature and salinity changes (Section 3.6.2). The sensitivity of the inference procedure to different deglaciation histories (ICE-3G vs. ICE-5G) is also tested (Section 3.6.3).

3.6.1 Methodology

1. The sea-level rates (mm/yr) from tide gauges (SL_{TG}) were first corrected for sea-level change arising from GrIS melt magnitudes of +1, 0, -1 mm/yr (SL_{MB}). As shown in Fig. 3.2b, the pattern of sea-level change on the US east coast is unaffected by the geometry of GrIS mass changes and so a simple uniform scaling of ice thickness change is employed to generate the fingerprint.

2. The tide gauge data are corrected for steric sea-level change (SL_{ST}), as computed in Section 3.4.

3. Both sets of residual rates (non steric-corrected (j=1) and steric-corrected (j=2)) are then compared to a suite of predictions for GIA-related sea-level change generated using a variety of Earth model configurations in which the parameters upper mantle viscosity (υ_{UM}) and lower mantle viscosity (υ_{LM}) are varied over the respective ranges: 0.05 x 10^{21} $\leq \upsilon_{UM} \leq$ 1 x10^{21} Pa s and 1x 10^{21} $\leq \upsilon_{LM} \leq$, 50 x 10^{21} Pa s. As the predictions are relatively insensitive to variation in lithospheric thickness an intermediate value of 96 km was adopted. The chi – squared (χ^2) goodness-of-fit of the residual ($SL_{RES}(j)$) to the GIA-related sea-level change (SL_{GIA}) is analysed using the following formula:

$$\chi^2 = \frac{1}{n-1}\sum_{n=1}^{n}\frac{[SL_{RES}(j) - SL_{GIA}]^2}{[\sigma^2]} \qquad \text{E3.1}$$

For *j*=1,2, and

$$SL_{RES}(1) = SL_{TG} - SL_{MB}$$

$$SL_{RES}(2) = SL_{TG} - SL_{MB} - SL_{ST}$$

Where *n* represents the number of data sites and σ represents the 1-sigma error bound on the observed tide gauge rates. The results of the chi squared analysis for a suite of earth models are shown in Fig. 3.5 (A, B & C for $SL_{RES}(1)$ and D, E & F for $SL_{RES}(2)$).

3.6.2 Results

The results for $SL_{RES}(1)$ (frames A-C) will be discussed first. For the case of no contribution from the GrIS to sea-level change (Fig. 3.5 B), the viscosity model that best fits the observations comprises a 3×10^{20} Pa s upper mantle and a 5×10^{22} Pa s lower mantle (for L=96 km). The region encompassed by the 95% confidence limit covers a large area of the viscosity space considered, indicating that the data are relatively poor at providing a tightly constrained inference of viscosity structure. Only models with a relatively modest or relatively large increase in viscosity between the upper and lower mantle are ruled out by the data in this case. The viscosity inference derived from Fig. 3.5 (B) agrees with that proposed by Davis and Mitrovica (1996).

On comparing the results in frames (A) and (C) to those in frame (B), it is evident that making the mass balance signal more negative (i.e. more ice melt) acts to shift the “best-fit” region of viscosity space towards values of larger upper mantle viscosity. However, it is important to note that there remains a significant portion of the “best-fit” region that overlaps when comparing the results in frames A and C, and so it is possible to specify a number of earth models that can provide equally good fits to the tide gauge data regardless of the GrIS mass balance value within the range considered. The lowest chi-squared value for these results (2.8) is for the +1mm/yr melt scenario and for upper and lower mantle viscosities of, respectively, 5×10^{20} Pa s and 2×10^{22} Pa s. This inference is, however, only weakly dependent on the range of GrIS mass balance scenarios considered. Previous inferences of mantle viscosity that did not consider the influence of GrIS mass balance are therefore not significantly biased.

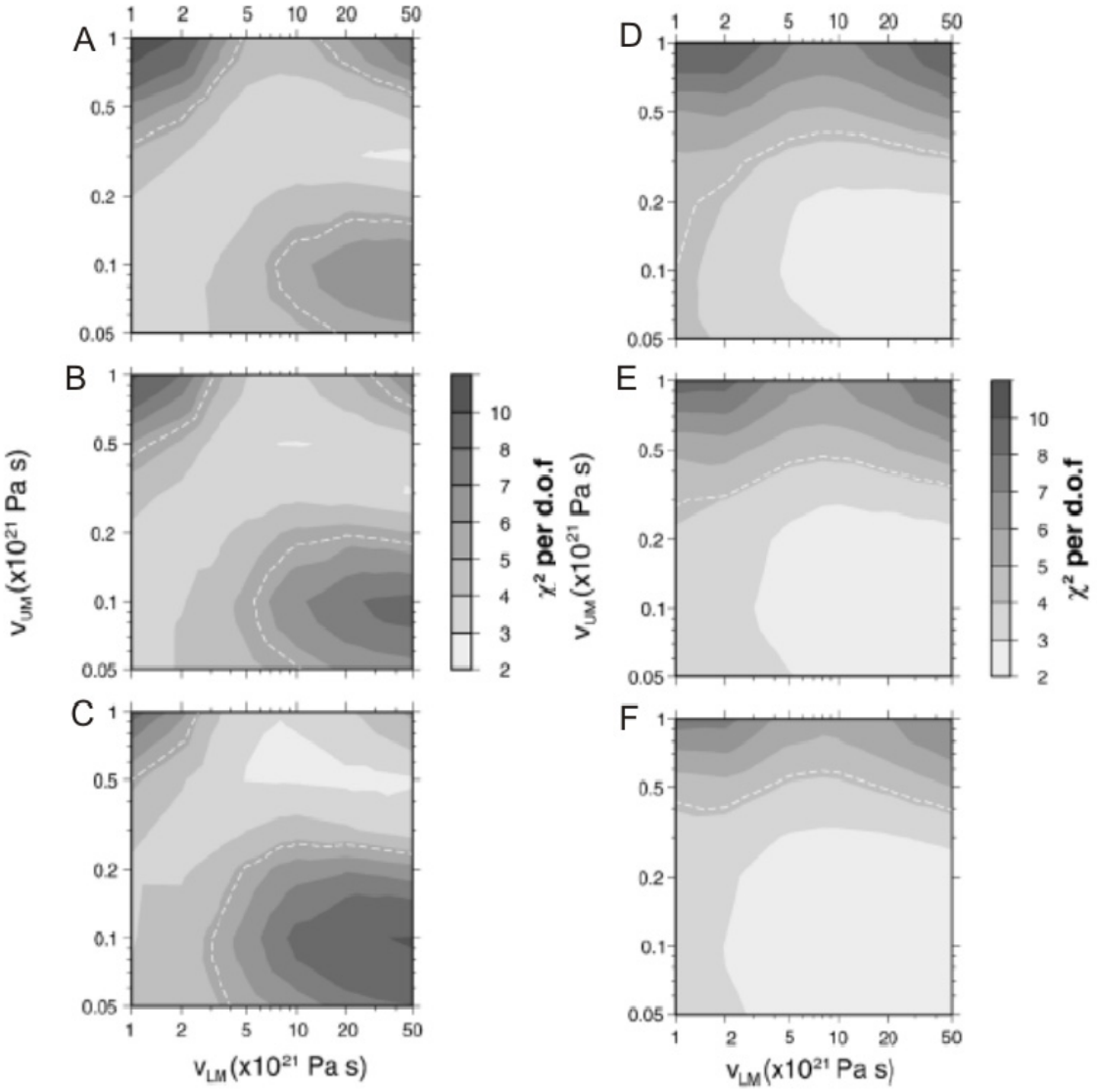

Fig. 3.5 Left-hand frames show normalised chi-squared values signifying the quality of data-model fit for a large suite of upper and lower mantle viscosity values and GrIS mass balance values of (A) −1 mm/yr, (B) 0 mm/yr and (C) 1 mm/yr of eustatic sea-level equivalent. Right-hand frames show results equivalent to those on the left except that the data have also been corrected for steric sea-level changes (as well as GrIS mass balance): (D) −1 mm/yr, (E) 0 mm/yr and (F) 1 mm/yr. The dashed white line in all plots shows the chi-squared value that marks the 95% confidence limit based on an F-test.

For the $SL_{RES}(2)$ results, frames D, E and F, it is clear that applying a correction for steric sea-level change has a considerable effect on the preferred viscosity structure. In all cases, the optimum solution space shifts to low- to medium upper mantle viscosities. On comparing the results in Fig. 3.5 (A,B,C) to those in Fig. 3.5 (D,E,F), it is clear that this component of the climate signal has, by far, the greater influence of the two climate signals This is not surprising given that the estimated steric signal overwhelms a plausible fingerprint signal originating from the GrIS. In order to compensate for the large steric signal at latitudes > 34^{o}N, a low

upper mantle viscosity is preferred to reduce this signal so that the total (combined) sea-level trend that is more compatible with the observed data. There is no strong preference towards a particular lower mantle viscosity – as spatial pattern of predicted rates display a similar trend to the overall signal. For example, the overall pattern displays a maximum rate of sea-level change between 37^{o}N and 41^{o}N (Fig. 3.2a). A similar pattern is modelled in Fig. 3.2d (black dashed line). The exception to this is when extreme low values of υ_{LM} are used (grey dashed line, Fig 3.2d). This shows a steady decline in relative sea-level change so the sensitivity to υ_{LM} is high. Note that the range of preferred lower mantle viscosity values (to 95% confidence) is not reduced, but in fact increased by applying the steric correction.

3.7 Investigating the Importance of Deglaciation History: ICE-5G vs. ICE-3G

The above viscosity inferences are based upon the ICE-3G loading history only, In order to consider the sensitivity of our results to the adopted ice model, a suite of predictions based on the more recent ICE-5G model were generated. I will briefly review the differences in the NAIS section of the model in the ICE-3G (Tushingham and Peltier, 1991) and ICE 5G reconstructions (Peltier, 2004) in the following sub-section before going on to consider the influence of this model component on the original viscosity inference results (Section 3.6.2).

Between 18kr and 15kyr, ICE-3G (Tushingham and Peltier, 1991) defines the main changes in global ice cover to occur over Northern Asia, with very little activity on the NAIS. By 11kyr, the Laurentide Ice Sheet had separated from the Cordilleran Ice Sheet, and the margin of Laurentide had retreated north over the Great Lakes region. Ice thickness in the Hudson Bay region was reduced from > 2000km to ~ 1000km from 15kyr to 11kyr. By 8kyr, Hudson Bay was completely ice-free, and the Cordilleran sector has gone. By 6kyr, the NAIS had deglaciated completely, and contributed 61m to the 115m of eustatic sea-level rise.

Refinement of ICE-3G was performed and later published in 1994 as 'ICE-4G' (Peltier, 1994). ICE-3G was modified by addition of newly-published datasets to constrain the history of global eustatic sea-level change. These include U-Th and ^{14}C dated corals from Barbados– a site well located to capture an approximation to global eustatic sea-level change. This record shows pulses of global eustatic sea-level of magnitude 20-30m and 10-15m occurring around 14.5kyr and 11kyr respectively. In order to facilitate a rapid sea-level rise, rapid deglaciation of the Laurentide Ice Sheet is initiated at 14.5kyr, with complete disappearance of the

Cordilleran sector by 11ka. Here, deglaciation occurred via mass wasting processes at high altitude, with valley glaciers being the last to disappear. The deglaciation of the Cordilleran sector was rapid and was completed in less than 5000 years (Clague and James, 2002). The extent and size of the present glaciers in British Columbia are similar to those at 9500 ^{14}C years BP. Note in ICE-3G (Fig. 3.6), the Cordilleran Ice Sheet is still present at 11ka. The ICE-4G version is not used in this analysis, but a review of the changes made from ICE-3G to ICE-4G is necessary to explain further modifications when constructing ICE-5G.

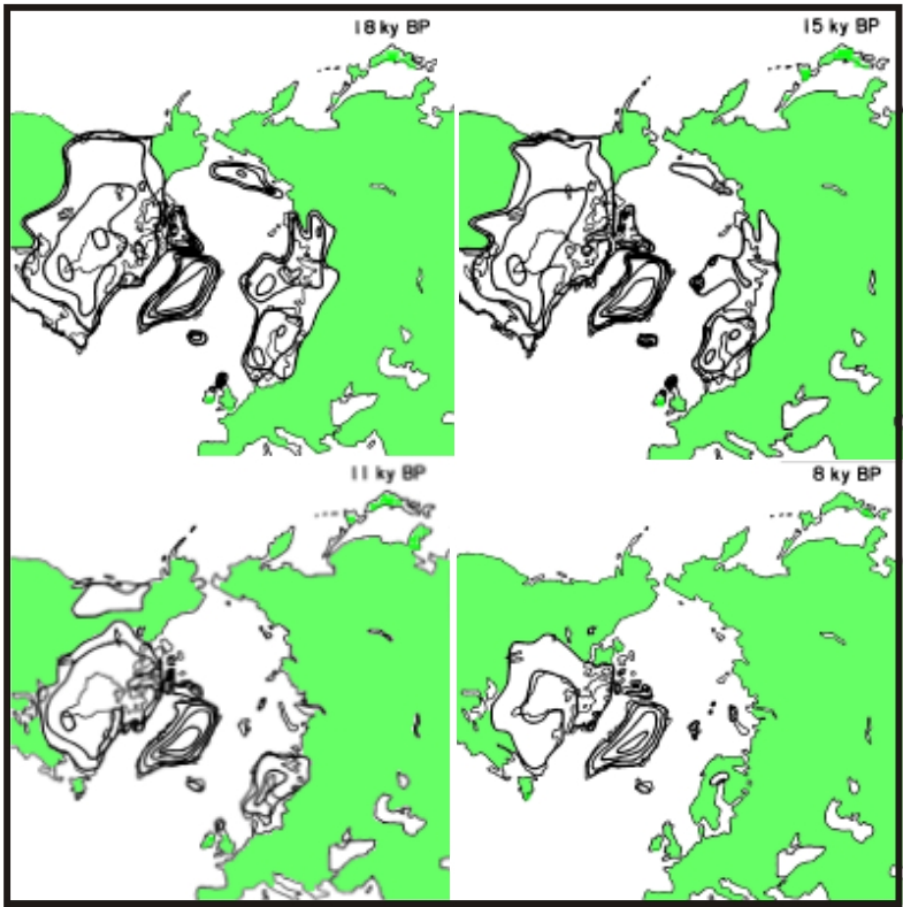

Fig. 3.6: Ice thickness at (clockwise from top left) 18, 15, 11 and 8kyr BP over North America, Canada and Greenland for ICE-3G deglaciation history. Each contour represents 1km increment in ice thickness

One of the main adjustments made to ICE-4G to create ICE-5G was to modify ice thickness south of Hudson Bay. Ice flows readily over unconsolidated sediments, but is more likely to be frozen to crystalline igneous basements. Hudson Bay is sediment filled, so ice flows rapidly and does not have a chance to accrete. Therefore, LGM ice thickness over Hudson Bay was reduced by ~500m compared to the ICE-4G version (Peltier 2004).

In order to account for the discrepancies between the measured and modelled (using ICE-4G) time-derivates of gravitational acceleration, the thickness of the Laurentide Ice Sheet in some areas was modified to recreate the spatial variation of this parameter from Churchill to Iowa (see Fig. 3.7). The reduction of gravitational acceleration (*g)* over time is under predicted using the ICE-4G deglaciation chronology. Addition of a thicker (up to 2000m) ridge of ice to the west of Hudson Bay in the ICE-5G model improves the fit to measured $\frac{dg}{dt}$.

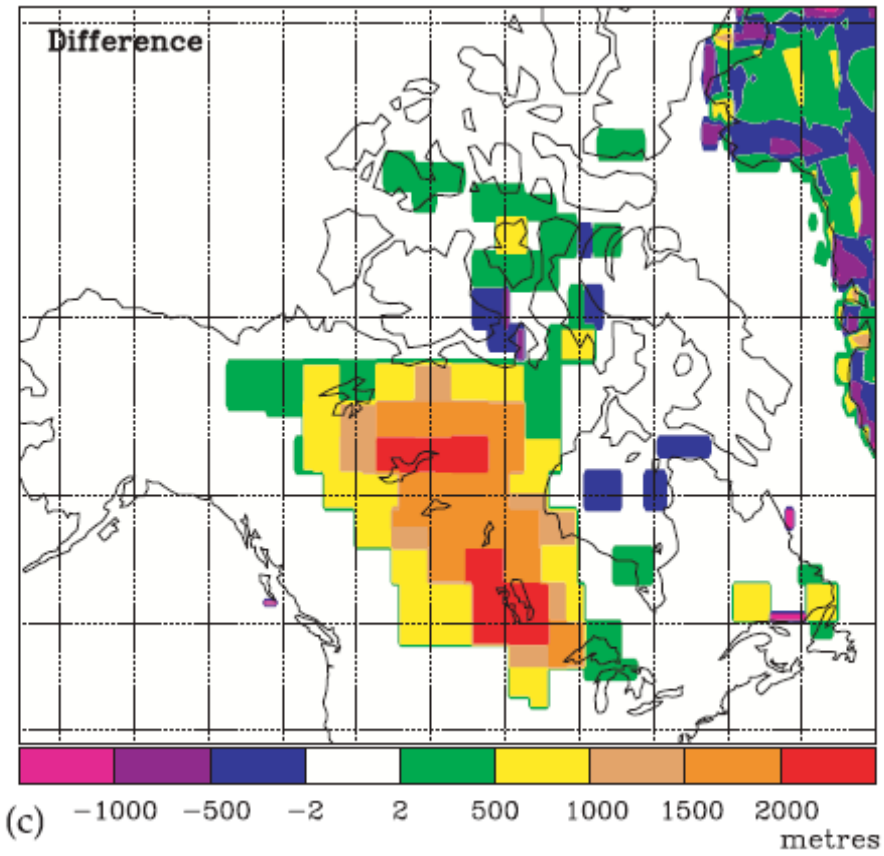

Fig. 3.7: Difference in ice thickness (ICE-5G minus ICE-4G) for the Laurentide Ice Sheet (From Peltier, 2002)

The chi-squared results based on the ICE-5G ice model are shown in Fig. 3.8 (for the steric-corrected case only). Comparing Fig. 3.8 to Fig. 3.5 (D, E & F) indicates that the ICE-5G inferences are compatible (to within 95% confidence) with those based on the ICE-3G model and so the differences between the two ice models do not have a significant impact on the viscosity inference using the steric-corrected tide gauge data. As for the ICE-3G results, the correction for Greenland Ice Sheet mass balance has little influence on the chi-squared values. The optimum fit (χ^2 =1.8) is achieved with a growth scenario of the GrIS and upper and lower viscosity values of, respectively, 5×10^{19} Pa s and 5×10^{22} Pa s (Fig. 3.8)

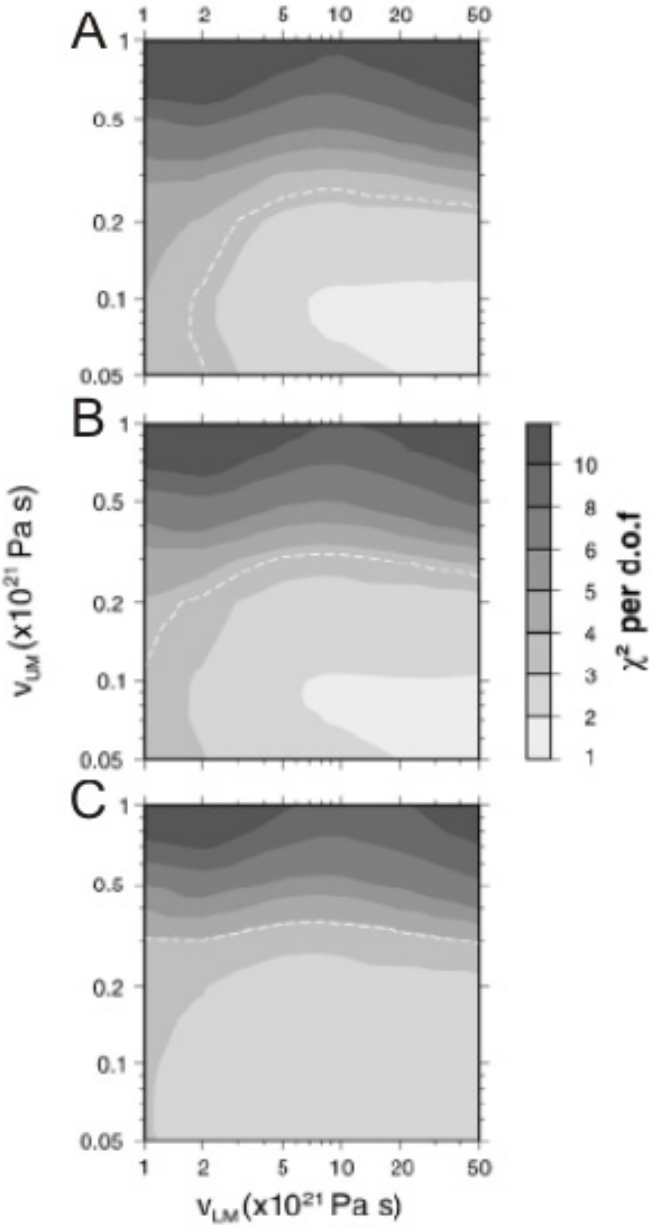

Fig. 3.8: As in Fig. 3.5 (D, E and F) except that residual sea-level change is compared to predictions generated using the ICE-5G deglaciation history.

3.8 Determining the Optimum Melt Rate from the GrIS from Tide Gauge Data

To address the primary aim of this chapter, the final stage of the analysis involved selecting an optimum Earth model to calculate and remove the contribution from GIA and retrieve a melt rate for the GrIS. The residual $SL_{RES}(j)$ in this case can then be directly compared to various GrIS melting scenarios to determine a preferred GrIS mass balance history. As in Section 3.6, the effect of including and omitting a steric correction was investigated. The χ^2 in this analysis is therefore:

$$\chi^2 = \frac{1}{n-1}\sum_{n=1}^{n}\frac{[SL_{RES}(j) - SL_{MB}]^2}{[\sigma^2]}$$

E3.2

$SL_{RES}(3) = SL_{TG} - SL_{GIA} - SL_{ST}$, and

$SL_{RES}(4) = SL_{TG} - SL_{GIA}$

Where j=(3,4).

Since the geometry of mass loss from Greenland does not affect the intermediate and far-field fingerprint, the residual is compared to growth/melt rates in the range of -4 to 4 mm/yr originating from an ice sheet undergoes spatially uniform mass changes.

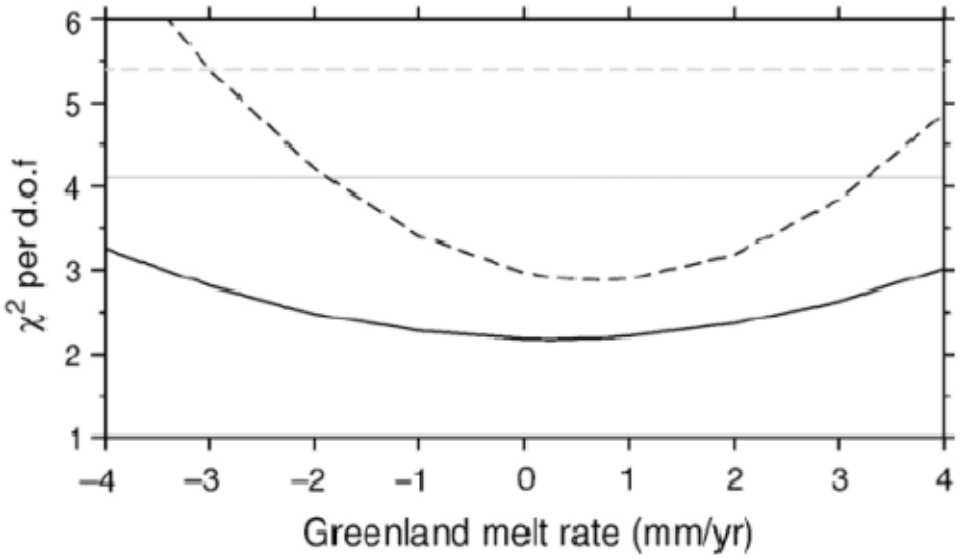

Fig. 3.9: Normalised χ^2 as a function of eustatic contribution from the GrIS. Black solid line signifies the case where the data have been corrected for steric sea-level changes and GIA using an earth viscosity model with υ_{UM} = 8×10^{19} Pa s and υ_{LM} = 5×10^{22} Pa s. The 95% confidence level is shown by a grey solid line. Black dashed line signifies the case where the data have *not* been corrected for steric sea-level changes. In this case the best-fitting viscosity model is characterised by υ_{UM} = 5x10^{20} Pa s and υ_{LM} = 2×10^{22} Pa s, and the 95% confidence level is shown by a grey dashed line. A lithospheric thickness of 96 km was adopted in both cases.

The optimum melt rate for the case of no steric correction ($SL_{RES}(4)$) is +0.7mm/yr. However, Fig. 3.9 shows that all values between -3.0 and +4.0 mm/yr are equally likely (within 95% confidence). For a +4mm/yr melt rate, the contribution to sea-level change on the US east coast ranges from +0.6 to + 3.0 mm/yr from north to south. The optimum melt rate for data corrected for both GIA and steric sea-

level change is +0.3mm/yr, with all melt rates considered providing a statistically equivalent fit (within 95%). These results indicate that the tide gauge data alone are not capable of producing a useful estimate of GrIS mass balance during the 20th century. The data-model fit for both of these optimum scenarios is plotted in Fig. 3.10

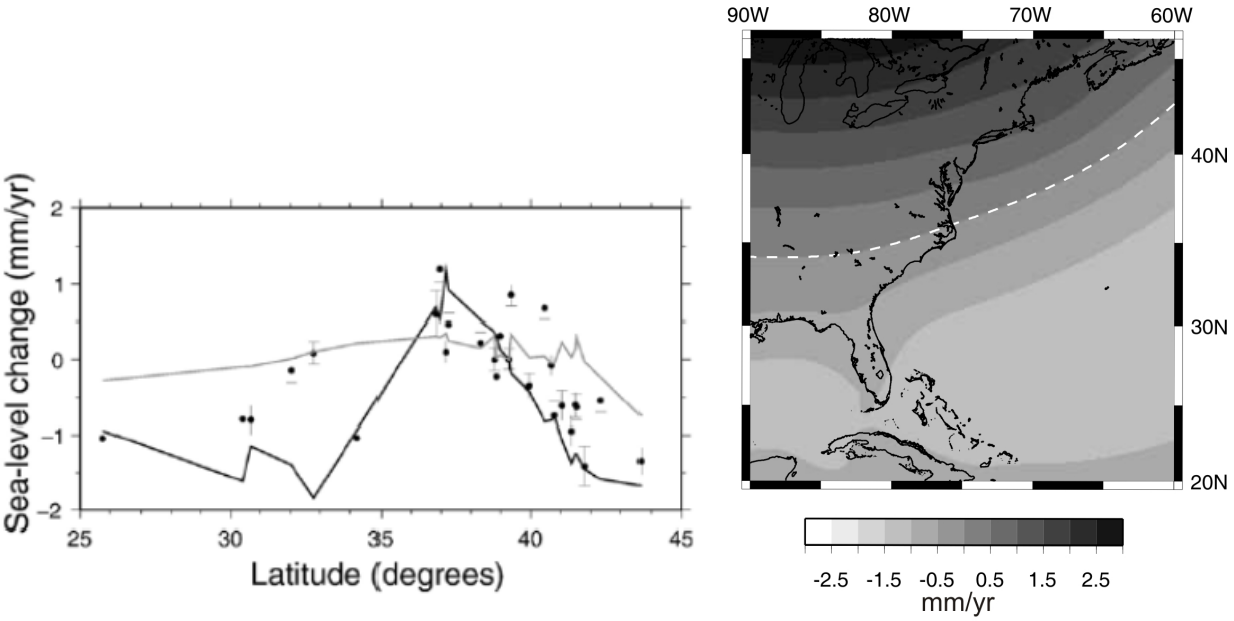

Fig. 3.10 (left): Optimum model fits to the US east coast tide gauge data. Grey line: Combined profile for GIA-related sea-level change (L=96km, υ_{UM} = 5x10^{20} Pa s and υ_{LM} = 2×10^{22} Pa s) and a Greenland melt rate of +0.7mm/yr. Black line: Combined profile for GIA-related sea-level change (L=96km, υ_{UM} = 8×10^{19} Pa s and υ_{LM} = 5×10^{22} Pa s, uplift pattern illustrated in Fig 3.10 (right)), a Greenland melt rate of 0.3mm/yr and steric sea-level changes. All values are calculated with respect to the Baltimore site. The ICE-3G ice model was used in producing these results.

From Fig. 3.10 it is clear that the optimum model including the steric sea-level component produces the best overall fit to the tide gauge data. This model returns a chi-squared value of 3.2, compared to 3.9 for the model with no steric component. The fit is dramatically improved at sites north of 37^{o}N. South of 37^{o}N, neither model accurately describes the sea-level trend. In order to predict the lower rates along this part of the coast of (< 0.0mm/yr; relative to Baltimore), inclusion of the steric effect is essential. The pattern of uplift associated with the optimum model in Fig 3.10 (right) is clearly different to that shown in Fig 3.4. The area of land experiencing uplift is larger, and there is a stronger North-South uplift gradient. This is the result of a highly contrasting upper-lower mantle viscosity, where most of the adjustment is focused in the weak upper layer. This model is facilitated by the need for higher subsidence rates (and therefore sea-level rise) at areas south of 35^{o}N due to the high rates of sea level-fall associated with steric sea-level change.

3.9 Discussion and Conclusions

The main conclusion arising from this chapter is that the tide gauge sea-level record from the US east coast cannot be used independently to constrain (within useful bounds) the mass balance of the GrIS. The two other processes considered in this chapter (steric changes and GIA) both produce a sea-level signal that is several times greater in magnitude than that associated with a 1mm/yr melt signal from Greenland. The processes acting in the US tide gauges, in order of dominance, (1) thermosteric-related variations in sea-level height, (2) GIA and (3) mass input (irrespective of geometry) from the GrIS.

With regard to using the tide gauge data to infer GIA model parameters, the above results show that correction of the tide gauge rates for the steric effect is essential if they are to be used to infer Earth structure**.** The sea-level change due to temperature and salinity changes dominates the US east coast tide gauge record, especially between the latitudes of 34^{o}N and 37^{o}N where the Gulf Stream is active. Correction for the steric effect shifts the inferred upper mantle viscosity to significantly lower values**.** The use of the tide gauge data in combination with GPS measurements of vertical crustal motion should result in a more robust constraint on earth viscosity structure. Currently, the best fit model requires a significant (~ 3 orders of magnitude) viscosity contrast between the upper and lower mantle. This produces and unusual pattern of RSL change where the sea-level gradually changes from a sea-level fall at high latitudes to a sea-level rise towards the south. However, Park et al. (2002) found that the best fit to GPS data was achieved using a GIA model with υ_{UM} = 0.2 x 10^{21} Pa s and υ_{LM} = 5 x 10^{21} Pa s. This model combination lies within the best-fit region (e.g. see Fig 3.5 D, E and F) when the data are initially corrected for steric sea-level change, indicating that the GPS data in North America support a pattern of GIA associated with an Earth model with a low-viscosity upper mantle.

The predicted pattern of steric sea-level bears some similarity with GIA-related sea-level change (e.g. compare Fig 3.2c and Fig 3.2d (black line)). Therefore, when the correction for steric-related sea-level change is applied first, it accounts for much of the north-south variation in sea-level change in Fig 3.2a which is thought to be primarily the result of GIA. However, the preference towards a very low viscosity upper mantle may also be the result of incorrect calculations of dynamic height trends. These inaccuracies may arise from the extrapolation of

dynamic height across the shelf and to the tide gauge, with no correction for local oceanography at the site.

A number of mass balance scenarios of the GrIS were considered, and their contribution to the sea-level change to each tide gauge site was calculated. The gradient of sea-level change on the US-east coast imposed by a +/-1mm/yr eustatic equivalent melt from Greenland is not large enough to significantly effect an inference of Earth viscosity structure using the tide gauge data. The study also shows that using the methods described, and correcting for steric sea-level change and GIA, the residual sea-level change cannot be utilised to distinguish between melt and growth scenarios. The contribution of the GrIS to present-day eustatic sea-level change (last decade) as determined from geodetic methods is observed to be no larger than ~+0.6mm/yr. The tide gauge data are not therefore able to constrain this climatic effect within useful bounds.

Chapter 4: Using Proxy Sea-level Data to search for a Near-field Sea-level Fingerprint from the Greenland Ice Sheet

4.1 Introduction

The theory of sea-level fingerprinting explained in Chapter 2 and illustrated in Fig. 4.1 describes how the Earth's solid surface and geoid are perturbed in the presence of a surface mass load. Within 10 degrees of the area of load application, these perturbations can cause the predicted sea-level change forced by a melting ice sheet to deviate significantly (factor of ~30) from the eustatic change. This is an important result given the small magnitude of the fingerprint signal relative to other signals in the intermediate field (Chapter 3). By considering changes close to the ice sheet, there is greater potential to isolate a GrIS fingerprint signal. The mechanism driving millennial scale change (viscous readjustment of the Earth) recorded by isolation basin data is also embedded in the proxy RSL data available from salt marshes. The millennial scale trend must be removed from the salt marsh data in order to see if sub-millennial changes in ice loading are large enough to force changes in the local sea level. If so, this will be reflected by a departure from the millennial scale trend in RSL.

The main aims of this chapter are to introduce the basic methodology for data collection of proxy salt marsh data and to demonstrate the potential of the near-field fingerprinting technique. The requirement for this data type was highlighted in Chapter 1 (Fig 1.6) where it is shown that a technique to bridge the data gap between decadal (e.g. tide gauges) and millennial-scale resolution RSL indicators (coral records and isolation basins) is needed. The need for RSL data in Greenland is further emphasized in this Chapter when the current Greenlandic tide gauge data are analysed with respect to their potential as reliable indicators of secular near-field sea-level change. The technique of modelling the differential in the near-field sea-level trend has not been attempted, so this Chapter and the rest of the thesis will highlight the strengths and weaknesses associated with the idea.

4.2 Predictions and Observations of Near-field Sea-level Change in Greenland

In Fig. 4.1, the 'near-field' sea-level change for ice loading models 1 and 2 described in Section 3.3 is presented. Both scenarios show complex patterns of

sea-level change close to the ice sheet, which are dependent on geometry of ice loss. Depending on the melt scenario, the sea-level code (Mitrovica and Milne, 2003) predicts a spatial difference in sea-level change of 0 to -8mm/yr over on ~1000km in the west of Greenland (Fig. 4.1, right). For the case of ice loss from the margins of the ice sheet, (Fig. 4.1 (left)), a very different pattern is predicted, with a smaller difference of 2mm/yr along the west coast. The differential gradient in sea-level change is enhanced when contrasting patterns of mass balance occur on small scales and perpendicular to the coast. Therefore, in the immediate vicinity of an ice sheet, the geometry of ice mass balance dictates the geometry and amplitude of the sea-level fingerprint.

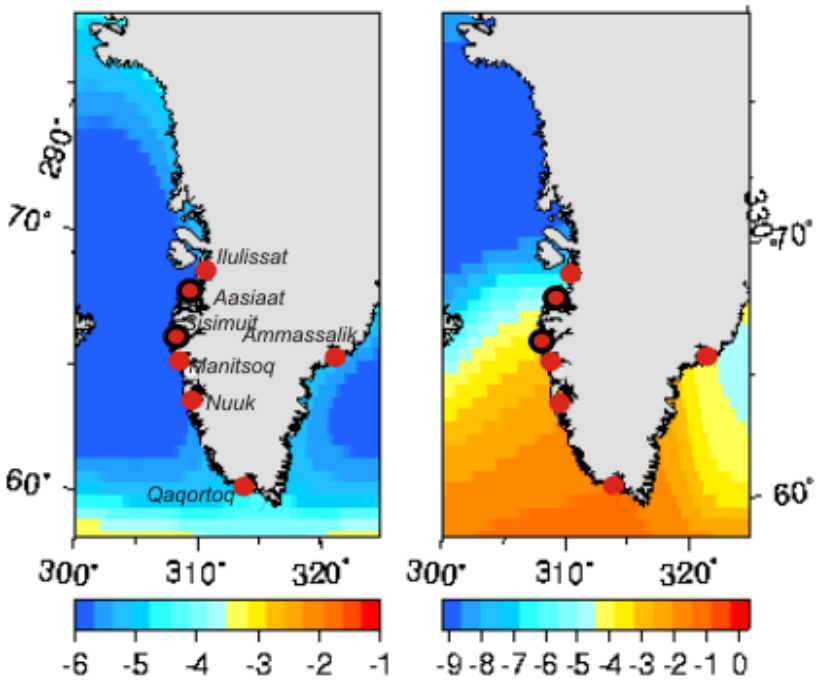

Fig. 4.1: Near-field sea-level change (mm/yr) for mass balance model 2 (left) and model 3 (right). Featured sites are PSMSL tide gauge locations (red). Salt marsh data sites located close to tide gauges are denoted by red circles with black outlines

Following on from the discussion in Section 4.1, it is instinctive to search for tide gauge records closer to Greenland, and analyse these in order to see if they display a spatial gradient of sea-level change compatible with the scenarios from Fig. 4.1. The PSMSL holds seven tide gauge records from Greenland, with data recorded up until 2002; the sea-level data and associated linear trends are shown in Fig. 4.2. The difficulty with analysing these trends is that sea level is not measured against a local reference frame (i.e. not an 'RLR' dataset). The Nuuk dataset spans ~ 40 years, and is recording sea-level rise of +1.94 mm/yr. Other sites have only recorded data over the past decade, so are not suitable for analysis of long-term

sea-level change. When the Nuuk dataset is analysed over the period 1990-2002, in line with the other sites, it shows a reduced trend of -2.5mm/yr. Again, this highlights the importance of using several decades of data to obtain an accurate measure of secular sea-level change. Fig. 4.2 demonstrates that the Greenland tide gauge data are not suitable for use in a fingerprinting analysis such as that in Chapter 3.

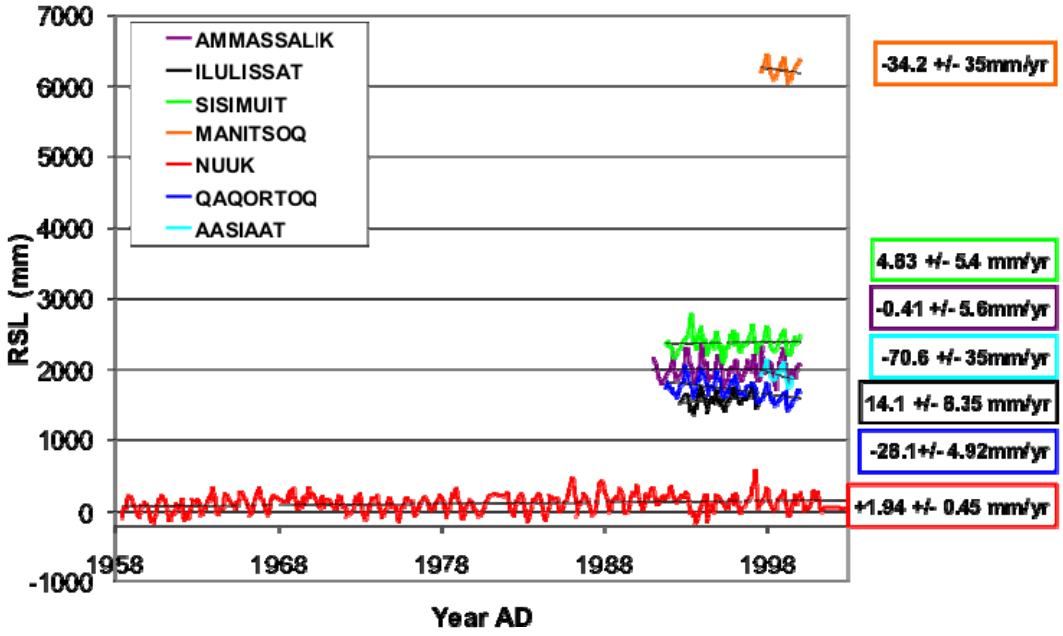

Fig 4.2: Monthly mean values of sea-level for various Greenland tide gauges (see Fig. 4.1 for locations). Values quoted on the right are rates of sea-level change and associated 1σ standard error calculated using linear regression

On the basis of the preliminary modelling results in Fig. 4.1, sites on the west coast of Greenland between Ilulissat to Qaqortoq were targeted for data collection. In this thesis the results from Nag (near Sisimuit) and Aasiaat are presented and analysed. At these sites there is also good observational data from isolation basin records that can constrain the millennial scale trend. A third site, located at Nanortalik (near Qaqortoq) was targeted, but the finalised results for this site were delayed during processing and were unable to be included in this study.

4.3 A New Type of Observational Data: Proxy Sea-level Records from Salt Marshes

Salt marshes are low-lying, vegetated areas of land overlying sediment and/or bedrock. They typically lie in the intertidal elevation range, with vegetation sensitive to fresh and salt water influences. Salt marshes can be expansive, stretching over 80km^2 in some areas (e.g. Great Marsh, New England, USA). Fig.

4.3 shows a typical salt marsh on the west coast of Greenland. In order for salt marshes to thrive, the environment has to experience only low to moderate wave action. Therefore, the salt marshes uncovered in west Greenland are sparse in number and small in extent. The sites where data were collected in the 2006 field season typically had salt marshes of area of less than $20m^2$.

Two types of microfossil (diatoms and foraminifera) are targeted as proxy sea-level indicators. Surface sediment samples of ~5cm thickness are collected from the contemporary salt marsh surface in order to assess the distributions of foraminifera and diatoms in the present day environment. The sample elevations are measured using a levelling technique and are calibrated to present day mean sea level. A 'transfer function' is a statistical tool applied to the historical distribution of foraminifera and diatoms in the salt marsh sediments in order to predict the historical salt marsh surface height using the present day distribution of microfossils as a guide. The robustness of the transfer function is tested against another contemporary dataset from the local area. Due to differences in tidal range, a locally-based transfer function is preferred to a 'regional' transfer function. Therefore the transfer function developed for the site at Aasiaat is not applicable at Nag (Woodroffe and Long, 2009). If a sufficient degree of correlation between actual and transfer function-derived elevation is achieved, the transfer function is applied to the historical biostratigraphy to convert the patterns of diatom and foraminifera distribution into a series of relative sea-level points.

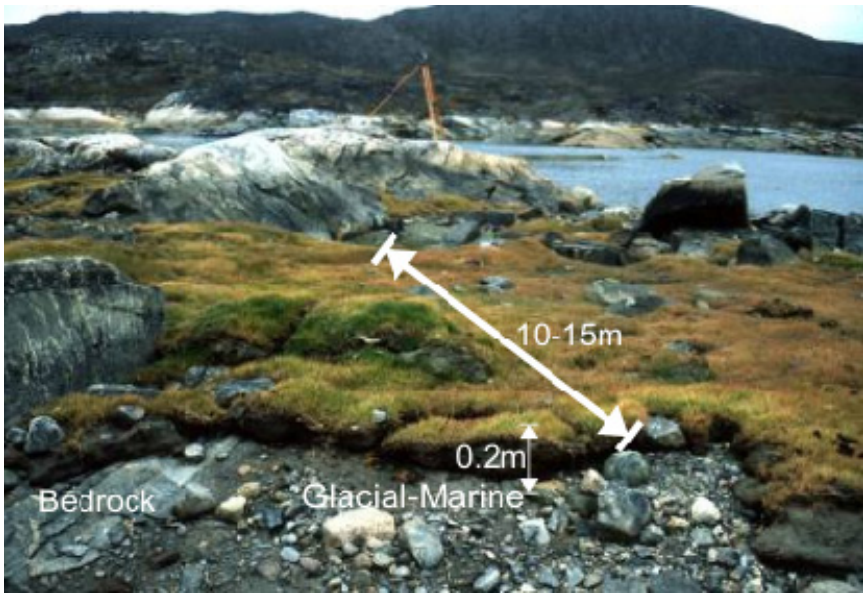

Fig. 4.3 Typical west Greenland salt marsh, overlying glacial-marine sediment (centre-foreground) and/or bedrock (left-foreground)

The historical biostratigraphy is sampled by removing a slab of salt marsh sediment (approximate dimensions: 0.15 x 0.1m, and thickness 0.25m) so that the entire stratigraphy from the bedrock/glaciomarine base to the surface is captured. The typical stratigraphy of the samples collected at Nag (near Sisimuit, see Fig. 4.1) and Aasiaat is shown in Fig. 4.4. All samples collected from Nag and Aasiaat show a transition from freshwater to saltwater conditions as shown by clear changes in the stratigraphy. The basal 0.1m of the sample is composed of freshwater peat, with the remaining 0.15m representative of accumulated salt marsh sediment. It is clear from this observation that there has been marine transgression in the area. However, only detailed analysis of the upper 0.15m of the sediment can reveal if the transgression was continuous or if it stabilised at any point in time. The salt marsh block is sampled at regular vertical intervals, and the relative distributions of freshwater/salt-tolerant diatoms and foraminifera were determined. In the case of these samples, the foraminiferal transfer function failed, as forams were insufficiently preserved at these sites, so sea level was reconstructed using a diatom-based transfer function only.

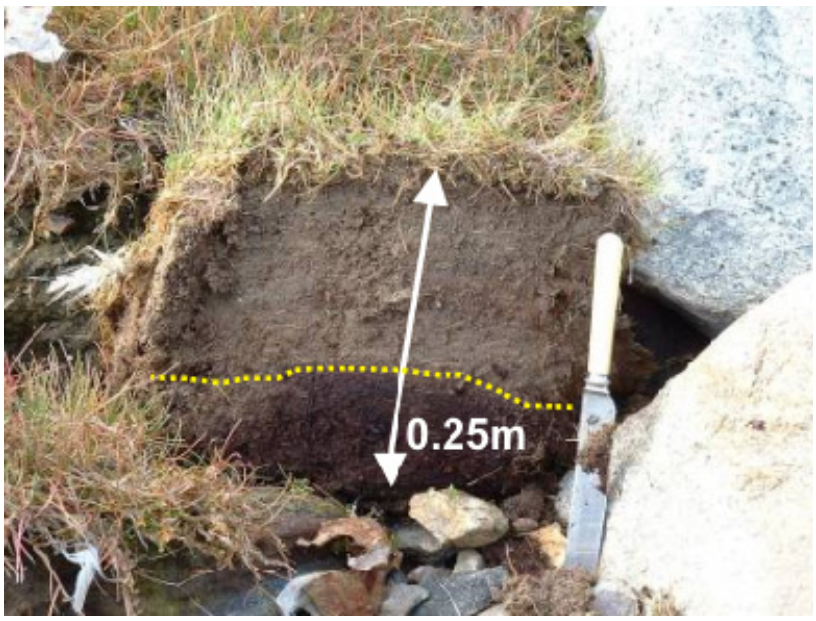

Fig. 4.4 Cross-section through a typical salt marsh in west Greenland, showing the transition (yellow dashed line) from fresh (lower) to saline (upper) conditions.

Once the distributions of diatoms have been recorded in combination with their elevation above mean sea level, the species configuration is dated. The dating techniques used were Accelerator Mass Spectrometry ^{14}C and ^{210}Pb chronologies. For the carbon-dating technique to be successful, the samples must contain carbon-rich macro fossils (seeds, leaves, roots) that have been buried in-situ. This is the

reason for producing a detailed documentation of the present-day surface vegetation. Assuming the distribution of surface vegetation in the historical sediments is similar to the contemporary, it is possible to eliminate macrofossils that are not common to a certain elevation interval and therefore reduce uncertainty in the assigned carbon date. The process of extracting sea-level records from salt marshes has proved successful in Iceland (Gehrels et al. 2006), Connecticut (Van der Plassche, 2000), Nova Scotia (Gehrels et al. 2005) and Gulf of Maine (Gehrels et al. 2002), but had not been attempted in Greenland prior to this project. The methodology outlined in this section is simplified, a more detailed description of the procedures used to reconstruct sea-level change at the Nag site can be found in Woodroffe and Long (2009) and Long et al. (2009b)

4.4 Results

The sea-level history of Nag and Aasiaat is quantified in Fig. 4.5. Prior to 2kyr BP, relative sea level in western Greenland fell, in an exponential-like manner, from around 90 m at the start of the Holocene. At Nag, data are not available prior to 6kyr BP but this site also shows a decline in sea level until 2kyr BP. The sea-level fall is in response to unloading of the crust in Greenland. There is some crustal subsidence originating from deglaciation of the NAIS, but this is not sufficient to offset the local sea-level fall in western Greenland that occurs throughout much of the Holocene. (Simpson et al. 2009).

The millennial-scale isolation basin RSL data give rates (with 1-sigma error level of) of 2.69mm/yr +/- 0.81 at Nag and 2.27 +/- 0.14 mm/yr at Aasiaat from 1.5kyr BP to present (Fig. 4.5, panels D and A respectively). Vertical errors on the data points are a result of the difficulty in attaining the correct location and depth of the sill in the isolation basin. This varies randomly from basin to basin. The neoglacial transgression at these locations in Western Greenland is though to be the result of a combination of crustal loading (and ensuing subsidence) due to expansion of the Greenland Ice Sheet and the collapse and migration of the forebulge of the North American Ice Sheets (Rasch, 2000; Simpson et al., 2009). In Figs. 4.5A and D, sea level reaches a minimum at ~ 2kyr before present then begins to rise in response to the neoglacial advance of the ice margin in west Greenland (Long et al. 2009a). Collection of salt marsh records recording sub-millennial changes in sea level reveal that RSL rise in west Greenland did not continue to present and was interrupted between 1500 and 1600AD (see Fig. 4.5C and E). Up

until 1500AD, the RSL trends obtained from salt marshes at Nag and Aasiaat are 3.29 +/- 0.6 mm/yr and 2.76 +/- 0.5 mm/yr (1-sigma), respectively. When considering 2-sigma error bounds, these rates are consistent with the isolation basin data. There are fewer index points from the period 1600 AD to present (none, in fact, for the Aasiaat site). However, qualitative interpretation of the stratigraphy indicates that RSL has remained within a few decimetres of present sea level since 1600AD. The ^{210}Pb data covering 1920-2005AD recovered from two different marshes at Nag (signified by different symbols in Fig 4.5C) are combined to give a rate of sea-level change for the 20th century of 0.42 +/- 1.66mm/yr.

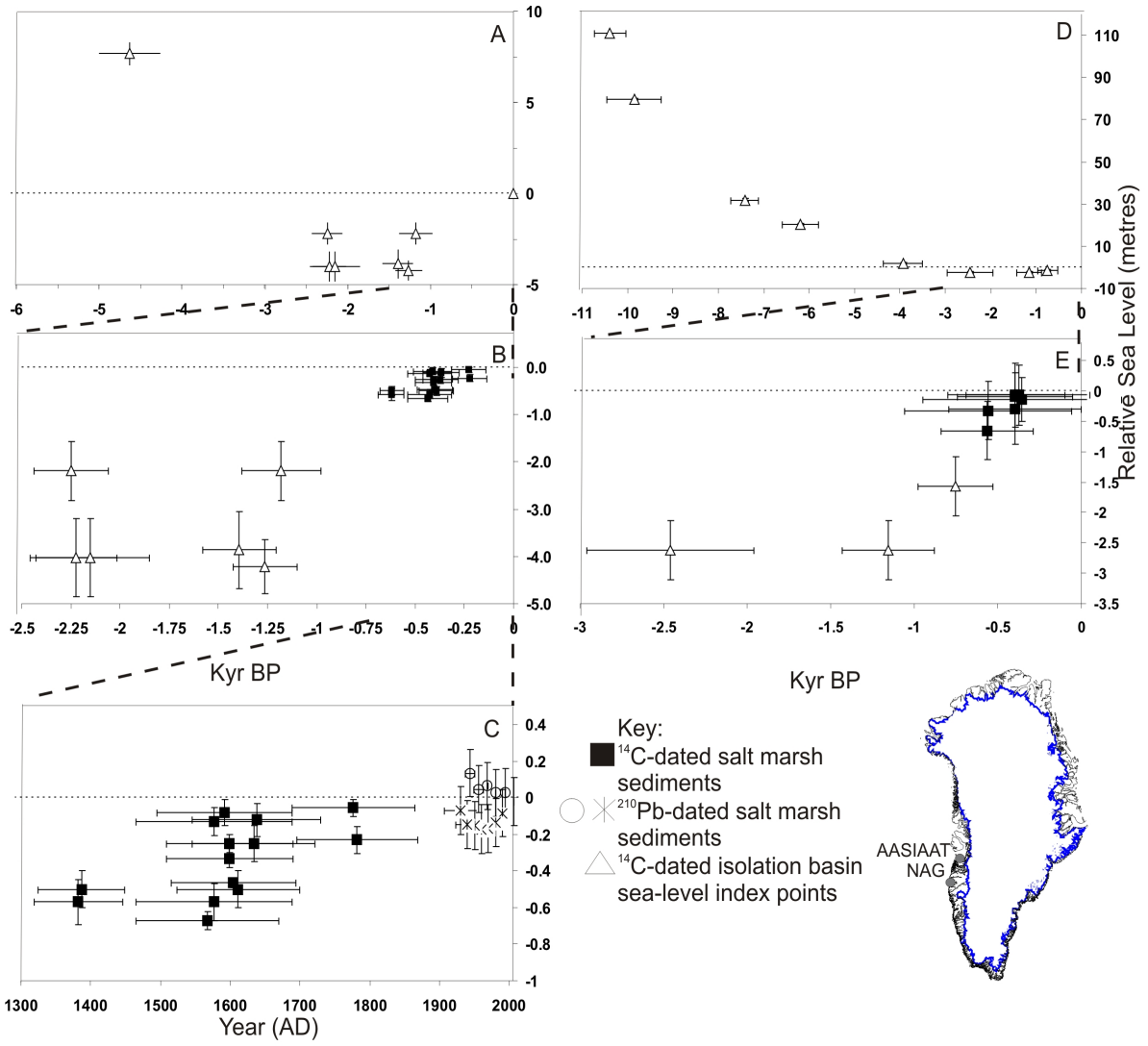

Fig. 4.5. Proxy sea-level records from Nag (A, B and C) and Aasiaat (D and E) showing millennial and century-scale trends in relative sea level. Panels B and C zoom in on the more recent RSL changes at Nag, whereas panel E zooms in on the last 3000 years at Aasiaat (D). The height errors in Panels A and D are associated with accurate location of the sill in isolation basins. Height errors in the salt marsh data (Panels B, C and E) are associated with the error in prediction from the diatom-based transfer function.

Given that the rates obtained are the same at each site (within error), it is reasonable to postulate that the rise up until ~1500AD, then deceleration and subsequent stability until present is likely to be the same at both sites. In this case, it is reasonable to apply the ^{210}Pb data collected at Nag to the Aasiaat site, in the absence of data describing the 20th century trend there. The process(es) driving these changes may therefore be identified as regional rather than local in extent. An RSL trend of approximately -3mm/yr is required to balance the late Holocene RSL rise associated with readvance and NAIS bulge subsidence to produce stable sea level from around 1600AD until present. In the following chapters, a number of processes are considered, mainly those driving mass changes of the GrIS, are considered to determine which is (are) the most likely cause(s) of the observed deceleration.

The salt marsh sediments have been used successfully in reconstructing century-scale trends over the period 1350AD until 1600AD. The vertical errors on the 20th-21st century data are larger than those for preceding years because of the inability of the transfer function to unequivocally reconstruct past distributions of diatom populations near the surface of the salt marsh samples.

4.5 Discussion and Conclusions

Isolation basin records show that the long-term sea-level change due to viscous land motion at Nag and Aasiaat is 2.69mm/yr and 2.27mm/yr respectively. Traditionally, this was assumed to continue linearly to present, but the salt marsh data at Nag and Aasiaat show that this trend only carried on until 1500-1600AD, with local RSL stable and close to present sea level thereafter. The data are not able to resolve fluctuations in sea level from 1600AD onwards due to the failure of the carbon dating technique at the advent of the industrial era. However, during this period, the sediments indicate stable sea level to within a few decimetres (Long et al., 2009) In order to estimate the error on the rate of 0.0mm/yr over this period, the errors from the ^{14}C and ^{210}Pb data are combined to give an error of 1.76mm/yr from 1600AD to the early 20th century. It is this transition between sea-level rise and stable sea level occurring at 1600AD and continuing through to present day which will be investigated in the following chapters.

In line with the original aims stated in Chapter 1, Chapter 5 will explore the ability of the 20th century proxy data to constrain the recent surface mass balance behaviour of the ice sheet. Chapter 6 will explore the possible contribution from

surface mass balance changes of the GrIS forcing the observed deceleration in RSL around 1500-1600AD. Chapter 7 will consider the possible effects on sea level from other processes not accounted for in Chapters 5 and 6 (most notably, those due to dynamic changes of the Jakobshavn outlet glacier and ocean temperature and salinity changes). Based on the results of these chapters, Chapter 8 concludes upon the success of the near-field fingerprinting technique as applied to the observations presented in the previous section. The preliminary results in Fig. 4.1 certainly demonstrate that the fingerprint signal is largest in the near-field. However, the more detailed modelling in subsequent chapters is necessary to determine how uniquely the sea-level signal can be interpreted in terms of GrIS mass changes.

Chapter 5: Trends in Mass Balance and Relative Sea Level since 1866 AD

5.1 Introduction

In this chapter, I present a time series of the annual surface mass balance (SMB) anomalies of the Greenland ice sheet for the period 1866–2005. In addition, I will report on how the spatial patterns of SMB vary over specified historic time intervals. This will place into context the current behaviour of the ice sheet, and specifically how SMB has varied both spatially and temporally during the late 19th century and early 21st century. Patterns of SMB are important indicators of the stability of an ice sheet under changing meteorological conditions. For example, peripheral thinning of an ice sheet and migration of the equilibrium line towards higher elevations denote that the ice sheet may be in a positive feedback cycle of decay. Observations and modelling of these processes over multi-decadal to century timescales are more important than measurements of outlet glacier discharge made over only a few years, which are shown to have interannual fluctuation (Howat et al., 2007), when considering the secular response of the ice sheet to climate change. A description of the mass-balance model used in this chapter is given (Chapter 2, Section 2.4.2.2)

I investigate the sensitivity of the model predictions to initial conditions and uncertainty in key model parameters in order to assess which aspects of the model have the largest influence on the output mass balance, and, therefore, local relative sea-level change. The SMB results are discussed primarily within the context of two applications: (i) comparison of the response of the ice sheet to warming in the past few decades and an earlier warm period during the 1920s (Chylek et al., 2006) to examine how exceptional the recent SMB changes are within a longer time context; and (ii) comparison of the model to observations of surface elevation changes from 1995 to 2005 to gauge qualitatively the relative contribution of SMB changes to the observed total surface changes.

The main aim of this chapter within the context of my thesis research is to produce a realistic ice model to input to the sea-level code in order to interpret the proxy sea-level data presented in Chapter 4. To meet this objective, the main processes contributing to mass change on an ice sheet (described in Chapter 2) must be identified and modelled accurately. The models used previously (e.g. Mitrovica et al. 2001; Wake et al. 2006) are not based on any underlying glaciological

principles and are too crude for a near-field analysis. The model will be developed in 2 stages. The ice model developed in this chapter uses high resolution temperature and precipitation data and covers the period 1866-2005. SMB changes prior to 1866AD are considered in Chapter 6. The ice model is limited to time-dependant changes in SMB only, but is a step away from previous (non-glaciological) models towards a full, 3D thermomechanical model with higher order stresses and a proper treatment of grounding line evolution. This order of complexity is beyond the scope of this thesis.

Ice thickness changes from the mass balance model were input to the sea-level code (Mitrovica and Milne, 2003) and the resulting sea-level changes were computed around Greenland using an earth model comprising an upper elastic lithosphere of thickness 120km, viscosity in the upper and lower mantle of 0.5×10^{21} Pa s and 1×10^{21} Pa s respectively. This earth model has been found to give a good fit to a regional, millennial-scale RSL data set (Simpson et al. 2009). The ice loading changes are discreticized into 10 year loading intervals. Higher resolution is not required due to the large errors associated with dating of the salt marsh sediments that span the 20th century.

5.2 Methodology for SMB Calculation

Surface mass balance was calculated by applying a runoff-retention model (Janssens and Huybrechts, 2000) based on the positive degree-day (PDD) method (Braithwaite and Olesen,1989; Reeh, 1991). (See Chapter 2 for background on SMB modelling.) The model is forced using monthly temperature and annual precipitation minus evaporation (P-E) datasets from two sources. For the period 1866 to 1957, the climatic data assembled from a spatio-temporal correlation between coastal meteorological and ice-core data and climate model (Polar MM5) output (Box et al. 2006a, 2009a,b; hereafter named 'BOX') was used. For the BOX dataset, the data are accumulation series, i.e. the solid fraction of incoming precipitation and surface temperature. In the accumulation zone, there is no liquid fraction, so this is a suitable methodology in this area of the ice sheet as the total precipitation anomaly is equivalent to modelled accumulation. In the margins of the ice sheet, scaling the P-E field by an accumulation anomaly will slightly underestimate the total precipitation at any point. In the ablation zone, the measured stratified accumulation will be a combination of snow, capillary water and refrozen runoff. Although this does not

strictly translate to total P-E, it is the closest approximation available. Solid and liquid fractions are re-calculated by means of the PDD model (see Chapter 2)

For the period 1958 to 2005, data assembled from European Centre for Medium-Range Weather Forecasts ERA40 reanalyses (Hanna et al. 2008), named 'ECMWF' are used. These data are projected onto a 5x5 km grid, on which the SMB is calculated at monthly intervals and integrated over the entire ice sheet to give an overall annual mass-balance figure. This study extends the work of Hanna et al. (2005, 2008) in two important respects. The period considered is longer (1866–2005 compared with 1958–2003) and climate forcing is applied in 'anomaly mode' to reduce sensitivity to biases in the input time series of precipitation and temperature. The temperature and precipitation are reduced to anomalies with respect to a baseline average established using the climate datasets. The parameterized temperature and precipitation fields are perturbed by their respective anomalies. A critical step required to run the model in anomaly mode is the selection of a baseline period during which the climatic variation is representative of a longer-term average. The length of the baseline period must be sufficiently long such that the occurrence of rare and extreme climate events does not significantly influence estimates of longer-term averages. The period 1961–1990 is chosen following Hanna et al. (2005), who found the total mass budget averaged over the entire ice sheet to be close to balance over this interval. For this analysis, the working assumption is made that such a balance is also valid down to the level of individual drainage basins, although it is not possible to support this assertion with strong evidence. Also, the reference precipitation dataset is homogenized to the 1961–1990 climate and is therefore representative of this period (Huybrechts et al. 2004).

For each point (x, longitude; y, latitude) on the ice sheet, the original datasets (T: Temperature and P: Precipitation) are reduced to their monthly (t_m) or annual (t_a) anomalies by the following methods:

$$T_{anom}(x, y, t_m) = T(x, y, t_m) - \overline{T}(x, y, 1961\_1990_m) \quad \text{E5.1}$$

$$P_{anom}(x, y, t_a) = P(x, y, t_a) / \overline{P}(x, y, 1961\_1990_a) \quad \text{E5.2}$$

Where the 'bar' denotes an average over the period indicated. It was necessary to splice the two datasets because the ECMWF datasets only extend back to 1958, and their use is favoured after 1958 because the data are reasonably well validated (Hanna and Valdes, 2001; Hanna et al., 2001). The BOX dataset is utilised

to extend the modelling back to 1866. Also, by applying the model in anomaly mode, any trend or bias introduced by splicing the two different climate time series is removed.

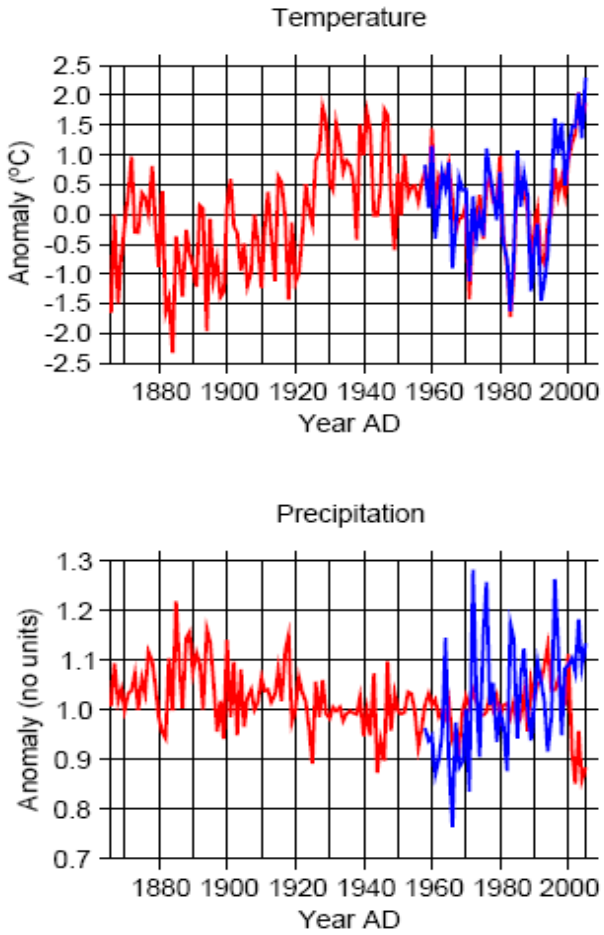

Fig. 5.1 Upper frame shows mean annual temperature anomaly averaged over ice-sheet area, assembled from two datasets: ECMWF re-analyses (blue) and BOX (red). Lower frame shows annual precipitation ratio averaged over ice-sheet area. Colour convention as in the upper panel.

Fig. 5.1 (upper frame) shows the overlap achieved by splicing the two temperature datasets. From 1958 onwards, both datasets mirror each other well which suggests that the second dataset will not distort results pre-1958. Over the climatological normal period 1961–90, neither dataset shows a convincing increase/decrease of mean annual temperature, but show comparable trends (BOX: –0.02 +/- 0.69^{o}C/yr; ECMWF:–0.02+/-0.77^{o}C/yr). A striking feature of the temperature series is the longer period (50 years) variation imprinted on the annual variation. Significant increases in the temperature anomaly are recorded about 1920 and 1995.

The precipitation anomaly series provided by the two datasets are very different (Fig. 5.1 lower). The BOX dataset shows lower variation and no discernible trend over the selected baseline period (–0.0001+/-0.0008 /yr). The ECMWF data show an increase of 0.005+/-0.0025 /yr, which is different in sign and 50 times that

recorded in the BOX dataset. The reason for the difference between the datasets is not known, but since no significant trend in the baseline period is recorded in either dataset, there is little consequence in the fact that the variability is not consistent, since the ice sheet is more responsive to temperature rather than precipitation changes. The precipitation series is treated differently. A precipitation field known to be representative of the 1961–1990 average (Huybrechts et al, 2004) is perturbed on an annual basis by the fractional difference in precipitation for the year compared with the 1961–90 annual average (P_{anom}).

The input data to the PDD model are temperature and precipitation (Fig. 5.1), which are the combination of the following

$$T(x,y,t_m) = T_{param}(x,y,t) + T_{anom}(x,y,t_m) \quad \text{E5.3}$$

$$P(x,y,t_a) = \overline{P_{1961-1990}}(x,y) \times P_{anom}(x,y,t_a) \quad \text{E5.4}$$

The monthly temperature (t_m=1 – 12) at any point (x,y) is a combination of the parameterisation, T_{param}, based on elevation and latitude (see Chapter 2, E2.7-2.9)) and T_{anom} as defined in equation E5.1. For the precipitation series, a field representative of the 1961-1990 average $\overline{P_{1961-1990}}$ is multiplied by a temporally evolving anomaly (P_{anom}), described in E5.2. The subscript 'm' denotes values calculated on a monthly basis, and subscript 'a' is for annually evolving values. Because elevation is part of the temperature parameterisation, an innovative technique is applied (in Section 5.3.3) to investigate the influence of annual surface elevation changes on SMB prediction and to correct the adopted elevation dataset (valid for 1994; Bamber et al., 2001a) for past years. This will facilitate a more realistic representation of elevation-related temperature changes, and therefore SMB. The change of ice-sheet elevation due to changes in SMB (in ice equivalent and so ignoring changes in density profiles) is treated as follows:

$$\partial H(x,y,t) = SMB(x,y,t) - \overline{SMB(x,y,1961-1990)} \quad \text{E5.5}$$

Where $\partial H(x,y,t)$ is the local surface elevation change arising from a SMB change in 1 year for a point on the ice sheet; SMB is the local SMB defined on an annual basis either at time 't' or as the average for the period 1961–1990, denoted by a bar in E5.5. For equilibrium at a point on the ice sheet (assumed for the period

1961–1990), $\partial H(x,y,t)$ =0. Any deviation from zero will result in a change of elevation. There are a number of assumptions implicit in the method described above. For example: (i) the parameterized monthly temperatures are valid for the 1961–1990 period (i.e. in the first approximation, the 1994 elevation produces temperatures representative of the 1961–1990 monthly means); (ii) the ice-sheet surface is in equilibrium with the 1961–1990 average climate; and (iii) from (ii) it is implicitly assumed that the 1961–1990 ice flow is constant over the whole integration period considered here, and that SMB anomalies may be equated to overall ice sheet mass balance. In effect, the second term in E5.5 provides a constant dynamic compensation on the ice sheet by subtracting a SMB field from the calculated SMB field each year (see Section 2.4). To correct for the effect of surface elevation changes on surface temperature, and hence SMB, the elevation changes are summed from the start of the model run (1866) until 1994. The 1994 elevation and ice thickness datasets are then corrected for these changes. The model is re-run until satisfactory convergence is obtained between ice-sheet averaged SMB and the SMB calculated from the first iteration. The year 1994 is chosen as the elevation and ice thickness dataset obtained from Bamber et al. (2001a) is a re-validation of a Greenland elevation model originally obtained from the ERS-1 mission which lasted from 1991 until 1994. By doing this, there is some confidence that a fairly realistic representation of the 1866 surface elevation is used. Satisfactory convergence is achieved after two iterations. It is assumed that the change in ice thickness $\partial I(x,y,t)$ is equivalent to a change in elevation $\partial H(x,y,t)$ so the 1994 ice thickness grid is corrected as described earlier (also, see E5.5). Although the surface elevation at 1866 cannot be independently validated, the iterative scheme used to modify surface elevation ensures that final model is at least self-consistent since the surface mass balance calculated for the year 1994 at the final iteration is within 5km^3 of the SMB calculated for 1994 using the original datasets.

5.3 Results

5.3.1 Finalised Mass Balance Series

Figure 5.2 shows the calculated changes in SMB with respect to the 1961–1990 average. Analysis of the SMB time series shows that the ice sheet was slightly losing surface mass overall during the period 1961–1990. Even though the input climate data suggest that there is no trend in the climate anomalies over this period, the ice sheet is still responding to year-on-year non-zero perturbations in temperature

and precipitation. The anomalies in temperature and precipitation do not balance each other to give an exactly zero SMB anomaly. The model indicates that the ice sheet is in an overall state of mass loss, and this neither accelerates nor decelerates significantly over the baseline period (+0.62 +/- 2km^3/yr). It was not possible to replicate such a close state of dynamic equilibrium with the use of other climatological normal baselines (e.g. 1971–2000).

There are a number of features evident in Figure 5.2. For the first 60 years of the study period, the ice sheet was mainly in a state of positive mass balance with respect to 1961–1990. This reflects the fact that temperatures in this period are lower than the 1961–1990 average in Greenland and worldwide. There is a distinct change to a period of prolonged negative SMB anomalies at about 1925 that persisted until about 1960. This change is clearly related to the relatively high temperatures experienced during this period, particularly between the mid-1920s and 1950. Between 1970 and the end of the 20th century the SMB predictions display high variability but give, on average, a slightly negative SMB anomaly.

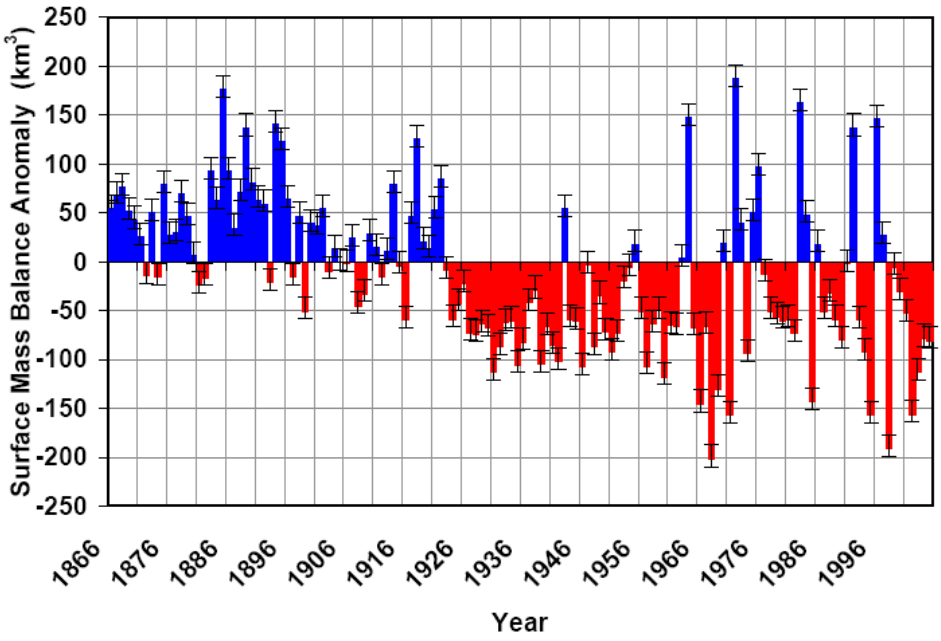

Fig. 5.2: Time series of annual surface mass-balance related volume anomalies for the period 1866–2005. Values are quoted in km^3 ice equivalent.

The final 6 years of the study period indicate a distinct and consistent negative mass-balance anomaly which correlates well with the elevated temperatures shown in Fig. 5.1. Over the entire period (1866–2005), the overall SMB of the ice sheet is almost constant, with surface volume being lost at a rate of 0.89+/-0.15km^3/yr based on a straightforward linear regression of the SMB time series.

Fig. 5.3 shows the spatial pattern of the cumulated SMB anomalies for the entire study period and indicates that most of the ice has been lost at the margin, with some areas having lost over 150m of ice since 1866. A feature that is persistent in time is the sharp transition between positive and negative cumulated SMB anomaly along the ice margin in the south and east. Although southeast Greenland receives high amounts of accumulation, the topography of East Greenland is steep, so the ablation zone is narrow compared with the west of Greenland. In the central portion of the ice sheet, a northeast/southwest divide of net lowering and net growth (respectively) is visible. Overall, the maximum amount of surface ice lost in this area is 5m, with up to of 5–10m of ice gained over some areas in the southwest. The time series presented in Fig. 5.2 provides a record of the mass-balance response of the Greenland ice sheet to temperature and precipitation variations during the past 140 years.

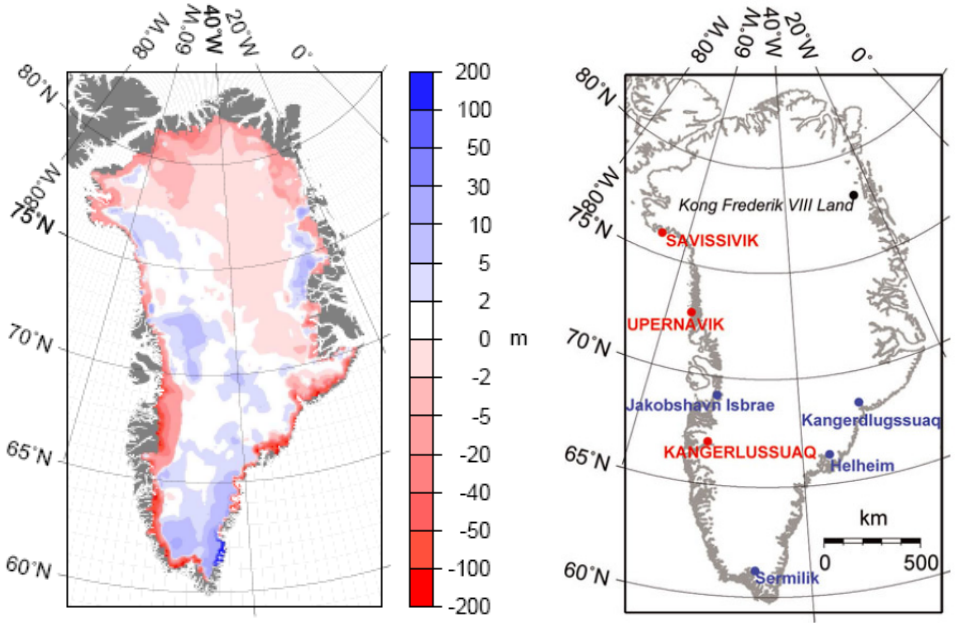

Fig. 5.3 Spatial pattern of total cumulated surface mass-balance change for the period 1866–2005 (left frame). Values are in metres ice equivalent. Right-hand frame shows locations mentioned in the text: Blue- outlet glaciers, Red- main towns, Black- regions.

Since much current attention is focused on the response of the Greenland ice sheet to the temperature increase over the past decade, an interesting application of the results is to place the more recent changes within a longer time context. A noticeable feature of the time series (Fig. 5.2) is the transition from lengthy periods of positive (1866–1922) to negative (1923–1953) SMB anomalies. This first sequence of positive SMB anomalies corresponds to the Greenland ice sheet emerging from the Little Ice Age. The Little Ice Age is a prolonged period of cooling beginning after the ‘Medieval Climatic Optimum’) (approximately AD 1200) and lasting until the early

20th century. During this period (1866–1922) there is an average annual SMB anomaly of 37 +/- 11 km^3/yr. Csatho et al. (2008) detected thinning of Jakobshavn Isbrae during 1902–1913, and linked this behaviour to the interaction of the ice dynamics with changes upstream of Jakobshavn Isbrae. An average annual ice loss of approximately 5m/yr between 65°N and 70°N on the western margins of the ice sheet is forecast, even though the majority of the ice sheet is in a state of positive mass balance. Interestingly, the results also show an area of thinning (average ice loss 0.02–0.10m/yr) during 1902–1913 in the drainage area east of Jakobshavn Isbrae between 68.5°N and 69.0°N and extending up to 500 km inland in an east-southeast direction (not shown here).

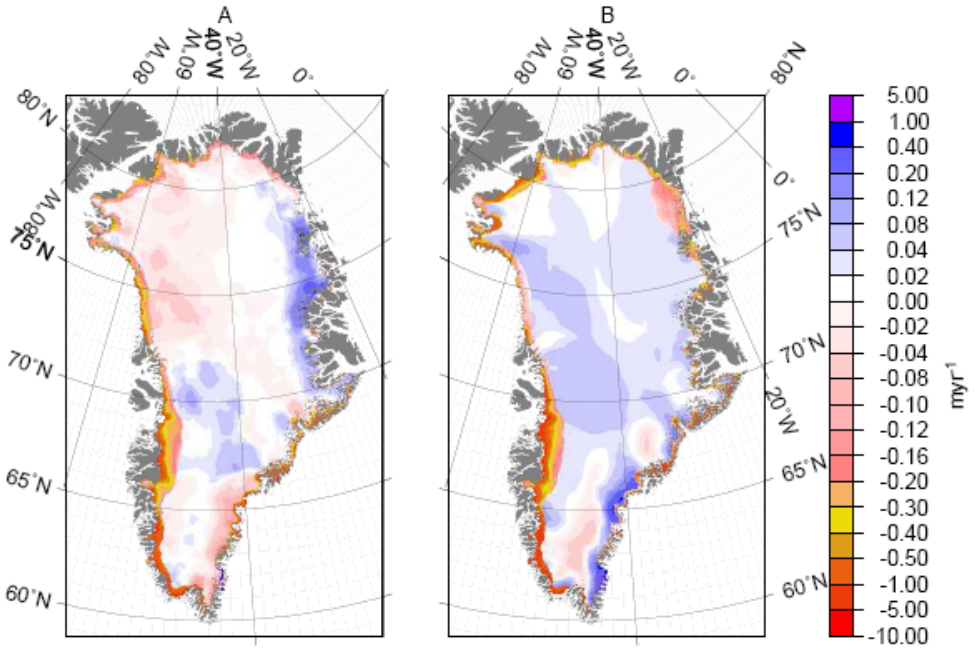

Fig. 5.4: Rate of change of surface mass-balance anomaly (calculated by linear regression) for the periods (a) 1923–1933 and (b) 1995–2005. Values are in metres per year ice equivalent.

Two periods are identified when the average annual SMB was similar relative to the 1961–1990 average (1995–2005: –69km^3/yr; 1923–1933: –67 km^3/yr). During 1995–2005, the rate of increase of mean annual temperature was almost twice that of the earlier period, and there are no discernible trends in the precipitation anomalies of either period (1995–2005: –0.007±0.008 /yr; 1923–33: 0.003±0.004 /yr). The rate of change of mean summer temperature anomaly (June, July and August) averaged over the ice-sheet area for the two periods is 0.17°C/yr (1995–2005) and 0.04°C/yr (1923–1933), respectively. In effect, the same overall SMB response is occurring during 1923–1933, but under a smaller increase in rate of change of mean annual and summer temperature than that experienced during 1995–2005.

The spatial patterns of the SMB changes during these two periods are not similar (Fig. 5.4). Both show high rates of peripheral lowering, but a larger area of the ice sheet displayed negative SMB anomalies during 1923–1933. Much of this thinning during 1923–1933 appears to have occurred in the accumulation area, with this lowering being driven by lower than average accumulation rates rather than higher than average ablation rates. The extensive growth for 1995–2005 was not sufficient to counteract the high (5–10m/yr) rates of peripheral lowering. The growth–thinning transition in the southeast is absent from the earlier period, but is a significant feature during 1995–2005. During the period 1923–33, the average annual temperature anomaly over the ice sheet increased by 0.75^{o}C compared with 1.9^{o}C for 1995–2005. The Greenland ice sheet overall has therefore responded in a similar fashion to a smaller temperature increase in the early 20th century, indicating that the current SMB anomalies are not entirely exceptional. Neither time period exhibits a pattern of loss that is comparable to the long-term net ice loss (Fig. 5.3). Based on the simulations of these two periods, it could as well be stated that the recent changes that have been monitored extensively (Krabill et al., 2004; Luthcke et al., 2006; Thomas et al., 2006) are representative of natural sub-decadal fluctuations in the mass balance of the ice sheet and are not necessarily the result of anthropogenic-related warming.

Predictions of ice loss due to SMB compare favourably to published studies of surface elevation changes. For 1997–2003, an average ice loss of –82 km^3 /yr is predicted, comparable to values obtained by Krabill et al. (2004). Laser altimeter studies by Thomas et al. (2006) record a doubling in mass loss over two periods 1993–98 and 1998– 2004 (4–50 Gt/yr and 57–105 Gt/yr). The modelling results are compatible with the higher values of these ranges (–59 Gt/yr and –97 Gt/yr, respectively). By matching these results with (Krabill et al., 2004) and (Thomas et al. 2006), it may be interpreted that many of the observed trends are caused mainly by changes in SMB, since the field used to correct for dynamic ice loss remains fixed over time. However, it is not possible to make firm conclusions on the respective role of ice dynamics vs. SMB changes on elevation changes because the assumption of equilibrium for 1961–1990 may not hold for individual points on the grid, even if such a balance has stronger support for the Greenland ice sheet as a whole.

Comparison of recent laser altimetry (2000) and older digital elevation models (1985) made by Podlech et al. (2004) shows that during 1985–2005 the area around Sermilik Glacier in South Greenland (Fig. 5.3 right) lost 90m of ice at approximately the 500m elevation contour. In this area, losses in the range of 100–

200 m are predicted. These are larger than the values obtained from observations, but lie in the range (–90 to –130 m) calculated by (Podlech et al. 2004). For the higher-elevation bands (500–750m and 750–1000 m) the predictions differ with the measurements with a significant annual average thinning of 8–12m/yr predicted. Again, this is likely to be a consequence of the assumption of ice-sheet-wide equilibrium for 1961–1990.

Over the measurement period 1997–2003, modelling of overall mass balance reflects some features of Krabill et al. (2004) such as (not pictured): lowering in the area of Kong Frederik VIII Land in the north (77–80^{o}N, 20–30^{o}W) and near balance in the central area north of 73^{o}N. However, there are also some important differences: the work of Krabill et al. (2004) reveals a wider area of negative elevation change in the eastern half of Greenland, whereas localized (up to 20 km) wide areas of extreme (>5–10m/yr) surface lowering are predicted by the model. Over the same period, considerable (0.3–1.0m/yr) thinning on the south dome of the Greenland ice sheet is predicted in contrast to the results of Krabill et al. (2004) who measure thickening of about 0.1m/yr. The model predictions display some short-wavelength features that would not be resolved adequately in the observations due to distances between flight lines. This might explain some of the data-model discrepancies.

The patterns of ice thickness change bear more similarity to those of Thomas et al. (2006) for the period 1993–98. A similar pattern of near balance to slight (0.1ma^{-1}) thickening through much of the central portions of the ice sheet is predicted. Although the resolution of the observation-based reconstruction is ten times less, it picks out important small-scale features present in this study: thinning of >0.6ma^{-1} between 65^{o}N and 70^{o}N east of Jakobshavn, and extreme thinning in Kong Frederik VIII Land (see Fig. 5.4, right) and in a narrow (<20 km) band between Savissivik (76.023^{o}N, 65.081^{o}W) and Upernavik (72.78^{o}N, 56.17^{o}W) in the northwest.

Using this model, contribution to eustatic sea-level change is 0.036mm/yr over 1866-2005, and 0.089mm/yr over 1961-2003. The latter estimate is in line with IPCC estimates for this time period (+0.05 +/-0.12mm/yr; Bindoff et al. 2007).

5.3.2 Sensitivity to Model Parameters

In the results presented in Section 5.3.1, the parameters in the PDD model are set at optimum values that best reconstruct the surface mass balance for 1994. In the PDD model, the most significant parameters that will affect the surface mass balance are variation of the rainlimit temperature and the parameter used to account

for daily variations in temperature. Fig. 5.5 shows the changes to the model output when these parameters are modified within reasonable bounds

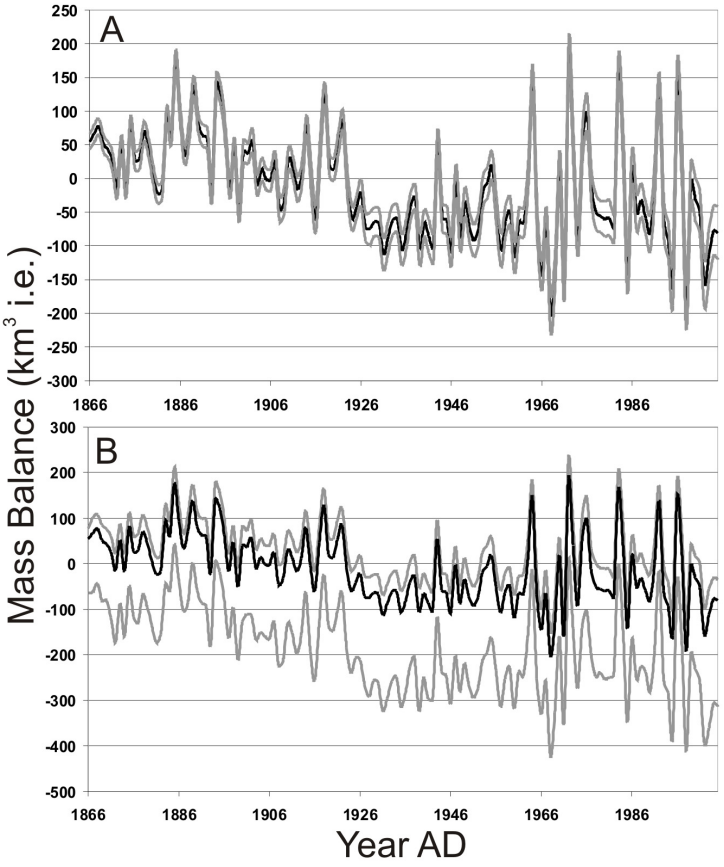

Fig. 5.5 (A) Graph showing the change in predicted mass balance when the rain limit temperature is varied between 0 and 2°C. (B) As in (A) except for the case of daily temperature variation between 3.8 and 5.0°C. The black line in both frames is the finalised mass balance series as in Fig. 5.2

The sensitivity to the rainlimit shows a maximum of +/- 50km^3/yr variability (at 2005 AD) with a slight divergent trend from the start of model run until the end. Lower rainlimits correspond to less formation of snow, and therefore more predicted run off due to reduced snowpack retention. Less formation of snow also means that ice is immediately available for melt, and this is represented by the lower grey line in Fig. 5.5A. A higher rainlimit allows for more snow formation in warmer, wetter areas. This has the effect of using up more PDDs compared to that if the ice surface was exposed, thus increasing the surface mass balance in these areas. These processes result in the predicted divergence of the mass balance time series as the runs progress. The ice-sheet averaged precipitation anomaly shows a net increase over 1866-2005 so in combination with a higher rainlimit (upper grey line in Fig. 5.5A), this is consistent with increasing SMB since more snow is formed to use up PDDs. Higher SMB increases the year-on-year elevation compared to the finalised run, which

interplays with the PDD calculation. The consequence is that the amount of PDDs calculated is not entirely independent of the rainlimit parameter. Therefore, the spatial importance of this parameter is higher at the margins of the ice sheet compared to in the centre where precipitation and melting are at a minimum.

Increasing the range of temperature variation has the effect of increasing the amount of melt. This leads to melting in areas where there was previously none. Both the intensity and duration of the melt season are increased when the temperature variation is allowed to reach 5^{o}C, and in some areas will initiate melting for the first time (in summer and winter). Linear regression of the series over the period 1916-1936 shows that the decline in mass balance is measured at -7.4km^{3}/yr when 3.8^{o}C of variation is allowed. When this is increased to 5.0^{o}C, the decline is measured at -10.1km^{3}/yr. The magnitude of the difference in mass balance reaches ~ 300km^{3}/yr which is approximately 1mm/yr of eustatic sea-level change over the period 1916-1946. As in the example shown in Fig. 5.5A, the discrepancy propagates from 1866 to present day due to the involvement of ice-elevation feedback.

5.3.3 Sensitivity to Elevation Corrections

In order to test the sensitivity of the surface mass balance predictions to, changes in how the surface elevation and ice thickness distributions are determined through a model run, four experiments were carried out for the period 1866-2005. Table 5.1 describes the four different scenarios considered.

	1994 elevation	1994 ice thickness	1866 ice thickness	1866 elevation	Annually iterated elevation	Annually iterated ice thickness
Run 1	x	x				
Run 2		x		x		
Run 3		x		x	x	
Run 4			x	x	x	x

Table 5.1: Table describing four experiments developing the level of complexity of the treatment of surface elevation and ice thickness changes. See text for details.

Run 1 is the most basic set up, it is based on the assumption that the 1994 elevation and ice thickness distributions are valid for each year in the 1866-2005 run. Annual changes in elevation and ice thickness are omitted. The same set up is

applied for run2, except that the 1866 elevation is generated using the results from run 1 and assuming that each deviation in SMB from a baseline average equates to a change in elevation (e.g. see E5.5). The ice thickness remains unchanged from run 1. In run 3, the effect of year-on-year iterated changes in elevation are considered as per the methodology outlined in E5.5. Again, the ice thickness distribution remains the same. In run 4, the corrected elevation and ice thicknesses are used with annual corrections applied. Ice thickness corrections are more important at the margin of the ice sheet where there is the possibility that points on the ice mask may disappear over the time period of 140 years. In each case the model is run through only once. For this reason, run 4 is not equivalent to the final results shown in Section 5.3.1, which was produced from a second iterate of the model using the same set up as run 4 in Table 5.1.

By taking into account the surface elevation changes from 1866-1994 (run 2), the predicted annual surface mass balance is increased by an average of 12.4km^3, indicating that the average surface elevation is lower when using the uncorrected version (see grey solid line in Fig. 5.6) . This change in mass balance amounts to -0.03mm/yr of eustatic sea-level change, which is the same order of magnitude as the predicted average contribution of mass balance to eustatic sea-level change over the period 1866-2005 (from model shown in Fig. 5.2). This difference remains steady throughout the series. There is no abnormal reaction to temperature increases at 1920 and 1990AD, so one can infer that the difference between the elevation distributions is not significant enough to push the ice sheet into sustained growth or decline.

Run3-Run2 (Fig. 5.6, dashed line) shows the influence of including annual variation in elevation change. Clearly, omission of the annual iteration scheme causes the surface mass balance to be over predicted. The results for run3-run2 bear no resemblance to the temperature or precipitation anomaly patterns in Fig. 5.1. This indicates a strong dependence on the contribution to PDDs from surface elevation, regardless of temperature anomalies. The two model runs (run3 and run2) become progressively more divergent over time, with smaller SMB predicted for run3. The divergent nature of the SMB predictions indicates that elevation changes in the ablation zone are the controlling factor on overall surface mass balance between the two runs. Very little melt takes place in the accumulation zone and, by extension, elevation change. Correcting for elevation changes in the central portions of the ice sheet has little effect on the amount of melting taking place, since the elevation changes in this area are precipitation-sourced, and are less dependent on melting.

This result (run3-run2) demonstrates that annual scale changes in elevation must be considered for accurate predictions of SMB over century time scales.

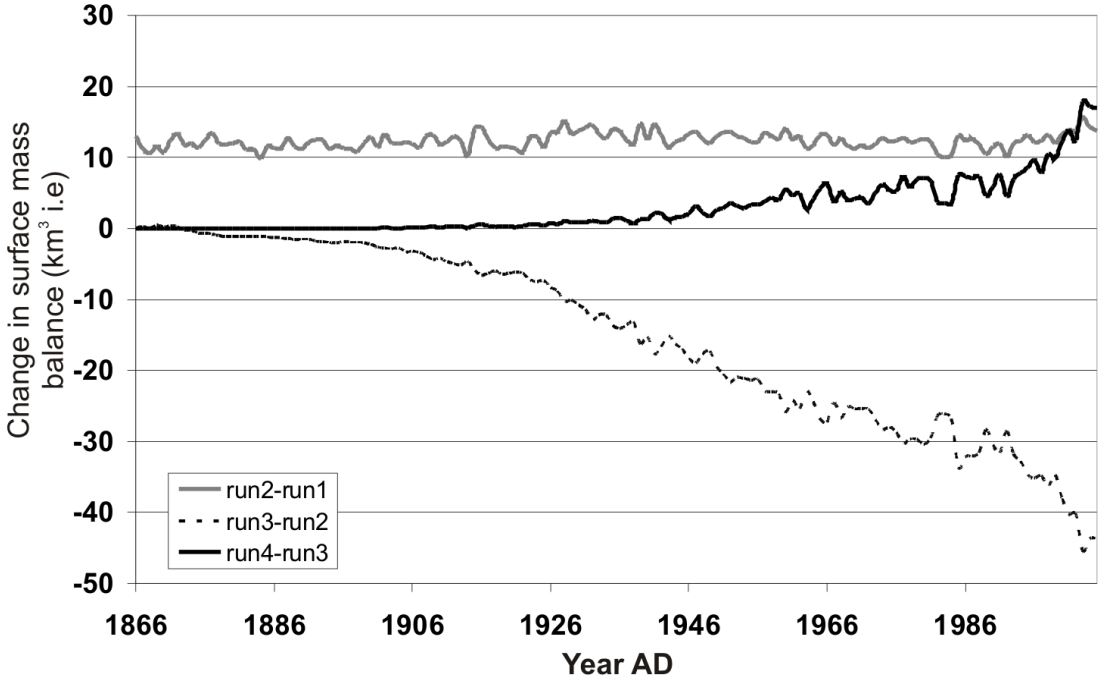

Fig. 5.6: Changes in mass balance predicted for models describing the different ways that surface elevation and ice thickness distributions evolve over time. See Table 5.1 for differences between each model run.

Once the corrected ice thickness grids are taken into account (run4-run3), surface mass balance increases. But this difference amounts to less than 15km^3 for any given year over the 1866-2005 period (see black line, Fig. 5.6). The divergence from zero occurs around 1926AD contemporaneous with the 1920's warm period when widespread melting is initiated and over predicted in run3 because no account was taken of grid points where thickness had reached zero. This modification to the modelling technique is less important than calculating changes in surface elevation over a 140 year period for two reasons: (1) Errors made in calculating ice available for melt in the centre of the ice sheet will not be larger than the actual ice melted. For example, there will be no outstanding PDDs in the central portion of the ice sheet left to melt any ice that shouldn't be there. (2) Even at the margins of the ice sheet, where the amount of PDDs is high, annual rates of ice loss are no larger than 10m/yr (Fig. 5.4). However, the effect becomes more prolific over time due to the eventual disappearance of ice nodes at the margin, which lower the contribution to ablation by their absence.

When all factors are taken into account, the most important modifications made to the model are accounting for surface elevation changes. The most

sophisticated model run predicts lower surface mass balance overall compared to run1. For this model configuration and input temperature and precipitation series, the increasing sophistication of the model reduces the eustatic sea-level contribution by 0.03 at the start of the model run to 0.11mm/yr at the end. Over the period 1866-2005, this amounts to an average of -0.07mm/yr on any given year.

5.3.4 RSL Changes predicted for 1866-2005

In Fig.5.7, the trends in relative sea-level, calculated using the sea-level code and Earth model configuration described in Section 2.3 and 5.1 respectively. The RSL trends are shown alongside predicted net change in ice thickness over the period 1866-2005. Overall net growth of 40-100m is expected over broad areas in western and southern Greenland. This is juxtaposed against a narrow 250km band of thinning (up to 250m net loss) in many margin areas. In some areas, the area of extreme (>200m) thinning is less than 100km wide but sea-level fall dominates even though overall the ice sheet has thickened inland.

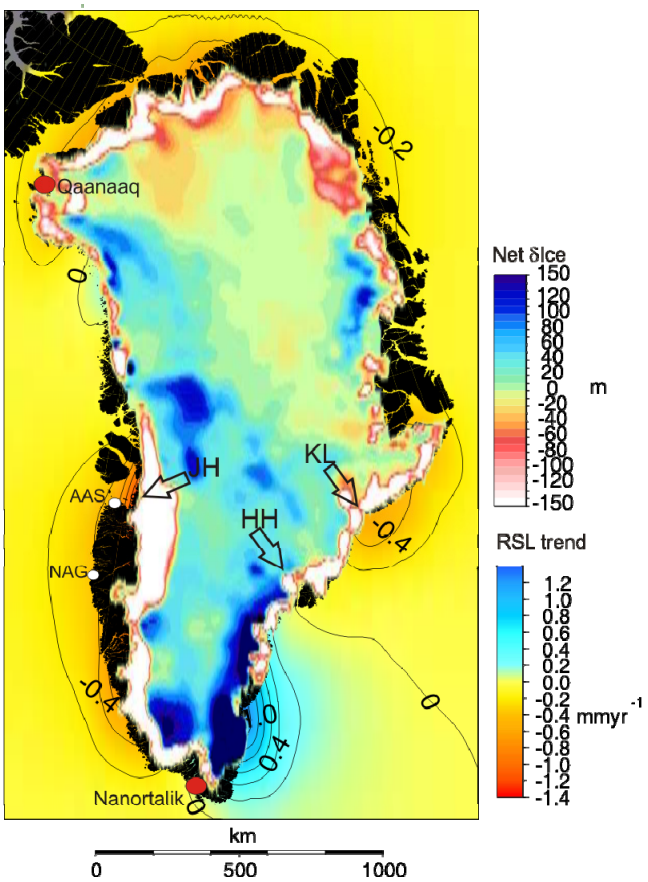

Fig. 5.7: Net change in ice thickness and corresponding trends in RSL for the period 1866-2005. Major outlet glaciers are marked by arrows (JH: Jakobshavn Isbrae, HH: Helheim, KL: Kangerdlugssuaq). Salt marsh data sites (AAS: Aasiaat and NAG) are marked by white circles. Locations mentioned in the text are denoted by red circles. Trends in RSL are contoured every 0.2mm/yr, and do not include the contribution to RSL change arising from millennial-scale changes in ice loading.

Extreme coastal regions (except those in fjords) are not expected to produce a significant differential from north to south (e.g. less than a magnitude of 0.4mm/yr from Nanortalik to Qaanaaq). Moving inland along fjords and close to the ice sheet however produces larger magnitudes of change due to proximity to the ice sheet. Between 200km north of Aasiaat and the town of Qaanaaq, there is very little sea-level response, with predicted trends in the range of +/- 0.2mm/yr. Even though the ice sheet is proximal to the coast, areas of thickening and thinning are interspersed and are of approximately the same magnitude (+/- 100 – +/-150m) resulting in a near-zero RSL trend.

On the south-east coast accumulation is predicted to dominate over ablation. A sharp contrast in sea-level change along this coast from Kangerdlugssuaq to Nanortalik is predicted. Between Nanortalik and Kangerdlugssuaq, the sea-level trend ranges from ~+1.0.mm/yr east of Nanortalik to -0.4mm/yr at Kangerdlugssuaq. Sea-level change of >1.2mm/yr is predicted for the extreme south east of Greenland, which should produce a resolvable differential in 20th century sediments in this area compared with those on the southwest coast. In the north of Greenland, no significant sea-level change is predicted over the 1866-2005 period.

Three time slices in Fig. 5.8 were selected to highlight the response of regional sea levels to contrasting climatic conditions over decadal timescales. Fig 5.8A shows the pattern of ice loss and relative sea-level change associated with conditions experienced during the termination of the LIA and Figs. 5.8B and C show the response to warmer periods. It is interesting to compare the periods of 1916-1936 and 1995-2005 as the former represents a period when the ice sheet experienced elevated mean annual temperatures comparable to that of today.

One feature that is prevalent for each of the three time periods is the sea-level rise in the south east of Greenland. A maximum of 3mm/yr RSL is predicted during the end of the LIA. In warmer periods such as 1916-1936 and 1995-2005, the sea-level rise is lower at 0.4mm/yr. There is a centre of high precipitation in south-east Greenland, due to the North Atlantic Oscillation. Also, the south-east displays a thinner, low elevation band of ablation. When juxtaposed with localised high-precipitation areas, this results in opposing trends in sea-level change on the south-east coast over distances less than 100km (Fig. 5.8B and C). Around the outlet glaciers of Helheim and Kangerdlugssuaq a steady sea-level fall of 0.6 to 0.8mm/yr is predicted. RSL change along the central to southern west coast of Greenland, the area of focus in this study, tends to respond in tandem with the climate conditions: falling during warm periods and rising during cold periods.

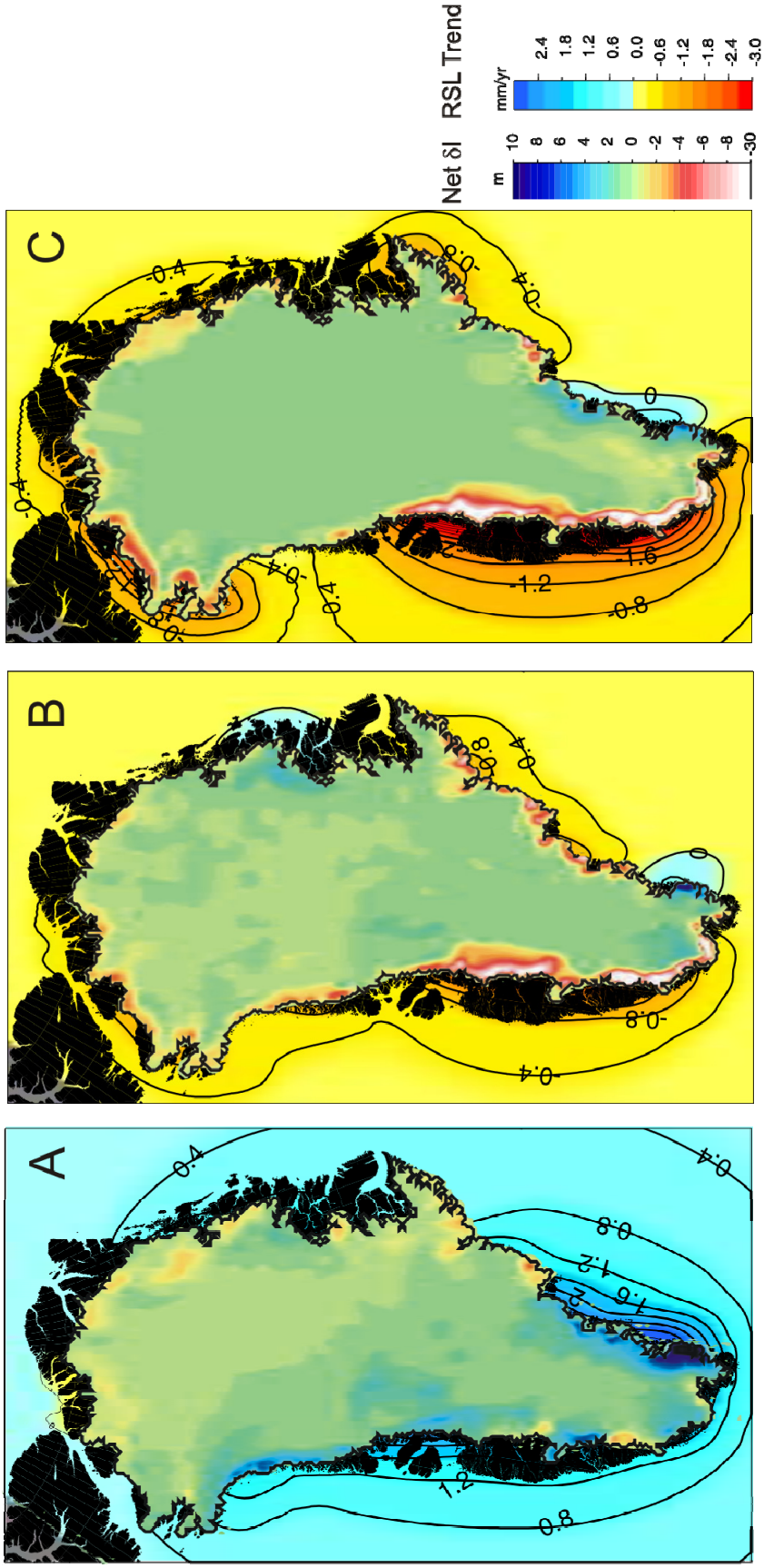

Fig. 5.8: Predicted net change in ice thickness and corresponding trends in RSL for the periods 1866-1886 (A), 1916-1936 (B) and 1995-2005 (C). RSL trends are contoured every 0.4mm/yr. As in Fig 5.7, these plots do not include the contribution to RSL change arising from millennial-scale changes in ice loading.

In comparison with the crude ice models considered in Chapter 3, the more realistic models generated in this chapter bear more resemblance to the peripheral melting scenario, albeit at a reduced magnitude. For all time periods considered, the patterns of mass loss produce sea-level fingerprints whose contours run approximately parallel to the coast, consistent with the predictions based on peripheral thinning scenario in Chapter 4 (Model 2, Fig. 4.1, left). Model 3 (Fig. 4.1, right) is not replicated here at century (Fig. 5.7) or decadal (Fig. 5.8) time scales. The configuration of ice loading change in the crude model is likely to be multi-annual. Also, the models in this chapter do not predict such sharp spatial gradients in sea level because the ice thickness changes are gradual and generally parallel to the coast in west Greenland.

The predicted contributions to 20^{th} century sea-level change at Nag and Aasiaat are projected against the trends obtained at Nag from the ^{210}Pb profiles (Fig. 5.9). A large range in relative sea level is predicted (solid grey lines) when the random daily temperature variation is allowed to fluctuate by 3.8^{o}C (lower limit) or 5.0^{o}C (upper limit).

Variation of the rain limit temperature over the range of 0-2^{o}C (i.e. the temperature at which liquid precipitation transforms to snow) has a relatively minor effect on the predicted rates and patterns of sea-level change at the data sites. Increasing the rain limit temperature to 2^{o}C (lower dashed line in Fig. 5.9A and B), acts to enhance the millennial-scale RSL rise, compared to a higher rainlimit. A 2^{o}C rainlimit means that more snow is formed in warmer areas, and the result of this is that more degree days are used melting snow rather than ice. Decreasing the rain limit from its pre-defined value of 1^{o}C to 0^{o}C (lower dashed line) acts to increase the rate of sea-level fall, as the temperature must reach zero before snow is formed. This means that less incoming precipitation will be accumulated and the positive degree days will immediately be used to melt ice. In all scenarios, additional melting or growth brought about by this parameter change will be enhanced by positive elevation feedback. This is reflected by the divergence in the trends (in contrast to the SMB results in Fig. 5.5, the divergence occurs as time is reversed due to the fact that RSL predictions are shifted to pass through zero height at present).

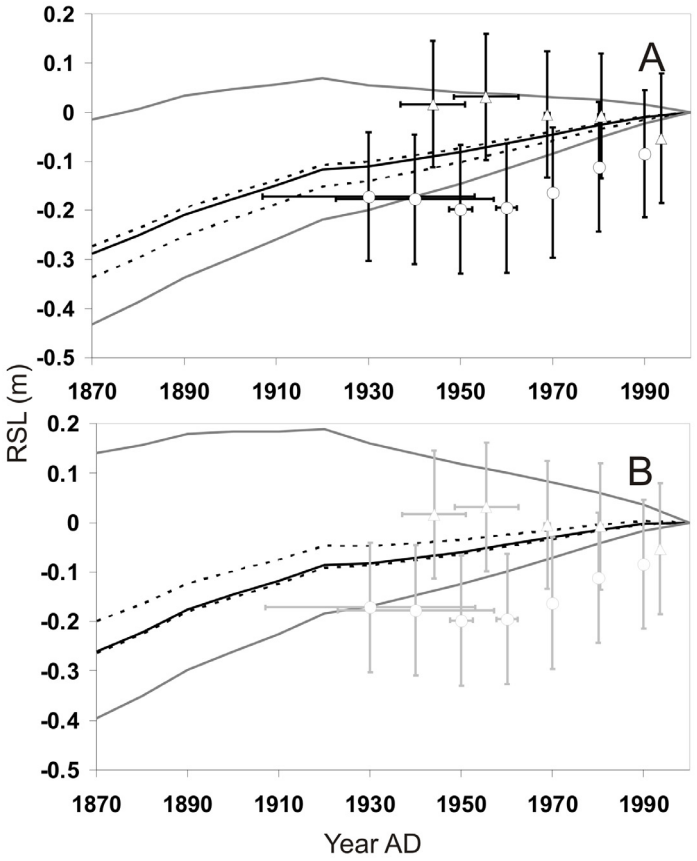

Fig. 5.9: Predicted relative sea level at Nag (A) and Aasiaat (B) for a range of model parameters. The dashed lines indicate the effect of varying the rain limit temperature and the grey lines indicate the effect of allowing daily temperature variations in the range of 3.8-5^{o}C. The solid black lines show predictions for the standard model runs (as in frame A). Note that the millennial-scale trends of 2.27 mm/yr (Aasiaat) and 2.69 mm/yr (Nag), estimated from the isolation basin RSL data, has been added to the predictions resulting from contemporary SMB changes. The data from the two Nag salt marshes are show in both frames for reference, and are applicable to the RSL history at Aasiaat (shown in grey, since they are not collected at this location)

Reducing the daily stochastic temperature variation causes reduction in the amount of melting as expected; but this reduction is limited to the inner areas of the ice sheet. Changing this value does not have a large effect at the extreme margins and low elevation areas as the temperatures are generally well above, or close to zero for most of the year. The biggest effect will be felt where summer and winter temperatures are at, or slightly below, zero. Allowing the daily temperature to fluctuate between +/-5^{o}C either side of the mean will initiate melting at places where previously there was none. Similarly, reducing the variability will reduce the overall area of surface melting. In the extreme centre of the ice sheet, summer and winter temperatures will be far enough below zero that daily fluctuations will not force the temperature above zero.

When the daily temperature variation is increased to 5^{o}C, the overall RSL rise over 1866-2005 is reduced (upper grey lines in Fig. 5.9A and B). During the termination of the LIA, the conditions become more favourable for melting at Nag and

Aasiaat when the variation is increased, so the RSL rise is less positive compared to the original trend. After ~1920AD, increasing the temperature variation allows the 20th century sea-level change to overcome the millennial scale trend at Aasiaat (Fig. 5.9B). At Nag, the net sea-level trend from 1920AD until present is close to zero. The lower grey lines in Fig. 5.9A and B correspond to decreased temperature variation and therefore increased RSL rise at both sites

This divergence (or sensitivity) is greater when the daily temperature variation is changed compared to the factor controlling the accumulation (rain limit) verifying that temperature is the most important control on the mass balance. Changing the daily temperature fluctuation parameter within reasonable bounds allows the predicted sea-level change to envelope most of the data points. Unfortunately, the data are not of high enough precision and accuracy to place useful bounds on ice model parameters.

5.4 Discussion and Conclusions

This chapter presents a SMB modelling study of the Greenland ice sheet since 1866, reflecting how the ice sheet has behaved under the climatic conditions of the 19th– 21st centuries. Over the time window of the study, the Greenland ice sheet has reacted to, and endured, a temperature increase similar to that experienced at present. Higher surface runoff rates similar to those of the last decade were also present in an earlier warm period in the 1920s and 1930s and apparently did not lead to a strong feedback cycle through surface lowering and increased ice discharge. Judging by the volume loss in these periods, it may be interpreted that the current climate of Greenland is not causing any exceptional changes in the ice sheet. Mass loss through glacier discharge is currently believed to dominate mass loss through SMB, and both processes are likely to be correlated. (Forman et al., 2007) report that the ice sheet retreated 1–2km inland at Kangerlussuaq, West Greenland, over the past 100 years. Although the model resolution is 5x5 km, the model predicts complete disappearance of some ice-sheet points in this area, in line with these observations. It is not possible to shed light on the relative contributions of ice dynamics vs. SMB to the current mass loss, but the study puts the modern day changes into the context of longer-term century-scale change.

It has been demonstrated that modification of parameters in the PDD model have a large effect on predicted surface mass balance. At the present time, there is no valid reason to choose one particular parameter combination over another (e.g.

higher rainlimits / high temperature variation), so these parameters are set at intermediate values in the case of the rainlimit (1^{o}C) and as an optimum modelling value (temperature variation = 4.2^{o}C) that best replicates SMB trends where constraining data are available. Increasing the complexity of the model with respect to the handling of elevation and ice thickness changes provides confidence that the process of dynamic-related ice thickness is being accounted for at least on a first-order level. This may not be strictly correct as there is likelihood that ice dynamics and SMB changes are correlated or lagged with respect to one another so generation of a spatially and temporally varying dynamics field is a target for further research and beyond the scope of this thesis.

Assuming that the ice model is reasonably accurate, the fingerprints show that the 20th century trends at the two data sites are a second order contribution to RSL compared to the millennial-scale trend associated with neoglacial regrowth.(+2 to 3mm/yr). The ^{210}Pb data do not resolve decadal fluctuations in relative sea level nor do they provide a precise measure of the 20th century trend. Therefore ice model accuracy over this period cannot be determined unless improved data are obtained. In all cases, the sea level is predicted to be above present and gradually fall to present day values, or to continually rise over the period 1866-2005, neither of which are compatible with the 'stable' sea-level reflected in the data. Given the scatter in the 20th century proxy data, and absence of data points in the latter part of the 19th century, it is not possible to determine if local sea level was rising or falling over the past ~ 140 years. On this premise it is not possible to identify the parameter set-up most suited to replicate 20th century sea-level changes, but the most realistic scenarios may be identified. The daily temperature is not likely to constantly vary by +/-5^{o}C, nor will the rain limit remain fixed. The large range in estimates achieved by PDD model parameter variation (Fig. 5.9) support sea level being stable over the entire 1866-2005AD period, in line with the proxy data.

Over a period of 140 years, there are no major changes in the pattern of the local sea-level fingerprint, with the long-term pattern of sea-level change around Greenland closely resembling those of the two warmer periods. The mass balance model predicts that the nature of mass balance in west Greenland is spatially invariable between the sites at Nag and Aasiaat, in line with data collected over the MCO-LIA transition, so this provides confidence that the 20th century trend ascertained from ^{210}Pb data at Nag may be applicable to Aasiaat. An important outcome of the modelling, which is central to the application of the fingerprinting technique, is that although the ice sheet appears to be in balance (i.e. 0.036mm/yr

eustatic contribution over 1866-2005), local sea level fluctuates significantly in time and space. Net negative ice sheet mass balance does not necessarily translate to coastal sea-level fall in all areas. The modelling tells us that local sea-level and overall mass balance is able to react to ice sheet-averaged increases in annual temperature of +3.5^{o}C, but a local RSL record is not a precise indicator of the health of an ice sheet.

Chapter 6: Exploring the Contribution to Regional Sea-level Change from GrIS Mass Balance over Century Timescales

6.1 Introduction

In this Chapter, I address the problem of simulating century scale changes in GrIS mass balance in order to replicate the observed sea-level changes at Nag and Aasiaat for the period 1000AD to 1860AD. In the absence of high-resolution gridded climate data like those used in Chapter 5, other options for forcing the ice model must be considered. Furthermore, over this longer time period (compared to that considered in Chapter 5), retreat and advance of the ice sheet becomes an issue in the modelling and so sensitivity of the mass balance results to changes in the dynamic (flow) field must be considered.

The Greenland Ice Core Project (GRIP) and other ice cores (Dye-3 and NGRIP) provide a suitable accumulation and temperature history for the past 1000 years (Fig. 6.1), and so were used in the first set of modelling experiments (presented in Section 6.3.1). Up until 1280AD, the ice sheet was generally drier than present with accumulation 6% lower than the long-term average. The accumulation rate over the time period 1020-1380AD is generally lower than average, with a sharp increase (magnitude 12%) over the period 1280-1400AD. From 1400AD onwards there is a general decline in accumulation. At other ice core sites in Greenland (Crete 71.12^{o}N, 37.32^{o}W; Milcent: 70.30^{o}N, 44.55^{o}W and NGRIP; 75.10^{o}N, 42.32^{o}W) , the accumulation data show significant interannual variability but little evidence of a long-term trend (Andersen et al. 2006). Over the time period spanned by the RSL datasets, the ice cores display a high degree of correlation when the accumulation rate is averaged over 5 years (Andersen et al. 2006). In order to gain a good approximation to ice-sheet wide changes in precipitation, the collective accumulation history of the GRIP, NGRIP and Dye-3 cores was used (Fig 6.1)

From 1020AD, the temperature at GRIP remained warmer than present until ~1320AD. This time period is known as the Medieval Climatic Optimum (MCO). From this time onwards, the temperature at the GRIP site shows the transition into the Little Ice Age (LIA), with two distinct minima in temperature at 1570AD and 1880AD (latter not shown in Fig. 6.1). Temperature data collected at DYE-3 show the same variation over the period 1000-1860AD but with slight differences in the magnitude of the anomaly due mainly to differences in altitude between the drill sites.

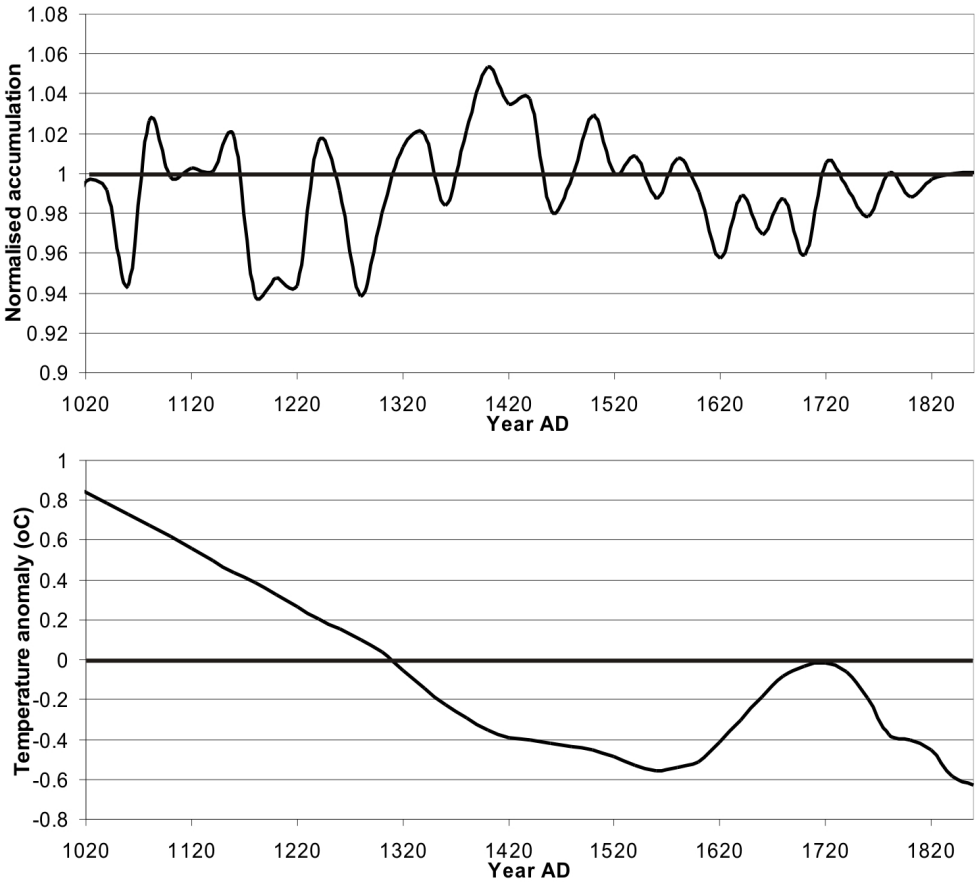

Figure 6.1: Optimal accumulation record assimilated from GRIP, NGRIP and Dye-3 ice cores (Andersen et al. 2006) and GRIP-only temperature anomaly (Dahl Jensen et al. 1998) at GRIP relative to present day values.

In the second set of modelling experiments (Section 6.3.2), the sensitivity of mass balance and sea-level change to a forcing mechanism governed by the North Atlantic Oscillation (NAO) index is explored. The NAO refers to the climatic variation in the North Atlantic and Europe induced by the difference in pressure between the Azores high and Icelandic low pressure systems. The precipitation bulls-eye in south east Greenland is related to the permanent low pressure system situated offshore. The difference in atmospheric pressure between the two areas does not remain constant. The NAO is often classified as ether being in a 'positive' or 'negative' phase depending on the pressure difference at a given time. A positive NAO phase (NAO+) occurs when the pressure difference is high. In this case, winters in Greenland are cooler and drier than usual. During a negative NAO phase (NAO-), Greenland experiences milder winter temperatures as fewer storms track cross the North Atlantic. Consequently, in northern Europe, winters are drier due to the southerly deflection of the west-east storm track. During this phase, southern Europe is warmer and milder.

A recent study by Trouet et al. (2009) provides a reconstruction of the winter NAO index from 1049AD until present (Fig. 6.2). The time series was reconstructed using previously published tree ring data from Morocco and speleotherm records from northern Scotland. These locations are ideally situated to capture the dipole of the NAO. The most striking feature of the time series is the shift from a ~400 year long period of positive NAO phase to a ~500 year long period of fluctuating phase. Multiannual periods of strong NAO- phases dominate the record from 1700AD onwards. The change in phase from NAO+ to NAO- occurs roughly at the same time at which RSL rise begins to decelerate in west Greenland (e.g. see Chapter 4, Fig. 4.5C). This signals a change from cold, dry winters to periods when winters were milder in west Greenland. The relationship of the NAO to west Greenland climate has been discussed previously (Appenzeller et al. 1998; Hanna and Cappelen, 2003, Chen et al., 2009). In Appenzeller et al. (1998), ice core data spanning 1650AD to present day from the west of Greenland reveal a correlation of 0.52 when comparing accumulation to winter NAO.

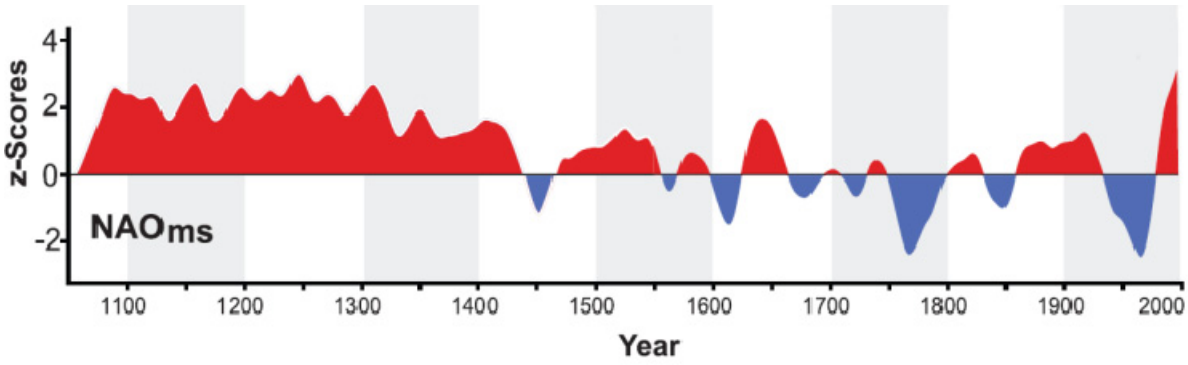

Figure 6.2: Winter NAO strength (ms) spanning the period 1049AD to present. From Trouet et al. (2009).

Hanna and Cappelen (2003) demonstrate a significant negative correlation (-0.71) between temperatures at southern Greenland coastal weather stations and NAO phase for the period 1958-2001. Over this time period, coastal temperatures in Greenland show a significant cooling of 1.29 +/- 0.63 ^{o}C, in contrast to an increase in global mean temperature of 0.53 +/- 0.16^{o}C. Fig. 6.3 shows that as the NAO index moves towards a more positive state, the temperature decreases and vice versa. For example, between 1991 and 1996, the NAO index decreases from approximately 2.5 to 0, coincident with an increase in temperature of ~2^{o}C. There is no obvious lag between the datasets in Fig. 6.3 to indicate whether NAO forces temperature or vice versa. It is interesting to note that the relationship evident in Fig. 6.3, when analysed in conjunction with Fig 6.2, suggests that the low-elevation, low-latitude portions of

the GrIS may have experienced relatively warm conditions compared to those observed in Europe during the LIA.

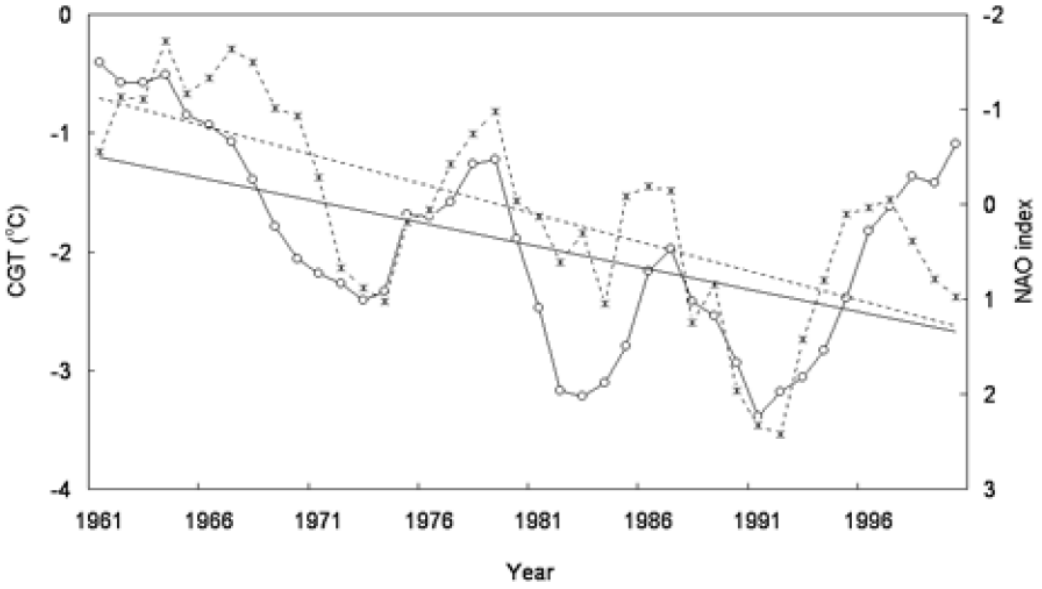

Figure 6.3: Composite Greenland Temperature (CGT) series assimilated from weather stations in west and east Greenland south of 69°N (open circles) versus NAO index (crosses). From Hanna and Cappelen (2003).

In order to investigate the possible influence of the NAO in the centre of the ice sheet, 20-yr averaged temperatures estimated from the GRIP and DYE-3 ice cores (Dahl-Jensen et al. 1998) were compared with 20-yr averaged NAO index data from (Trouet et al. 2009). This comparison gives correlations of 0.61 (GRIP) and 0.49 (DYE-3) over the period 1060-1860AD. This contrasts to the negative correlation at the margins. When comparing the normalised ice core accumulation to NAO index, no correlation is found. Since no correlation with accumulation at GRIP is observed, it can be assumed that even though temperatures may track NAO, the mass balance in the centre is not dictated by this process since the temperatures remained far enough below zero to prevent significant melting, and therefore the imprinting of themselves on the overall mass balance. Mosely-Thompson et al. (2005) confirm that the NAO is most noticeably manifested in ice core accumulation data in central-west Greenland, where accumulation is negatively correlated to NAO index, indicating a similar relationship to coastal temperatures as found by Hanna and Cappelen (2003). In summary, the NAO appears to exert a significant control at least on the low-latitude southern areas of Greenland. Therefore, I utilised the results from previous studies of NAO variability to develop an NAO-based forcing mechanism and generate a GrIS mass balance time series for the period 1060-1860AD (Section 6.3.2).

The main objective of this chapter is to explore the possibility that mass balance changes of the GrIS can produce the observed RSL time series at Aasiaat and Nag. As outlined above and described in the next section, a crude climate forcing scheme based on ice core records and NAO index was used for this purpose. Of particular interest is the ability of these climate forcings to generate the observed deceleration in RSL between 1500 and 1600AD. The RSL predictions were generated using the same sea-level model as used in Chapter 3. The Earth model used is identical to that used in the analysis in Chapter 5, Section 5.1. Also, different scenarios of dynamic related mass change were applied to each run to investigate the influence of this model component on the results obtained

6.2 Methodology

In the first experiment, the temperature from the GRIP site and the collated accumulation history (Andersen et al. 2006) from 1000-1860 were used to force the PDD model. Present day surface elevation and ice thickness grids (Bamber et al., 2001a, 2001b) were corrected using output from the modelling study of Simpson et al. (2009) in order to create a surface elevation and ice thickness configuration that is more representative of 1000AD. The surface elevation and ice thickness grids are therefore relative to present. The precipitation field used in Chapter 5 is perturbed by the precipitation anomaly (see E6.1) described in Fig. 6.1 (upper panel). In accordance with the elevation and ice thickness corrections, the precipitation anomalies are expressed with respect to present day values. It is assumed that the GRIP ice core temperature history is recalling mean annual temperature. The anomaly is added to the mean annual temperature (E6.2).

$$P(x,y,t) = P(x,y)_{1961-1990} \times P_{anom}(t) \qquad \text{E6.1}$$

$$TMA(x,y,t) = TMA_{parameterised}(x,y,t) + T_{anom} GRIP(t) \qquad \text{E6.2}$$

where $P_{anom}(t)$ is the normalised accumulation from the collective ice cores (Fig 6.1, top). This is expressed relative to present-day conditions in order to ensure that past conditions are adequately reflected with respect to present.

In the second experiment, the temperature and precipitation anomalies are governed by the NAO index. In order to make sure the PDD model is forced by a precipitation field that evolves along with NAO index, a precipitation field

representative of conditions during 1961-1990 (as in Chapter 5) is perturbed by anomalies characteristic of NAO+ and NAO- periods. These precipitation anomalies are shown in Fig 6.4. The major differences between NAO- and NAO+ periods are shown to occur in the extreme north of Greenland where precipitation can fluctuate between +/- 20%. In marginal areas of eastern Greenland, precipitation supply increases during NAO+ periods. This is expected due to intensification of the low pressure system between Iceland and Greenland during NAO+. On the southern tip of Greenland there is less variation during the NAO dipole years.

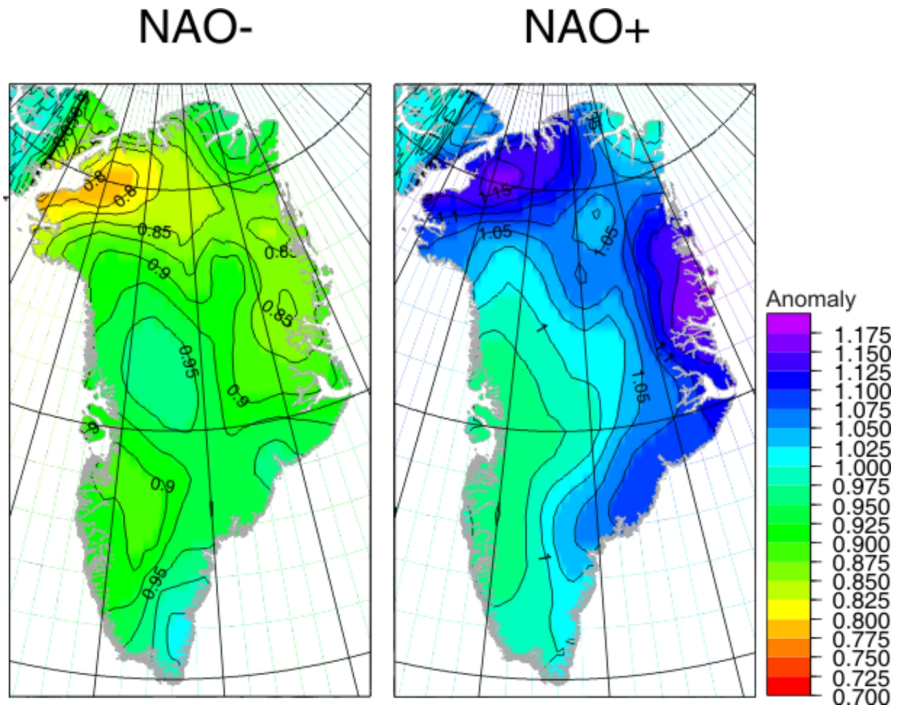

Fig. 6.4: Average annual precipitation anomalies representative for NAO- (1958-1969; left) and NAO+ (1984-1995; right). The precipitation anomalies are calculated using the ECMWF (Hanna et al. 2008) dataset (see Chapter 5, Section 5.2)

Of interest to this study are the precipitation variations in the west of Greenland. Conditions in west Greenland are ~ 7.5% drier during a NAO- phase. The variation between NAO dipoles is less obvious in the west compared to the east. In this experiment, the precipitation field was calculated via:

$$P(x,y,t) = P_{1961-1990}(x,y) \times P_{anom} NAO^{m}(x,y,t) \qquad \text{E6.3}$$

where t is set at increments of 20 years, as in the first experiment The time dependence in the term $P_{anom} NAO^{m}$ is due to the change of NAO phase over time. The integer 'm' in E6.3 refers to NAO phase, and is not a numerical power. It will have a value of -1 or +1 and identifies which of the two precipitation anomalies in Fig.

6.4 is used. This ensures a temporally evolving precipitation field in accordance with NAO state. Although Appenzeller et al (1998) reconstructed NAO based on accumulation rates in west Greenland, apart from a high correlation between accumulation and NAO variability, they did not make clear how the amplitude of NAO index and accumulation are related. Therefore, in this analysis the NAO precipitation anomalies (E6.3) are not scaled with respect to NAO index strength.

Temperature variations are based on the interpretation of the results from Hanna and Cappelen (2003) and Trouet et al. (2009). The amplitude of the NAO strength is assumed to be directly proportional to temperature anomaly, as is shown for the positive phase. The temperature at any point in Greenland is prescribed thus:

$$T(x,y.t) = T_{param}(x,y,t) + T_{anom}NAO(x,y,t) \quad \text{E6.4}$$

$$T_{anom}NAO(x,y,t) = NAO_{strength} \times m \times S(z) \quad \text{E6.5}$$

For NAO+, *m*=-1; and for NAO-, *m*=+1 in E6.5. The letter 'm' is incorporated into the equation to ensure that when the NAO index is positive, the temperature anomaly is subtracted, and vice versa for the negative NAO phases. The quantity $NAO_{strength}$ is equivalent to the strength as shown in Fig 6.2. The NAO-related temperature anomaly may be assigned to mean annual temperature, winter (DJF) or summer (JJA) temperature. The quantity $T_{param}(x,y,t)$ is the part of the temperature governed by latitude and elevation. The sensitivity of the annual mass balance to the perturbation of seasonal temperatures is examined in Section 6.3.2.

In order to incorporate a level of elevation-based sensitivity in the temperature anomaly, the term $T_{anom}NAO(x,y,t)$ is scaled by a quantity, *S(z),* in accordance with elevation, *E* (metres). The *S(z)* values chosen are arbitrary but introduce some elevation-based sensitivity to the NAO forcing. No latitude-based sensitivity is included, but this is accounted for to some extent in the parameterisation of the base temperature ($T_{param}(x,y,t)$). Also, work carried out by Appenzeller et al. (1998) shows that pressure variations at sea level can be correlated to differences in snow accumulation. Fig. 1 in Appenzeller et al. (1998) shows that the pattern of NAO-modulated pressure variations that can be explained with a 1-sigma deviation in snow accumulation follow an elevation-based rather than latitude-based pattern. It is important to note that, because of inadequate or inaccurate representation of NAO influences at higher latitudes, estimates of the overall mass balance of the ice sheet will not be particularly accurate.

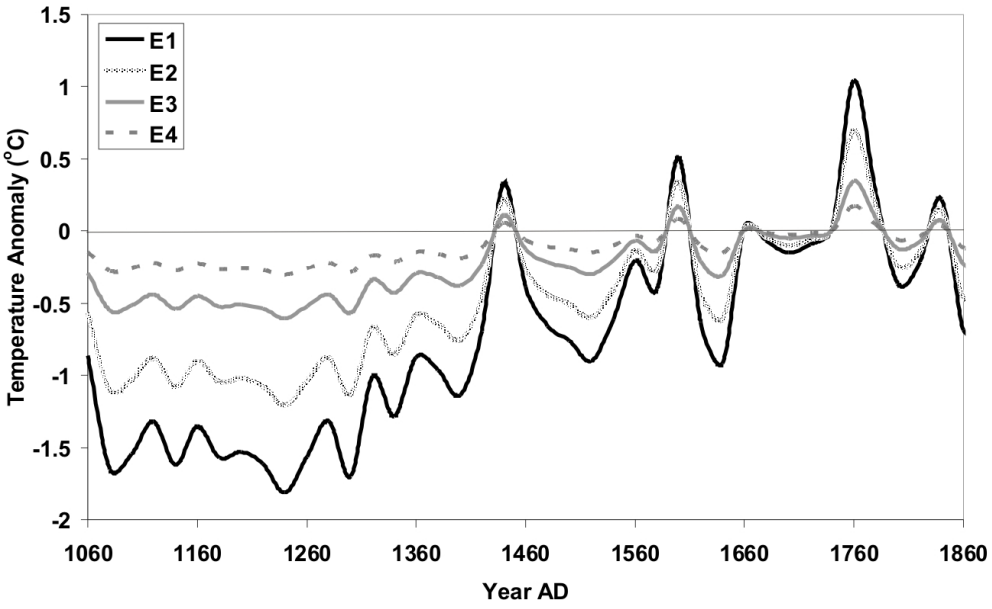

Fig 6.5: NAO-based temperature forcing for elevation bands E1-E4: S = 0.6 for 0m < E1 < 1000m, S = 0.4 for 1000m < E2< 1500m, S = 0.2 for 1500m < E3 < 2000m, S = 0.1 for E4 > 2000m.

In both of the SMB experiments presented below, the starting surface elevation and ice thickness distributions are not accurately known. Therefore, several scenarios were considered to test the sensitivity of the RSL and mass balance predictions to this uncertainty. The correction term for ice dynamics (see E6.6) was generated using 1-140 year average surface mass balance distributions gained from modelling the period 1866-2005. Elevation and ice thickness (∂I) changes are prescribed using the following equation:

$$\partial I(x,y,t)_n = SMB(x,y,t) - \partial I_{dynamics}(x,y) \qquad \text{E6.6}$$

where ∂I is the ice thickness change due to the difference between SMB and the flux gradient which is calculated from one of the six SMB distributions shown in Fig 6.6 (the parameter n in E6.6 denotes the specific time period used). The quantity $\partial I_{dynamics}$ is simply a SMB field (Fig 6.6), subtracted from the SMB in order to simulate areas of mass gain to mass loss and vice versa. In effect, the 'reversed' SMB fields describe the elevation change associated with the submergence (or emergence) velocity acting in areas of accumulation (or ablation, recall Section 2.4.3). This term has no time dependence because it the contribution of ice dynamics to elevation and ice thickness change is assumed to be stable over the entire time period. The change in ice thickness is multiplied by 20 to represent the time increment in the modelling run.

The SMB periods considered for Experiment A are n:1866-1886, 1995-2005, 1916-1936, 1866-2005, 2005 and 1961-1990 (see Fig. 6.6). The periods 1995-2005 and 1916-1936 are indicative of surface mass balance during warmer climates in Greenland, with average annual ice-sheet wide SMB of 202km^3 and 232km^3 water equivalent, respectively. When these are applied as corrections for emergence velocity, low SMB fields (e.g. where SMB near the ice margin is extremely negative) produce a high supply of ice from the centre to the margins. The period 1866-1886 is indicative of average SMB at the end of LIA, with SMB of 313km^3; roughly one third higher than that during the warmer periods. Longer-term SMB patterns from 1961-1990 and 1866-2005 are used to represent periods when the ice sheet is overall in balance (i.e. no significant contribution to sea-level change), with SMB of 263 km^3 and 248km^3, respectively. SMB for 2005 using the present day surface elevation only is also used, so the calculated mass balances may be interpreted as anomalies with respect to present.

The SMB distributions in Fig 6.6 share one common feature with respect to the central-west coast of Greenland. Ablation dominates over accumulation, so any ice loss occurring is result of the 20-year SMB being more negative than the SMB distribution used for the dynamic correction. During 1995-2005, the western margin of the GrIS shows the most negative mass balance. In all cases, apart from the 2005 distribution, extreme (5-10m/yr) thinning is predicted for the western margin in a narrow (<50km wide) area in the south east. For the majority of the ice sheet, the mass balance is positive.

Some of the model experiments presented below are run through to 2005, using the detailed (1860-2005) climate history described in Chapter 5. SMB and RSL results for the end period (1866-2005) of these longer runs are compared to those generated in Chapter 5 to determine the importance of the starting elevation and ice thickness at 1866AD for mass balance calculations over the period 1866-2005. An underlying aim of this chapter is to determine whether robust predictions for relative sea-level change in west Greenland can be generated using differing parameterisation and modelling techniques.

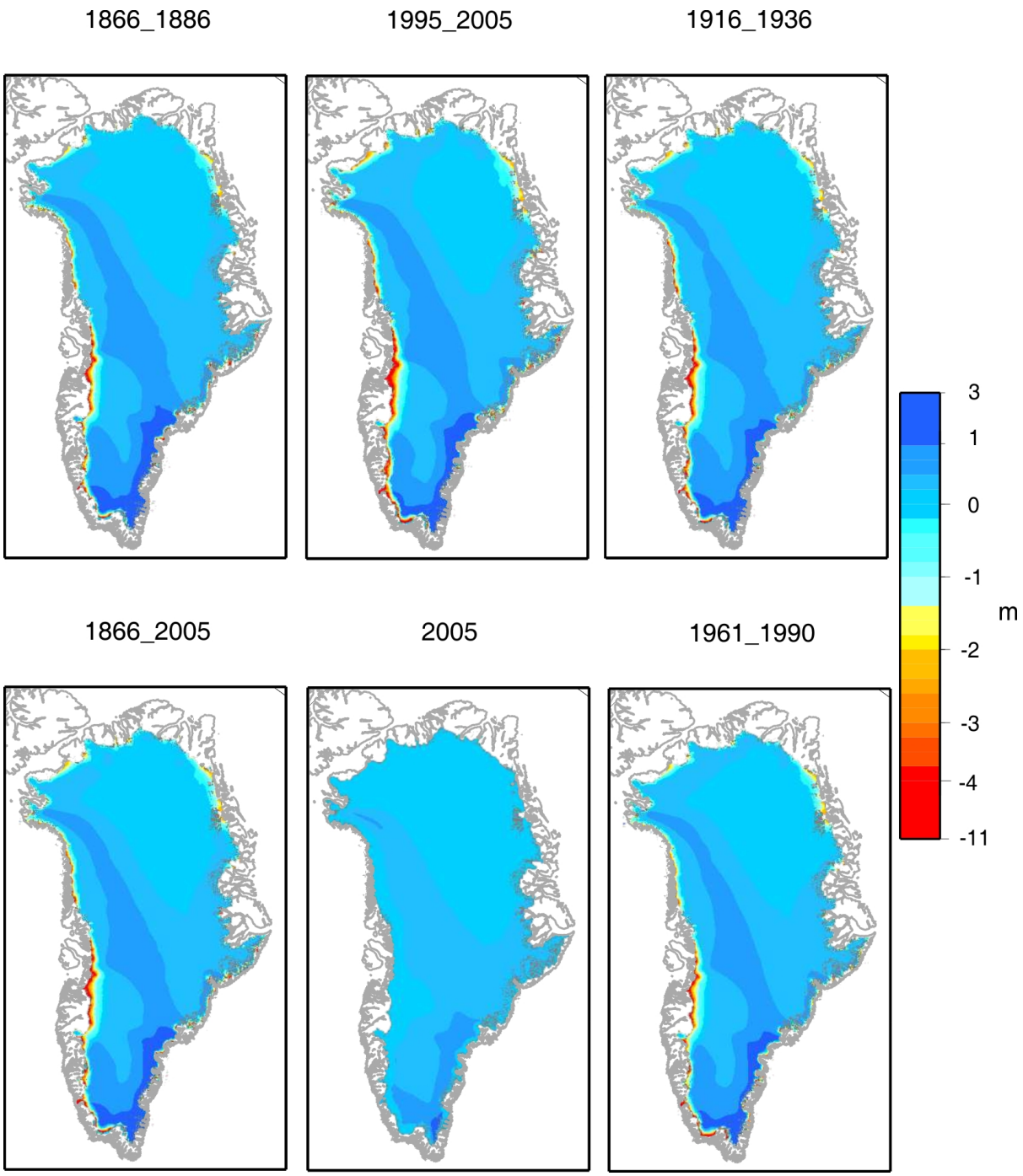

Fig 6.6: SMB distributions used to determine corrections for dynamic compensation ($\partial I(x,y)_n$). Negative SMB values lead to ice replenishment whereas positive values lead to ice depletion through this correction term (see E6.6). Colour divisions on the scale bar correspond to SMB in metres of water equivalent. In Experiment B, only two dynamic fields (1961-1990 and 1866-1886) were considered since the main focus is to explore effect of the NAO forcing on surface mass balance.

6.3 Results

6.3.1 Experiment A (Ice core forcing)

Fig 6.7 shows the ice sheet wide mass balance and contribution to relative sea-level change. The RSL change shown is the average value of contributions at Nag and Aasiaat. The variation between Nag and Aasiaat is shown as an error bar on the data, depicting 'range' of RSL predictions rather than error.

In four (red, orange, purple, green) out of the six scenarios, the ice sheet reaches a stable state of accumulation after 1400AD. Surprisingly, this coincides with a decline in accumulation rate recorded in the ice cores. This is a likely consequence of prolonged ice-build up increasing the surface elevation during the period 1020-1400AD under falling temperatures and a fairly stable accumulation rate. In these four scenarios, decadal variation in mass balance is on the order of +/-25km^3 or less with no overall trend from 1400-1860AD. The same variation is predicted for all four scenarios and is therefore dominated by accumulation rather than ablation due to the lowered temperatures forcing ablation to a minimum. The time-constant dynamics correction means that for the centre of the ice sheet there is little variation in elevation so the temperature evolution parameterised through elevation changes remains relatively constant. The dominant variation in temperature is provided by the GRIP forcing.

Two scenarios (Blue; Black) are markedly different to those described above: mass balance predictions are generally negative (in the range of 0 to -100km^3/yr) and the initial positive trend in mass balance is smaller. This is due to the surface mass balance gain being less than the mass lost through dynamic flux. These two particular dynamic corrections force the ice sheet to become more sensitive to temperature and accumulation changes. After 1400AD, the response to drier, colder conditions becomes more of a response to the accumulation – a cooling climate still allows for some degree of ablation due to increased surface lowering compared to the 4 previous scenarios but less accumulation also contributes to surface lowering. Similar interannual variation of +/-25km^3 is predicted, but is projected on to a declining mass balance trend from 1400-1860AD onwards.

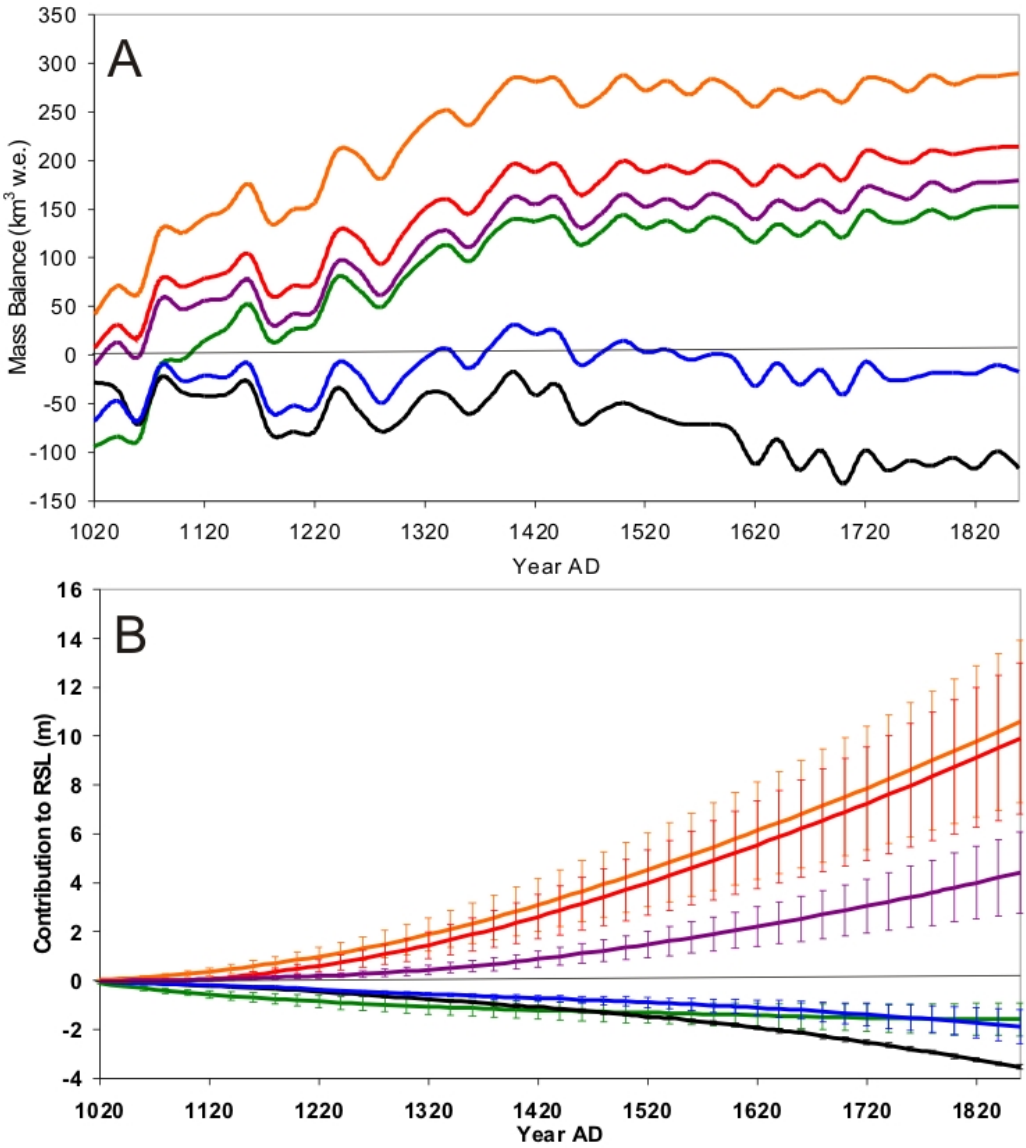

Fig. 6.7: Ice sheet averaged mass balance predictions (A) and the respective relative sea-level change (B) (averaged for Nag and Aasiaat). Colours refer to specific dynamic corrections (n) applied in each model run: 1866-2005 (purple); 1916-1936 (red); 1866-1886 (blue), 1961-1990 (black), 2005 (green); 1995-2005 (orange.) Fig 6.6 shows the SMB patterns these dynamic contributions are calculated from. The contributions to RSL change from millennial scale changes in ice loading are not incorporated into the results in Panel B

The results of the six experiments carried out so far highlight the importance of the dynamic field correction term. Interannual variation of +/-25km^3 is prevalent throughout all experiments, with only two scenarios (n:1961-1990 and n:1866-2005) recording a response to the longer-period decline in accumulation initiating at 1420AD. This response is absent from the other scenarios as the ice sheet, overall, has entered a very cold and dry period, which coupled with increased surface elevation, forces ablation to a minimum

In comparison to the model results for the 1866-2005 period (Chapter 5), the range of magnitudes of mass balance for four scenarios (blue, black, green and purple) is not significantly different. Note that the suppressed interannual variability in

the longer runs performed in this chapter (compare results in Fig. 6.9 to those in Fig. 5.2, Chapter 5) is the result of using larger time steps (20 yr compared to 1 yr) and a smoother forcing history. For the scenarios using the 1916-1936 and 1995-2005 distributions (Fig 6.7A, red and orange lines respectively), the mass balance values are considerably higher than those calculated in Chapter 5. For these two cases, average rates of eustatic sea-level fall are predicted to be, respectively, 0.44 and 0.66mm/yr over the period 1000-1860AD. These positive rates are more representative of the contribution over the period 1000-1400AD and reflect that the build up of ice over this period is sufficient to offset any reduction in ice mass during the proceeding dry period. Table 6.1 summarises the eustatic and local sea-level trends determined for each mass balance scenario.

Period >	1020-1860 AD				1020-1500AD		1500-1860AD	
Dynamic Scenario	Eustatic	Nag	Aasiaat	Nag-Aasiaat Average	Nag	Aasiaat	Nag	Aasiaat
1961-1990	0.2	-3.9	-4.1	-4.02	-2.8	-3.0	-5.95	-6.05
1866-2005	-0.35	3.9	6.6	5.3	2.0	3.4	6.2	10.6
1916-1936	-0.44	9.6	15	12.3	6.0	9.8	12.5	21.7
1866-1886	0.05	-1.5	-2.6	-2.07	-1.35	-1.85	-1.9	-3.9
2005	-0.26	-1.1	-2	-1.55	-1.8	-2.8	-0.36	-1.36
1995-2005	-0.66	10	15.7	12.8	6.9	10.7	12.8	22.2

Table 6.1 Summary table showing predicted sea-level rates (mm/yr) calculated using linear regression for each scenario considered in Experiment A. The contributions to RSL change from millennial scale changes in ice loading are not incorporated into the results

For all dynamic correction scenarios considered, the contribution to eustatic sea-level change lies in the range of -0.66 to 0.19mm/yr for the period 1020-1860AD. In order to replicate the RSL change obtained from proxy sea-level data at Nag and Aasiaat, mass balance changes must drive a fall in RSL at a magnitude of ~3 mm/yr that initiates between 1500 and 1600 AD (see Chapter 4). Based on this and the constraint that the site differential in rate is less than ~1.76 mm/yr, it is possible to rule out three scenarios (1916-1936, 1995-2005, and 1866-2005). The century-scale RSL trends for the scenarios that produce a sea-level fall for the past ~400 years are shown in Fig 6.8.

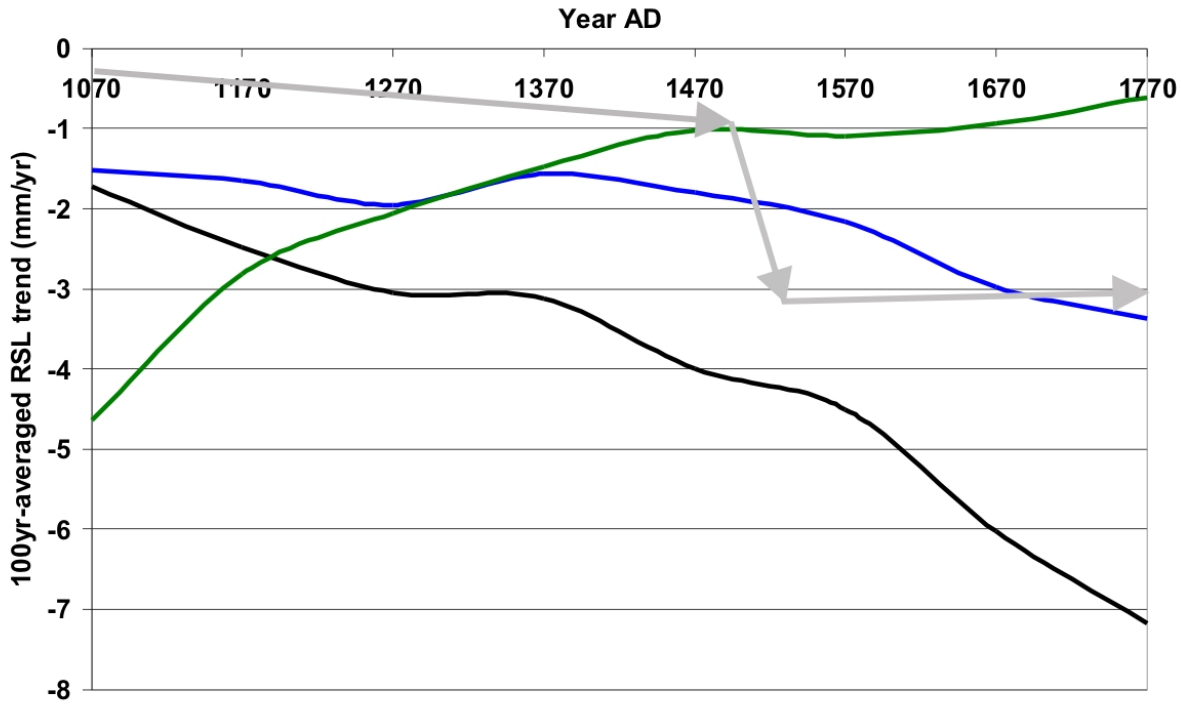

Fig. 6.8: Century-scale trends in relative sea-level for three scenarios in Fig. 6.7A (black, 1961-1990; blue,1866-1886; green, 1866-2005). Graph shows the average value for Nag and Aasiaat. The grey arrows indicate the trend required to overcome millennial-scale RSL rise. The contributions to RSL change from millennial scale changes in ice loading are not incorporated into the trends

The first feature evident from inspection of Fig 6.8 is that no trend closely replicates the desired scenario (grey line) to counteract the millennial-scale late Holocene RSL rise. The 1866-2005 dynamic correction (green line) produces century-scale RSL fall but the rate of fall decreases over the time of the model run from 4.6mm/yr to 0.6mm/yr. The scenario which provides the minimum differential of RSL between Nag and Aasiaat (1961-1990, black line) does not replicate the change in rate needed around 1500AD (also, the magnitude of RSL fall is too large throughout the model run). The 1866-1886 scenario (blue line) produces the best result in that it most closely matches the signal required to fit the data. However, the magnitude of RSL fall is too great at the start of the model run (-1.5mm/yr), which increases to -3.4mm/yr by the end of the model run. The final RSL rate is sufficient to offset the Holocene trend and a 1.5mm/yr fall at the start of the modelling period cannot be confidently ruled out due to lack of RSL data points from 1000 to ~1400AD. Also, the increase in RSL fall occurs too early (1370AD) and is too gradual compared to the signal that would closely fit the observations.

6.3.2 Experiment B (NAO forcing)

In this section, several experiments are considered where the timing of the temperature anomaly is varied in conjunction with two different dynamic distributions. The experiment characteristics are outlined in Table 6.2, with the main focus on varying the seasonal forcing rather than the dynamic scenario. The results from Experiment A demonstrate that uncertainty in the initial ice surface distribution (and its influence on the dynamic correction) has a significant impact on the mass balance predictions. There is no strong argument in favour of any particular dynamic scenario and so the two considered in this experiment ($\partial I(x,y)_n$, where n=1866-1886 and n=1961_1990) are those from the previous section that most closely matched the RSL observations. The precipitation shift (PPT shift) in Table 6.2 is applied to each point in the background 1961-1990 field (Huybrechts et al., 1994). Since this analysis focuses on exploring conditions that are required to create mass loss and sea-level fall, it is not necessary to explore scenarios where positive changes in precipitation are enforced. The mass balance results calculated from the scenarios described in Table 6.2 are shown in Fig. 6.9.

Scenario	NAO forcing			Dynamic Field	PPT shift
	A	JJA	DJF		
EXP1	X			1866_1886	0%
EXP2	X			1961_1990	0%
EXP3	X			1866_1886	-10%
EXP4	X			1961_1990	-10%
EXP5			X	1866_1886	0%
EXP6			X	1961_1990	0%
EXP7			X	1866_1886	-10%
EXP8			X	1961_1990	-10%
EXP9		X		1866_1886	0%
EXP10		X		1961_1990	0%
EXP11		X		1866_1886	-10%
EXP12		X		1961_1990	-10%

Table 6.2: Details of the climatic forcing used in the NAO-based mass balance analysis (Experiment B). Columns 2-4 explain which months (All (A), Summer (JJA) and Winter (DJF)) have their temperatures forced by NAO. Column 5 denotes the SMB field used for the dynamic correction (refer to Fig 6.6 for spatial plot). Column 6 denotes the enforced ice-sheet wide additional change in precipitation.

Linear regression shows that for each scenario considered (except EXP8), the mass balance increases up until approximately 1420AD, after which it becomes relatively stable (in terms of the multi-century average). The parameterisation

adopted assumes that positive NAO corresponds to cooler coastal conditions, so the ice sheet is allowed to build up and remain in a positive state of mass balance even after the onset of NAO- at around 1420AD (see Fig. 6.2). In all cases, the results indicate that the applied changes in atmospheric conditions (related to NAO-) are insufficient to force a secular decline in total ice sheet mass balance. The overall eustatic contribution to RSL change over the period considered lies in the range of -0.63 to +0.33mm/yr.

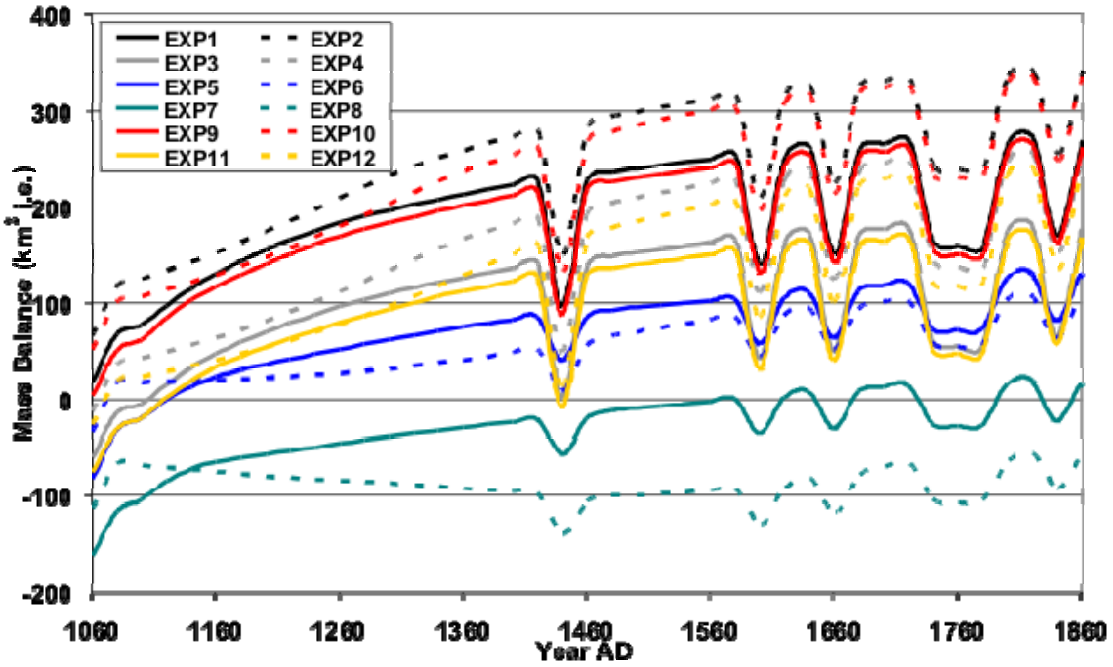

Fig. 6.9: Ice sheet averaged mass balance (1060-1860) for all scenarios in Experiment B. See Table 6.2 for details

Reducing the precipitation by 10% and forcing summer temperatures produces a less significant effect. The mass balance is generally reduced (e.g. compare EXP7 and EXP9), but reducing the precipitation by 10% does not affect the difference between the two different dynamic runs (compare EXP10 minus EXP9 and EXP8 minus EXP7). If there is no winter melting in an area, reducing the precipitation simply reduces accumulation but doesn't force immediate melting of the ice layer. In the winter forcing scenario, the reduction of precipitation produces a significant difference between runs using equivalent dynamic scenarios (EXP5 vs. EXP7 and EXP6 vs. EXP8), as this is working in tandem with warmer (compared to EXP1-4 and EXP9-12) summer temperatures up until 1460AD.

Encouraging winter melting as opposed to summer melting (e.g. EXP 5-8 vs. EXP 9-12) reduces the variability in the mass balance signal and the overall mass balance from 1060 to 1860 AD. The extensive NAO+ period at the beginning of the model run allows for cooling in all seasons (EXP1-4) and summer (EXP9-12) where

the vast majority of the PDD sum is generated. When temperature anomalies are applied to winter months only, the major effect is not to increase mass balance in the winter months, but to prevent cooling (and therefore reduced melting) in the summer. The mass balance up until 1420AD is being inadvertently modulated by not allowing cooling of summer temperature and, to a lesser extent, during NAO- periods by extending the melt season through warming the winter temperature.

The shorter-term fluctuations (post 1420 AD) in mass balance are suppressed when the temperature forcing is applied over winter rather than summer. Reduced variability occurs between mass balance years as the largest portion of melt is generated in the summer months. The onset of NAO- in the mass balance record is not easily recognised when the temperature anomaly is applied to the winter months.

In all cases, as with the mass balance runs shown in Section 6.3.1, the divergence increases over time between the high and low dynamics scenarios. Using the scenario n:1961-1990 (dashed lines in Fig. 6.9) reduces the overall ice sheet-averaged mass balance compared to the 1866-1886 scenario. However, this situation only arises when winter temperatures are forced by NAO, reflecting and important interplay between timing of application of the temperature anomaly and choice of dynamic scenario. This is an interesting result. For EXP5-8, the margins of the ice sheet do not undergo modulation of summer temperatures, so the summer temperature variation is controlled by elevation only. Summer melting throughout the time series will be felt significantly at the margins, but there will be some compensation by the ice flow. More ice will be provided by the dynamics scenario with the highest emergence velocity, which in this case is 1866-1886. But, the 1866-1886 dynamics scenario also provides a high submergence velocity in the central portions of the ice sheet. Very little ablation occurs in the centre of the ice sheet, so although more mass will be lost using the 1866-1886 dynamics correction in the centre, marginal mass loss dominates the overall annual mass balance sum.

In the summer temperature forcing scenarios, use of the 1866-1886 distribution produces lower mass balance, although overall ice sheet mass balance remains positive for both scenarios. This is because changes at the periphery do not dominate the ice sheet wide mass balance sum in these cases (EXP1-4 and EXP9-12). Use of the 1866-1886 dynamic correction provides a higher submergence velocity compared to the 1961-1990 correction and so central accumulation is lower than when the 1961-1990 correction is used.

The next step in the analysis is to use the mass balance models generated from the NAO forcing to calculate the contribution to RSL at Nag and Aasiaat. The results are shown in Fig. 6.10 and Table 6.3.

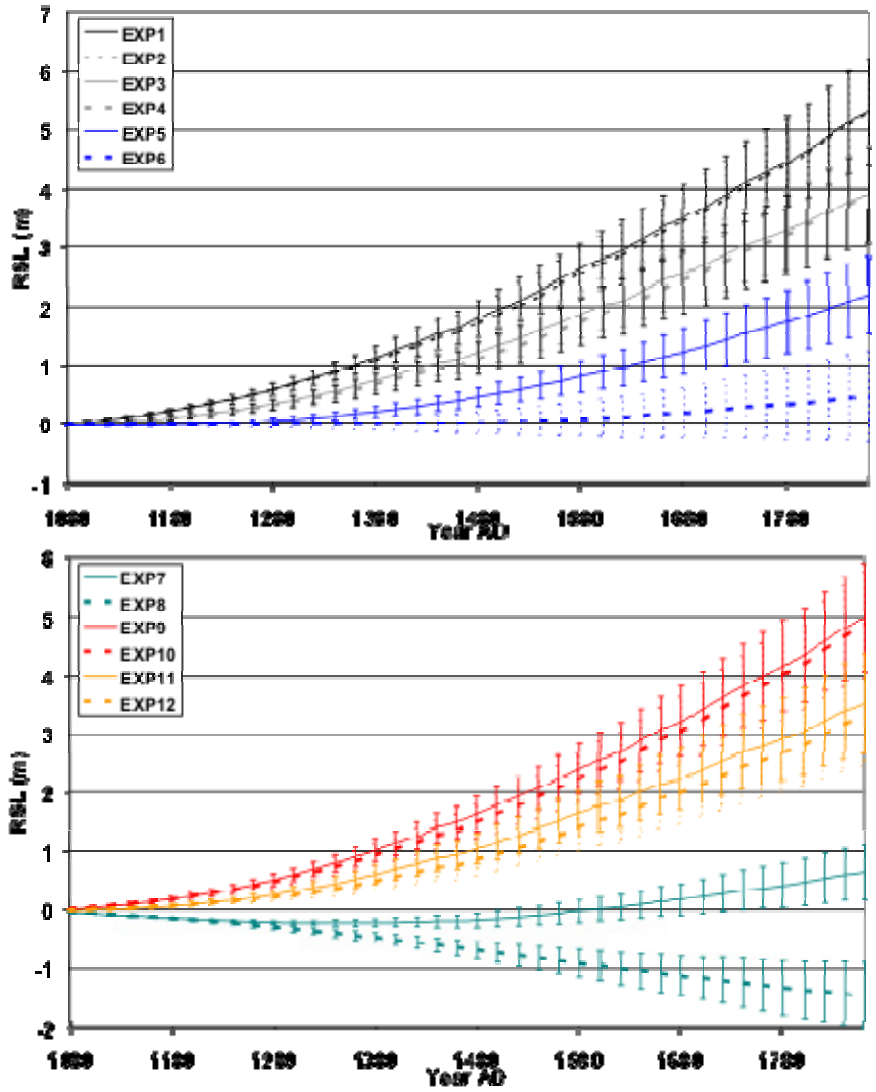

Fig 6.10: Predicted contributions to RSL change in west Greenland. The lines on the graph show the average contribution to sea level at Nag and Aasiaat, with error bars showing the variation between the two sites. The results shown are based on the ice model runs described in Table 6.2. The contributions to RSL change from millennial scale changes in ice loading are not incorporated into the results

The magnitudes of local sea-level rise reflect the contributions to eustatic sea-level change, e.g. EXP1-2 predicted the highest contribution to relative sea-level at Nag and Aasiaat and the highest overall mass balance gain (eustatic sea-level fall). A similar correlation was found in Experiment A, suggesting that the predicted relative sea level in west Greenland mirrors the overall ice-sheet averaged mass balance trend over time, at least in the in the case of this modelling. In all cases, the contribution to RSL rise at Nag is less positive compared to that at Aasiaat (see Table 6.3), which was not found in Experiment A. As discussed above, sea-level rise

is not a viable scenario represented in the salt marsh records, so EXP1-7 and EXP9-12 can be rejected if local sea-level change was dominated by changes in mass balance. EXP8 is the only model which is close to producing the required RSL fall in west Greenland to counteract the millennial scale rise.

RSL rates (mm/yr)	Period 1060-1860				Period 1060-1500AD		Period 1500-1860AD	
Scenario	E	Nag	Aasiaat	Nag-Aasiaat Average	Nag	Aasiaat	Nag	Aasiaat
EXP1	-0.5	5.8	8.5	7.15	3.9	5.3	7.8	11
EXP2	-0.63	5.6	8	6.8	3.6	5.2	8.0	11.2
EXP3	-0.27	4	6.8	5.4	2.6	4.0	5.6	8.6
EXP4	-0.4	3.9	6.1	5	2.1	3.7	5.9	8.9
EXP5	-0.18	2	3.7	2.85	0.9	1.7	3.3	5.9
EXP6	-0.14	-0.38	1.5	0.56	-0.39	0.61	-0.3	2.9
EXP7	0.08	0.3	1.5	0.9	-0.76	0.2	-0.3	4.3
EXP8	0.23	-2.7	-1.2	-1.95	-2.1	-1.3	-3.2	-0.8
EXP9	-0.47	5.3	7.7	6.5	3.5	5.0	7.2	10.6
EXP10	-0.59	5.1	7.4	6.25	3.1	4.5	7.4	10.6
EXP11	-0.23	3.6	5.8	4.7	2.2	3.5	5.0	8.2
EXP12	-0.33	3.2	5.4	4.3	1.5	2.9	5.0	8.2

Table 6.3: Contributions to local (Nag and Aasiaat) and eustatic (E) sea-level change from scenarios in Experiment B.

The dynamic correction provides a significant change in the model set up to enable larger, more sustained areas of ice loss. In the case of winter forcing (EXP5-8), there are significant differences predicted for RSL depending on precipitation and dynamics. These differences evident in the model runs may provide clues to the possible MCO-LIA mass balance at the periphery of the ice sheet, which are the primary driver of sea-level changes. Even though EXPs5-7 may be ruled out, it is therefore important to investigate the development of the loading configurations on the western margin as precipitation is decreased (EXP5 vs. EXP7 and EXP6 vs. EXP8) and ice flow to the margin is reduced (EXP5 vs. EXP6 and EXP7 vs. EXP8). Loading changes associated with these experiments are shown in Fig. 6.11. The loading histories for EXP1-4 and EXP9-12 predict ice gain at the western margin of the Greenland Ice Sheet (which would enhance the local sea-level rise) and so are not shown.

Comparing loading histories when precipitation is varied shows that loading patterns in the west of the ice sheet are similar and predict loss of maximum 250m over 800 years. The central portions of the ice sheet lose more ice as the precipitation is decreased and the dynamics scenario is switched from the 1961-1990

inverted average SMB field to the 1866-1886 field , although this difference does not amount to more than +/- 100m over 800 years.

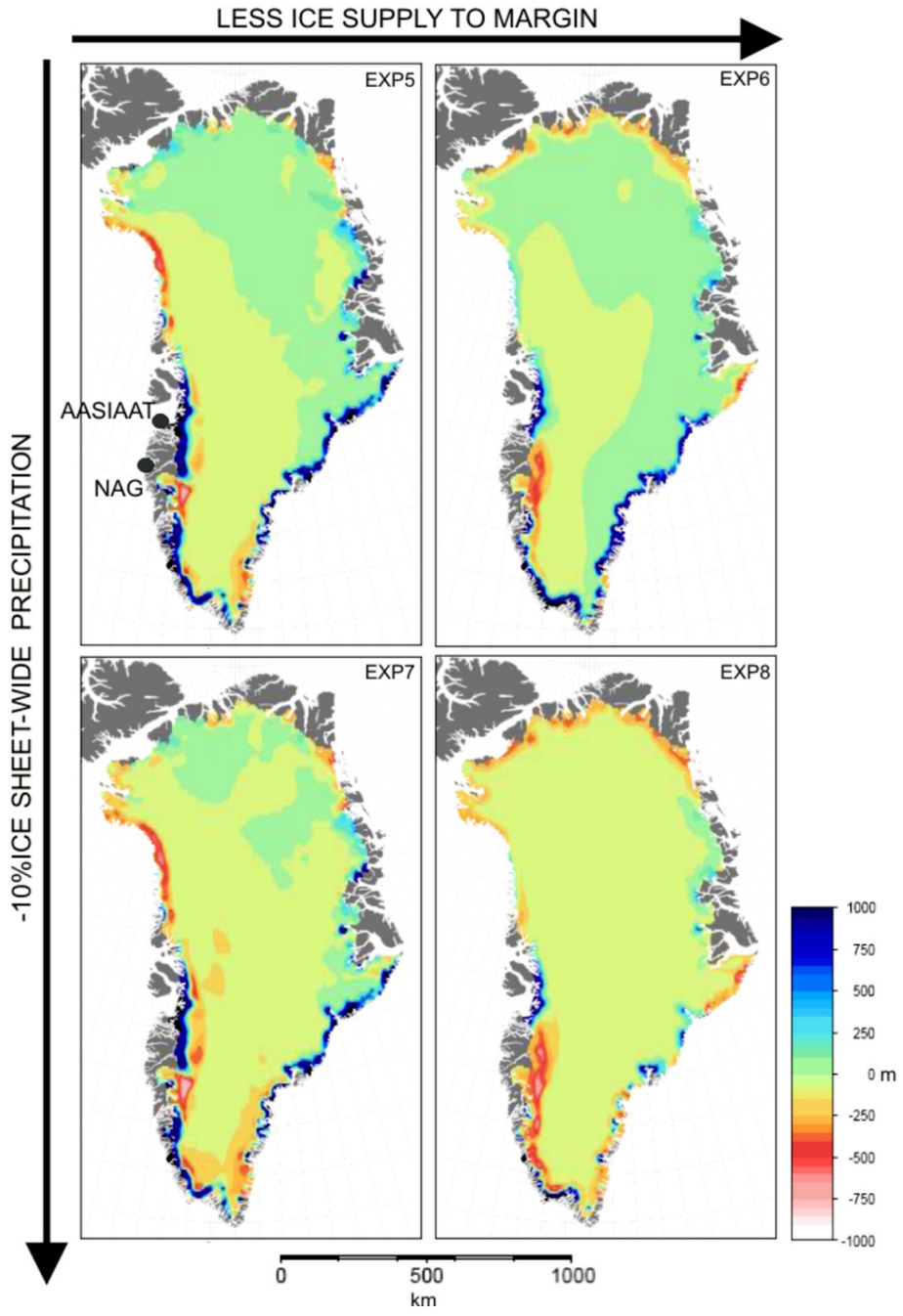

Fig 6.11: Loading changes for the period 1060-1860AD for EXP5-8 in Experiment B. See Table 6.2 for model set-up in these experiments.

The difference in dynamic regime has less of an impact on central loading compared to the western margin of the ice sheet. The key differences between EXP5 and EXP8 are the predicted loading changes at the margin. In a drier climate , the ice dynamics field is able to replenish the increased ablation at the margin (EXP7). This is not the case for EXP8, where significant lowering is predicted to occur. Ice gain around Jakobshavn is predicted because the SMB does not melt enough ice to

counteract the supply from the centre of the ice sheet. Although this is a likely characteristic of cooler conditions, the gain of 1km of ice around the margins is very unlikely since the present day ice thickness 100km east of the margin at Nag is less than 1000m thick.

Loading changes for EXP6 and EXP8 provide insight into the reason behind differing RSL trends predicted at Nag and Aasiaat. The rate of RSL fall at Aasiaat is lower due to the proximity of the site to an area of growth in the Jakobshavn Isbrae area, although it is still affected by the intensification of ice loss from the south. As the intensity of ice loss is gradually modified by decreasing input precipitation and changing the nature of the dynamics, the area of ice loss expands north and southwards. This is an interesting result because it suggests that climate conditions in the west become more favourable for mass loss compared to other areas as the area of negative mass balance propagates north and south.

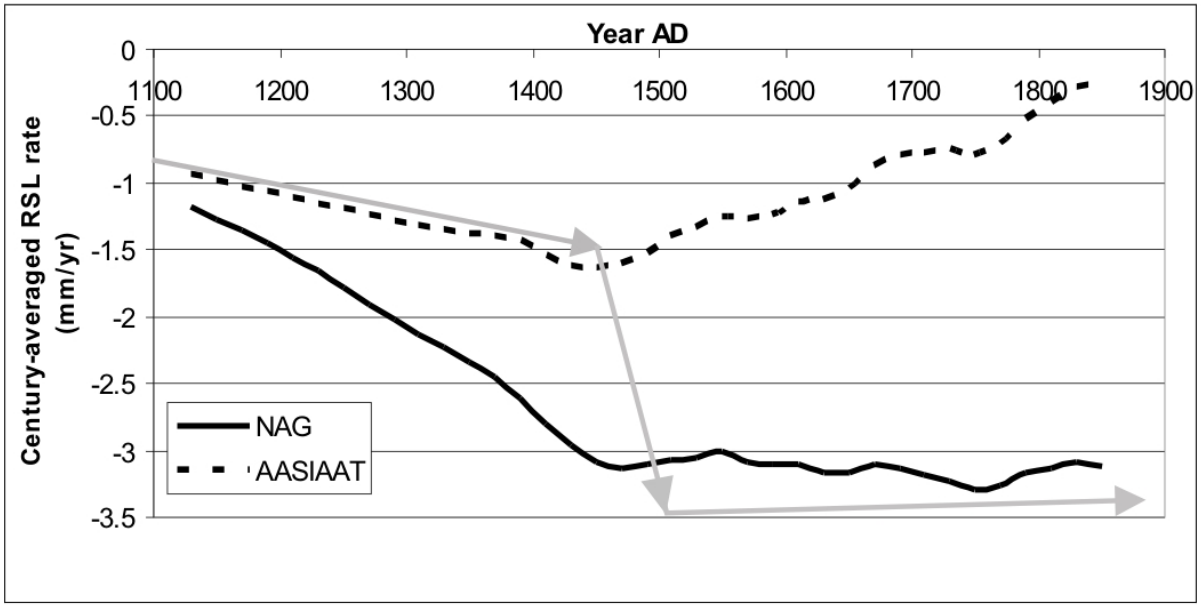

Fig 6.12: Century-averaged RSL change for Nag and Aasiaat sites for climatic conditions described by EXP8. The grey arrows indicate the trend required to overcome millennial-scale RSL rise. The contributions to RSL change from millennial scale changes in ice loading are not incorporated into the results

The change in RSL fall across 1500AD is only -0.3mm/yr (Table 6.3) and inspection of the century-averaged trends at each site (Fig. 6.12) shows that the trend at Nag is fairly stable after 1500AD and does not accelerate. The Nag and Aasiaat sites behave differently in this case, with the signal at Nag more closely representing the required pattern of mass balance related sea-level change. This change of rate at Nag will gradually counteract the millennial-scale contribution from neoglacial regrowth of the western margin of the ice sheet. The Aasiaat site displays

an initial increase in the rate of fall but this starts to decline shortly before 1500AD. The dichotomy of the trends is not compatible with the salt marsh data which rule out a difference of greater than 1.76 mm/yr (see Chapter 4). However, Aasiaat is close to Jakobshavn Isbrae which is not modelled to any degree of realism in this study. The sea-level signature at this site could be significantly influenced by changes in the extent of this glacier (see Section 7.3).

6.3.3 Implications for Modelling SMB and RSL from 1866 to 2005

The modelling carried out thus far has focused on two exclusive time periods: 1866-2005 (Chapter 5) and 1000AD to 1860AD (this chapter). In this subsection, the mass balance and local RSL is calculated for the period 1000-2005 AD by combining these models. Although secondary to the main aims of this chapter, this experiment is carried out to: (i) investigate further the variation introduced to the 1866-2005 SMB model output due to uncertainty in the initial distributions of surface elevation and ice thickness and (ii) consider the influence of 1000-1860 loading changes on RSL predictions during 1866-2005. Note that, in the model runs described in this section, the dynamic correction used over the 1866-2005 period is equivalent to that used in Chapter 5.

Surface elevation and ice thickness grids from the runs generated using n:1961-1990 and n:1866-1886 dynamic corrections in Experiment A are used as initial conditions for the higher resolution 1866-2005 run. These particular surface elevation and ice thickness distributions were chosen as they reproduced the closest approximation to the RSL change required to fit the salt marsh data (Fig. 6.8). EXP8 from Experiment B is also chosen for this same reason. All results are presented in Fig. 6.13

The results show that the interannual variation remains, no matter which elevation distribution is used at the start of the high resolution model run. The original result from Chapter 5 lies outside the range of values bound by the three new time series during the period 1920-1950. This is a consequence of the new results showing a weaker response to increased temperatures in the 1920s and 1930s. The same behaviour is reflected from 1980AD onwards when the ice sheet may react to either temperature or precipitation increase (see Chapter 5, Fig. 5.1). Applying linear regression to the original results from 1980AD shows that mass balance decreases at a rate of -3.3km^3/yr, but this increases to -0.54, -0.29 and -0.79km^3/yr in Experiment A (n=1961-1990), (n=1866-1886) and Experiment B (EXP8) respectively.

Temperature and precipitation forcing remains the same in all experiments, so from 1980AD onwards, the increase in rate indicates higher sensitivity to precipitation forcing and/or lower sensitivity to increased temperatures. Despite these differences, it is encouraging that the original results are fairly well replicated using output surface elevation from Experiment A (1961-1990). The results do not overlap due to each model run being initiated by a different starting elevation, allowing for either a weakened or strengthened response to temperature or precipitation forcing.

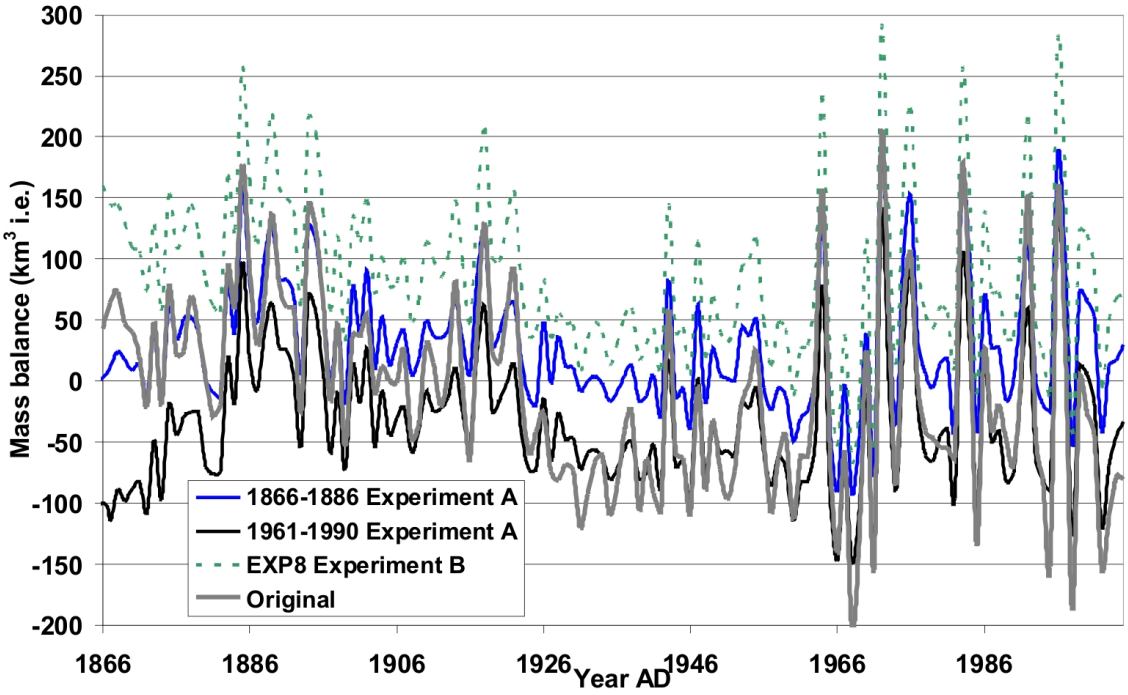

Fig 6.13: Revised mass balance series for 1866-2005 using output from Experiments A and B (see text for details). The original mass balance series (presented in Chapter 5) is shown as the grey line.

When considering the influence of start-up conditions generated from Experiment A, the contribution to eustatic sea-level change over the period 1866-2005 is 0.1mm/yr for the case n:1961-1990 and -0.07mm/yr for n:1866-1886. These values encompass the estimate obtained using the original series (0.03mm/yr), and are not deemed significant contributions as they are not larger than uncertainties on estimates of Greenland-sourced eustatic RSL rise over the period 1961-2004 (Bindoff et al. 2007) . In the case of EXP8 from Experiment B, the mass balance series produced a eustatic sea-level fall of 0.22mm/yr, which is not compatible with observations made over the latter half of the 20th century

Different start-up conditions produce different rates of local RSL change compared to the original series. For n:1961-1990 (black line, Fig. 6.14 Panel A) this decreases to -1.2mm/yr and -2.4mm/yr at Nag and Aasiaat compared to -0.66 and -0.88mm/yr

(Table 6.4). This is directly the result of a lowered surface elevation in west Greenland at the start of the model run, increasing the sensitivity to temperature variation. When the 1866-1886 dynamic correction is used, the local RSL contribution at Nag and Aasiaat over 1866-2005 becomes 0.44 and -1.4mm/yr (Table 6.4). Ideally, the RSL curves should show trends close to 0.0mm/yr, but this is not achieved at either site with any
experiment.

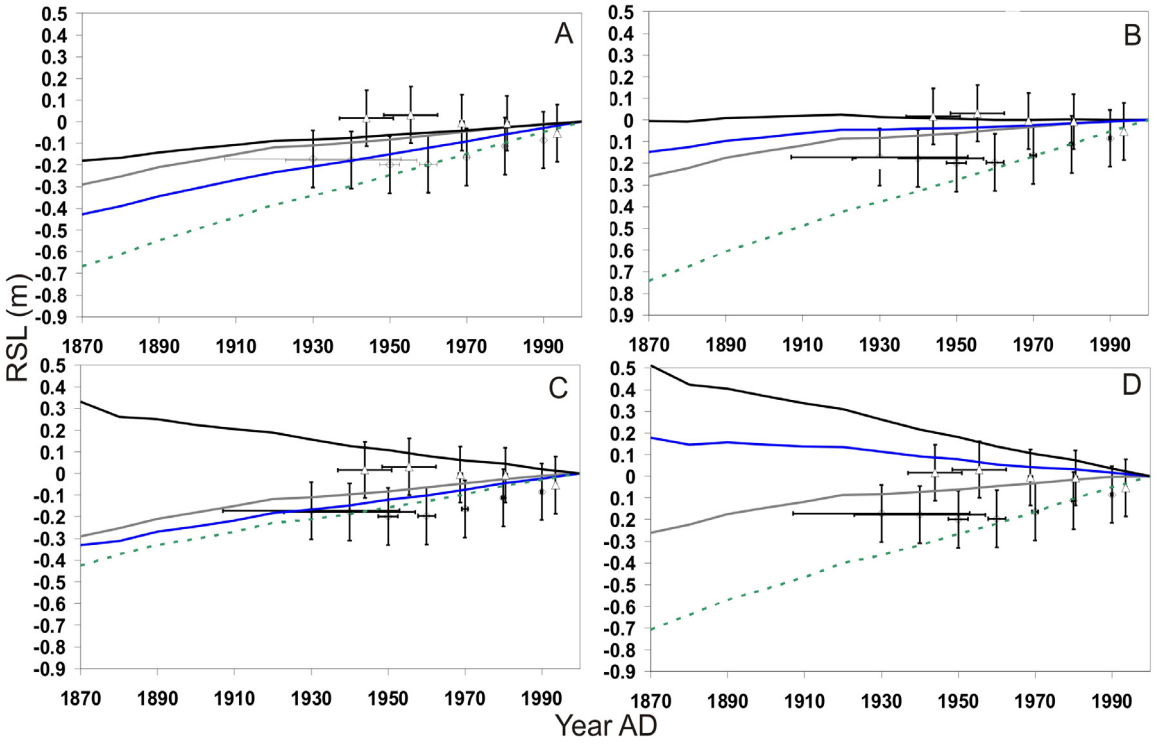

Fig. 6.14: Relative sea level predictions for Nag (A,C) and Aasiaat (B,D) from 1866-2005 using output from Experiment A and B with specific dynamic fields applied over 1020-1860 (blue for n:1866-1886, black for n:1961-1990, green dashed line for EXP8 from Experiment B). Original RSL series from Chapter 5 are shown as a grey line. The results in panels C and D are the same as those in A and B except that they include the influence of loading changes during the spin-up period 1020-1860AD. Salt marsh data points from the Nag data site are also shown in the Aasiaat frames as the signal is believed to be similar at both sites (see Chapter 4). Note that, as in Chapter 4, the late Holocene millennial-scale trends at Nag (2.69mm/yr) and Aasiaat (2.27mm/yr) have been added to the model predictions.

In some of the model runs considered, the predicted loading changes over the period of 1020-1860AD significantly change the contribution to RSL fall over the 1866-2005 period (Fig 6.14 A vs. C and B vs. D; see also Table 6.4, rows 9,10 and 11). The largest signal is found for the case of Experiment A (n:1961-1990; black line), in which the loading during the spin-up period raises the predictions such that sea level is predicted to be above present and continually fall from 1866. There is no evidence for sub aerial exposure in the sediments and so even though this model is compatible with one of the salt marsh data sets (M4-M1), it is not consistent with the

sedimentology and so can be ruled out. The results for the Experiment A (n:1866-1886) scenario are the most compatible with the observations.

Period	1866-2005 (mm/yr)			1020-1500 (mm/yr)			1500-2005 (mm/yr)		
Scenario	E	Nag	Aasiaat	E	Nag	Aasiaat	E	Nag	Aasiaat
Original	0.03	-0.66	-0.88						
1866 start-up									
1866-1886	-0.07	0.44	-1.4						
1961-1990	0.1	-1.2	-2.4						
EXP8	-0.22	2.3	3.2						
Continuation Series									
1866-1886	-0.07	-0.24	-3.8	0.05	-1.2	-1.9	0.9	-1.4	-3.7
1961-1990	0.1	-5	-6.1	0.14	-2.7	-3	0.28	-5.9	-6.2
EXP8	-0.22	0.35	2.8	0.19	-2.04	-1.27	0.1	-2.29	0.18

Table 6.4: Summary of contribution to eustatic (E) and local sea level change from selected analyses from Experiment A and B. Experiments entitled '1886 start-up' refer to the re-run of the mass balance model in Chapter 5 using output from the specified scenarios. The 'Continuation Series' models allow for the ice loading changes prior to 1886 to be accounted for. The rates are calculated contributions to RSL changes, highlighting the ability of each model run to offset the millennial-scale trend.

Using output from EXP8, a significant positive contribution to eustatic sea-level change over the period 1866-2005 is predicted, in contradiction with the original experiment carried out in Chapter 5. When averaging over 1500-2005, there is an overall sea-level fall of 2.29mm/yr at Nag, in the range of values required to offset the millennial scale trend. The transition to high resolution modelling at 1866AD causes the trend at Nag to reverse to a sea-level rise of 0.35mm/yr, indicating that the method of splicing of the two model runs has not been satisfactory in this case.

In Summary, Panels C + D in Fig 6.14 provide most 'correct' treatment of mass balance-related RSL changes, as prior variation in ice loading are shown to have a significant impact on 20th century rates and so must be accounted for.

6.4 Discussion and Conclusions

The work in this Chapter shows that the MCO-LIA transition is not the cause of RSL fall at 1500-1600AD as it is counterintuitive to cause RSL fall under cooler conditions. Immediate ice loss at the beginning of the Little Ice Age, creating an instantaneous sea-level fall coherent with the salt marsh trends is not compatible with climate conditions at 1500AD. In Experiments A and B, the RSL curves over the

period 1080-1860AD show the increasing domination of viscous deformation, and do not show RSL instantaneously reacting to changes in mass balance regime. The viscous contribution from mass loss due to the MCO has the potential to be a major driver forcing sea-level fall through the LIA, although the change is too gradual compared to the observed trend (e.g. see arrows in Fig 6.12).

Since the RSL trends calculated from EXP8 output have been deemed the closest approximation to the required change in trend required to occur at 1500AD, RSL predictions from EXP8 were isolated into the contributions to RSL change arising from viscous (time dependant) and elastic (instantaneous) adjustment of the Earth. The Earth model used had a lithospheric thickness of 120km, an upper mantle viscosity of 0.5 x 10^{21} Pa s and lower mantle viscosity of 1 x 10^{21} Pa s. Prior to 1500AD, the elastic signal is the strongest at both sites, but the viscous signal becomes more dominant thereafter. Between 1500-2005AD, the average rate of RSL fall due to elastic adjustment at Nag decreases compared to the period 1080-1500AD (-0.89mm/yr vs. -0.31mm/yr), and changes sign at Aasiaat (-0.48mm/yr vs. 0.57mm/yr). This reflects directly the decreased mass loss after 1500AD and, in the case of Aasiaat, the local loading predicted around Jakobshavn. The viscous component of sea-level fall at Nag dominates over the elastic component at 480 years after the onset of loading when the rates of sea-level change are -1.22 and -1.12 mm/yr respectively. At Aasiaat, the dominance of the viscous effect occurs earlier (360 years after the onset of loading), due to the closer proximity to the ice sheet margin. Here, the relationship between elastic and viscous changes is more complicated since Aasiaat is close to contrasting patterns of mass balance. In Fig 6.12, the RSL fall slows down around 1420AD, when the ice loss around Jakobshavn Isbrae decelerates and loading is initiated.

Although it is possible to generate a sea-level fall at the RSL data sites from changes in mass balance, there are limitations in the methodology. The major areas for improvement are the treatment of ice dynamics and accurate calculation of starting elevation for model initiation. The method employed in Chapter 5 for iteration of 1866 surface elevation is more accurate than the methodology in this chapter because of the fact that the model could only incorporate a time constant dynamics correction. Stable ice dynamic fields are less likely over time periods of 800 years that span two distinct climatic regimes, so applying a stable field to generate estimates of surface elevation will produce inaccurate predictions of ice thickness change and RSL contribution. Also, the inaccuracies are amplified and propagate through the model run due to the temperature-elevation feedback. One of the

limitations of the dynamics correction method is the SMB-dynamic imbalance as illustrated in EXP5 and 7 (Fig 6.11) where an area of overall ice loss (200-500m) appears behind the area of loading. The likelihood of these loading configurations is low, since this would cause the ice sheet to break up first in the centre, rather than marginal retreat based on elevation and latitude. This is a relic of the dynamics correction used, confirmed by comparing the 1866-1886 to the 1961-1990 field in Fig 6.6. There is a more gradual transition from positive to negative mass balance regimes at the western margin for n:1961-1990 compared to n:1866-1886, translating in a steady change from submergence to emergence velocity. Also, any mass balance differences resulting from error in the elevation correction based on (Simpson et al. 2009) are amplified depending on the dynamic correction applied to calculate annual elevation changes.

If the NAO is prescribed as an annual or summer-only forcing, conditions are not favourable to replicate the observed RSL trends. Forcing winter months only is similar to allowing the model to progress with NAO-modulated precipitation forcing only, since application of temperature anomalies to the winter months has a minor effect on mass balance. In conclusion, of the two forcing methods explored (ice cores and NAO) the ice core forcing technique (Experiment A) was the more successful in that is provides a forcing that can initiate MCO melting to force RSL fall, beginning at the MCO and accelerating through the LIA via viscous adjustment of the solid Earth in response to MCO-induced mass changes. Experiment A is also a more realistic reconstruction since the ice cores provided direct observations of temperature and accumulation conditions. However, a key assumption in applying this method is that temperature anomalies in the ice core records translate to the margins. EXP8 from Experiment B produced a good approximation of the required century-scale RSL trend at NAG, and although there is a clear negative correlation between NAO index and temperature at the margins over the past 42 years (see Fig. 6.3), there is no direct evidence that this relationship held during the LIA and MCO or if it is solely a response to global warming.

Chapter 7: Other Potential Causes of Sea-level Change in West Greenland

7.1 Introduction

Apart from the surface mass balance of the Greenland Ice Sheet considered in Chapter 6, other processes may have contributed to the observed decadal and century-scale changes in sea level. These are investigated in this chapter.

The contribution to changes in sea level arising from density variations in the water column is considered in Section 7.2. Due to low elevation thinning and variations in run-off, the contribution from salinity driven steric change could be important. Salinity changes contribute significantly to sea-level change in the North Atlantic and at high latitudes (Ishii et al., 2006) but observed reduction of salinity in the world's oceans over the past 50 years is only thought to account for 10% of the estimated steric contribution to global mean sea-level rise (Antonov et al., 2002). The steric process was shown to be important in the analysis in Chapter 3, where the effect is dominated by temperature changes, but it is less well understood and quantified at high latitudes.

Drawdown of ice from outlet glaciers in Greenland causes extremely large, localised loading changes (Joughin et al., 2008a, Joughin et al., 2008b) that are not captured by the mass balance modelling studies carried out in Chapter 6. Detailed dynamic modelling of Jakobshavn Isbrae is out of the scope of this project. However, the results of flux-gate measurement studies, radar interferometry surveys and digital photography comparisons may be utilised to map changes in the calving front and grounding line migration and deduce variations in the volume of ice calved. In Section 7.3, studies of calving flux and repeat Airborne Topographic Mapping surveys are utilised to create crude estimates of calving-related ice thinning in the vicinity of Jakobshavn Isbrae. These estimates will be used to investigate whether calving-related drawdown of ice produces a measurable change in relative sea level along the west coast of Greenland and if a significant (observable) differential in relative sea-level change between the Aasiaat and Nag datasites exists because of this process.

Mass balance changes of the Antarctic Ice Sheet and globally distributed mountain glaciers (e.g. Alaska, Patagonia and the Canadian Arctic) have the potential to impact local sea level in west Greenland. The possibility of a significant contribution from non-Greenland ice is considered briefly in Section 7.4

7.2 Modelling of Steric Changes in Sea Level

The analysis is made up of two parts; (1) utilising available temperature and salinity data from west Greenland to calculate trends in dynamic height during the 20th and 21st centuries to assess the contribution of steric changes to sea level in this region (Sections 7.2.1 and 7.2.2), and (2) perturbing temperature and salinity profiles representative of 20th century conditions to investigate the changes needed to replicate the observed 1500-1600 AD slowdown in relative sea-level rise (Section 7.2.3). Comprehensive temperature- and salinity-depth observations are not available for the time period spanning the LIA and so performing a sensitivity analysis is the only viable option to determine if steric changes could have made a significant contribution to the observed RSL signal. As described below, this is done by perturbing distinct water bodies such as the West Greenland Current (WGC) and Polar Water (Lloyd, 2006a) with temperature and salinity anomalies. These perturbations are assumed to occur over the period 1600 until present, and the trend is RSL is calculated for each scenario.

7.2.1 Data Selection and Average Temperature and Salinity Profiles

Temperature and salinity profiles were downloaded from the online 2005 World Oceanographic Database (WOD05, Boyer et al., 2005). The data take the form of conductivity-temperature-depth profiles, ocean station data and profiling floats. These raw data types have been analysed and published as a dataset interpolated to 0.5 x 0.5 degree grid points and at 33 standard depth levels ranging from 0 to 3000m. This interpolated dataset is known as the World Ocean Atlas (WOA, Locarnini et al., 2006). In this study, raw oceanographic profiles from the WOD are used in preference to WOA data in order to reduce any bias that may have been introduced during the interpolation process (Miller and Douglas, 2004).

The first step is to generate temperature and salinity profiles characteristic of the ocean near the sites of data collection. Some profiles with observations dating back to the 1920s are available, but are sparse in both space and time. Typically, the depths at which data were collected vary from study to study. The selected data were located on the continental shelf, in waters no deeper than 600m. Some individual profiles were not consistent on an annual basis in terms of sampling depths, type of instrument used and location. In order to produce an average profile for each 2x2 degree area that is typical of the oceanographic conditions at each site, a tolerance

was adopted when assigning temperature and salinity at standard depth levels. The tolerance adopted was 2 m for the top 20 m, 5 m for the depth range 20-75 m and 15 m for the range 75-500 m. As an example, for depth levels between 0 and 20m, the temperature and salinity values assigned to the standard depth levels of 0, 10 and 20m are correct to within 2m. Data at specific depth levels that did not have paired temperature and salinity values were omitted. The average profiles are presented in Fig. 7.1.

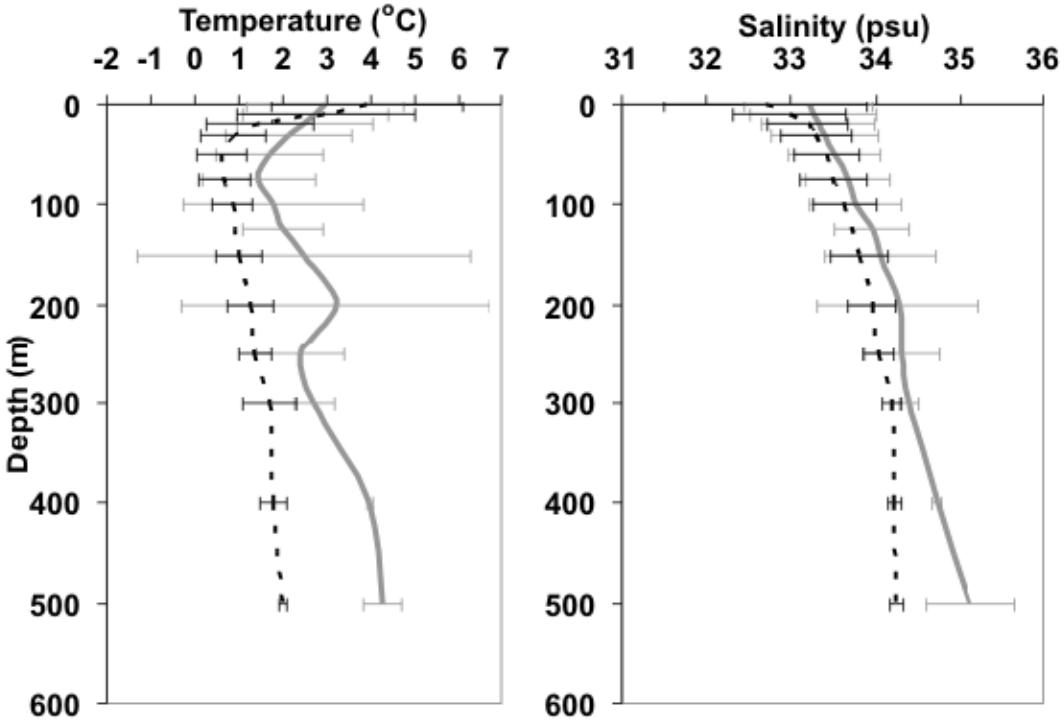

Fig. 7.1: Average temperature and salinity profiles for the ocean water adjacent to Nag (solid line) and Aasiaat (dashed line). Error bars indicate the standard deviation of measurements due to both temporal and spatial (1x1 degree area) variability.

The mean and standard deviation of temperature and salinity for each depth level are calculated using the maximum possible amount of profiles that pass the criteria tests specified above. Below 500m-600m, datasets are sparse. The continental shelf in west Greenland extends for ~100km from the coast at the Nag site where the water depth remains between 200 and 400m. In Disko Bay, north of the Aasiaat data collection site, the water depth remains shallower than 500m, apart from a narrow trough of ~ 800m depth extending from the mouth of Jakobshavn Isbrae. The surface layers are the freshest part of the water column, with salinity typically less than 34 psu. (Practical Salinity Units: 34 psu = 34g of salt per 1000g of water) In general, salinity increases with depth, with an increase noted deeper than 300m at Nag. Although the variation of salinity (typically ±1 psu at the 1σ level) tends to decline with depth this is most likely an artefact of limited numbers of data

points at depths below 500m. At the Aasiaat site, the upper 30-50m of water is influenced by discharge from Jakobshavn Isbrae and this is reflected in the lower salinity compared to Nag.

The main stratification differences between the sites occur in the temperature profiles, with a larger variation at Nag compared to Aasiaat. At Aasiaat there is a steep thermocline in the upper 50m of the water column. Upper waters are generally warmer due to solar heating, but the incursion of Polar Water (Lloyd, 2006a) or Arctic Water (Tang et al., 2009) at depths between 50m and 300m (Lloyd, 2006a) reduces the temperature between these levels. This is not clear in the profiles presented in Fig. 7.1, but is a prevalent feature in the Disko Bay profiles presented in Lloyd (2006b). At depths greater than 200-300m the temperature increases by ~ 2^{o}C at Nag and less than 1^{o}C at Aasiaat. The larger deep-water thermocline at Nag is due to the northward movement of the WGC. This is characterised by warm (2-4^{o}C), saline (> 34 psu) conditions. The influence of this current is less apparent in the Aasiaat profile (Fig. 7.1), due to the dominating influence of cooler, fresher waters originating from Jakobshavn Isbrae. Again, the calculation is dependant on the number of profiles included, but the reduced variation at Aasiaat is likely due to the proximity to Jakobshavn Isbrae, i.e. the suppressive effect that continuous ice discharge will have on surface temperatures and subsequent mixing. The Nag datasite is more susceptible to open ocean influences which result in the higher temperature variation at depth.

7.2.2 Trends in Steric Height

In this analysis, the effects of changing salinity and temperature on the steric height of the sea surface offshore west Greenland are considered. Steric height is calculated by integrating over depth the density (and therefore specific volume) changes in the water column due to temperature and salinity perturbations. Specific volume (υ) is defined as the reciprocal of density of sea water at temperature (T) and salinity (S) and pressure (p). The standard for the specific volume anomaly (δ) is defined as;

$$\delta = \upsilon(S,T,p) - \upsilon(35,0,p) \qquad \text{E7.1}$$

(from Fofonoff and Millard, 1983, Fortran program provided by S Holgate, *pers. comm.*) At all depths in the water column, the specific volume of sea water is

calculated relative to the specific volume occupied by sea water of salinity 35 psu and temperature 0°C at the same pressure (i.e. depth) in the water column. The calculations are restricted to a specific depth interval, assuming a level of no motion below this level (i.e. no variation of δ). The steric height calculated reflects the expansion or contraction experienced by a column of water relative to the standard conditions as specified in E7.1. As in the analysis presented in Chapter 3, Section 3.4, raw datasets are preferred to interpolated grids from the World Oceanographic Atlas. Use of the interpolated datasets can produce significant errors in steric height as shown by Miller and Douglas (2004). Profiles that met the criteria stated in Section 7.2.1 were used to produce time series of dynamic height adjacent to the Nag and Aasiaat sites (Fig. 7.2). Steric height anomalies were calculated for four specific depth ranges (0-50m, 0-150m, 0-300m and 0-500m) in the water column. These levels were chosen to reflect approximate depths of transition between specific water bodies (Polar Water ~ 50m to 300m; WGC ~ below 300m) and sharp changes in the thermocline (upper 50m).

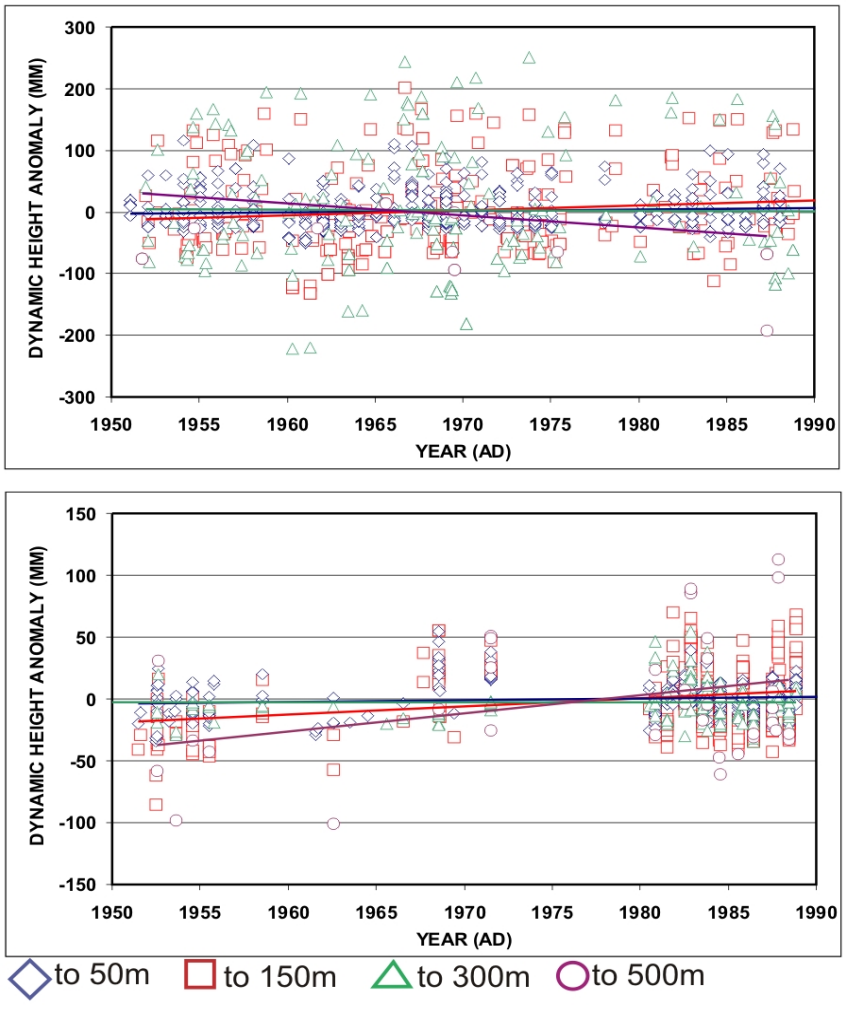

Fig.7.2: Trends in steric sea surface height at the Nag (top panel) and Aasiaat (bottom panel) sites calculated with reference to specific depth levels.

A standout characteristic of the data is the significant (tens of centimetres) variation in the calculated anomalies at each depth level and the lack of apparent trend in the data. The trends and associated confidence intervals for each calculation are shown in Table 7.1

Interval (m)	Site / N (data)	Trend *	Upper * 95%	Lower * 95%
0-50	Nag (516)	0.23	0.47	-0.02
	Aasiaat (331)	0.12	0.24	0.01
0-150	Nag (253)	0.81	1.67	-0.05
	Aasiaat (256)	0.66	0.97	0.34
0-300	Nag (165)	-0.09	1.49	-1.67
	Aasiaat (125)	0.99	1.66	0.31
0-500	Nag (17)	-1.00	6.10	-8.11
	Aasiaat (35)	1.45	2.96	-0.05

Table 7.1: Steric height trends calculated over 4 depth intervals at Nag and Aasiaat, with 2σ errors. (*Values are in mm/yr.)

For steric height variations calculated to a reference level of 50m, linear regression performed on the series shows a trend in dynamic height at Nag and Aasiaat of 0.23± 0.24mm/yr and 0.12± 0.12mm/yr (2σ uncertainty), respectively. Although there is a lot of scatter in the data, the trends are significantly different from zero, indicating a small sea-level rise due to changes in the upper 50m at both sites. Integrating over the upper 150m produces similar results at both sites, indicating that the temporal changes in ocean stratification in this depth range are the same at both sites. Integrating to 300m depth introduces changes to the trends calculated at both sites. The sea-level rise predicted for the NAG site switches to a sea-level fall, indicating the increasing influence of the warm, high salinity West Greenland Current. Conversely, at Aasiaat, the trend continues to show a sea-level rise. This may indicate an important difference in oceanographic regime between the two sites. Integration over the entire depth interval of 500m shows opposing trends at both sites of -1.00mm/yr and 1.45mm/yr.

Statistical analyses performed on the datasets confirm that they do not provide any useful constraints on steric height trends over the past 50 years. At depths greater than 500m, although the calculated trends are opposing in sign, the range of the 95% confidence intervals indicates that the difference is statistically insignificant. As well as the gaps in the time series (e.g. around 1975-1980), the data are restricted as they only provide an insight into summer trends. At the Nag data site, temperature and salinity profiles collected in June, July and August make up 30-

50% of the profiles used in the linear regression. Further analysis on the data at Nag shows that steric height follows an annual sinusoidal variation with maximum steric height being recorded in August-September. It is not clear if a similar signal occurs at Aasiaat due to a high concentration of data being collected in the summer months when the area is more accessible.

Summing to specified depth levels gives insight into the contribution to steric height from each water body. The trends that are presented above highlight the importance of integrating over the largest allowable depth range, as a considerable component of the signal is driven by changes at depth. The large change in steric trend when summing over 300m and 500m is likely due to data gaps over time at this depth level as well as a change in oceanographic regime. The increase of steric height in the upper 50m suggests that warming and/or freshening has occurred over the past 50 years which is likely to reflect changes in runoff from the ice sheet.

7.2.3 Exploring the Sensitivity of Steric Height to Imposed Changes in Temperature and Salinity

In this part of the analysis, the average temperature and salinity profiles at Nag and Aasiaat were perturbed by temperature and salinity anomalies in order to investigate the effects of prolonged variation in these parameters on steric height. The temperature and salinity variations were applied over specific depth ranges which are given in each example. The average temperature and salinity profiles calculated from contemporary data (Fig. 7.1) are assumed to be representative of conditions at 1500- 1600 AD in light of the lack of data available for this period. In all cases, steric height is calculated by integrating to a depth of 500m. Temperature and salinity anomalies are added or subtracted to the layers specified in Fig. 7.1 to vary the characteristics of the water column. The temperature and salinity anomalies are applied linearly over time, with the total accrued anomaly assumed to occur over a 400 year period in order to represent gradual change occurring from 1600 AD to present.

In the first set of scenarios (Fig. 7.3), the ‘upper’ and ‘lower’ sections of the water column (above and below 200m respectively) are perturbed the same way (i.e. the perturbations show are for the entire 500 m water column). This first sensitivity analysis serves mainly to illustrate the effects on steric height of a wide combination of temperature and salinity variations applied uniformly with depth. The sensitivity analysis presented in Fig 7.3 was carried out using individual average profiles for

both sites as well as a single average profile for the two sites combined. The difference in the predicted trend for dynamic height using these approaches was 0.1mm/yr or less and so the more straightforward approach of using a single average profile by combining data from both sites will be followed for the remainder of this sensitivity analysis.

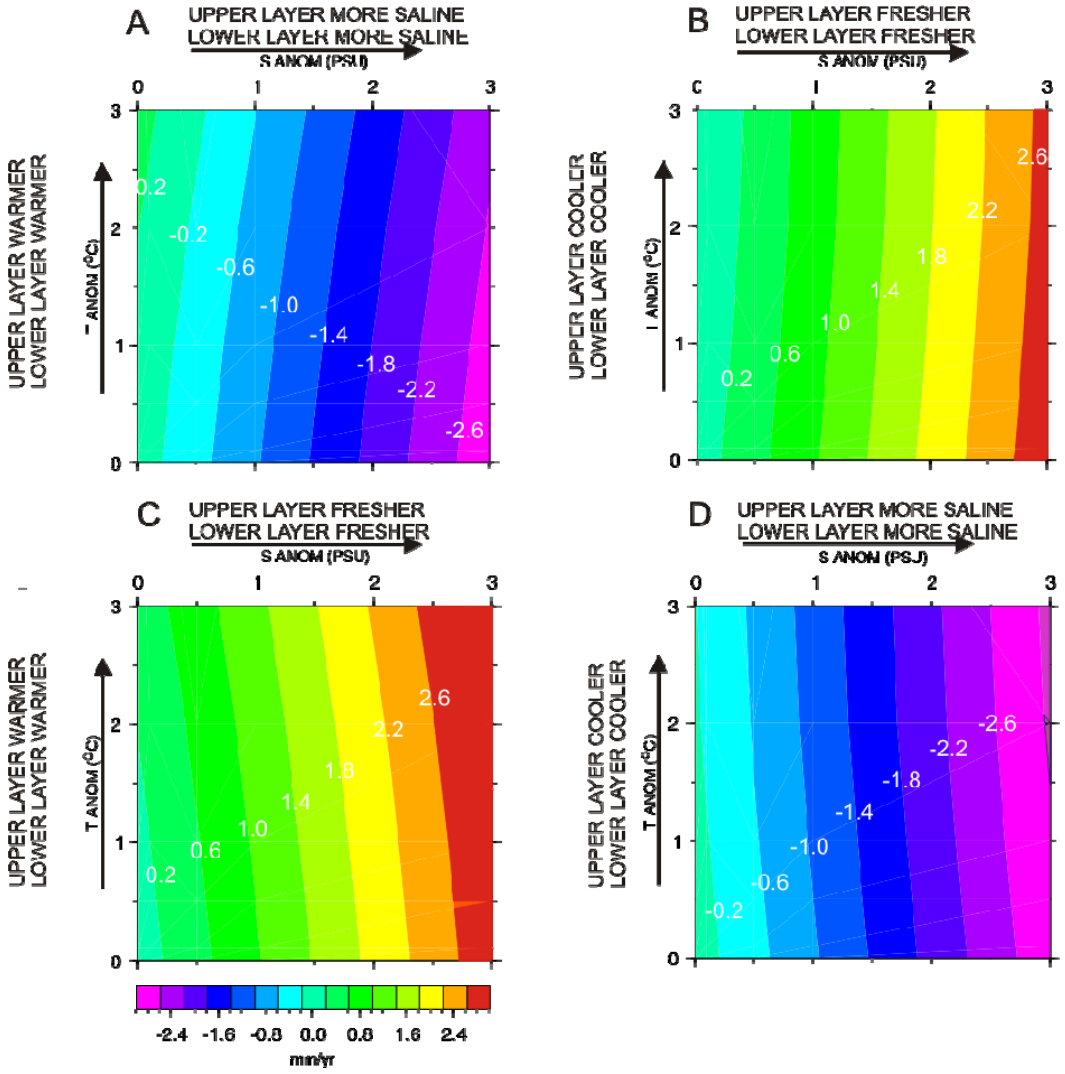

Fig. 7.3: Predicted trends in steric height (mm/yr) using an average combined temperature and salinity profile perturbed by a combination of anomalies.

A large range of trends can be predicted depending on the combination of anomalies used. The curvature of the contours in Fig. 7.3 shows that there is a linear dependence with salinity and a non-linear dependence with temperature. It is clear that changes in salinity exert the strongest control on steric height as the trends vary by > 2.6mm/yr over the 0-3psu anomaly range. However, note that a secular change of +1psu and over depth extent is highly unlikely (see Section 7.2.4). In such a situation, depending on which temperature scenario is adopted, the maximum rate of

steric sea-level change that can be achieved is in the range of -1.0 and +1.2mm/yr assuming the temperature and salinity anomalies have been reached after 400 years.

Some scenarios in Fig. 7.3 are more realistic than others. Scenarios A and B in Fig. 7.3 are the most physically viable given the proximity of land ice, but such temperature and salinity variations are unlikely to occur in a uniform manner over such a large depth range and time span. More saline conditions are required to force a significant negative contribution from steric sea-level change. If salinity remains fixed, the maximum possible contribution to sea-level fall is 0.2mm/yr (Fig. 7.3A). Assuming the salinity of the layers increases by at least 1 psu in scenario A, with minimum increase in temperature, the contribution to sea-level change becomes -0.8mm/yr. Scenario B recreates oceanographic conditions that may occur due to increased freshwater runoff and/or increased iceberg production. Realistically, if this situation is representative of LIA conditions, the contribution to sea-level change would be less than 1mm/yr. In this case, steric variation contributes positively towards post 1600 RSL change and so a fall of > 3mm/yr is required from other sources, such as ice mass changes.

For a fixed salinity increase of 1psu, a significant temperature anomaly of 3^{o}C would only slightly offset the sea-level fall from increased salinity by 0.4mm/yr (Panel A, Fig. 7.3). The scenarios indicate that a given steric signal can be produced in a number of ways. For instance, a steric sea-level change of +0.2mm/yr may be explained by a temperature anomaly (+2.2-3^{o}C) occurring in conjunction with a small change in salinity (+0 to +0.02psu) (e.g. Fig. 7.3 A, top left of plot). Similarly, a steric change of +0.2mm/yr may be recorded under cooler (0 to -3^{o}C), fresher (+0.025 to +0.04psu) conditions (Fig. 7.3 B).

Examples in Fig. 7.4 highlight how opposing temperature and salinity trends at different depth levels can affect changes in steric height. The range in dynamic height variations in both examples in Fig. 7.4 (Panel A: -0.05-0.35mm/yr and Panel B: (-0.3 – 0.25mm/yr) is greatly reduced compared to the scenarios considered in Fig. 7.3 (A-D). In panels 7.3A and B, conditions are intentionally prescribed to create opposing trends at each depth interval (e.g. warmer (positive steric trend) vs. more saline conditions (negative steric trend)). In Panel B, the conditions prescribed to each layer were reversed. Opposing trends in dynamic heights are recorded, and the effects do not balance each other.

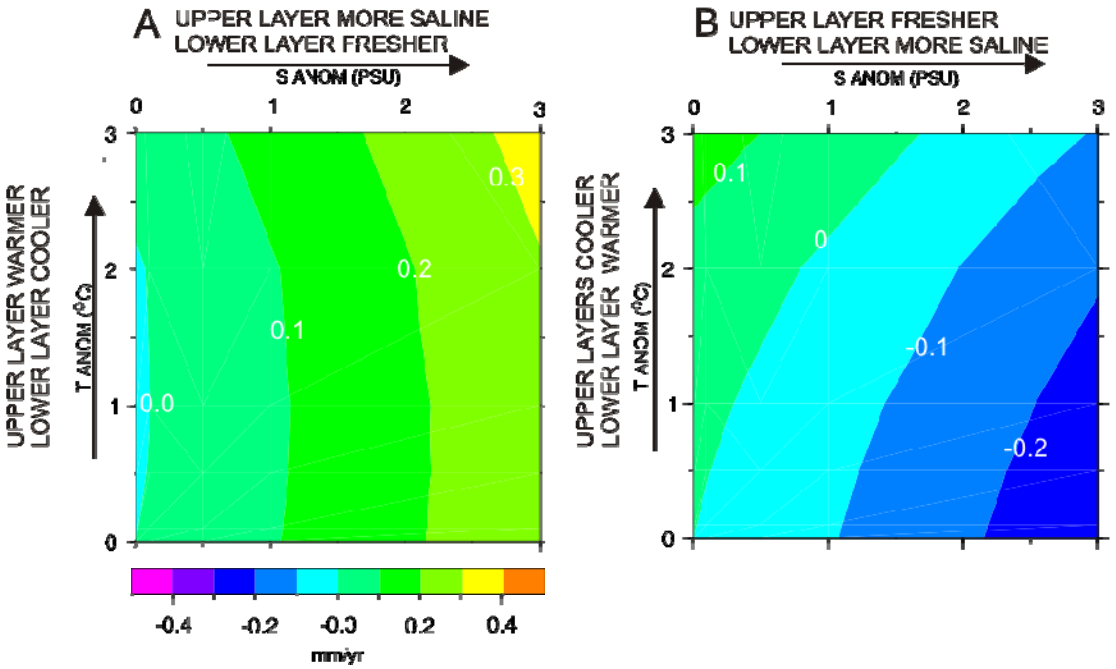

Fig.7.4 Predicted trends in steric height (mm/yr) using an average combined temperature and salinity profile perturbed by a combination of anomalies reflecting opposing trends in temperature and salinity in upper and lower depth levels

In Panel A, mainly positive trends are recorded for all combinations of temperature and salinity variations, except for when salinity is fixed and temperature anomalies of magnitude 0 to 2°C are applied, where the rate of change is slightly negative. Increasing the magnitude of the temperature anomaly above 2°C causes a maximum positive contribution of +0.05mm/yr. The change in sign at zero salinity anomaly is recording when the warming of the upper layers becomes significant enough to oppose the negative steric trend caused by cooling of the lower layers. Panel B confirms that salinity anomalies applied at depth are the dominating factor controlling steric trends. For a fixed temperature profile (i.e. no anomaly at any level) the salinification of the lower layers dominates the steric trend, contributing 0 to -0.28mm/yr. The oceanographic scenario considered in panel B is one of the more realistic due to the proximity of the data sites to Jakobshavn Isbrae. Even so, both salinity and temperature would have to display a sustained variation of magnitude 3psu and 3°C respectively over 400 years to make any impact on sea-level change for this particular configuration of ocean stratigraphy.

In the final part of this analysis, scenarios to represent mixing of the water column and increasing influence of the WGC in the upper layer are considered (Fig. 7.5). In order to increase the influence of the WGC, salinity was increased over the depth interval of 400-500m (Fig. 7.5, panel A) and then over the interval 100-500m,

Fig. 7.5 panel B). Choices for this range of depths for the WGC were based on Lloyd (2006a).

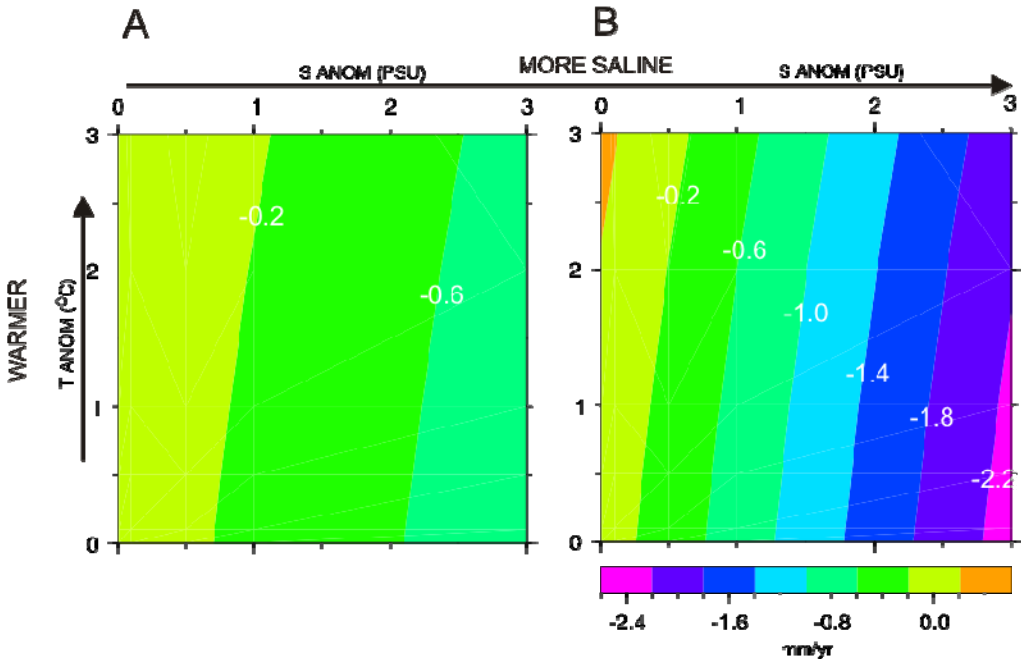

Fig. 7.5: Changes in steric height as a function of temperature and salinity anomalies applied to the depth interval of 400-500m (Panel A) and 100-500m (Panel B)

As expected, increasing the influence of the WGC in the upper layers causes an overall reduction in steric height. With small increases in temperature (less than 1°C), and moderate increases in salinity (1 psu), this becomes a mechanism to contribute significantly (-0.8mm/ yr) to the observed sea-level fall (Fig. 7.5, panel B). For a fixed salinity anomaly, the temperature influence on steric height change is -0.13 mm/yr per °C for increasing temperatures. For salinity, the steric height is reduced at a rate of 0.73mm/yr per psu at a fixed temperature anomaly. In Panel A this relationship is weaker (0.03mm/yr per °C and -0.26mm/yr per psu) due to the anomaly only being applied to the deepest part of the column.

7.2.4 Discussion and Conclusions

To wholly account for the ~ 3mm/yr sea-level fall, the salinity of the water column must have increased by at least 3psu at all levels, which is highly unlikely. The limited data from near the RSL data sites indicate that salinity changes have been restricted to ~ 1psu and with limited depth extent over the latter half of the 20th century (Section 7.2.1). The analysis shown above indicates that the addition of temperature and salinity anomalies at depth forces the largest changes in steric height

All the cases in this chapter are calculated with a sustained temperature and salinity change, with the total anomaly accrued over 400 years. However, present day salinity data suggest that salinity is unlikely to show a net increase or decrease of ~1psu over 400 years and that these variations are more likely to occur on an interannual basis rather than over a sustained period of time. For example salinity variations of 0.26psu/yr occurring over 3 years in the early seventies have been recorded in the upper 10 metres of the North Atlantic (Schmitt, 1996), but do not translate at depth, where salinity is fairly stable over the same time period. Over longer time periods, a modelling study by Sedlacek (2008), demonstrated that the maximum difference between the average salinity at high latitudes between 1500-1850 and 1850-2000 at any depth level was no larger than 0.1psu. Other evidence to argue against a major contribution from steric changes is found in a study by Levine and Bigg (2008), who demonstrated that major climatic variations such as Heinrich events are unlikely to cause significant long-lasting changes in salinity.

There are a number of limitations in the data which impact the accuracy of the steric sea-level change estimated in Section 7.2.2. Firstly, the data do not represent true annual dynamic heights since the bulk of the data are collected in the July months, with peak heights recorded in late summer and early autumn. Processing of the data suggests that this annual variation occurs throughout the water column (to 500m depth) at Nag. The same pattern is hard to determine at Aasiaat due to lack of data, which is another problem in this area. A more universal problem with calculating steric changes is the horizontal contraction/expansion of water which is a difficult process to quantify and will force an additional sea-level fall/rise at the coast.

To conclude, whilst variations in temperature and salinity can produce the desired sea-level fall, the oceanographic regime must undergo dramatic and secular changes for steric variation in sea level to account for the required 3mm/yr sea-level fall. After considering a more plausible temperature and salinity anomalies, steric variation is only able to account for at most 25% of the required fall. In a study by Lloyd (2006b) it is shown that oceanographic conditions from the onset of the Little Ice Age caused cooling of the WGC, and increased melt water flux due to advance of Jakobshavn Isbrae. It is plausible to liken the post 1476AD situation to that in Fig. 7.3 (Panel B). Assuming a positive salinity anomaly of 0.1psu occurs at any depth interval (in line with the estimates of Levine and Bigg, 2008), this situation suggests that even with a significant ($3^{o}C$) cooling, the maximum attainable sea-level change is positive and still lies within the error of the rates calculated from the proxy sea-level data.

7.3 The Sensitivity of Sea-level Predictions to Mass Changes associated with Discharge from Jakobshavn Isbrae

7.3.1 Introduction

In recent years, Jakobshavn Isbrae (JI) is estimated to have been discharging up to 50km^3 of ice per year (Joughin et al., 2004); an increase from 26.5km^3 of ice per year in 1986. Overall the glaciers in Greenland have been retreating over the period 1992-2006 but some south-east Greenland glaciers have advanced between 0.1 and 0.5km/yr since 2006 (Moon and Joughin, 2008). Jakobshavn is the most extensively monitored glacier in Greenland and has been showing overall long-term retreat since 1850 when the terminus was located approximately 40km west of its present position (Csatho et al., 2008). Jakobshavn is thought to drain ~ 7% of the ice sheet, with the largest ice thickness changes (> 10m/yr) occurring within 5-10km of the calving front for the years 1998-2007 (Joughin et al., 2008). Krabill et al. (2004) use ATM mapping to track surface elevation changes from 1993/94 to 1998/99 and show a clear area of negative surface elevation change extending eastward of JI into the drainage area. Surface elevation changes in the range of -0.6 to -0.02m/yr are observed. In both studies, ice loss increases significantly near the mouth of Jakobshavn. Calving rate is defined as the difference between the average velocity through a vertical column of ice ($\overline{U_t}$) and the change of glacier length (dL) over a given time period (dt). Calving rate increases due to increased velocity and/or enhanced retreat (-dL) (Benn et al., 2007):

$$U_c = \overline{U_t} - \frac{dL}{dt} \qquad \text{E7.2}$$

Retreat and advance of glaciers, along with surface velocity measurements have been measured directly over the past 10-15 years using remote monitoring techniques. Terminal and lateral moraines that record periods of advance and thinning respectively are found in the JI area, but corresponding historical estimates of velocity cannot be obtained. Also, re-advance of the glacier can destroy older moraines, so a complete history of glacier extent cannot be reliably estimated.

7.3.2 Methodology and Results

In this section, the ice sheet is assumed to be in balance with the contribution from JI the only source of relative sea-level change in the area. The ice discharged

from JI is assumed to have been sourced from an area immediately to the east of the calving front. The sensitivity of the local sea-level fingerprint to changes in the source area for the calving-related ice thickness changes is investigated. Scenarios are considered in which the ice discharge is kept fixed at 50km^3/yr but the source area is varied in spatial extent. The discharge value of 50km^3/yr is chosen to reflect the upper range of estimates for JI over the past decade; therefore the resulting sea-level fingerprints may be seen as providing maximum, end member values due to this process. Table 7.2 defines how the assumed volume change is distributed over the area east of the present day terminus. Note that the sea-level predictions shown in Fig. 7.6 can be linearly scaled to show the fingerprint associated with lower discharge rates.

The sea-level fingerprints associated with the scenarios defined in Table 7.2 are shown in Fig. 7.6. Each scenario represents the predicted fingerprint (mm/yr) arising from a local volume change of 50km^3/yr, with the ice thickness changes arranged as prescribed in Table 7.2. The one feature common to all scenarios is the predicted differential in sea-level change between the two data sites. The rate of RSL fall at Aasiaat is predicted to be approximately twice that at Nag.

Scenarios 1-3 show the effect of increasing the size of the source area of the discharge (0.38-1.89% of total GrIS area). Scenario 1 can be ruled out as the predicted sea-level rates are far larger (-12mm/yr at Aasiaat, -6.2mm/yr at Nag) than those recorded in the salt marsh datasets. For a reduced discharge of 25km^3/yr, which is representative of calving over the period of 1985-2000 (Rignot and Kanagaratnam, 2006; Joughin et al., 2004), prior to the speed-up recorded in recent years, the predicted sea-level fingerprint is exactly half that shown in all plots. Even when applying a 50% reduction in calving rate for Scenario 1, the site-differential sea-level fingerprint is still too large, at a magnitude of ~3mm/yr.

Spreading the 50km^3 volume loss over a larger area results in a reduced sea-level fingerprint (Scenarios 2 and 3). Reduced spatial differentials of 2.5mm/yr and 1.5mm/yr are predicted for Scenarios 2 and 3 respectively, but these are still larger than or close to the range of error associated with the sea-level trends calculated from the salt marsh datasets at Nag and Aasiaat. As there are few sea-level index points covering the period from 1800AD until the early 20th century, the error in the post 1600AD sea-level trend is relatively large (1.76mm/yr, see Fig 4.5) compared to that for the earlier part of the record (0.5-0.6mm/yr)

Scenario	Discharge (km^3/yr)		Area Coordinates	dl per grid point(m/yr)	Area (km^2)	% ice sheet
1		**50**	**68.5-69.5°N, 50-48.5W**	**-7.4**	**6667**	**0.38**
2		**50**	**68.25-69.75°N, 50-47W**	**-2.5**	**19950**	**1.14**
3		**50**	**68.25-69.75°N, 50-45W**	**-1.5**	**33210**	**1.89**
4	30		69.75-68.25°N, 50-48.5W	-3.3	9926	
	15		69.75-68.25°N, 48.5-46.5W	-1.1	13308	
	5		69.75-68.25°N, 46.5-42.5W	-0.18	33210	
Total		**50**			**56444**	**3.21**
5	30		69.75-68.25°N, 50-48.5W	-3	9926	
	10		69.75-68.25°N, 48.5-46.5W	-0.73	13308	
	10		69.75-68.25°N, 46.5-42.5W	-0.36	33210	
Total		**50**			**56444**	**3.21**
6		**50**	**67.5-70.5.N, 50-40.5W**	**-0.41**	**121305**	**6.9**
7	30		67.5-70.5N, 50-47W	-0.86	34509	
	15		67.5-70.5N,47-44W	-0.38	39226	
	5		67.5-70.5N, 44-40.5W	-0.11	47570	
Total		**50**			**121305**	**6.9**
8	20		67.5-70.5N, 50-47W	-0.57	34509	
	20		67.5-70.5N,47-44W	-0.51	39226	
	10		67.5-70.5N, 44-40.5W	-0.21	47570	
		50			**121305**	**6.9**
9	20		67.5-70.5N, 50-47W	-0.57	34509	
	15		67.5-70.5N,47-44W	-0.38	39226	
	15		67.5-70.5N, 44-40.5W	-0.31	47570	
Total		**50**			**121305**	**6.9**

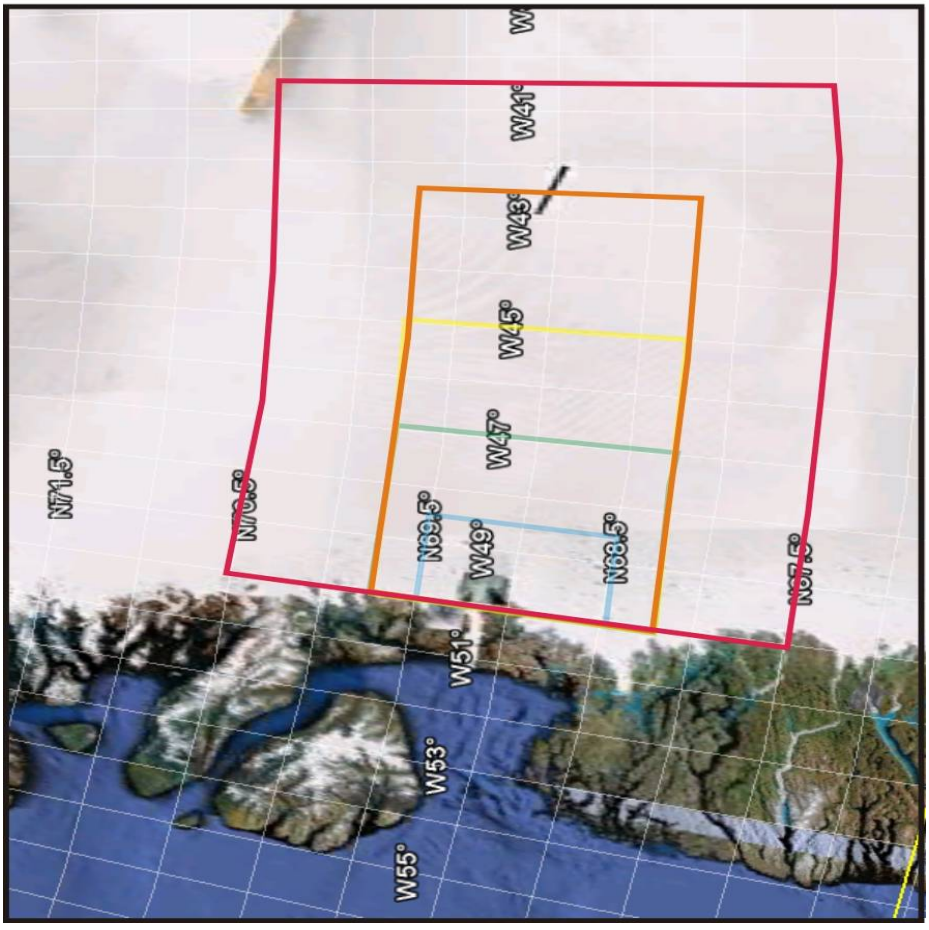

Table 7.2 (and illustration, source: Google Earth): Distribution of calving-related ice thickness changes over specified areas to the east of Jakobshavn Isbrae calving front.

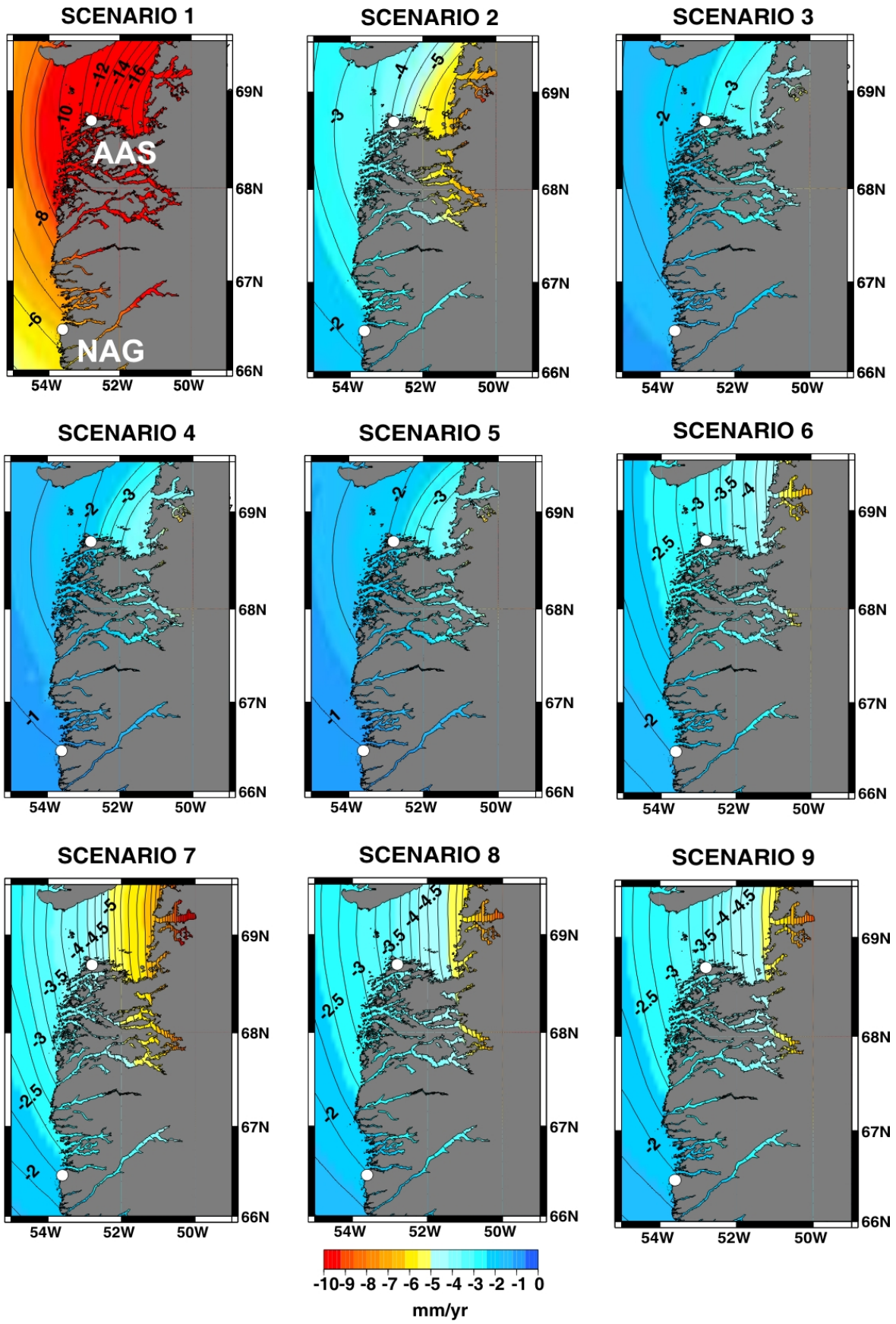

Fig. 7.6 Sea-level fingerprints associated with the scenarios described in Table 7.2. Salt marsh data collection sites are labelled in the upper left panel, in which data are contoured every 1mm/yr. In all other cases, data are contoured every 0.5mm/yr

Increasing the source area to 3.21% (Scenarios 4 and 5), which represents just under half of the area drained by JI, produces the two corresponding fingerprints shown in Fig. 7.6. This increase in source area reduces the sea-level change at Aasiaat and Nag to, respectively, -2mm/yr and -1mm/yr, which is closer to what is required to produce the slowdown in sea-level at 1500-1600AD. Furthermore, the fingerprints associated with Scenarios 4 and 5 show a differential between the two field sites that is consistent with the observations.

To fully consider the effect of JI, the percentage of the ice sheet drained was increased to 6.9%, close to the true extent of JI drainage area. In order to distribute 50km^3 of ice in a uniform manner, -0.41m must be lost over this area (Scenario 6). This results in sea-level change of -3mm/yr at Aasiaat and -1.75mm/yr at Nag. With the exception of Scenario 1, the ratio of the sea-level change between the two sites is in the range of 1.5-2. This remains the case for when the source area is extended to 7%. One effect of considering the total drainage area is less curvature in the contours. This is a consequence of significantly extending the area of ice thickness change to the north and south.

Reconfiguring the volume loss over sub-domains of different areas (Scenarios 4, 5, 7, 8 & 9) results in some difference in the predicted sea-level rates, although predictions for Scenarios 8 and 9 are the same. In Scenario 7, 60% of the volume loss in concentrated in 28% of the total catchment area. This acts to increase the sea-level change at both sites, as well as increase the between site differential, compared to Scenario 6.

7.3.3 Discussion and Conclusions

The above results show that ice thickness changes associated with discharge from Jakobshavn can account for a significant portion of the observed sea-level slowdown if the magnitude of mass loss can be sustained at tens of km^3/yr over century timescales.

Over long periods of time, the source area of the ice stream is expected to remain relatively stable, with the largest ice thickness changes and highest variation occurring at the grounding line. But, as indicated above, a discharge rate of 50km^3 per year is likely to be restricted to years of warmer temperatures and not reflective of LIA conditions. Measurements of the output of Jakobshavn are restricted to the past couple of decades, so it is not possible to speculate on output during the MCO and LIA. It is fair to assume that the scenarios presented here represent an upper bound

on the associated sea-level trends in this area. If the discharge is reduced by 50%, and the ice sheet drains 7% of the ice sheet area (Scenario 6), this reduces the predicted site differential to below the level resolvable in the salt marsh records. Assuming this is a reasonable estimate for discharge under cooler climatic conditions, this process can account for a significant portion (30-50%) of the required RSL fall.

In conclusion, although this analysis has shown that dynamic-related mass loss can account for a significant portion of the RSL change required in west Greenland, the relationship between the timing of MCO and LIA with variations in discharge must be investigated further to conclude with some certainty that this is a dominant mechanism. In some recent studies (Zwally et al., 2002, Joughin et al., 2008b), a link between ice velocity and surface melt intensity was shown to occur on sub-annual timescales, with summer horizontal ice flow increasing by >10% compared to the winter velocity (Zwally al. 2002). This becomes a likely mechanism for speed up if this sub-annual process is projected onto a decadal timescale. But, the onset of the Little Ice Age suggests that glaciers will advance which would act to reduce the calving rate (see Equation 7.2).

7.4 Other Potential Sources of Sea-level Change

Mass gain of non-Greenland ice may also account for the observed sea-level slow down in west Greenland. Given that the slowdown occurred near the onset of the LIA this possibility seems quite reasonable. At a minimum, this would require a 1m fall in eustatic sea-level over 400 years (~ 900 km^3 /yr gain in ice). There is no consistent and convincing evidence for this in other high resolution sea-level records. For example the salt marsh records that exist in Maine (Gehrels et al. 2002) and Connecticut (Van de Plaasche, 2000) do not show a convincing fall from 1500AD, but all display significant rise from 1800AD, a feature absent from the marshes in Greenland. This is consistent with the recent IPCC report which states that there have been no significant changes (at the tenths of mm/yr level in sea-level equivalent) in global ice volume during the past few millennia leading up to the Industrial Revolution, and the ongoing response of the ice sheets to past changes is also insignificant and not a major contributor to eustatic sea-level (Lemke et al. 2007). While there is evidence for advancing glaciers during the LIA (Espizua and Pitte, 2009 (Andes), Barclay et al., 2009 (Alaska), Ivy-Ochs et al., 2009 (Alps)) it is

difficult to place useful constraints on the global volume change, particularly given uncertainties for Antarctic ice sheet.

7.5 Chapter Summary

It is possible to rule out the processes considered in this chapter as dominant contributors to the RSL trends in west Greenland. However, a combination of these processes could have produced a dominant signal assuming their contributions summed together.

The analysis of steric sea-level change is limited but it indicates that a sustained and compatible variation in temperature and salinity throughout 500m of the water column is required to force significant sea-level fall. Prolonged and large (>1psu) salinification will be reflected in the biostratigraphy and there is no evidence for such a change. In the Disko Bay area, a change from warm, saline conditions to fresher and cooler conditions occurs from ~1500AD onwards (Lloyd, 2006b); which are not conducive to significant sea-level fall. Also, when considering salinity changes as the source of sea-level fall, one must consider the volume of fresh water being lost in terms of an equivalent change in eustatic sea-level. Work by Wadhams and Munk (2004) show that for a halosteric-related sea-level rise of 0.05mm/yr an equivalent eustatic sea-level rise of 1.8mm/yr is required. The changes in salinity required to force several mm of sea-level over a 500m column of water in west Greenland are unrealistic when converted to equivalent eustatic sea-level changes.

In order for a change in dynamics arising from the configurations of ice loss described in Table 7.2 to be the dominant factor controlling the local sea-level post 1500 AD, the ice stream must reactivate from relative dormancy or increase mass output to a few tens of cubic kilometres per year (and maintain this change for ~ 400 years). Sea-level fall of 3mm/yr at Nag is attainable via this process. However, these scenarios are unlikely to totally explain post-1500AD sea-level fall because (1) it is counter-intuitive to accelerate the discharge under colder temperature (unless there is a lagged response to MCO conditions) and (2) the loading configurations produce a differential in sea-level change which is not apparent in the salt marsh data. Based on the sensitivity analysis presented in Section 7.3.1 and assuming that there are no other processes (e.g. surface mass balance) contributing to a difference in RSL between the two sites the data limit the contribution from JI dynamics to 30-50% of the observed signal.

Mass accumulation of Antarctic ice and mountain glaciers as the source of post-1500AD sea-level change in southwest Greenland is unlikely due to the magnitude of change required and the lack of both glaciological and sea-level evidence quantifying ice mass change of the required magnitude. In particular, high resolution RSL records from Maine (Gehrels (2002) and Connecticut (Van de Plaasche, 2000) do not show a large (~ 1m) and secular sea-level fall between 1500AD and the present.

Chapter 8: Closing Discussion and Further Work

8.1 Discussion

In this section, I summarise the key results from Chapters 3-7 within the context of the original objectives stated in Chapter 1. I briefly discuss the wider relevance of the research, new ideas and the contribution my work has made to the current debate on the response of the GrIS to climate change, and its contribution to eustatic sea-level change over the past ~600 years. In Section 8.2, I present ideas and targets for further research

In Chapter 3, the tide gauges of the US east coast were analysed with respect to contributions from viscous readjustment of the solid earth to unloading of the North American Ice Sheets, changes in ocean density, and hypothesised mass input from the GrIS. Due to the small size of the sea-level fingerprint compared to the errors on trends at the tide gauge sites, the tide gauge data are unable to resolve contributions from the GrIS that are within the range -3 to +4 mm/yr. Even if errors in the trends are reduced, the influence of the steric sea-level signal at these sites dominates the fingerprint associated with a eustatic contribution of 0.6mm/yr from the GrIS. The analysis in this chapter was not able to narrow the current range of estimates of the contribution of the GrIS to present day eustatic sea-level change; however, it highlighted that caution must be taken when inverting tide gauge data to determine earth structure. Tide gauges in Europe were not considered for two reasons; (1) The tide gauges only sample a small percentage of the sea-level fingerprint associated with the Greenland Ice Sheet (e.g. see Fig. 1b in Mitrovica et al., 2001) and (2) The tide gauges in Europe can capture trends associated with mass changes in mountain glaciers (e.g. Svalbard and Iceland, see Fig 1.c in Mitrovica et al. 2001), making this an additional variable to consider.

Having demonstrated in Chapter 3 that available intermediate-field data from the US east coast are unable to constrain the contribution from the GrIS to 20th century eustatic sea-level change, Chapter 4 shows that the amplitude of the fingerprint is considerably larger in the near-field and so should be detectable using high-resolution proxy sea-level data. In addition, the model predictions based on two different mass loss scenarios produced very different patterns of sea-level change, indicating the possibility of applying fingerprinting technique to constrain the geometry and magnitude of GrIS mass changes. I hypothesised that the GrIS reacted to increased global temperatures, particularly in the latter half of the 20th

century, and that this would be manifested in the near field data as a departure from the background millennial scale sea-level trend. Although this is shown in the ^{210}Pb data covering 1920-2005AD, the records from two marshes in the same locality display opposing trends in RSL (see Fig. 4.5C) suggesting that the observations are less precise than the error bars indicate.

In line with the original aims of the project, and central to producing more realistic near-field RSL fingerprints, high-resolution modelling of the 19th and 20th century GrIS surface mass balance was presented in Chapter 5. The results from this chapter show that although local sea-level and overall mass balance is able to react to ice sheet-averaged increases in temperature of +2^{o}C spanning a decade, this does not significantly alter the long term trend once millennial and century-scale changes are taken into account (e.g. Fig. 6.14). The fingerprint maps produced show that a single RSL record is not a precise indicator of the health of the ice sheet because net negative ice sheet mass balance does not necessarily translate to sea-level fall in all coastal areas (Fig 5.8).

The contribution of the final surface mass balance GrIS model to 20th century eustatic sea-level is insignificant (+0.036mm/yr; insignificant in the sense that the contribution is smaller than the uncertainty on global mean sea-level rise for this period). Clearly, this estimate does not include additional ice loss associated with discharge from outlet glaciers in Greenland, which can amount to +0.4mm/yr eustatic sea-level change over subdecadal timescales. However, there is no evidence to suggest a large and sustained output of this magnitude for the 20th century and so the modelling results suggest that obtaining a contribution of 0.6 mm/yr – as inferred from far-field sea-level fingerprinting – is difficult. In terms of validating and calibrating the surface mass balance model against the local salt marsh data, the results were disappointing. The large vertical scatter and time errors in the ^{210}Pb salt marsh data prohibited any useful constraints to be placed on the model.

The most robust signal in the data is a deceleration in RSL beginning around 1500AD that results in sea level lying close to the present value (to within a few decimetres) for the past ~400 years. The scatter in the data points indicate that RSL is slowing down and this is backed up by evidence in the sedimentology. But there is the possibility that the apparent rapidity of the slowdown at 1500AD, and rise prior to 1500AD may be the result of sampling frequency and errors in the transfer function and dating technique Also, even though the RSL rise recorded pre 1500AD is likely to be recording the same RSL signal as evident in the isolation basins, one must consider the possibility that the rise is a response to the temporary climatic

conditions, e.g. the end of the MCO. This can be resolved by collecting data points that extend back to ~ 1000AD. . Explaining this signal is a key focus of Chapter 6.

In order to interpret the deceleration in RSL around 1500AD, two different forcing mechanisms were developed to generate an ice model for the period 1000AD to present (Chapter 6). The first was a forcing history dictated by accumulation and temperature from ice cores, the second was a NAO index-based precipitation and temperature parameterisation. Both forcings reproduced a large range of sea-level change scenarios but only a handful of these, with specific boundary conditions and parameter settings, were able to produce the required sea-level fall in west Greenland. The change of NAO conditions at 1500AD, as well as the initiation of the LIA described by the GRIP data, do not appear to be major drivers of sea-level fall at 1500-1600AD for the following reasons: (1) the GRIP data predicts a change to cooler conditions at 1500AD and (2) the appearance of NAO- phases are interspersed with NAO+ which do not cause a significant impact on the long-term ice sheet response. It is most likely that the sea-level fall is due to a significant viscous solid earth response to mass loss during the MCO. This is the primary finding of the work carried out in Chapter 6. This supports the conclusion made in Chapter 5 that the RSL trends are not reliable indicators of the contemporary mass balance of the ice sheet due to the lags in the solid Earth response.

Chapter 7 addressed the possible contribution to local sea level in West Greenland from steric, ice dynamic and distal cryospheric sources. It was demonstrated that steric sources are not likely to be a significant contributor at high latitudes over the 20th century, but this inference may partly be the result of sparse data and uneven temporal sampling. The steric effect is also not expected to dominate the sea-level fall from 1500-1600AD onwards because the required salinity and temperature changes are large and must be sustained over several hundred years. The analysis has limitations, however, due to the uncertainty in how expansion/contraction of water several hundred kilometres offshore affects sea-level change at the coast.

The potential of the Jakobshavn Isbrae drainage area as a major source for ice thickness changes is demonstrated, albeit to a first order level of accuracy. Jakobshavn Isbrae has the potential to contribute to RSL fall in west Greenland, more so at Aasiaat compared to Nag. The prerequisite of Jakobshavn Isbrae being a major contributor is that the ice stream has to reactivate from relative dormancy pre 1500AD, and that the RSL trend has to be of similar magnitude at each site. In recent studies (Rignot and Kanagaratnam, 2006), Jakobshavn Isbrae has been shown to be

a major regulator of GrIS mass balance over the past decade or so but this level of discharge is unlikely to be sustained over hundreds of years. Jakobshavn Isbrae will have been active for the duration of the modelling period, but a study of time dependent dynamics changes will help to clarify the predicted contribution of this component (see next section).

Cryospheric sources outside of Greenland are not responsible for the deceleration in West Greenland after 1500AD. For this to be the case, non-Greenland ice would have had to drive a sea-level fall of magnitude ~ 3 mm/yr since 1500AD. As in Greenland, there is a paucity of RSL data around the globe covering the period from 1000AD, at least until the early 1800s. The data that do exist are located in the north east US (Van de Plaasche, 2000, Gehrels et al. 2002), and neither show a response consistent with that required.

To summarise, one of the main aims was to investigate periods in recent history when the GrIS faced similar climatic conditions to those at present, as this would put the recent behaviour into context. The modelling shows that, on decadal timescales, it is possible to generate RSL fall of 2mm/yr in west Greenland with local net changes in ice thickness of -10 to -30m over ten years. For this to be sustained since 1500AD, an average of 750m of ice must be removed from the local area in a period of 500 years. This was confirmed by the modelling in Chapter 6. While the results obtained in this thesis do not show conclusively that the recent large magnitude changes in the GrIS are not anomalous, they at least suggest that changes of this magnitude have likely occurred in the past few centuries.

With respect to these first attempts at century-scale mass balance reconstructions, key results are that although the GrIS is sensitive to century scale climate fluctuations, the sea-level response is not necessarily dominated by contemporary changes and the contribution from ice dynamics is significant when modelling the surface mass balance and local RSL change. Ideas for improvement of this aspect are suggested in the next section.

In terms of the potential and sophistication of the data and models, the strength of the proxy sea-level technique has been demonstrated on century timescales, but there is room for improvement in the modelling at this level of resolution. On the other hand, models of ice sheets on *decadal* timescales are further advanced than the constraining data at this point in time. Suggestions are given in the next section to improve the potential of the near-field fingerprinting method by advancing aspects of the models applied in this study.

8.2 Further Work

Accurate modelling of leads and lags in the cryosphere-ocean-earth system is crucial for correctly interpreting the salt marsh data. Lags in the RSL response are brought about by the non-elastic response of the earth to loading changes, and this component of the response appears to be key in explaining the observed RSL trend in West Greenland. Given this fact, and the considerable degree of lateral heterogeneity of the crust and mantle in this area (see Section 1.2) the development and application of 3D earth models with more accurate representation of internal structure are an important next step.

As specified in the previous section, the sharp decline in sea-level rise shown by the data is not replicated precisely by assuming the slowdown is solely the result of viscous isostatic adjustment. An additional mechanism is required to accelerate the RSL fall when coupled with the viscous response. This hypothesis may be investigated by including a time dependent component to the ice dynamic modelling. Accurate modelling of the dynamic component is crucial to this study for two main reasons. Firstly, the modelling of the dynamic response to SMB changes on the ice sheet and the response of ice streams is of high importance since one of the data sites is proximal to Jakobshavn Isbrae. Secondly, accurate modelling of the dynamic contribution is essential to the evolution of the surface elevation of the ice sheet and therefore crucial to application of the PDD model over century timescales. Also, improved modelling of the dynamic component may improve estimates of calving flux from JI and so could unlock the potential of IRD data, such as that in Lloyd (2006b), by allowing it to act as a constraint on calving over century timescales.

The RSL curves attained from west Greenland salt marshes alone are not reliable indicators of the overall health of the ice sheet. But, improvements in dating 20th C sediments along with suitable criteria for choosing a network of field sites may allow this technique to be potentially powerful for constraining local, and therefore ice sheet-wide mass balance. The work carried out here identifies the west of Greenland to be one of the most climatically sensitive areas due to lack of precipitation, shallow elevation gradient and JI dynamic-related losses, all of which are factors that collectively force, in a warming climate, the regional mass balance, and therefore RSL, towards negative trends. The development of a network of salt marsh data sites could indicate whether the GrIS has entered a phase of deglaciation by comparing these with RSL patterns from isolation basin data spanning warm periods.

Isolation basin data collected in the far north of Greenland (Fig 1.9) do not show any sensitivity to Neoglacial readvance, unlike those collected in the south. Salt

marsh data collected in the north may be able to determine the sensitivity of ice at high latitudes to previous temperature changes and test whether a temperature 'threshold' must be exceeded in northerly areas before ice sheet wide deglaciation gets underway . In order to choose a site that is recording changes in mass balance only, some criteria could be applied to future selection of sites; (1) the sites must be distal to outlet glaciers; (2) ideally, the millennial-scale RSL signal should be close to 0mm/yr. The data would then be recording only century-scale changes in sea-level. An example of a site fitting these criteria is Mesters Vig, which is located in the east of Greenland, distal to major ice streams, and has displayed stable sea-level from 6 kyr BP (Simpson et al. 2009).

This work has shown that caution must be taken when analysing RSL trends from isolation basin data and salt marshes. Ice models calibrated by isolation basin data are employed to correct data from the GRACE mission for gravity shifts related to mantle movement. It would be interesting to compare these results with the predictions for mass changes when an ice model, calibrated using both millennial and century-scale RSL changes, is used to correct for GIA.

References

Andersen, K.K., Ditlevsen, P.D., Rasmussen, S.O., Clausen, H.B., Vinther, B.M., Johnsen, S.J., and Steffensen, J.P. Retrieving a common accumulation record from Greenland ice cores for the past 1800 years. Journal of Geophysical Research, 2006, **111**.
doi:10.1029/2005JD006765.

Andrews, J. T. *Glaciers of North Canada* in *Glaciers of North America*, in *Satellite image atlas of glaciers of the world: U.S. Geological Survey Professional Paper* 1386-J-1. Williams, R.S., Jr., and Ferrigno, J.G., Editors. 2002, p525 .

Antonov, J. I., R. A. Locarnini, T. P. Boyer, A. V. Mishonov, and H. E. Garcia, *World Ocean Atlas 2005, Volume 2: Salinity*. In *NOAA Atlas NESDIS 62*. Levitus, S. Editor. 2006. U.S. Government Printing Office, Washington, D.C., 182p

Antonov, J. I., Levitus, S., Boyer T. P. *Steric sea level variations during 1957–1994: Importance of salinity.* Journal of Geophysical Research 2002, **107**(C12) 8013 doi:10.1029/2001JC000964.

Appenzeller, C., Stocker, T. F. and Anklin, M. *North Atlantic Oscillation Dynamics Recorded in Greenland Ice Cores.* Science, 1998. **282**: p446-449

Bamber,J. L., Ekholm, S. and Krabill, W. *A new, high-resolution digital elevation model of Greenland fully validated with airborne laser altimeter*, Journal of Geophysical Research, 2001a. **106**: p 6733-6745.

Bamber, J.L., R.L. Layberry, S.P. Gogenini. *A new ice thickness and bed data set for the Greenland ice sheet 1: Measurement, data reduction, and errors*. Journal of Geophysical Research 2001b. **106**: p 33773-33780. Data provided by the National Snow and Ice Data Center DAAC, University of Colorado, Boulder, Colorado USA.
Available for download at http://nsidc.org/data/nsidc-0092.html.

Barclay, D. J. Wiles, G. C. and Calkin, P. E. *Holocene glacier fluctuations in Alaska*. Quaternary Science Reviews, 2009. **28**(21-22): p2034-2048

Benn, D. I., Warren, C. R., Mottram, R. H. *Calving processes and the dynamics of calving glaciers*. Earth Science Reviews, 2007. **82**: p143–179.

Bennike, O. and Bjorck, S. *Chronology of the last recession of the Greenland Ice Sheet.* Journal of Quaternary Science, 2002. **17**: p211–219.

Bindoff, N.L., Willebrand, J., Artale, V., Cazenave, A., Gregory, J., Gulev, S., Hanawa, K., Le Quéré, C., Levitus, S., Nojiri, Y., Shum, C. K. ,Talley, L. D. and Unnikrishnan, A. *Observations: Oceanic Climate Change and Sea Level Contribution.* In: *Climate Change 2007: The Physical Science Basis. Contribution of Working Group I to the Fourth Assessment Report of the Intergovernmental Panel on Climate Change 2007*, D. Qin, M. Manning, Z. Chen, M. Marquis, K.B. Averyt, M. Tignor and H.L. Miller, Editors. 2007. Cambridge University Press, Cambridge, United Kingdom and New York, NY, USA.

Bingham, R. J. and Hughes, C. W. *The signature of the Atlantic meridional overturning circulation in sea level along the east coast of North America*. Geophysical Research Letters, 2009. **36**. L02603. doi:10.1029/2008GL036215

Bougamont, M., Bamber, J. L. and Greuell, W. *A surface mass balance model for the Greenland Ice Sheet*. Journal of Geophysical Research, 2005. **11.** F04018, doi:10.1029/2005JF000348

Box, J.E.,Yang, L., Bromwich, D. H. and. Bai, L.-S. *Greenland ice sheet surface air temperature variability: 1840-2007*. Journal of Climate, 2009a. **22**: p4029-4049.

Box, J.E., Yang, L., Bromwich, D. H., Mosely-Thompson, E., Das, S. and McConnell, J. *Greenland ice sheet accumulation reconstruction: 1784-2006*. Journal of Climate, 2009b. Submitted.

Box, J.E., Bromwich, D. H., Veenhuis, B. A., Bai, L-S. , Stroeve, J. C., Rogers, J. C., Steffen, K., Haran, T. and Wang, S-H. *Greenland Ice Sheet Surface Mass Balance Variability (1988-2004) from Calibrated Polar MM5 Output*. Journal of Climate, 2006. **19**: p2783-2800.

Box, J. E. and Steffen, K. *Sublimation on the Greenland Ice Sheet from automated weather station observations*. Journal of Geophysical Research, 2001.**106**: p33965-33981

Boyer, T. P., Antonov, J.I. , Garcia, H.E., Johnson, D. R., Locarnini, R. A., Mishonov, A.V., Pitcher, M.T., Baranova, O.K., Smolyar, I.V. *World Ocean Database 2005* in *NOAA Atlas NESDIS* 60, S. Levitus, Editor. 2006. U.S. Government Printing Office, Washington, D.C., 190 p.

Braithwaite, R. J. *Positive degree-day factors for ablation on the Greenland ice sheet studied by energy balance modelling*. Journal of Glaciology, 1995. **41** (137): p 153-160.

Braithwaite, R. J. and Olesen, O. B. *Calculation of glacier ablation from air temperature, west Greenland.* In *Glacier Fluctuations and Climatic Change*, J. Oerlemans, Editor. 1989. Kluwer Academic Publisher (Dordrecht), p219-233.

Braun A., Kim H. R., Csatho, B. and von Frese, R. R. B. *Gravity-inferred crustal thickness of Greenland*. Earth and Planetary Science Letters 2007. **262**: p138–158.

Broecker, W. S., Bond, G., Klas, M., Bonani, G., and Wolfli, W. *A salt oscillator in the glacial Atlantic? 1. The concept*. Paleoceanography, 1990. **5**: p 469-477.

Cazenave, A., Dominh, K., Guinehut, S., Berthier E., Llovel, W., Ramillien G., Ablain,M, and Larnicol, G. *Sea level budget over 2003–2008: A re-evaluation from GRACE space gravimetry, satellite altimetry and Argo*. Global and Planetary Change, 2009. **65**: p83-88.

Cazenave, A., Lombard, A., and Llovel, W. *Present-day sea level rise: a synthesis*. Comptes Rendus Geoscience, 2008. **340**: p 761–770.

Cazenave, A., and Nerem, R. S *Present-day sea level change: Observationand causes*, Reviews in Geophysics, 2004. **42**: RG3001, doi:10.1029/2003RG000139.

Chen, L., Johannessen, O. M., Khvorostovsky, K. and Wang, H. *Greenland Ice Sheet Elevation Change in Winter and Influence of Atmospheric Teleconnections in the Northern Hemisphere.* Atmospheric and Oceanic Science Letters, 2009. **2**(6):p376-380

Chylek, P., Dubey, M. K. and Lesins, G. *Greenland warming of 1920-1930 and 1995-2005*.Geophysical Research Letters, 2006.**33**:L11707. doi:10.1029/2006GL026510.

Clague J. J. and James, T. S. *History and isostatic effects of the last ice sheet in southern British Columbia*, Quaternary Science Reviews, 2002. **21**: p71–87.

Clark, P. U. and Mix, A. C. *Ice sheets and sea level of the Last Glacial Maximum*, Quaternary Science Reviews, 2002. **21**: p1–7.

Csatho, B., Schenk, T., Van der Veen, C. J. and Krabill, W. R. *Intermittent thinning of Jakobshavn Isbræ, West Greenland, since the Little Ice Age*. Journal of Glaciology, 2008. **54** (184): p131-144.

Dahl-Jensen, D., Mosegaard, K., Gundestrup, N., Clow, G. D., Johnsen, S. J., Hansen, A.W., and Balling, N. *Past temperatures directly from the Greenland Ice Sheet*. Science, 1998. **282**: p 268-271.

Darbyshire, F. Larsen T. B., Mosegaard K., Dahl-Jensen, T., Gudmundsson, O., Bach, T., Gregersen, S., Pedersen, H. A. and Hanka, W. *A first detailed look at the Greenland lithosphere and upper mantle using Rayleigh wave tomography*. Geophysical Journal International, 2004.**158**: p267–286.

Davis, J.L. and Mitrovica, J.X. *Glacial Isostatic Adjustment and the Anomalous Tide Gauge Record From Eastern North America*, Nature, 1996. **379**: p331-333.

Di Donato, G. Mitrovica, J. X., Sabadini, R. and Vermeersen, L. L. A., *The influence of a ductile crustal zone on glacial isostatic adjustment: geodetic observables along the U.S. East Coast*. Geophysical Research Letters, 2000. **27**: p3017–3020.

Domingues, C. M., Church, J. A., White, N. J., Gleckler, P. J., Wijffels, S. E., Barker, P. M. and Dunn, J. R. *Improved estimates of upper-ocean warming and multi-decadal sea-level rise*. Nature, 2008. **453**: p1090-1093.

Douglas, B. C. *Global Sea Level Rise*. Journal of Geophysical Research 1991. **96**(C4): p6981–6992.

Driscoll N. W. and Haug, G.H. *A Short Circuit in Thermohaline Circulation: A Cause for Northern Hemisphere Glaciation?* Science, 1998. **282**: p436-438.

Dyke, A. S., Andrews, J. T., Clark, P. U., England, J. H., Miller, G. H., Shaw, J. and Veillett, J. J. *The Laurentide and Innuitian ice sheets during the Last Glacial Maximum*. Quaternary Science Reviews, 2002, **21**: p 9–31.

Dziewonski, A. M. and Anderson D. L. *Preliminary reference Earth model*. Physics of the Earth and Planetary Interiors, 1981. **25**: p297–356.

Eldrett J. S., Harding I. C.,Wilson P. A., Butler, E. and Roberts A. P. *Continental ice in Greenland during the Eocene and Oligocene*. Nature, 2007. **446**: p176-179.

Espizua, L. E. and Pitte, P. *The Little Ice Age glacier advance in the Central Andes (35 degrees S), Argentina*. Palaeogeography, Palaeoclimatology, Palaeoecology, 2009. **281**(3-4): p345-350

Fahnestock, M., Abdalalti, W., Joughin, I., Brozena, J. And Gogineni, P. *High Geothermal Het Flow, Basal Melt and the Origion of Rapid Ice Flow in Central Greenland*. Science 2001. **294**: p2338-2342

Farrell, W. E. and Clark J. T. *On postglacial sea level*. Geophysical Journal of the Royal Astronomical Society, 1976. **46**: p647–667.

Fleming, K. and Lambeck, K. *Constraints on the Greenland ice Sheet since the Last Glacial Maximum from observations of sea-level change and glacial-rebound modelling*. Quaternary Science Reviews, 2004. **23**: p1053-1077.

Fofonoff, N. P. and Millard, R. C. *Algorithms for computation of fundamental properties of seawater*. UNESCO Technical Papers in Marine Science, 1983. **44**: 55p

Forman, S. L. , Marín, L., Van Der Veen C., Tremper, C. and Csatho, B. *Little Ice Age and neoglacial landforms at the Inland Ice margin, Isunguata Sermia, Kangerlussuaq, west Greenland*. Boreas, 2007. **36**(4): p341-351.

Frankignoul, C., de Coetlogon, G., Joyce T.M., and Dong, S.F. *Gulf stream variability and ocean-atmosphere interactions.* Journal of Physical Oceanography, 2001. **31**(12): p3516-3529.

Gehrels, W. R., Marshall, W. A., Gehrels M. J.,Larsen, G., Kirby, J. R.,Eiriksson, J, Heinemeier, J. and Shimmield, T. *Rapid sea-level rise in the North Atlantic Ocean since the first half of the nineteenth century*. The Holocene, 2006. **16**(7): p949 -965.

Gehrels, W. R. , Kirby, J. R., Prokoph, A., Newnham, R. M., Achterberg, E. P, Evans, H.,Black, S. and Scott, D. B. *Onset of recent rapid sea-level rise in the western Atlantic Ocean* Quaternary Science Reviews, 2005. **24**: p2083–2100.

Gehrels, W. R.,Belknap D. F., Black, S. and Newnham R. M. *Rapid sea-level rise in the Gulf of Maine, USA, since AD 1800*. The Holocene, 2002. **12**: p383-389.

Gornitz, V., Lebedeff, S. and Hansen, J. *Global sea level trend in the past century.* Science, 1982. **215**: p1611-1614.

Hanna, E., Huybrechts, P., Steffen, K., Cappelen, J., Huff, R., Shuman, C. . Irvine-Flynn, T., Wise, S. and Griffiths, M*. Increased runoff from melt from the Greenland Ice Sheet: a response to global warming*. Journal of Climate, 2008. **21**: p331-341.

Hanna, E., Huybrechts, P., Janssens, I., Cappelen, J., Steffen, K. and Stephens, A. *Runoff and mass balance of the Greenland Ice Sheet: 1958-2003*. Journal of Geophysical Research- Atmospheres, 2005. **110**(D13): D13108

Hanna, E., and Cappelen, J. *Recent cooling in coastal southern Greenland and relation with the North Atlantic Oscillation*. Geophysical Research Letters, 2003. **30**(3): 1132.
doi:10.1029/2002GL015797

Hanna, E. and Valdes, P. *Validation of ECMWF (re)analyses surface climate data, 1979-98 for Greenland and implications for mass balance modelling of the Ice Sheet*. International Journal of Climatology, 2001. **21**(2): p171-195.

Hanna, E., Valdes, P. and McConnell, J. *Patterns and variations of snow accumulation over Greenland, 1979-98, from ECMWF analyses, and their verification*. Journal of Climate, 2001, **14**(17): p3521-3535.

Henriksen, N., Higgins, A. K., Kalsbeek, F., Pulvertaft, T C. R. *Greenland from Archaean to Quaternary*, Geology of Greenland Survey Bulletin 2001. **185**: 93pp.

Hock, R. *Glacier Melt: A review of processes and their modelling.* Progress in Physical Geography, 2005. **29**:p362-391

Howat, I. M., Joughin, I. and Scambos, T. A. *Rapid changes in ice discharge from Greenland outlet glaciers*. Science 2007. **315**(5818): p1559-1561.

Howat, I. M., Joughin, I. and Gogineni, S. P. *Rapid retreat and acceleration of Helheim Glacier, east Greenland*. Geophysical Research Letters, 2005, **32:** L22502. doi:10.1029/2005GL024737

Huybrechts, P., Gregory, J. and Janssens, I. *Modelling Antarctic and Greenland volume changes during the 20th and 21st centuries forced by GCM time slice integrations.* Global and Planetary Change, 2004. **42**(1-4): p83-105.

Huybrechts, P. *Sea-level changes at the LGM from ice-dynamic reconstructions of the Greenland and Antarctic ice sheets during the glacial cycles*, Quaternary Science Reviews, 2002. **201**: p203-231.

Huybrechts, P., and. de Wolde, J. *The Dynamic Response of the Greenland and Antarctic Ice Sheets to Multiple-Century Climatic Warming.* Journal of Climate, 1999. **12**(8): p2169-2188.

Ishii, M., Kimoto, M., Sakamoto, K. and Iwasak, S*. Steric Sea Level Changes Estimated from Historical Ocean Subsurface Temperature and Salinity Analyses*. Journal of Oceanography, 2006. **62**: p155-170.

Ivins, E. R., Dokka, R. K., and Blom, R. G. *Post-glacial sediment load and subsidence in coastal Louisiana*, Geophysical Research Letters, 2007. **34**: L16303. doi:10.1029/2007GL030003.

Ivy-Ochs, S., Kerschner, H., Maisch, M.,Christl, M. Kubik P.W. and Schluchter, C. *Latest Pleistocene and Holocene glacier variations in the European Alps.* Quaternary Science Reviews, 2009. **28**(21-22): p2137-2149

Janssens, I. and Huybrechts, P. *The treatment of meltwater retention in mass-balance parameterizations of the Greenland ice sheet.* Annals of Glaciology*,* 2000. **31**: p133-140.

Joughin, I., Howat, I., Alley, R. B., Ekstrom, G., Fahnestock, M., Moon, T., Nettles, M., Truffer, M. and Tsai, V. C. *Ice-front variation and tidewater behavior on Helheim and Kangerdlugssuaq Glaciers, Greenland*. Journal of Geophysical Research, 2008a. **113**: F01004.
doi:10.1029/2007JF000837.

Joughin, I., I. Howat, M., Fahnestock, M., Smith, B., Krabill, W., Alley, R. B., Stern, H. and Truffer, M. *Continued evolution of Jakobshavn Isbrae following its rapid speedup*. Journal of Geophysical Research, 2008b. **113**: F04006. doi:10.1029/2008JF001023.

Joughin, I. *Greenland Rumbles Louder as Glaciers Accelerate*. Science, 2006. **311**: p1719-1720.

Joughin, I., Abdalati, W. and Fahnestock, M. *Large fluctuations in speed on Greenland's Jakobshavn Isbrae glacier*. Nature, 2004. **432**(7017): p 608-610

Kendall, R., Mitrovica, J. X. and Milne, G. A. *On post-glacial sea level – II. Numerical formulation and comparative results on spherically symmetric models*. Geophysical Journal International, 2005. **161.** p679-706

Krabill, W., Hanna, E., Huybrechts, P., Abdalati, W., Capellen, J., Csatho, B., Frederick, E., Manizade, S., Martin, C., Sonntag, J., Swift, R., Thomas, R. and Jungel, R. *Greenland Ice Sheet: Increased coastal thinning.* Geophysical Research Letters, 2004. **32**: L24402.
doi:10.1029/2004GL021533

Krabill, W., Abdalati, W., Frederick, E., Manizade, S., Martin, C.,Sonntag, J., Swift, R., Thomas R., and Yungel J. *Aircraft laser altimetry measurement of elevation changes of the Greenland ice sheet: Technique and accuracy assessment*. Journal of Geodynamics, 2002. **34**: p357– 376.

Krabill W., Abdalati, W., Frederick E., Manizade, S., Martin, C., Sonntag, J., Swift, R., Thomas, R., Wright, W., Yungel, J. *Greenland Ice Sheet: High-Elevation Balance and Peripheral Thinning*. Science, 2000. **289**(5478): p428–430.
doi: 10.1126/science.289.5478.428

Kumar, P., Kind, R., Hanka, W., Wylegalla, K., Reigber, Ch., Yuan, X., Woelbern, I., Schwintzer, P., Fleming, K., Dahl-Jensen T., Larsen, T. B., Schweitzer, J., Priestley, K., Gudmundsson, O., Wolf, D. *The lithosphere–asthenosphere boundary in the North-West Atlantic region*. Earth and Planetary Science Letters, 2005. **236**: p249– 257.

Lemke, P., Ren, J., Alley, R.B. , Allison, I. , Carrasco, J. , Flato, G. , Fujii, Y. Kaser, G., Mote, P. , Thomas, R.H. and Zhang, T. *Observations: Changes in Snow, Ice and Frozen Ground*. In: *Climate Change 2007: The Physical Science Basis. Contribution of Working Group I to Fourth Assessment Report of the Intergovernmental Panel on Climate Change.* Solomon, S., Qin, D., Manning, M. Chen, Z. Marquis, M., Averyt, K. B., Tignor, M. and Miller, H. L., Editors. Cambridge University Press, Cambridge, United Kingdom and New York, NY, USA.

Leuliette, E. W. and Miller, L. *Closing the sea level rise budget with altimetry, Argo, and GRACE*. Geophysical Research Letters, 2009. **36**: L04608.
doi:10.1029/2008GL036010.

Levine, R. C., and Bigg, G. R. *Sensitivity of the glacial ocean to Heinrich events from different iceberg sources, as modelled by a coupled atmosphere-iceberg-ocean model*. Paleoceanography, 2008. **23**: PA4213.
doi:10.1029/2008PA001613.

Levitus, S., Antonov, J. I.; Boyer, T.P. , Garcia, H.E. and Locarnini, R.A. *Linear trends of zonally averaged thermosteric, halosteric, and total steric sea level for individual ocean basins and the world ocean*, *(1955-1959)-(1994-1998).* Geophysical Research Letters, 2005. **32**(16): L16601 doi:10.1029/2005GL023761

Lloyd, J. M. *Modern distribution of benthic foraminifera from Disko Bugt, West Greenland*. Journal of Foraminiferal Research, 2006a. **36**(4): p 315-331.

Lloyd, J. M. *Late Holocene environmental change in Disko Bugt, West Greenland: interaction between climate, ocean circulation and Jakobshavn Isbrae*. Boreas, 2006b. **35**: p35 -49.

Locarnini, R. A., Mishonov, A. V. , Antonov, J. I., Boyer, T. P. and Garcia, H. E. *World Ocean Atlas 2005, Volume 1: Temperature*. In: *NOAA Atlas NESDIS 61*. Levitus, S. Editor. 2006. U.S. Government Printing Office, Washington, D.C, 182 pp.

Lombard A., Cazenave, A., Le Traon, P. and Ishii, M*. Contribution of thermal expansion to present-day sea-level change revisited.* Global and Planetary Change, 2005. **47**(1):p1-16.

Long, A. J., Woodroffe, S. A., Dawson, S., Roberts, D. H. and Bryant, C. L. *Late Holocene relative sea level rise and the Neoglacial history of the Greenland Ice Sheet*. Journal of Quaternary Science, 2009a. **24**: p. 345–359.

Long, A. J., Woodroffe, S. A., Milne, G. A., Bryant, C. L. and Wake, L. M. *Relative sea level change in west Greenland during the last millennium.* Quaternary Science Reviews, 2009b. 17pp. Article in Press.

Lunt, D. J., de Noblet-Ducoudre, N. and Charbit, S. *Effects of a melted greenland ice sheet on climate, vegetation, and the cryosphere.* Climate Dynamics, 2004. **23**: p679–694.

Luthcke, S. B., Zwally, H. J. , Abdalati, W. , Rowlands, D. D. , Ray, R. D. , Nerem, R. S. , Lemoine, F. G. , McCarthy, J. J. and Chinn, D. S. *Recent Greenland Ice Mass Loss by Drainage System from Satellite Gravity Observations*. Science, 2006. **314**(5803): p1286-1289.

Mann, M. E., Bradley, R. S. and Hughes, M. K. *Global-scale temperature patterns and climate forcing over the past six centuries*. Nature, 1998. **392**:p779-787.

Mikkelsen, N., Kuijpers, A. and Arneborg J. *The Norse in Greenland and late Holocene sea-level change.* Polar Record, 2008. **44**(228): p45–50.

Miller, L, and Douglas, B. C. *Mass and volume contributions to twentieth-century global sea level rise.* Nature, 2004. **428**: p 406-409.

Milne, G. A., Mitrovica, J. X. and Davis, J. L. *Near-field hydroisostasy: the implementation of a revised sea-level equation*. Geophysical Journal International, 1999. **139**: p464–482.

Milne, G. A. and Mitrovica, J. X. *Postglacial sea-level change on a rotating Earth*. Geophysical Journal International, 1998. **133**: p1–19.

Mitrovica, J.X., Wahr, J., Matsuyama, I. and Paulson, A. *Reanalysis of Ancient Eclipse, Astronomic and Geodetic Data: A Possible Route to Resolving the Enigma of Global Sea Level Rise*. Earth and Planetary Science Letters, 2006. **243**: p390-399.

Mitrovica, J. X. and Milne, G. A. On *post-glacial sea level: I. General theory.* Geophysical Journal International, 2003. **154**: p253–267.

Mitrovica, J. X., Tamisiea, M., Davis, J. L. and Milne, G. A. *Recent Mass Balance of Polar Ice Sheets Inferred From Patterns of Global Sea-Level Change*. Nature, 2001. **409**: p1026-1029.

Moon, T., and Joughin, I. *Changes in ice front position on Greenland's outlet glaciers from 1992 to 2007*. Journal of Geophysical Research, 2008. **113**: F02022. doi:10.1029/2007JF000927.

Mosley-Thompson, E., Readinger, C. R., Craigmile, P., Thompson, L. G. and Calder, C. A. *Regional sensitivity of Greenland precipitation to NAO variability*. Geophysical Research Letters, 2005. **32**: L24707, doi:10.1029/2005GL024776.

Munk, W. *Twentieth century sea level*: *An enigma.* Proceedings of the National Academy of Sciences of the United States of America, 2002. **99**(10): p6550-6555

Officer, C.B., Newman, W.S., Sullivan, J.M. and Lynch, D.R. *Glacial isostatic adjustment and mantle viscosity*, Journal of Geophysical Research,1988. **93:** p6397–6409.

Ohmura, A. *Physical Justification for the Temperature-Based Melt-Index Method*. Journal of Applied Meteorology, 2001. **40**: p753-759

Ohmura, A. *New temperature distribution maps for Greenland.* Zeitschrift für Gletscherkunde und Glazialgeologie, 1987**. 23**: p1-45

Park, K-D., Nerem, R., S., Davis, J. L., Schenewerk,M. S., Milne, G. A. and Mitrovica, J. X. *Investigation of glacial isostatic adjustment in the northeast U.S. using GPS measurements.* Geophysical Research Letters, 2002. **29**(11) 1509. doi: 10.1029/2001GL013782.

Paterson, W. S. B. *The Physics of Glaciers (3rd Edition)*, 1994. Elsevier Science Ltd, UK.

Peltier, W. R. *Global Glacial Isostasy and the Surface of the Ice-Age Earth*: The ICE-5G (VM2) Model and GRACE, Annual Review of Earth and Planetary Sciences, 2004. **32**:p111–49.

Peltier, W. R. *Ice Age Paleotopography*, Science, 1994. **265**(5169): p195-201

Peltier, W. R. *The impulse response of a Maxwell earth*. Reviews of Geophysics and Space Physics, 1974. **12**: p649-669

Pfeffer, W. T., Meier, M. F. and Illangasekare, T. H. *Retention of Greenland runoff by refreezing: implications for projected future sea level change*. Journal of Geophysical Research, 1991. **96**(C12): p22117-22124.

Plag, H-P. *Recent relative sea-level trends: an attempt to quantify the forcing factors*. Philosophical Transactions of the Royal Society (A), 2006. **364**: p821-844

Plag, H. P. and Juttner, H *Inversion of global tide gaue data for present-day ice load changes*, Memoirs of the National Institute of Polar Research Special Issue, 2001. **54**: p301-317

Podlech, S., Mayer, C. and Egede-Boggild, C. *Glacier Retreat, Mass-Balance and Thinning: Sermilik Glacier, South Greenland*. Geografiska Annaler 2004. **86A**(4): p305-317

Ramillien, G., Lombard, A., Cazenave, A., Ivins, E.R., Llubes, M., Remy, F. and Biancale, R. *Interannual variations of the mass balance of the Antarctica and Greenland ice sheets from GRACE.* Global and Planetary Change 2006. **53**:p198-208

Rasch, M., *Holocene relative sea level changes in Disko Bugt, West Greenland*. Journal of Coastal Research, 2000. **16**: p306-315.

Reeh, N. *Parameterization of Melt Rate and Surface Temperature on Greenland Ice Sheet*. Polarforschung, 1991. **59**(3): p113-128.

Rignot, E., Box, J. E., Burgess, E. and Hanna E. *Mass balance of the Greenland ice sheet from 1958 to 2007*. Geophysical Research Letters, 2008. **35**: L20502 doi:10.1029/2008GL035417.

Rignot, E. and Kanagaratnam, P. *Changes in the Velocity Structure of the Greenland Ice Sheet.* Science, 2006. **311**(5763): p986-990.

Rignot, E., Braaten, D. Gogineni, S. P., Krabill, W. and McConnell, J. R.. *Rapid ice discharge from southeast Greenland glaciers*. Geophysical Research Letters, 2004. **31:**(L1401).
doi:10.1027/2004GL019474

Rignot, E. and Thomas, R. H. *Mass Balance of the Polar Ice Sheets*. Science, 2002. **297**:p1502-1506.

Rinterknecht, V., Gorokhovich, Y., Schaefer, J. and Caffee, M. *Preliminary ^{10}Be chronology for the last deglaciation of the western margin of the Greenland Ice Sheet*. Journal of Quaternary Science, 2009. **24**: p 270–278.

Roberts D. H., Long, A. J., Schnabel, C. ,Freeman, S. and Simpson, M. J. R *The deglacial history of southeast sector of the Greenland Ice Sheet during the Last Glacial Maximum*. Quaternary Science Reviews ,2008. **27**: p1505– 1516

Roedelsperger, S., Kuhn, M., Makarynskyy, O., Gerstenecker, C. *Steric Sea-Level Change and its Impact on the Gravity Field caused by Global Climate Change*. Pure & Aplied Geophysics ,2008. **165**(6): p 1131-1151.

Ruddiman, W. F. *Earth's Climate: Past and Future.* 2001, W H Freeman and Company, New York.

Schmitt, R. W. *If rain falls on the ocean, does it make a sound*? Oceanus, 1996. **39** (2): p4-8 in Woods Hole Oceanographic Institute Online Magazine: http://www.whoi.edu/oceanus/index.do

Sedlacek, J. and Mysak, L. A. A *model study of the Little Ice Age and beyond: changes in ocean heat content, hydrography and circulation since 1500*. Climate Dynamics, 2008.
doi:10.1007/s00382-008-0503-6

Seidov, D., Samthein, M., Stattegger, K., Prien R. and Weinelt, M. *North Atlantic ocean circulation during the last glacial maximum a nd subsequent meltwater event*: A numerical model. Journal of Geophysical Research, 1996. **101**(C7): p16,305-16,332.

Simpson, M. J. R., Milne, G. A. , Huybrechts, P. and Long, A. J*. Calibrating a glaciological model of the Greenland ice sheet from the Last Glacial Maximum to present-day using field observations of relative sea level and ice extent*, Quaternary Science Reviews 2009. **28**(17-18): pp1631-1657

Smeets, C. J. P. P. and van den Broeke, M. R.. *Temporal and Spatial Variations of the Aerodynamic Roughness Length in the Ablation Zone of the Greenland Ice Sheet.* Boundary-Layer Meteorology , 2008. **128:**p315–338

Sohn, H-G., Jezek, K. C. and Van der Veen, C. J. *Jakobshavn Glacier, West Greenland: 30 years of space borne observations.* Geophysical Research Letters, 1998. **25**(14): p2699-2702

Tamisiea, M. E., Mitrovica, J. X., Davis, J. L., and Milne, G. A. *Long Wavelength Sea Level and Solid Surface Perturbations Driven by Polar Ice Mass Variations: Fingerprinting Greenland and Antarctic Ice Sheet Flux*. Space Science Reviews, 2003. **108**: p81-93.

Tamisiea, M., Mitrovica, J.X. , Milne, G.A. and Davis, J.L. *Global Geoid and Sea-Level Changes Due to Present-Day Ice Mass Fluctuations*. Journal of Geophysical Research, 2001. **106**: p30849-30863.

Tang, C. C. L., Ross, C. K., Yao, T., Petrie, B., DeTracey, B. M. and Dunlap, E. *The circulation, water masses and sea-ice of Baffin Bay*. Progress in Oceanography, 2004. **63**: p183–228.

Thomas, R., Frederick, E., Krabill, W., Manizade, S. and Martin, C. *Progressive increase in ice loss from Greenland*. Geophysical Research Letters, 2006. **33**(L10503)
doi:10.1029/2006GL026075

Thomas, R., Akins, T., Csatho, B., Fahnestock, M., Gogineni, P., Kim, C. and Sonntag, J. *Mass balance of the Greenland ice sheet at high elevations*. Science, 2000. **289**: p426–428.

Tripati, A. K., Eagle, R. A., Morton, A., Dowdeswell, J. A., Atkinson, K. L., Bahé Y., Dawber, C. F. , Khadun, E., Shaw, R. M. H.,Shorttle, O. and Thanabalasundaram, L. *Evidence for glaciation in the Northern Hemisphere back to 44 Ma from ice-rafted debris in the Greenland Sea.* Earth and Planetary Science Letters, 2009. **265**: p112-122

Trouet, V., Esper, J.,Graham, N. E., Baker, A., Scourse, J. D., Frank, D.C. *Persistent Positive North Atlantic Oscillation Mode Dominated the Medieval Climate Anomaly*, Science, 2009. **324**: pp78-80

Tushingham A. R. and Peltier W R. Ice-3G' *A New Global Model Of Late Pleistocene Deglaciation Based Upon Geophysical Predictions Of Post-Glacial Relative Sea Level Change*. Journal of Geophysical Research, 1991. **96**(B3): p 4497-4523

Van der Plassche, O. *North Atlantic Climate–Ocean Variations and Sea Level in Long Island Sound, Connecticut, since 500 cal yr A.D.* Quaternary Research, 2000. **53**: p89–97

Van de Wal, R. S. W., Boot, W., van den Broeke, M. R., Smeets, C. J. P. P., Reijmer, C. H., Donker, J. J. A, Oerlemans, J. *Large and Rapid Melt-Induced Velocity Changes in the Ablation Zone of the Greenland Ice Sheet*. Science, 2008. **5855**: p111-113

Van Tatenhove, F.G.M., van der Meer, J.J.M., and Koster, E.A. *Implications for deglaciation chronology from new AMS age determinations in central west Greenland*: Quaternary Research, 1996. **45**: p 245-253.

Velicogna. I. and Wahr, J. *Acceleration of Greenland ice mass loss in spring 2004*. Nature, 2006. **443**(7109): p329-331.

Wadhams, P., and Munk, W. *Ocean freshening, sea level rising, sea ice melting*. Geophysical Research Letters, 2004. **31:** L11311,. doi:10.1029/2004GL020039.

Wake, L.M., Milne, G.A. and Leuliette, E. *20th Century sea-level change along the eastern US: unravelling the contributions from steric changes, Greenland ice sheet mass balance and Late Pleistocene glacial loading.* Earth and Planetary Science Letters, 2006. **250**(3-4): p572-580.

Weidick , A. and Bennike, O. *Quaternary glaciation history and glaciology of Jakobshavn Isbrae andthe Disko Bugt region,West Greenland: a review*. Geological Survey of Denmark and Greenland Bulletin, 2007. **14**:13pp

Woodroffe, S. A. and Long, A. J. *Salt marshes as archives of recent relative sea level change in West Greenland* .Quaternary Science Reviews, 2009. **28**(17-18): p 1750-1761.

Woodworth, P.L. and Player, R. *The Permanent Service for Mean Sea Level: an update to the 21st century*. Journal of Coastal Research, 2003. **19**: p287-295.

Wouters, B., Chambers, D. and Schrama, E. J. O. *GRACE observes small-scale mass loss in Greenland.* Geophysical Research Letters, 2008. **35**: L20501. doi:10.1029/2008GL034816.

Zwally, H. J., Giovinetto, M. B. , Li, J., Cornejo, H. G. , Beckley M. A., Brenner, A. C., Saba, J. L. and Yi, D. *Mass changes of the Greenland and Antarctic ice sheets and shelves and contributions to sea level rise 1992-2002*. Journal of Glaciology, 2005. **51**(175): p509-524.

Zwally, H. J., Abdalati, W., Herring, T., Larson, K., Saba, J. and Steffen, K. *Surface Melt–Induced Acceleration of Greenland Ice-Sheet Flow*. Science, 2002. **297**: p218-222.